

Dem Fachbereich Physik/Elektrotechnik
der Universität Bremen
vorgelegt von

Ismael Núñez-Riboni

September 2005

Alfred Wegener Institut für Polar- und Meeresforschung,
Bremerhaven.



1. Gutachter: Prof. Dr. Peter Lemke
2. Gutachter: Prof. Dr. Reiner Schlitzer

Cover illustration: chart of surface currents in the South Atlantic Ocean, by Krümmel, O. (1882), *Bemerkungen über die Meeresströmungen und Temperaturen in der Falklandsee*. Aus dem Archiv der Deutschen Seewarte, V, Hamburg, Nr. 2, 25 pp.

dejo un decilitro de ola atlántica
que guardo en un frasco verdiazul
para que no extrañe

Mario Benedetti

Contents

Contents	1
Abstract	3
Table of abbreviations and acronyms	5
Introduction	7
0.1 The South Atlantic ocean	9
0.2 AAIW discovery	9
0.3 AAIW characteristics	10
0.4 AAIW formation	11
0.5 AAIW circulation	13
0.6 Transports of AAIW	16
0.7 AAIW dynamics	18
Chapter 1 Fundamentals	21
1.1 Floats	21
1.2 Neutral density surfaces	28
Chapter 2 Data description	29
2.1 Float data	29
2.2 Neutral surfaces	30
2.3 Vertical selection of float data	35
2.4 Geostrophic projection: a test	39
Chapter 3 Data analysis	41
3.1 Space-time average	41
3.1.1 Choice of the best grid	44
3.1.2 Error ellipses	46
3.2 Objective Analysis: theory	49
3.2.1 The error matrix	51
3.2.2 Vector fields	53
3.2.3 The longitudinal covariance function (LCF)	54
3.2.4 Estimation of the LCF under cylindrical symmetry	57
3.2.5 Estimation of the LCF without assumption of symmetry: an attempt	62
3.2.6 The stream function	64
3.2.7 Summary	66
3.3 Objective Analysis: application	66
3.3.1 Scalar OMSTA (objective mapping with space-time averages)	67
3.3.2 Vectorial OMSTA (objective mapping with space-time averages)	67
3.3.3 OMPFV (objective mapping with primal float velocities)	67
3.3.4 The mapping area	68
3.4 Transports	69
3.4.1 Volume transport	71
3.4.2 Temperature transport	72
3.4.3 Salinity transport	73
3.4.4 Freshwater transport	74
3.4.5 Input data	75
Chapter 4 Results	77
4.1 Space-time averages and error ellipses	77
4.2 Objective maps and the flow pattern	77
4.3 Volume transports	81
4.3.1 Mean zonal transport	81
4.3.2 Basin wide meridional transport	84

4.3.3	Transport balance	86
4.4	Temperature transport	86
4.5	Salinity and freshwater transports	88
4.6	Western boundary currents.....	90
Chapter 5	Discussion	95
5.1	Comparison of methods and data sets	95
5.1.1	Isobaric versus isoneutral data set.....	95
5.1.2	Scalar versus vectorial OM approaches	97
5.1.3	OMFPV versus vectorial OMSTA	97
5.2	Currents and transports.....	101
5.2.1	The subtropical region.....	101
5.2.2	Tropical region	102
5.2.3	Western boundary currents.....	104
5.2.4	Volume transport	106
5.2.5	Temperature transports.....	109
5.2.6	Freshwater transport	114
Chapter 6	Summary and conclusions.....	117
Appendix 1	The Gauss-Markov theorem.....	121
Appendix 2	Estimated error.	125
	Index of results' figures.....	127
	Bibliography	129
	Acknowledgements	145

Abstract

This study uses a data set of 611 float years in the south and tropical Atlantic to describe the flow of Antarctic Intermediate Water (AAIW). The data set includes pop-up and acoustically tracked floats that drifted within more than one decade in the area 60°W to 30°E and 70°S to 10°N. Float data is constrained in the vertical according to two isoneutral surfaces ($\gamma^{\sigma} = 27.25$ and $\gamma^{\sigma} = 27.55$), according to the characteristics of AAIW. Velocity space-time averages are calculated for various grid resolutions and with cells deformed to match the bathymetry, f/H or f/h (with H being the water depth and h being the thickness of the AAIW layer). Judged by the degree of alignment between respective isolines and the resulting average velocity fields, the best grid is based on a cell size of 3° (latitude) by 4° (longitude) with cells deformed according to f/h . Using this grid, objectively estimated mean currents (and their associated errors), as well as meridional and zonal volume transports are estimated. Since these space-time averages and the corresponding objective maps were unable to reveal the Intermediate Western Boundary Current (iWBC), an alternative approach based on an objective mapping with primal data in overlapping subsets was also applied. With this goal, an isotropic longitudinal covariance function was estimated considering cylindrical symmetry and neglecting the long-range zonal covariance.

Results show an anticyclonic Subtropical Gyre centered near 36°S and spanning from 23°±0.5°S to 45° ± 0.5°S. The South Atlantic Current (SAC) meanders from 35°S to 45°S and shows a mean speed of $12.4 \pm 8.4 \text{ cm s}^{-1}$ ($7.1 \pm 3.9 \text{ Sv}$). The northern branch of the Subtropical Gyre (nBSG) is located between 22°S and 32°S and flows westward with a mean speed of $4.7 \pm 3.3 \text{ cm s}^{-1}$ ($8.2 \pm 4.7 \text{ Sv}$). The Agulhas Current shows a speed of $25.3 \pm 14.2 \text{ cm s}^{-1}$ and the Agulhas Return Current of $22.9 \pm 13.2 \text{ cm s}^{-1}$. An eastward current lies immediately north of the Subtropical Gyre (20°S). The tropical zone presents 8 zonal jets whose magnitudes and positions are discussed in comparison with previous studies. The stream function suggests the existence of a Tropical Gyre, flow of the SAC farther into the Indian Ocean, weak advective connections between the SAC and the nBSG as well as between the Agulhas System and the South Atlantic Subtropical Gyre (in agreement with the notion of a Subtropical Supergyre, yet the flow would be inhibited by the Cape Cauldron). Volume transport estimates expose the Subtropical Gyre as a non-balanced system with a divergence point at 27°S: the Santos bifurcation. From this point, two western boundary currents flow along the South American coast carrying most of the meridional transports: the iWBC northwards and the Intermediate Brazil Current (iBC) southwards. Volume, temperature and freshwater transports of AAIW are compared with transport values found in the literature, and the role they play in the meridional circulation is discussed.

Keywords: Antarctic Intermediate Water (AAIW), floats, neutral density surfaces, South Atlantic, general circulation, transports, objective analysis.

Table of abbreviations and acronyms

Acronym	Connotation
AABW	Antarctic Bottom Water
AAIW	Antarctic Intermediate Water
ACC	Antarctic Circumpolar Current
ALACE	Autonomous Lagrangian Circulation Explorer
AMOC	Atlantic Meridional Overturning Cell
AOML	Atlantic Oceanographic and Meteorological Laboratory
APEX	Autonomous Profiling Explorer
APFZ	Antarctic Polar Frontal Zone
Argo and Argos	The “all-seeing” in the Greek mythology
AWI	Alfred Wegener Institute
BC	Brazil Current
BLUE	Best Linear Unbiased Estimation
CMOS	Complementary Metal Oxide Semiconductor
CORC	Consortium on the Ocean’s Role in Climate
cSEC	Central South Equatorial Current
CTD	Conductivity-Temperature-Depth instrument
DBE	Deep Basin Experiment
EIC	Equatorial Intermediate Current
eSEC	Equatorial branch of the South Equatorial Current
FS	Forschungsschiff (research vessel in German)
HMS	Her (or His) Majesty's Ship
iBC	Intermediate Brazil Current
iWBC	Intermediate Western Boundary Current
KAPEX	Cape of Good Hope Experiment
LCF	Longitudinal Covariance Function
MAR	Mid-Atlantic Ridge
Marvor	Breton word for sea horse
MATLAB	Matrix Laboratory
MODE	Mid-Ocean Dynamics Experiment
NADW	North Atlantic Deep Water
NBC	North Brazil Current
nBSG	Northern Branch of the Subtropical Gyre
NICC	Northern Intermediate Countercurrent
nSEC	Northern branch of the South Equatorial Current
NSTF	North Subtropical Front
OM	Objective Mapping / Objective Analysis
OMPFV	Objective Mapping with Primal Float Velocities
OMSTA	Objective Mapping with Space-Time Averages
PALACE	Profiling ALACE
PF	(Antarctic) Polar Front
Provor	Profiling Marvor

Table of abbreviations and acronyms (continued)

PSS-78	Practical Salinity Scale (year 1978)
PW	Petawatts, 1 PW = 1×10^{15} Watts
RAFOS	SOFAR spelled backwards
RMS	Root-Mean-Square
SAC	South Atlantic Current
SAMBA	SubAntarctic Motions in the Brazil Basin
SAMW	SubAntarctic Mode Water
SAVE	South Atlantic Ventilation Experiment
SAW	SubAntarctic Surface Water
SECC	South Equatorial Countercurrent
SEUC	South Equatorial Undercurrent
SF	Scotia Front
SICC	Southern Intermediate Countercurrent
SOFAR	Sound Fixing and Ranging
SOLO	Sounding Oceanographic Lagrangian Observer
SSTF	South Subtropical Front
Sv	Sverdrups, 1 Sv = 1×10^6 m ³ s ⁻¹
WOCE	World Ocean Circulation Experiment

Introduction

Since atmosphere and ocean form a coupled system, the ocean (by means of its interior circulation) plays a major role in the distribution of the planet's heat content and of gases like oxygen, carbon dioxide (CO₂) and chlorofluorocarbons (CFCs). This, together with formation of water masses and air-sea exchange of heat and freshwater, influences the climate on the Earth on a broad spectrum of timescales. Therefore, to understand climate and its change, a diverse range of oceanic processes (such as up and downwelling, small scale and eddy diffusion, as well as buoyancy fluxes) and oceanic phenomena (such as the thermohaline circulation, Rossby and Kelvin waves as well as wind effects on the surface and in the deep of the ocean) must be understood. The overall effect of these processes and phenomena influencing the movement of water in the long term has been conceptualized by the "ocean conveyor belt" (Gordon, 1986; Broecker, 1987 and 1991; Schmitz, 1995; Figure 0.1 below).

In the three-layer model of Schmitz (1995), the ocean conveyor belt consists of a circuit of warm water (red path in Figure 0.1) flowing near the surface, cool water at middle (though not intermediate) depths (green path in Figure 0.1) and cold waters along the bottom (blue path in Figure 0.1). The warm water cools in the North Atlantic, downwelling eventually, whereas the cool water upwells in the Southern Ocean. More detailed, the general circulation of the world ocean comprises several basin scale cells. One of them is the Atlantic Meridional Overturning Cell (AMOC), forming the Atlantic part of the conveyor belt: cold North Atlantic Deep Water (NADW), produced in the Norwegian and Labrador Seas, flows southwards along the western boundary of the Atlantic basin. Fresh Antarctic Intermediate Water (AAIW) and salty Antarctic Bottom Water (AABW) flow northwards above and below the NADW, as depicted by the vertical section in Figure 0.2.

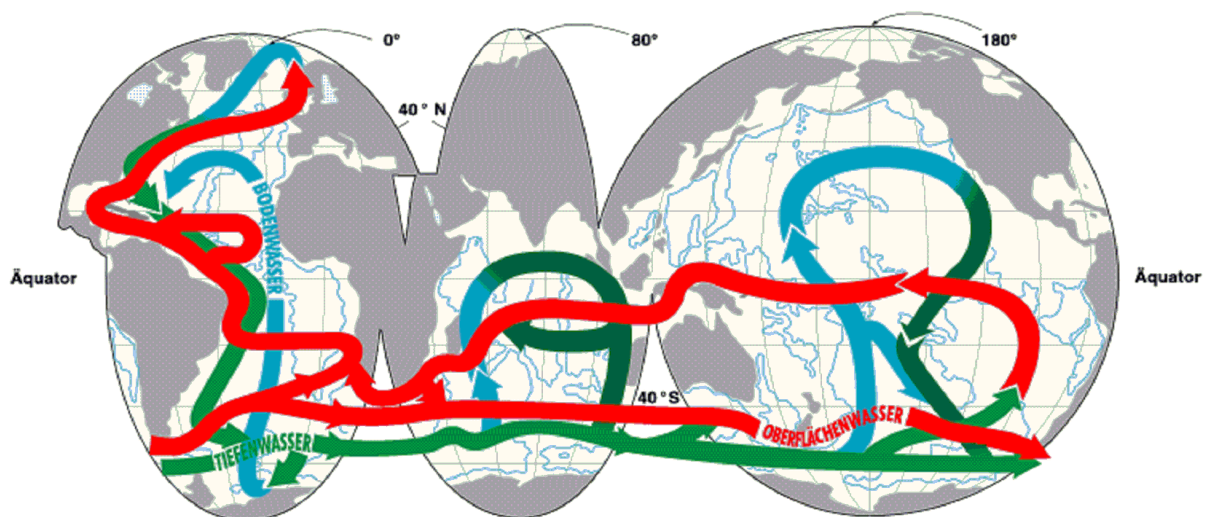


Figure 0.1 Schematics of the ocean conveyor belt (after Schmitz, 1995).

Most prominently, the AMOC's influence on climate manifests itself in the formation rate of NADW, which depends on atmospheric cooling and the surface salinity of the North Atlantic (Broecker et al., 1985). In turn, this salinity is determined either by an excess of evaporation over precipitation and river run off due to an atmospheric water transport from the North Atlantic to the North Pacific (Broecker et al., 1985; Broecker, 1991) or by a

positive feedback of the ocean conveyor belt (Rahmstorf, 1996 and 1999). The transport of water from the ocean to the atmosphere influences the air temperature because this transport carries heat (4×10^{21} calories each year; Broecker, 1991) and because “water vapor is the atmosphere’s most powerful greenhouse gas” (Broecker, 1997a, page 5). Hence, the production rate of NADW is strongly linked to Europe’s climate. This notion has been corroborated through the analysis of two Greenland ice cores together with pollen proxy data collected throughout Europe, which revealed several abrupt temperature and rainfall changes in the area climatologically affected by the North Atlantic during the last glacial period (Broecker et al., 1985; Broecker, 1991). These climate oscillations were correlated to variations in the strength and pattern of the ocean conveyor belt by computer models, sedimentary records and “the temporal record of the changes in the $^{14}\text{C}/^{12}\text{C}$ ratio in the atmosphere and upper ocean reservoir, as recorded in tree rings, coral, and varved sediments subject to independent dating” (Broecker, 1997b, p. 1585).

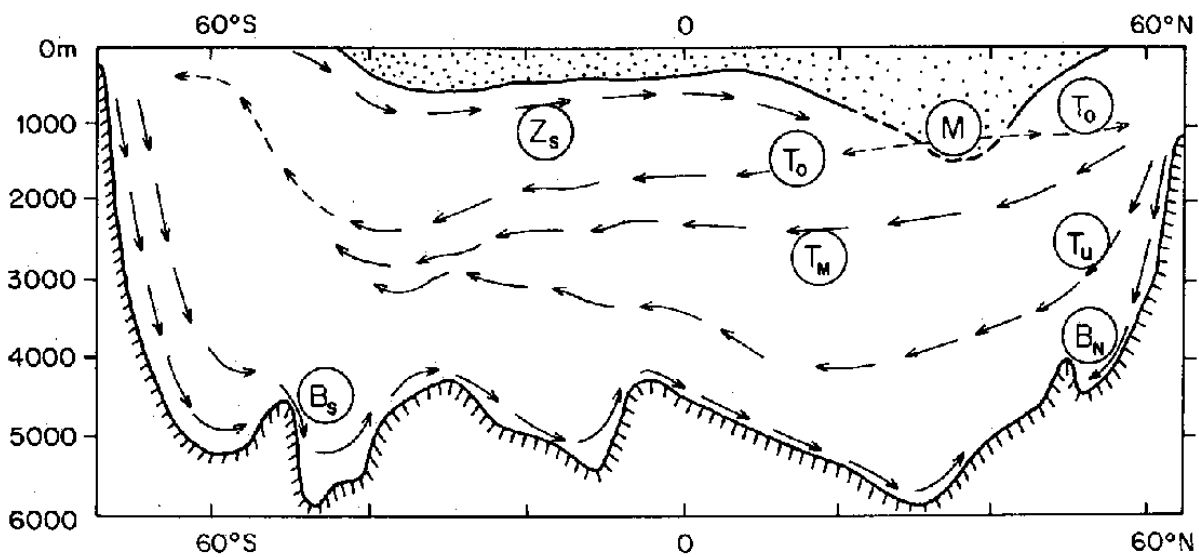


Figure 0.2. Meridional-vertical section of the Atlantic Ocean exhibiting the Atlantic Meridional Overturning Cell (AMOC), as conceived by Wüst (1935) (simplified by Schmitz, 1995). Z_S denotes Antarctic Intermediate Water (AAIW); B_S and B_N denote bottom water south and north; T_O , T_M and T_U denote upper, middle, and lower deep water; M denotes Mediterranean influence. The stippled layer is the “warm water sphere”.¹

Therefore, variations in the ocean conveyor belt could make the coupled ocean-atmosphere system change from one quasi stable mode of operation to another, yielding rapid climate variations. In an extreme situation, if the AMOC would turn off, “the mean annual temperature of the lands around the North Atlantic basin would drop by 5 to 10°C” (Broecker, 1997b, p. 4). Such a break of the ocean conveyor belt could have triggered a millennial duration cold event occurred order of ten thousands years ago (the Younger Dryas; Broecker, 1997b, 1990 and 1999). In contrast with the slow climate changes related to Milankovich cycles, regional climate changes triggered by perturbations in the ocean conveyor belt could occur in time periods as short as a decade (Broecker, 1997a and 1990; Rahmstorf, 1999). Hence, to understand the different mechanisms involved in the ocean conveyor belt and monitor its transports (Schmitz, 1995; Ganarchaud and Wunsch, 2000) is relevant because this knowledge yields a better understanding of the impact of the ocean

¹ The non conventional nomenclature of Wüst (1935) is understandable when considering the names of the water masses in German: Z_S stands for *subantarktisches Zwischenwasser*; T_O , T_M , T_U stand for *obere, mittel- and untere Tiefwasser*; B_S and B_N denote *Bodenwasser (Nord and Süd)*.

circulation on climate. In particular, the quantification of the production rate of NADW necessitates an understanding of the AMOC and its components, i.e., the flow of AAIW in the South Atlantic and the transports of temperature and salt associated with it.

Therefore, the main objective of this study is to provide a circulation scheme and the associated estimates of volume, salt and temperature transports within the AAIW layer. With this purpose, all historic and recent trajectory float data for the South Atlantic was gathered, yielding a comprehensive data set. Computations of objectively mapped velocity fields result in estimates of the abovementioned transports. The study will proceed with a summary of the current knowledge of AAIW in the South Atlantic regarding its origin, circulation and the underlying dynamics. This is followed by a technical description of the instrumentation used, i.e. floats of various types and of the variable used to constrain AAIW in the vertical (neutral density) in Chapter 1. Chapter 2 describes the float data itself, as well as the hydrographic one. The data analysis is presented in Chapter 3, whereas results are shown in Chapter 4 and discussed in Chapter 5. Chapter 6 includes a summary and conclusions. The two appendices are related to the main method used to analyze the data (objective mapping).

0.1 The South Atlantic ocean

The South Atlantic ocean (Figure 0.3) forms the connection between the South Pacific, the North Atlantic and the Indian Ocean. It covers the region from the equator to Antarctica (according to the International Hydrographic Bureau) or to the Subtropical Front (in the context of oceanography; Tomczak and Godfrey, 1994). It is bound by South America in the west and Africa in the east. Its morphology is rather simple and void of adjacent seas. The South Atlantic is divided equally into eastern and western basins by the Mid-Atlantic Ridge (MAR), located at approximately 18°W. West of the MAR, the Argentine and Brazil Basins are separated by the quasi-zonal Rio Grande Rise. East of the MAR, the Angola and Cape Basins are separated by the Walvis Ridge, which stretches from the MAR at 40°S to the African coast at 20°S. The only important asymmetry between the eastern and western basins lies in the topography of the Rio Grande Rise and the Walvis Ridge: the first has the Rio Grande Gap to the west, which permits northward flow of deep water up to 4000 m, whereas the Walvis Ridge does not permit any flow at the same depth. The Romanche Fracture Zone, near the equator, allows water flow between the western and eastern deep basins at 4500 m depth (Tomczak and Godfrey, 1994).

0.2 AAIW discovery

AAIW was first identified in the South Atlantic and its discovery is commonly assigned either to Wüst (1935) or Deacon (1933), after their expeditions of 1925-1927 with the FS Meteor and the HMS Discovery, respectively. However, while both, Deacon and Wüst, provided the first enduring theory about the origins of AAIW, they did not identify the water mass for the first time. In fact, the first measurements exhibiting the vertical salinity minimum were collected during the HMS Challenger expedition from 1872 to 1876 (Buchanan, 1877, as cited by Talley, 1996). Later, measurements during the “second German expedition to Antarctica” during the years 1911 to 1912, directed by Wilhelm Filchner on board the FS Deutschland,¹ detected the salinity minimum as well. After analyzing these data, Brennecke published a paper in 1921, which describes the motion at the salinity minimum layer as a “sub-Antarctic deep current” and “gives its origin as the surface drift out of the Weddell Sea” (cited from Deacon, 1933, page 222). Thereafter, Merz

¹ The FS Deutschland left from the port of Bremerhaven, the hometown of the Alfred Wegener Institute, on May 4th, 1911.

and Wüst's publication of 1922 presents a complete meridional salinity section, which clearly shows the salinity minimum (Talley, 1996). In his publication from 1927, the German polar researcher Erich von Drygalski uses data from the "first German expedition to Antarctica" (directed by himself) from 1901-1903 on board the FS Gauss. He describes the water mass related to the salinity minimum as being of Antarctic origins (Deacon, 1933). Hence, when discussing the discovery of AAIW, Buchanan (1877) and Brennecke (1921) need mentioning, as these researchers actually discovered the water mass. Probably, Brennecke was the first researcher providing a theory about AAIW's origin.

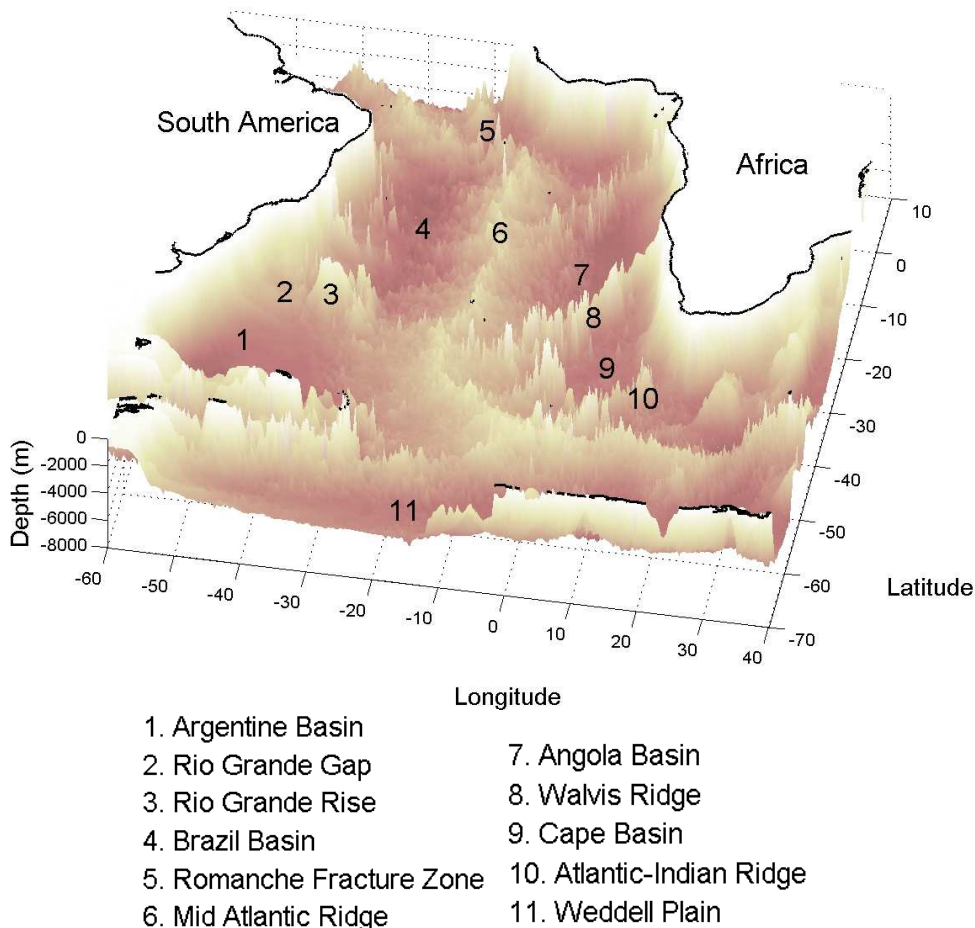


Figure 0.3. South Atlantic main topographic features after the Smith and Sandwell (1997) bathymetry.

0.3 AAIW characteristics

AAIW is a water mass that can be found in the three world oceans, is an integral part of the AMOC and can be conceived as a stratum or tongue of water located in the middle of the water column (Figure 0.2 and Figure 0.4). The two main characteristics of AAIW are salinity minimum (see Figure 0.4 and Figure 2.6) and oxygen maximum. In the South Atlantic, AAIW occupies a depth ranging from 650 to 1050 meters (Reid, 1994; Figure 2.5) and features a temperature and salinity of 2.2 °C and 33.8 close to its formation area, respectively (Tomczak and Godfrey, 1994). A particle of water in the AAIW layer flows northwards from the AAIW's southern origin, as it participates in a sequence of gyres spanning the entire Atlantic basin. The salinity core of AAIW can be recognized as far north as 21°N, however, by its silica signature, AAIW can be tracked up to 30°N (Talley, 1996).

AAIW salinity in the South Atlantic ranges from 34.2 to 34.7. As the water flows to the north, it mixes with the relatively saltier layers from above and below, increasing its salinity; similarly, it warms, exhibiting potential temperatures that range from 3°C (at 45°S) to 6°C (at 5°N).

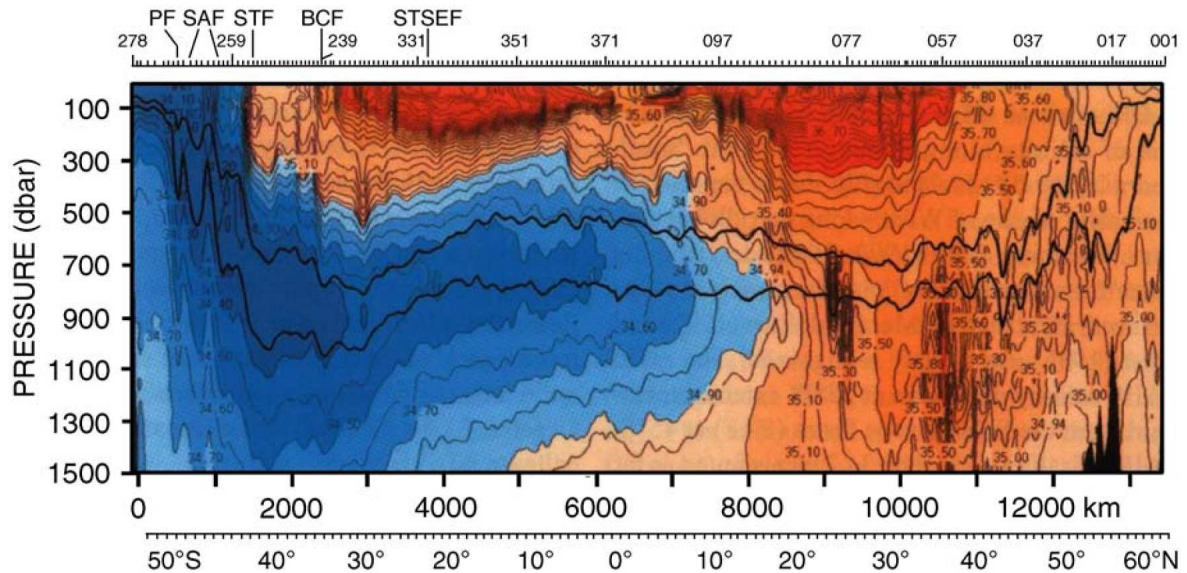


Figure 0.4. Meridional section of AAIW salinity along approximately 25°W, from South Georgia Island to Iceland, from 1988-1989. The two curves passing through the AAIW are the 31.7 and 31.9 σ_t isopycnal contours. Modified from Talley (1996, her Figure 1 (a)).

0.4 AAIW formation

Formation of AAIW is strongly related to the frontal structure of the Southern Ocean, which is composed by (from south to north; Figure 0.5): next to the continent, the Antarctic Zone; near 58°S the Scotia Front (SF); around 50°S the Antarctic Polar Frontal Zone (APFZ) (Emery, 1977) delimited by the (Antarctic) Polar Front (or Antarctic Convergence; Belkin and Gordon, 1996; designated PF in Figure 0.5) and the Subantarctic Front (designated SAF in Figure 0.5); the Subantarctic Zone, limited to the north at around 40°S by the Subtropical Front (or Subtropical Convergence), which is the limit of the Southern Ocean and is formed by two fronts (Belkin and Gordon, 1996): the South Subtropical Front (SSTF) and the North Subtropical Front (NSTF); farther north lies the Subtropical Zone of the South Atlantic.

In the vicinity of fronts, the water becomes fully homogenous in the vertical particularly during winter, due to strong convection produced by cooling (Tomczak and Godfrey, 1994; Hanawa and Talley, 2001). This yields a parcel of water with almost constant temperature and salinity, which becomes isolated from the surface during spring when the seasonal thermocline develops. This water is called Mode Water. The winter water in the Subantarctic Zone is referred to as Subantarctic Mode Water (SAMW; Figure 0.6). The origins of AAIW are related to SAMW flowing out of the APFZ. The three hypothesis on AAIW formation read as follows (oldest to newest):

- 1) Deacon, 1933 and Wüst, 1935. "The Antarctic surface water (...) sinks at the Antarctic convergence (and) mixes with Subantarctic Surface Water (SAW, in Figure 0.6) in a region of intense vertical mixing just north of the Antarctic convergence (in the South Atlantic). The mixture of water then sinks downwards towards the north, and spreads

over the whole of the South Atlantic Ocean” (cited from Deacon, 1933, page 220). Later, this notion has been supported by Molinelli (1981).

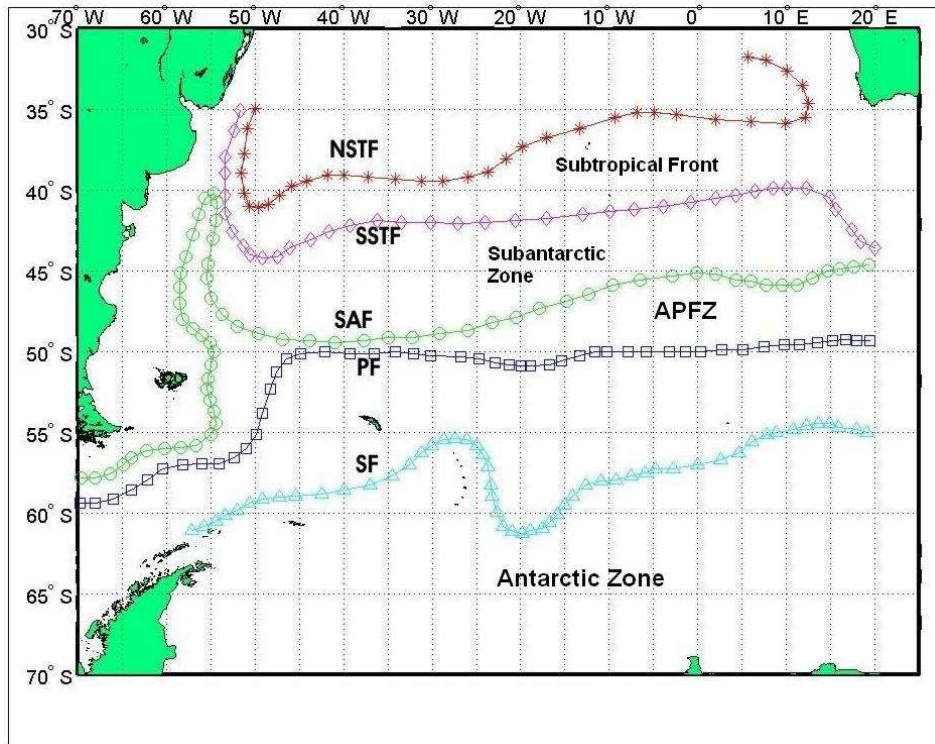


Figure 0.5 Fronts in the Southern Ocean and South Atlantic (kindly provided by Igor Belkin in a personal communication). NSTF: North Subtropical Front; SSTF: South Subtropical Front; SAF: Subantarctic Front; APFZ: Antarctic Polar Frontal Zone; PF: Polar Front; SF: Scotia Front.

- 2) McCartney, 1977. The formation of AAIW occurs in the eastern *South Pacific* at the Subantarctic Front, starting as SAMW. From there, the densest/coldest variety of SAMW (colder than 4.5°C) flows with the ACC through the Drake passage, feeding into the Malvinas/Falkland Current. Along this route, SAMW rises to the surface, freshens by precipitation and gains oxygen through air-sea interaction. Finally, it reaches the Brazil-Malvinas Confluence Zone: the region off South America where the northwards Malvinas/Falkland Current faces the southwards-flowing Brazil Current (BC, from now on; Stramma et al., 1990). At this point, the SAMW is injected into the Subtropical Gyre as AAIW, sinking to ca. 800 m below the warmer SAMW due to the formers greater density.
- 3) Piola and Gordon, 1989. This hypothesis can be interpreted as a combination of the previous two: Piola and Gordon also accept the formation of AAIW in the southern Pacific and its subsequent advection to the Brazil-Malvinas Confluence Zone as described above, but they argue that the change in properties during this process is too strong to be explained solely by the interaction with the atmosphere. Hence, they suggest that mixing with an Antarctic water mass is required. To support their theory, they used data from continuous *in situ* temperature and salinity hydrographic stations with high quality water samples collected between 1975 and 1984, and tracked the changes in the hydrographic properties of certain water parcels with particular densities. More recently Sloyan and Rintoul (2001b) support the notion of Piola and Gordon (1989) by means of inverse calculations.

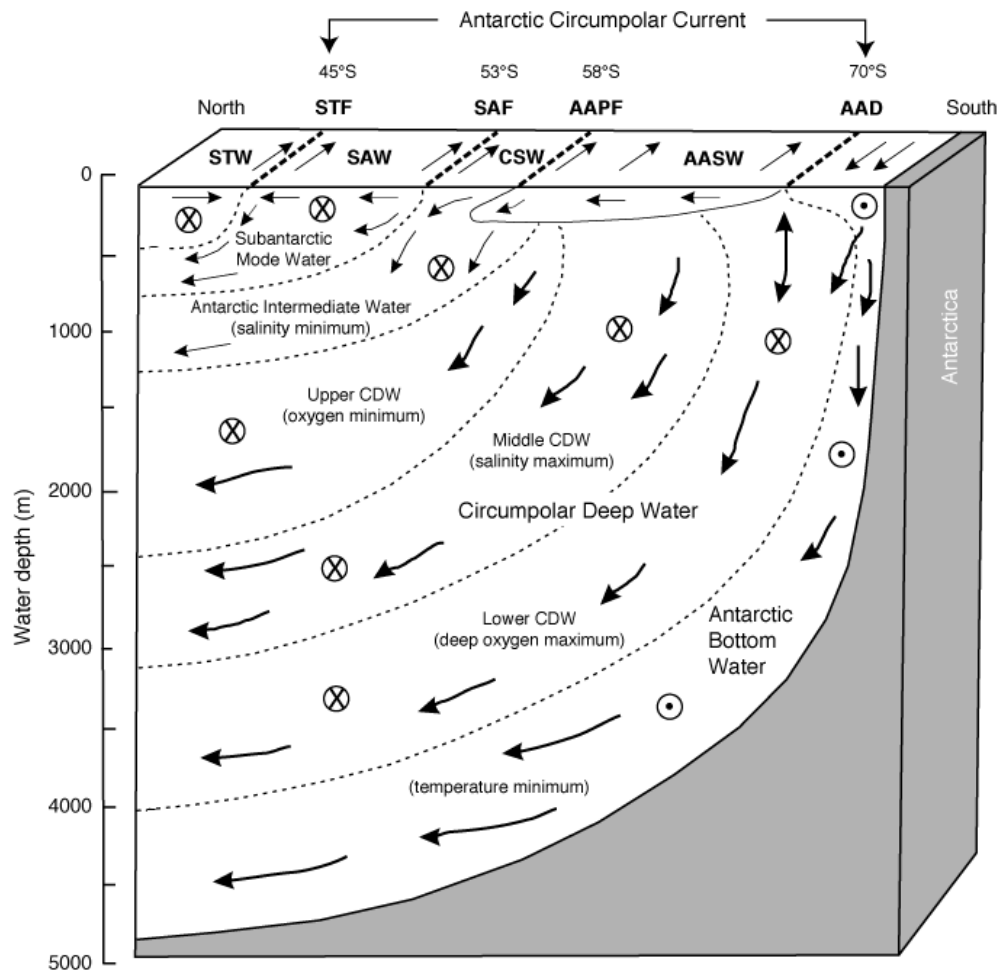


Figure 0.6. Water masses, fronts, and circulation patterns that characterize the *southwest Pacific* section of the Southern Ocean (modified from Carter et al., 2004; their Figure F5). STF = Subtropical Front, SAF = Subantarctic Front, AAPF = Antarctic Polar Front, AAD = Antarctic Divergence, CDW = Circumpolar Deep Water, STW = Subtropical Water, SAW = Subantarctic Water, CSW = Circumpolar Surface Water, AASW = Antarctic Surface Water.

The notion of SAMW flowing through the Drake Passage and being injected into the Subtropical Gyre at the Confluence Zone (as AAIW) has been defended by Rintoul (1991), Macdonald (1993) as well as by Sloyan and Rintoul (2001b). Rintoul et al. (2001) further assert that the SAMW that supplies the AAIW in the South Atlantic is coming from the Indian Ocean and traveling with the ACC all the way around Antarctica before reaching the eastern South Pacific.

0.5 AAIW circulation

The fact that the AAIW has a net northward flow was deduced by Deacon (1933) and Wüst (1935) from their hydrographic measurements. Deacon and Wüst suggested a basin wide, sluggish northward flow of AAIW, with Wüst (1935) proposing a slightly intensified flow along the Brazilian shelf for latitudes lower than 20°S in addition. Subsequent geostrophic calculations (Defant, 1941; Figure 0.7) suggested a continuous northward intermediate western boundary current from 30°S to the equator and beyond, while retaining significant interior northward currents for the region south of 25°S. More recent geostrophic estimates (Reid, 1989; Gordon and Bosley, 1991 Suga and Talley, 1995, Talley, 1996), modified this concept to one being comprised of several gyres on a basin scale. The main circulation

structure could be ruled by two basin scale, zonally stretched gyres: an anticyclonic gyre centered near 34°S, called the Subtropical Gyre, and the cyclonic Tropical Gyre (Gordon and Bosley, 1991) centered at about 10-15°S, also called the South-Equatorial Gyre. Local recirculation cells might occur inside these gyres. Suga and Talley (1995) assert that three narrower gyres were to be found inside the tropical gyre: two cyclonic cells at the northern and southern limits of the gyre, and an anticyclonic cell sandwiched between them (centered at about 13°S).

In these concepts, freshly formed AAIW is injected into the southern branch of the Subtropical Gyre, successively navigates the gyres to the north and eventually cross the equator into the North Atlantic. Even though it is possible that other intrusion points exist along the southernmost limb of the Subtropical Gyre (Boebel et al., 1999a), the Brazil-Malvinas Confluence Zone seems to be the foremost point of entrainment (Piola and Gordon, 1989; Boebel et al., 1999b and c). (Figure 0.8): The collision of the Malvinas/Falkland current with the BC at the Confluence Zone yields the eastward flowing South Atlantic Current (SAC; Reid, 1977; Stramma and Peterson, 1990), which meanders across the South Atlantic basin until it meets the Agulhas System (Figure 0.; Lutjeharms, 1996; Boebel et al, 2003). The Agulhas System is formed by the Agulhas Current (the western boundary current of the Indian Ocean along the east coast of Africa; Peterson and Stramma, 1991), the Agulhas Retroflexion (Lutjeharms and van Ballegooyen, 1988) and the resulting Agulhas Return Current (Peterson and Stramma, 1991), which flows back into the Indian Ocean. The Agulhas Retroflexion folds back on itself, shedding a pool of Indian Ocean water of around 250 Km in diameter and more than 1000 m depth (Lutjeharms, 1996), with an average frequency of six per year (de Ruijter et al., 1999). These Agulhas Rings can travel across the South Atlantic basin up to its western boundary. Together with the Agulhas filaments (Lutjeharms and Cooper, 1996), Agulhas Rings are considered the main conduit of water from the Indian Ocean to the South Atlantic.

AAIW's flow back to the Confluence Zone occurs along the Northern Branch of the Subtropical Gyre (nBSG), which emerges from the Benguela Current (Garzoli and Gordon, 1996; Richardson and Garzoli, 2003) along the African coast. This current separates eventually from the coast and flows westwards (where it is called Benguela Current Extension) across the basin, until it reaches the South American coast. There, it splits at the Santos Bifurcation (Boebel et al., 1997; Boebel et al, 1999a) into an Intermediate Western Boundary Current (iWBC; Boebel et al., 1999c) and an intermediate expression of the BC (iBC, from now on; Boebel et al., 1999b), which closes the circuit of the Subtropical Gyre. Hence, recirculated AAIW is drawn into the Confluence Zone while fresher water is injected from the Subantarctic Front. After mixing, this mélange is frequently expelled into the Subtropical Gyre by a quasi-stable cyclonic vortex observed at 40°S and 50°W (Boebel, et al., 1999c). The iWBC flows along the Brazilian coast into the tropical Atlantic, where a series of zonal jets are observed (Boebel et al, 1999a and c, Schmid et al., 2001, Molinari et al., 1981, Reid, 1996, Talley, 1996, Ollitrault, 1994, Richardson and Schmitz, 1993).

The existence of the Subequatorial Gyre is however disputed and the strengths of the basin-wide gyres are not well known, as are the branching ratios of those parts of AAIW that remain in each gyre or transfer to an adjacent one, either during their trans-Atlantic journey or at the ocean boundaries. Similarly, the interaction between the SAC and the Agulhas System is not clear. One theory (Stramma and Peterson, 1990; Garzoli and Gordon, 1996) asserts that part of the SAC deflects to the North along the South African coast and becomes part of the Benguela Current, whereas the other part would flow eastwards into the Indian Ocean near 40°S (as depicted in Figure 0.8). Nevertheless, "Gordon et al. (1992) conclude on the basis of differences in the equilibrium ratio of chlorofluoromethane-11 to chlorofluoromethane-12 between the Benguela Current and the (SAC), that the SAC does not flow directly into the Benguela Current" (Sloyan and Rintoul, 2001b, page 1026).

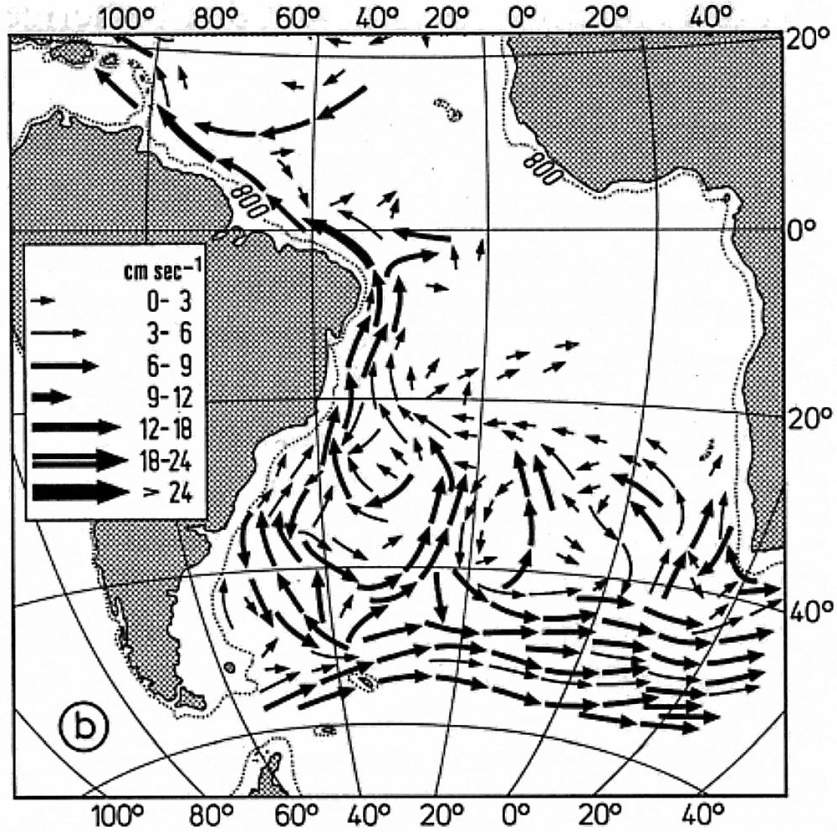


Figure 0.7 Geostrophic currents at 800 m depth (modified from Defant, 1941). The dotted line is the 800 m isobath.

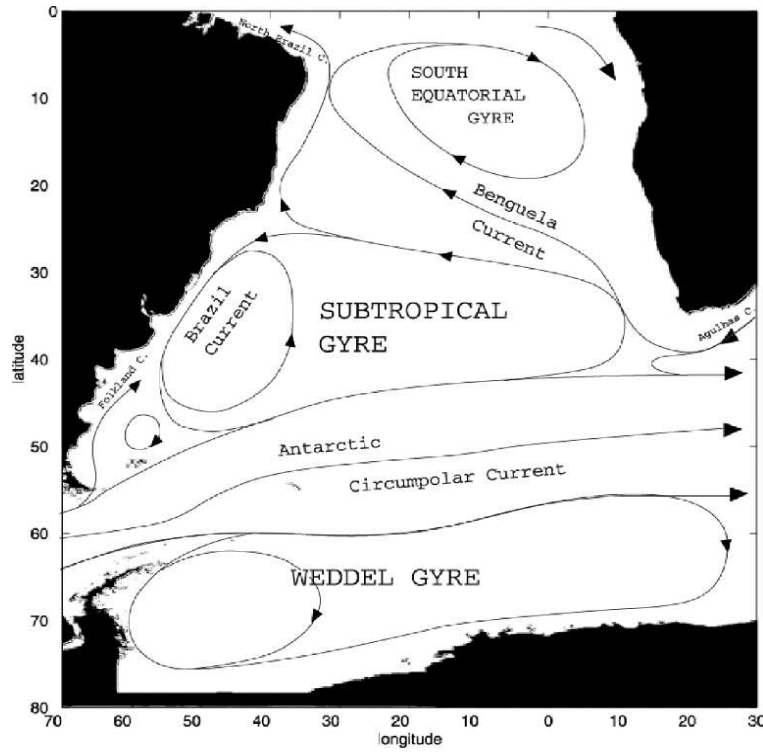


Figure 0.8 Schematics of AAIW circulation in the South Atlantic (adapted from You, 1999; his Figure 16).

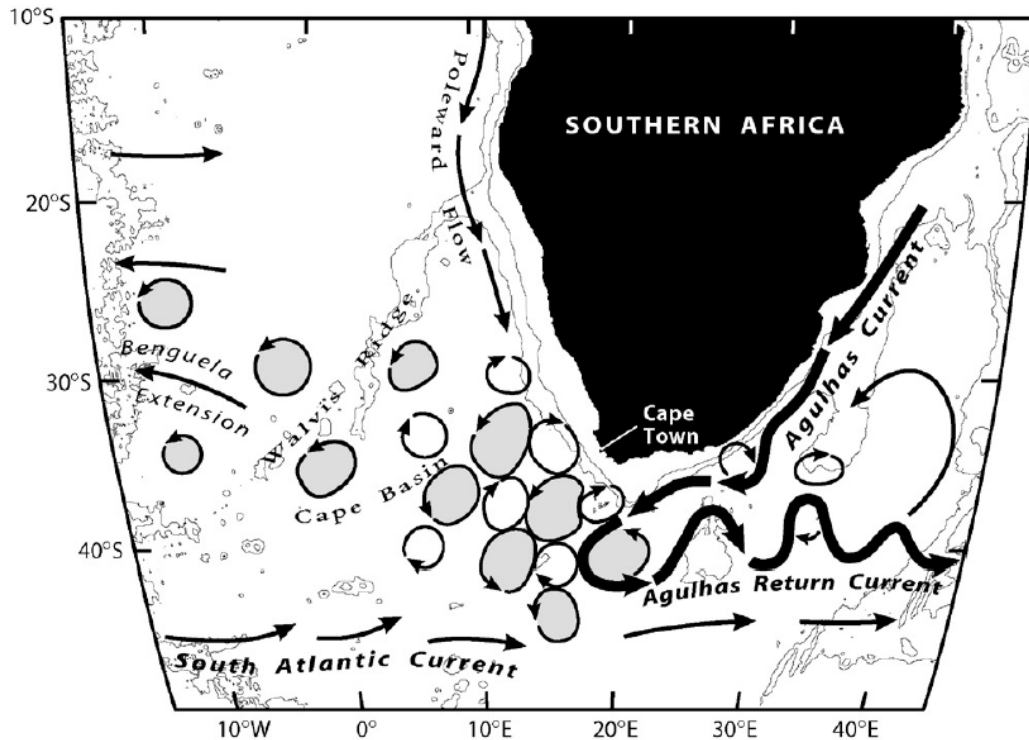


Figure 0.9 Schematic of the traditional view of oceanic flow patterns around southern Africa for the upper and intermediate water layers. Oceanic features are labeled in italics, geographic features in regular font. Topography is delineated by the 1000 and 3000 m isobaths. From Richardson et al., 2003.

Along the same line, the possibility of an advective connection between the Agulhas System and the Subtropical Gyre has been disputed. Speich et al. (2002) suggest that part of the Agulhas Current eventually continues as part of the Benguela Current, based on the notion that the Indian Subtropical Gyre is coupled through wind stress with the Atlantic Subtropical Gyre in a “Subtropical Supergyre” (de Ruijter, 1982; Gordon et al., 1992). De Ruijter et al., (1999) however state, that the exchange of water between these oceans is too small to support the theory, since “local dynamical processes in the highly nonlinear regime around South Africa play a crucial role in inhibiting the connection between the two oceans” (De Ruijter, et al., 1999, page 20,885). Boebel et al. (2003) back up this notion, based on an analysis of floats trajectories from KAPEX (Boebel et al., 2000) as well as sea-surface height data, establishing that the region between the Agulhas System and the Subtropical Gyre (the Cape Cauldron) is so turbulent that no continuous advection between the two prevails.

To fill all these gaps of knowledge, the present study examines the flow patterns of AAIW across the entire South Atlantic basin for the first time, addressing the following key questions:

- Is there an advective connection between the Agulhas System and the South Atlantic Subtropical Gyre?
- Is there an advective connection between the SAC and the nBSG?

0.6 Transports of AAIW

Volume (or, equivalently, mass) transport estimates are necessary to compute other kinds of oceanographic property transports, like nutrients, salt and heat. Particularly, estimates of the meridional volume transports of AAIW in the South Atlantic are important because AAIW could supply a third part of the flow balancing the export of NADW (Rintoul, 1991; Sloyan

and Rintoul, 2001b). In spite of the convoluted AAIW circulation patterns in the South Atlantic, it is believed that the meridional volume transport of AAIW is basically northward at all latitudes (Deacon, 1933; Wüst, 1935; McCartney, 1977). This is particularly true north of 27°S, where the iWBC starts flowing northwards (Boebel et al., 1999c). This current is believed to be the main conduit of water and physical properties at the AAIW horizon to the South Atlantic tropics and further into the northern hemisphere (Defant, 1941, Gordon and Bosley, 1991, Boebel, et al., 1999c, Jochum and Malanotte-Rizzoli, 2003).

Of the different oceanic processes, heat transport might be the one that influences Earth's climate by far the most. The ocean plays the role of a heat buffer to the atmosphere, absorbing heat during summer and releasing it during winter, as well as transporting heat from mid- to high latitudes. Estimates of the magnitude of the ocean's heat transport have shown that it is comparable to the atmospheric (Hsiung, 1985).¹

The case of meridional heat transport in the South Atlantic is unique, since it is “the only major ocean basin in which the meridional heat flux is equatorward at mid-latitudes, counter to the global requirement that the ocean-atmosphere system carry heat from the equator to the poles (Model, 1950; Jung, 1955; Bryan, 1962; Bennett, 1978; Hastenrath, 1982)” (Rintoul, 1991, page 2675). The cause of this “atypical” heat transport is related to a net heat gain in the Pacific Ocean and a comparable loss in the Atlantic Ocean (Hastenrath, 1980, as cited by Fu, 1981), due to the excess of evaporation over precipitation in the North Atlantic mentioned above. Hence, there is a net (sensible and latent) heat transport from the North Atlantic to the atmosphere. Under stationary conditions, this heat transport would be balanced by a heat transport in the ocean “...from the Pacific to the Atlantic through the Antarctic Circumpolar Current” (Fu, 1981, page 1191).

A similar idea is supported by Holfort and Siedler (2001): “The excessive heat loss of the North Atlantic to the atmosphere has to be compensated by heat provided from the other oceans, and this results in a northward mean meridional heat flux throughout the Atlantic” (Holfort and Siedler, 2001, page 5). This notion goes back to Wüst (1957), who determined by geostrophy a meridional heat transport northward in the South Atlantic. However, this flux disagreed so much with his intuitive picture of a symmetrical heat transport away from the equator, that he decided not to publish his findings (according to a letter from Wüst's assistant to H. Stommel, as cited by Fu, 1981, page 1,171 and by Rintoul, 1991, page 2675).

Which water mass is responsible for the anomalous northward heat transport in the South Atlantic? Suga and Talley (1995) assess that AAIW plays a prominent role: “AAIW spreading into the North Atlantic can be a major warm source of NADW. Owing to this overturning cell, the meridional heat transport in the mid-latitude South Atlantic is equatorward rather than poleward” (page 13,441). This agrees with Hall and Bryden (1982), who found that the *northward* velocity in the South Atlantic (in a zonal mean) has a maximum at the AAIW horizon. However, despite the large number of inverse calculations (Table 5.2 in Subsection 5.2.5), layer resolved temperature transports are unavailable and, hence, the specific contribution of AAIW to the meridional heat transport of the South Atlantic is unclear.

Similarly, the transport of freshwater and salt at the AAIW horizon remains unresolved. Oceanic salt and freshwater transport contribute to the balance between seawater evaporation and advective ocean processes and are a key parameter in the planetary energy budget (Wijffels, 2001). Estimates of these transports help to understand the global hydrologic cycle, ocean dynamics and global climate (Stewart, 2002). However, results from previous studies of net freshwater transport in the South Atlantic are quite discordant.

¹ However, in a recent study, Trenberth and Caron (2001) assest that this is true only from the equator to 17°N, while “at 35° latitude the atmospheric transport accounts for 78% of the total in the Northern Hemisphere and 92% in the Southern Hemisphere” (Trenberth and Caron, 2001, p. 3433).

Rahmstorf (1996 and 1999) proposes a northward flow of fresh water due to the wind driven Subtropical Gyre of the South Atlantic, and a southward flow in the ocean interior due to NADW. The ocean's upper layers become more and more saline as they drift towards the north, due to the excess of evaporation over precipitation in the North Atlantic. On the other hand, remaining unmixed, the fresh water transport due to the AMOC in the deep of the ocean prevails, overcoming the surface drift at certain latitude. As a consequence, the meridional fresh water transport at the equator and further north in the North Atlantic is effectively southward: "...the Atlantic basin north of 30 °S is a net evaporative basin, losing freshwater at a rate of 0.2–0.55 Sv. This freshwater loss must be balanced in equilibrium by a net freshwater inflow from the ocean circulation" (Rahmstorf, 1996; page 807).

Results from other studies (Oort and Piexoto, 1983; Barnier et al., 1996; Wijffels, 2001) are in agreement with Rahmstorf's proposition. However, some studies (Holfort, 1994; Holfort and Siedler, 2001; Sloyan and Rintoul, 2001b) yielded a southward fresh water transport at all latitudes in the South Atlantic. In particular, the AAIW contribution to the fresh water budget in the South Atlantic is yet unknown as is the impact of its contribution to the conveyor belt. Hence, key questions addressed in this thesis related to transports are:

- What is the property transport in the AAIW layer of the South Atlantic?
- Is the iWBC the main carrier of heat and freshwater into the tropics and the northern hemisphere?
- Are the meridional contributions of AAIW inside the AMOC significant in comparison with the other water masses?

Answers to these questions will be attempted in Section 4.4.

0.7 AAIW dynamics

Dynamics of AAIW are directly related to the wind-driven circulation of the ocean. Due to Ekman transport, a gyral wind pattern drives surface waters towards the center of the gyre, raising the surface of the ocean in a dome shape and pumping water downwards (Ekman pumping). This piled water and the resulting pumping contributes to the horizontal pressure gradient throughout the water column. Therefore, under geostrophic balance (in the ocean interior and below the thermocline) Ekman transport and pumping induce a flow parallel to the wind-stress (Bearman et al., 1989). In the subtropical South Atlantic, the gyral, basin scale wind-pattern induces a Subtropical Gyre which reaches down to 1200 meters (Schmid et al., 2000). Only the first 100 to 200 meters, i.e. the Ekman layer, are influenced directly by wind friction. Hence, the wind forcing on the Ekman layer yields differences between the near-surface Subtropical Gyre (which is ageostrophic) and the Subtropical Gyre at intermediate depths (which is geostrophic). For instance, while the nBSG is mainly zonal at the AAIW horizon, at the surface it has a marked meridional tendency, flowing from 21 to 19°S as it crosses the basin from east to west (Berger and Wefer, 1996).

Subtropical gyres comprising upper 1000 m of the ocean are predicted by solutions of the equations of motion by Stommel (1948), following the work of Sverdup (1947). Sverdup considered a sinusoidal variation of the wind stress with latitude, no friction, geostrophic balance and a semi-infinite ocean bounded in the east. His results predicted eastern boundary currents and the corresponding meridional transport of water M , i.e., the *Sverdrup transport*:

$$M = 1/\beta \text{curl } \tau,$$

where β is the rate of change of the Coriolis parameter f with latitude and τ is the wind stress (i.e., the curl of τ is the wind torque). Sverdrup transport is a consequence of the vertical

squeezing layers of water due to Ekman transport/pumping, which causes water to move to latitudes where the Coriolis parameter compensates the difference in potential vorticity. After this, Stommel (1948) considered a more realistic wind field (a gyral wind field), a rectangular ocean with friction with the coast and took into account the variation of the Coriolis parameter with latitude (in a linear approximation). The results from Stommel showed a complete Subtropical Gyre with westward intensification.

The westward intensification in the Subtropical Gyre is a consequence of the variation of angular momentum with latitude. The water flowing in the Subtropical Gyre has vorticity due to three reasons: the gyral motion itself, the change in latitude (due to planetary vorticity) and shear (since inner currents in the gyre are slower than the outer currents). Because the state is steady, the *absolute* vorticity in the gyre must remain constant. This is the “natural” situation in the eastern boundary, where the loss of relative vorticity with latitude is compensated by a gain of positive vorticity due to the gyral motion. However, in the western boundary there is a net loss of relative vorticity that can only be compensated by velocity shear. By stretching the stream lines and increasing the flux, the velocity shear is increased as well (Pond and Pickard, 1978, p. 149; Stewart, 2002, p. 207).

The notion of a Subtropical Gyre reaching intermediate depths in the South Atlantic has been supported by Martineau, 1953; Taft, 1963; Kirwan, 1963; Buscaglia, 1971; Molinelli, 1981; Piola and Georgi, 1982, and Boebel et al., 1997. In a recent study, Schmid, et al. (2000) gave a description of geostrophic transports of the intermediate depth Subtropical Gyre, through recent and historical hydrographic data. Additionally, Lagrangian transports of the gyre were provided by float data. These observations were compared with outputs of Sverdrup transport models, as well as models of the ventilated thermocline,¹ showing a good agreement and supporting the notion that “the AAIW layer is likely to be part of the Subtropical Gyre” (Schmid et al., 2000, p. 3201).

For greater depths, Treguier et al. (2003) drew similar conclusions. Float measurements at the depth of the NADW (2500 m) have shown a pattern of alternating zonal jets in the interior of the Brazil Basin (Hogg and Owens 1999). To investigate possible origins of these jets, Treguier et al. (2003) analyzed results of two primitive equations, z -coordinate models. Comparing with an idealized model forced by winds only and by carrying out an experiment without wind forcing, they concluded that both, the wind forcing and thermohaline effects, are a source of zonal jets and that some of these jets are “the deep ocean response to the surface wind forcing” (Treguier et al. 2003, p. 595). Furthermore, they state that the models are “realistic enough to support the wind as a primary source of the observed deep zonal flows in the Brazil Basin” (ditto, p. 596).

Dynamics of the tropical region at the AAIW horizon are also wind-influenced. Munk (1950) extended Stommel’s study by adding lateral and vertical eddy viscosity, considering a rectangular ocean spanning from the equator to 60°N. His results not only predict a more realistic Subtropical Gyre than Stommel’s, but also show currents observed in the tropical region of the real ocean: the North Equatorial Current, the Equatorial Counter-Current and the South Equatorial Current. In the tropical Atlantic, these currents have been observed to be subject of a strong seasonal variability, which could be a consequence of planetary waves (Molinari et al., 1999; Schmid et al., 2003).

¹ “Models of the ventilated thermocline are based on Sverdrup dynamics. In contrast to the simple Sverdrup model, however, they resolve the circulation in the vertical” (Schmid et al., 2000, p. 3201).

Chapter 1 Fundamentals

This chapter discusses the fundamental concepts involved in the present dissertation.

1.1 Floats

Floats are free drifting underwater buoys. Their compressibility is less than or equal to seawater and, hence, they gain positive buoyancy as they sink. For this reason, float pressure cases are often made of aluminum or glass (Stewart, 2002; Gould, 2005).¹ At a certain depth, the buoyancy force acting on the pressure case equilibrates with the weight of the float and it stops sinking. This physical concept, called neutral buoyancy, is the basis of floats (Figure 1.1): At depth D_1 , the float has a higher density than the water surrounding it. Hence, the float sinks to deeper layers, where the water is denser. As the float sinks, its density increases, but to a smaller extent than the density of surrounding water due to the float's lesser compressibility. Hence, the float gains relative buoyancy. Eventually the float reaches an equilibrium depth D_2 , where water and float have the same *in-situ* density. Below this depth, both water and float density continue to increase if displaced down, but again, the water is compressed more than the float. Hence, at depth D_3 the float is surrounded by water with a higher density than its own and it is subject to a restoring buoyancy force that drives it back up to the equilibrium depth.

Floats drift in the ocean interior at depths ranging from some hundreds to some thousand meters. They can be located by satellites (currently Systeme Argos²) when at the sea surface, or by means of SOFAR (SOund Fixing And Ranging) sound signals transmitted by moored sound sources and received by the floats. Since the positions of the sound sources are known, the positions of the floats can be calculated retrospectively by triangulation. This, however, is possible only after the floats terminated their mission and ascended to the sea surface to transmit their data by satellite. Floats that are located exclusively by satellites must ascend periodically to the surface to be positioned, which suggested the term “pop-up” floats for this type.

A major difference between pop-up floats and acoustically tracked floats is the frequency of their localization. Whereas acoustically tracked floats are located once or twice a day, pop-up float positions are obtained at periods ranging from one to two weeks. The fact that pop-up floats rise to the surface periodically, where they are subject to displacement by currents different from the interior flow, renders individual deep displacements to be uncorrelated in many cases (Schmid et al., 2001). While useful in a statistical sense, the concept of a pop-up float complicates the interpretation of a given trajectory as long-term flow of water. Such interpretation needs verification on a case-by-case basis (particularly with regard to the degree of baroclinicity of the velocity field). Acoustically tracked floats, by contrast, approximate the long-term flow of water, as their sub-surface trajectory is continuous. These floats are mainly used to study mesoscale processes (such as eddies and short-term meanders along currents) in a dynamical context, while pop-up floats are used to study basin scale currents in a statistical, descriptive context.

¹ Swift and Riser (1994) measured the mean compressibility of quasi-isobaric RAFOS floats as being approximately $2.71 \times 10^{-6} \text{ db}^{-1}$. For profiling floats this value is even smaller: $2.23 \times 10^{-6} \text{ db}^{-1}$ (Izawa et al., 2002). The compressibility of seawater is $4.5 \times 10^{-6} \text{ db}^{-1}$ (D'Asaro et al., 1996).

² This is not an acronym. Argus (in Latin), was the “all-seeing” in the Greek mythology. See the webpage: http://www.cls.fr/html/argos/welcome_en.html.

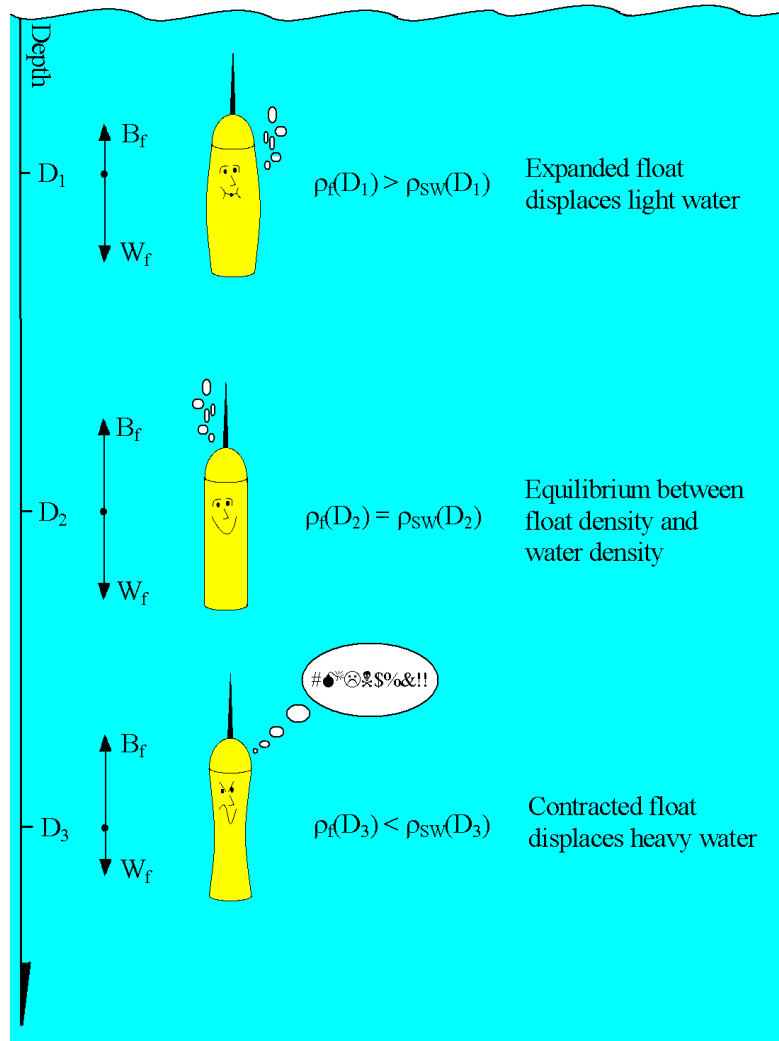


Figure 1.1. Neutral buoyancy and floats. ρ_f stands for float's density, ρ_{sw} for density of seawater, B_f for buoyancy force acting on the float and W_f for the float's weight.

Another categorization of floats is related to their ability to follow vertical displacements of the surrounding waters. Since the compressibility of seawater is higher than the compressibility of the float, a pressure change (for instance, due to Rossby waves, thermohaline fronts or meanders of adjacent currents) will make the water rise or sink more than the float. Hence, floats only approximate isopycnal flow, cannot describe the motion of water in the vertical and tend to maintain the same depth. Because of that, floats are generally classified as *quasi-isobaric*. To better approximate isopycnals, a float must have the same compressibility as seawater. This can be achieved by adding a device called “compressee”, which matches the compressibility of the float system (i.e. float plus compressee) to that of seawater. However, even though a quasi-isobaric float does not follow the vertical movement of water, “in many applications, an isobaric float is every bit as useful as one that follows vertical motion” (Davis, 1991, page 49). This is because vertical motion of water can be inferred from the hydrographic measurements of floats if they measure some conservative property like temperature, salinity or density (Davis, 1991).

Using floats to track oceanic flow for periods of years was not possible until the introduction of CMOS technology in microelectronics, due to the low energy consumption of these devices (Stewart, 2002). Contemporary float missions last as long as five years before batteries expire. During this extended period, floats can follow complex trajectories

over distances of thousands of kilometers. Superposition of many trajectories (spaghetti plots) tend to be scrawled. To expose the underlying flow structure, a statistical analysis of the trajectory (or displacement) data is needed.

The following overview will summarize the historical evolution of floats and enumerate their principal types (Gould, 2005, presents a broader historical synopsis):

Swallow floats. (Figure 1.2) These quasi-isobaric floats designed by the British oceanographer John Swallow (1955) were the first neutrally buoyant floats. They were acoustically tracked from ships, but only over relatively small distances (hundreds of meters). The resulting data provided the absolute velocity for a reference depth for the Gulf Stream, yielding the first absolute transport measurement for this current (Swallow and Worthington, 1961)



Figure 1.2 John Swallow onboard RRS Discovery II assembling a float. From Gould, 2002.

SOFAR floats (Sound Fixing and Ranging; Figure 1.3). These quasi-isobaric floats were designed by Rossby and Webb (1970). They were acoustically tracked by means of SOFAR signals. The float itself acted as sound source, which demanded a length of 5 meters for the float's case, a weight of 430 kg and significant costs to build and use (Davis, 1991). The floats and the sound receivers had precise clocks synchronized with each other. By measuring the delay in the sound signal, they were able to calculate the distance between the receiver and the float. SOFAR floats facilitated studying mesoscale processes at mid-depths for the first time, in particular during the MODE experiment (Bretherton et al., 1976).

RAFOS floats (Ranging and Fixing of Sound or SOFAR spelled backwards; Figure 1.4). These floats were designed by Rossby et al. (1985 and 1986) and are the most widespread acoustically tracked floats. Their localization is based on the same principle as SOFAR floats, but in this case the sound sources are moored and the floats receive the sound signal. The floats store the arrival time of the sound signal, and at the end of the mission (from one to three years) they ascend to the sea surface and transmit their entire data set to communication satellites (currently Systeme Argos). These floats are significantly less expensive, smaller and lighter than the SOFAR floats. RAFOS' compressibility can be adjusted to obtain a quasi-isobaric or isopycnal response.



Figure 1.3 Prototype SOFAR float. From Gould, 2005.

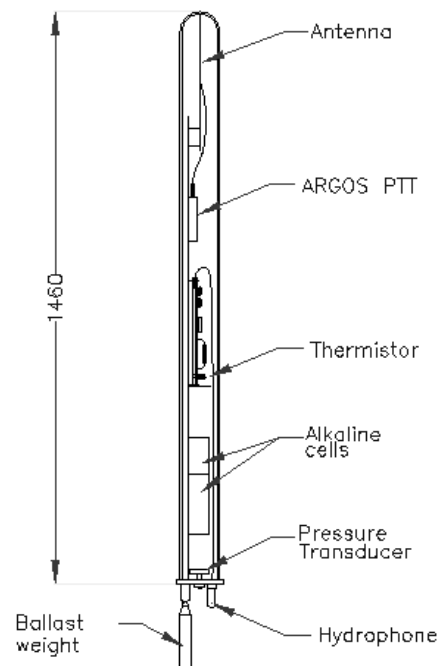


Figure 1.4 Technical drawing of the IfM/Seascan RAFOS float. From Ollitrault et al., 1995.

ALACE floats (Autonomous Lagrangian Circulation Explorer; Figure 1.5), designed by Davis et al. (1992). These are quasi-isobaric floats tracked by satellites. Their mission is comprised of under-water-drifts (around one or two weeks), interrupted by periods of ascent and surface drift during which the instrument transmits data to Systeme Argos. These

satellite transmissions are used by Argos to determine the float's position. After the transmission period, the float descends to drift depth again to start the next cycle. For the floats to ascend, a piston pump moves oil from an internal reservoir to an external rubber bladder, reducing the floats' density. To descend, a latching valve is opened to allow the oil to flow back into the internal reservoir. ALACE floats were widely used in the World Ocean Circulation Experiment to determine mid-level currents in remote regions, especially the Antarctic Circumpolar Current (Davis et al., 1996; Davis, 1998).

PALACE floats (Profiler ALACE; Figure 1.6). ALACE floats equipped with a CTD, to measure a profile of temperature and salinity as they ascend.

APEX floats (Autonomous Profiling Explorer; Figure 1.7). This float type is the successor of the ALACE design and can be programmed to follow isobaric or isopycnal surfaces (Webb Research Corporation, 2004). The special design of the APEX's hydraulic subsystem permits it to be deployed from transmitting merchant ships or even aircrafts. The latest models include oxygen (Emerson et al., 2002) or CO₂ (Bishop et al., 2002) sensors. RAFOS sensor became optionally available.

ALFOS floats (ALACE-RAFOS). Floats based on the ALACE design, but with additional acoustic tracking option. They listen for signals from sound sources but periodically rise to the surface, like the ALACEs, to transmit the data to Argos.

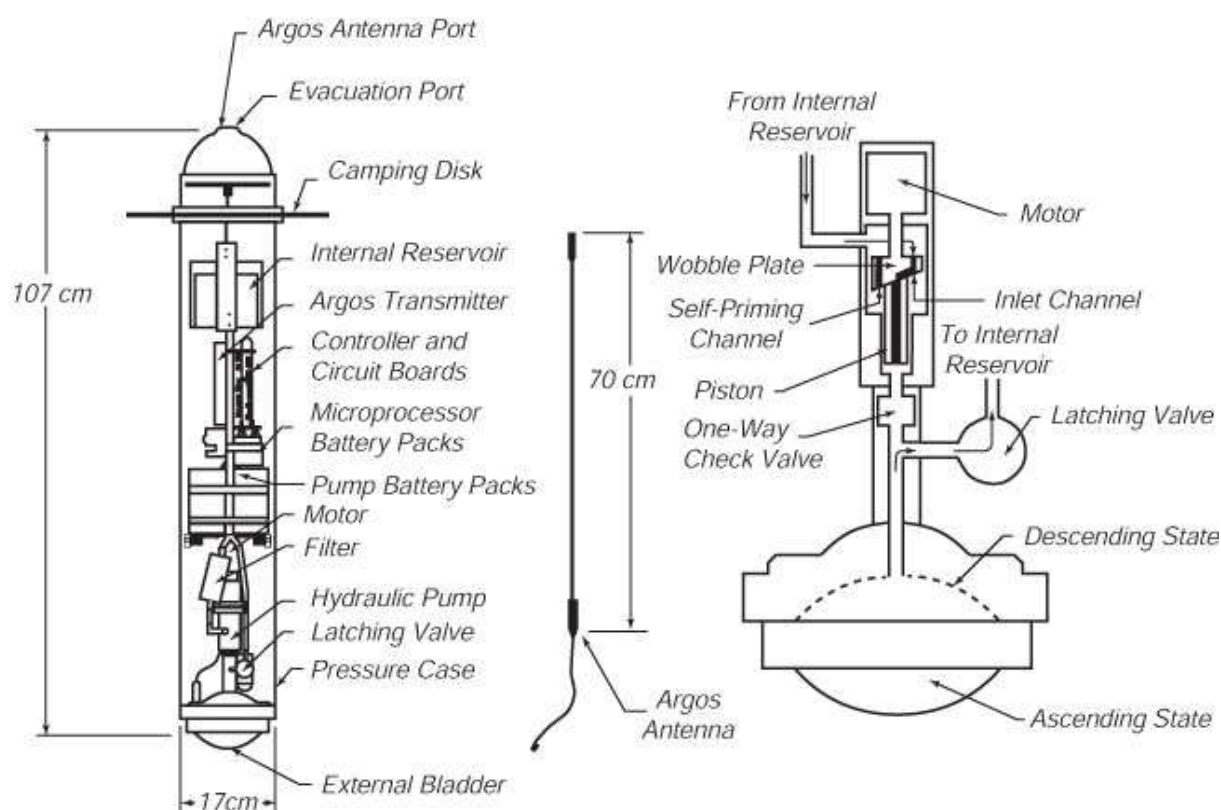


Figure 1.5 Schematic of an ALACE float (left panel), with an expanded diagram of its hydraulic system (right panel) (from Davis et al., 1992).

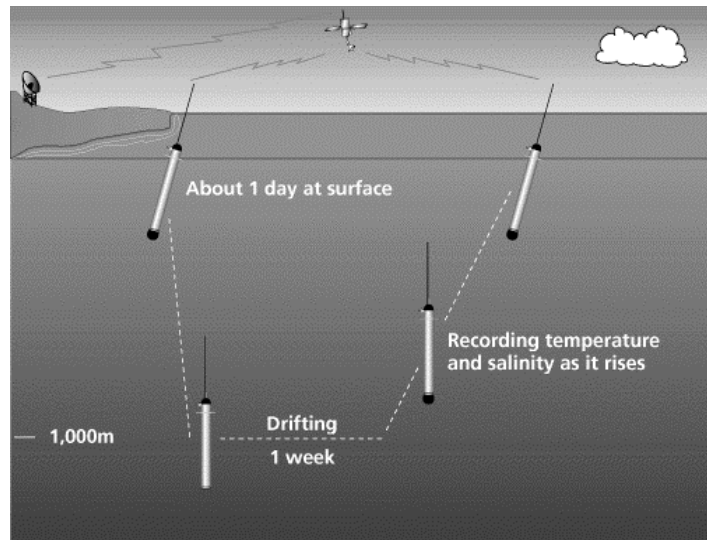


Figure 1.6. The mission of a PALACE float. From Woods Hole Oceanographic Institution, 2003.

Marvor floats (Breton word for *sea horse*; Figure 1.8). Pop-up floats with additional acoustic tracking between surfacings, designed by Ollitrault et al., 1994. Due to their active depth control, Marvor floats (as used in the SAMBA experiments included in this study; Ollitrault, 2005, personal communication) effectively drift at a well-approximated isobaric surface (within ± 30 dbar) by regularly measuring pressure (pumping oil between an internal reservoir and an external bladder).

Provor floats.- Isobaric pop-up floats based on Marvor floats, without the latter's option of acoustical tracking. They include a CTD and use lithium batteries, which extend their lifetime. These floats drift to a predetermined depth for ten days and then sink deeper (normally 2000 m) to begin profiling.

SOLO floats. (Sounding Oceanographic Lagrangian Observer; Figure 1.9). Pop-up floats that include an additional external air rubber bladder to reach higher over the waves and have a better transmission to the satellites. They were designed by the Scripps Institute of Oceanography.

NEMO floats. Floats similar to SOLO, modified and further developed "with the specific objectives of deployment under ice, positioning through GPS and RAFOS, as well as the integration of new sensors to determine phytoplankton distribution and composition in the upper water column" (OPTIMARE Sensorsysteme AG, 2005).

Argo float. This is not a float type, but a term used to describe floats funded in collaboration with the International Argo project (International Argo project, 2005). While most of the floats in this project are APEX or SOLO, some of them are NEMO, Provor and NINJA (the Japanese Argo float).



Figure 1.7 APEX float launch during METEOR cruise 50/4 (Institut für Meereskunde, IfM, Kiel, Germany). From Webb Research Corporation (2004).



Le flotteur de subsurface MARVOR.

Figure 1.8 Top cap of a MARVOR float. From Institut français de recherche pour l'exploitation de la mer, (2004).

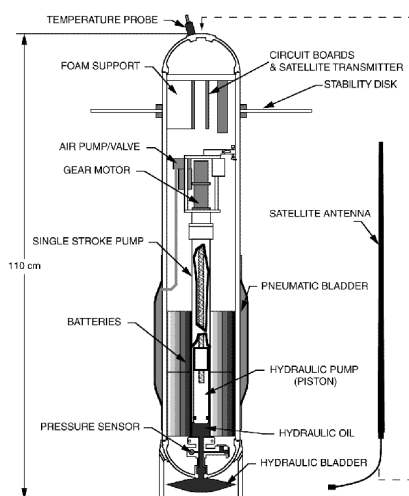


Figure 1.9 Design schematic of a SOLO float. From University of California San Diego (2004).

1.2 Neutral density surfaces

During its transit across the South Atlantic, the AAIW's salinity and temperature change because of mixing with adjacent water layers. Even though isopycnal mixing is much larger than diapycnal (Stewart, 2002), the non-linearity of potential density makes the surface of minimum salinity north of 5°S be located at a greater depth than the isopycnal surface that best describes it at southern latitudes (Figure 0.4). Hence, potential density surfaces provide only a poor proxy for the AAIW layer: To trace water masses using potential density (Reid, 1994) a set of various isopycnals with different reference pressures is needed, which is cumbersome to work with. On the other hand, isohalines are also an inadequate descriptor of the AAIW layer, since mixing makes them converge towards the north.

The AAIW core can alternatively be described by a single *neutral density surface* (You, 1999), which is the continuous analog of Reid's method. Neutral surfaces (McDougall, 1987; Jackett and McDougall, 1997) are defined so that small isentropic and adiabatic displacements of a fluid parcel along them do not produce a buoyant restoring force on the parcel. Therefore, a neutral surface is one on which no work is required to move a water parcel. In mathematical terms, a neutral surface is defined by:

$$\alpha \nabla_n \theta = \beta \nabla_n S,$$

where θ is potential temperature, S is salinity, α the thermal expansion coefficient, β the saline contraction coefficient and ∇_n refers to the two-dimensional gradient along the neutral surface. According to this mathematical definition, the expansion that a water parcel would experience due to temperature changes as it is moved along a neutral surface is compensated by the contraction due to salinity changes. Hence, neutral surfaces provide a suitable framework to describe the movement of water masses through the ocean even under isopycnal mixing (McDougall, 1987; Jackett and McDougall, 1997). A physical argument supporting this notion is of energetic nature: water masses use less energy if they move along neutral surfaces because they do not need to act against buoyancy.

Chapter 2 Data description

This study is based on two types of data: float trajectory data and hydrographic data. Float trajectories provided direct Lagrangian current measurements within the intermediate depth layer. Hydrographic data was used to construct neutral density surfaces to describe the position of the core, the upper and the lower boundaries of the AAIW layer. These surfaces were used to constrain the float data in the vertical and “isolate” the movement of the AAIW layer. The hydrographic data was also used further to calculate geostrophic current shear within the AAIW layer and project float velocities onto the AAIW’s core layer.

2.1 Float data

A comprehensive unprecedented float data set was gathered by combining data from 7 historic and present-day oceanographic projects, embracing more than 13 years of float data in the South Atlantic. Float displacements were selected if within the box bounded by latitude from 70°S to 10°N and longitude from 60°W to 30°E (Figure 2.1). Floats were counted in the data description by float projects shown in Figure 2.1 and Table 2.1 even if only part of its trajectory was inside this box. However, for the calculation of float days (Figure 3.5), as well as for the final data set used in the analysis, only the float trajectory segments inside the box were included.

The entire float data set comprises 611 float years, including 19 APEX floats from the Alfred Wegener Institute (AWI) prior to the Argo project, 105 APEX floats from Argo, 1 float from AOML (Atlantic Oceanographic and Meteorological Laboratory) previous to the Argo project, 42 ALACE and PALACE floats from WOCE (World Ocean Circulation Experiment) and CORC (Consortium on the Ocean’s Role in Climate) programmes, 98 RAFOS floats from KAPEX (Cape of Good Hope Experiment), 74 RAFOS floats from WOCE/DBE and 97 MARVOR floats from SAMBA (SubAntarctic Motions in the Brazil Basin) experiment, including all SAMBA1 and SAMBA2 data. See Table 2.1 for references and explanation of acronyms of float types.

Most of the pop-up floats cycled on a 10-days basis, however, those from AWI cycled on a 7-days basis. In some cases, (subsurface) displacements exceed 10 days due to lost positions. These can arise when the float was not received by the satellite or the float failed to surface altogether (typical at high latitudes due to ice). On the other hand, the acoustically tracked floats, like RAFOS floats, obtained positions on a daily basis. To generate a consistent statistical analysis from such diverse data, the underwater drift time was homogenized: On the one hand, acoustically-tracked float data was subsampled to mimic pop-up-float behavior by picking up one position each ten days (Richardson, 1992). On the other hand, a maximum drift-time of ten days was set for the pop-up floats, neglecting longer trajectory segments (11 cases out of 36403). These measures provided a statistically consistent data set of 10-day float displacements.

Float velocities were calculated by dividing the distance of an underwater drift vector by its duration. Hence, these velocities already represent a velocity average of the interior flow. A crude quality check was applied by testing for velocities larger than 3 m s^{-1} . However, no such event occurred.

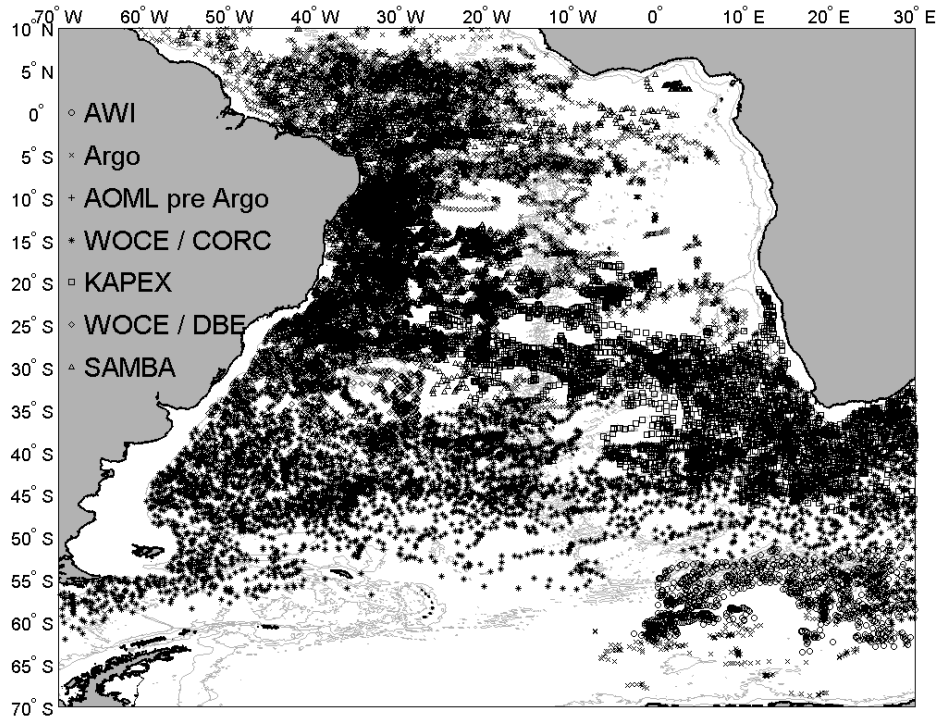


Figure 2.1 Float trajectory data. Each float programs is represented by a unique symbol. For clarity, only the start position of displacement vectors is shown. However, due to the density of measurements, individual trajectories are indistinguishable. Most of the floats drifted between 400 and 1200 dbar with a cycle duration of 10 days. Acronyms are given in the caption to Table 2.1.

2.2 Neutral surfaces

The vertical position of neutral density surfaces for the AAIW core and bounding layers are based on historical and recent hydrographic data, including WOCE. Objectively mapped neutral density surfaces on a grid of $1^\circ \times 1^\circ$ resolution comprise for pressure, potential temperature and salinity at the core ($\gamma^n = 27.40$), upper ($\gamma^n = 27.25$) and lower boundaries ($\gamma^n = 27.55$) of AAIW in the South Atlantic.¹ The data for the major part of the South Atlantic were taken from You, 1999 (4113 stations covering 70W-30E, 80S-0; Figure 2.2). Surfaces around South Africa were corrected with data from You et al., 2003 (5684 stations covering 10°W-50°E, 50°S-20°S; Figure 2.3). The equatorial band was covered by data from You, 2002a (13748 stations covering from 10°S-10°N, 60°W-10°E; Figure 2.4). The core's neutral surface was chosen to approximate the position of the AAIW's salinity minimum, and the neutral surfaces for the boundaries were chosen for values where the isohalines started to diverge (You, personal communication). The resulting isoneutral surfaces and the salinity and potential temperature distribution within are shown for the core in Figure 2.5 to Figure 2.7.

¹ These surfaces were kindly provided by Dr. John Y. You from the University of Sydney Institute of Marine Science (USIMS) in a personal communication.

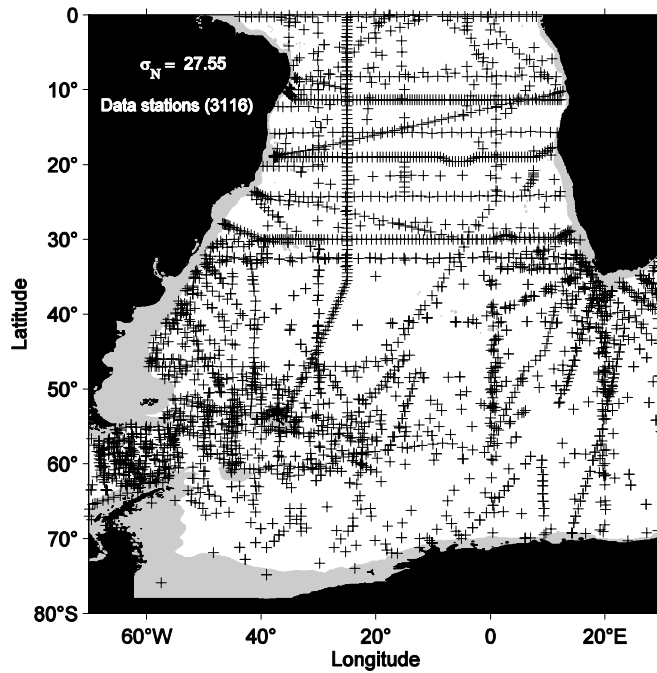


Figure 2.2 Hydrographic database used to build neutral density surfaces in the South Atlantic, including 4113 stations. From You 1999 (his Figure 1) or You, 2002b (his Figure 2).

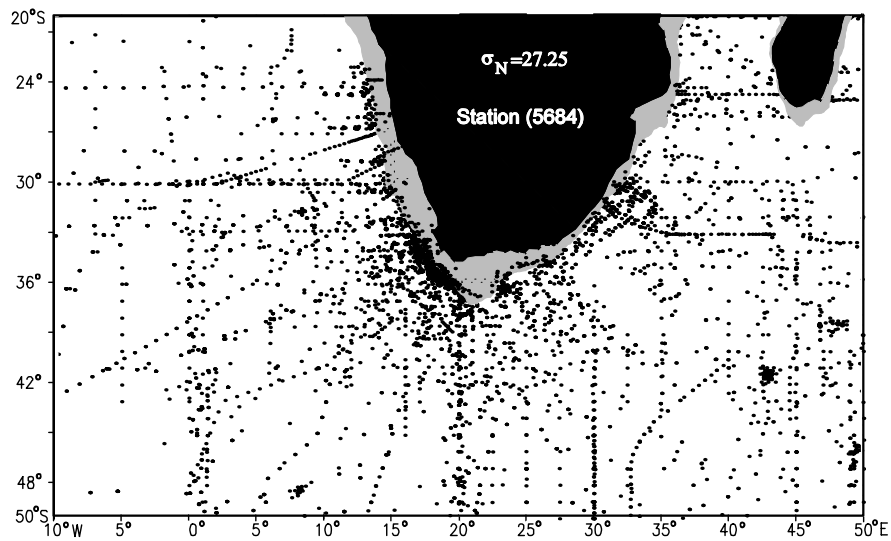


Figure 2.3 Hydrographic database around South Africa (including 5684 stations) used to correct the neutral density surfaces in the South Atlantic. From You et al., 2003 (their Figure 1).

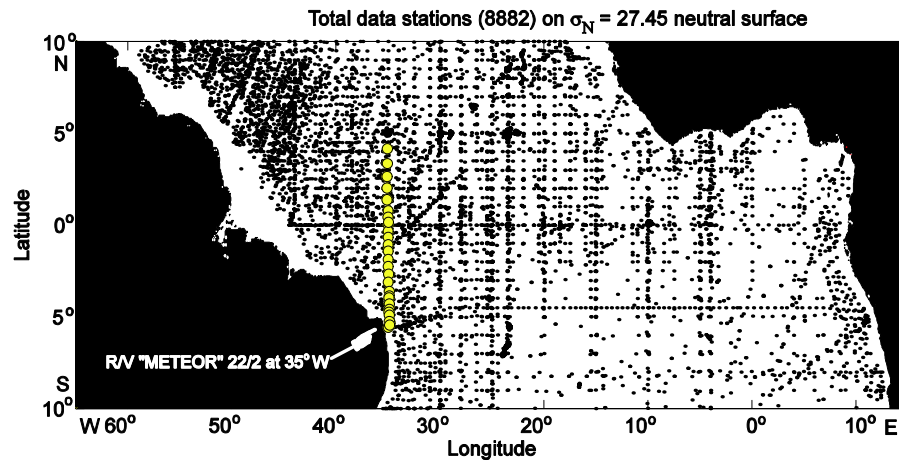


Figure 2.4 The tropical Atlantic database used to build neutral density surfaces. It includes 13748 stations. From You, 2002a (his Figure 1).

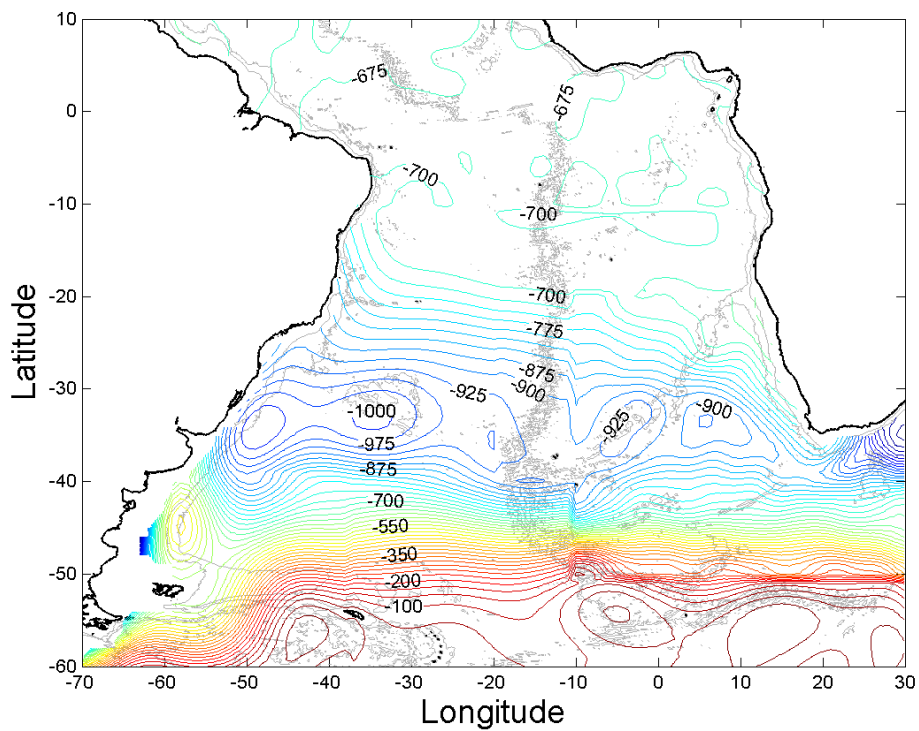


Figure 2.5 Pressure (dbars) along the AAIW core as defined by the isoneutral surface $\gamma^{\rho} = 27.40$.

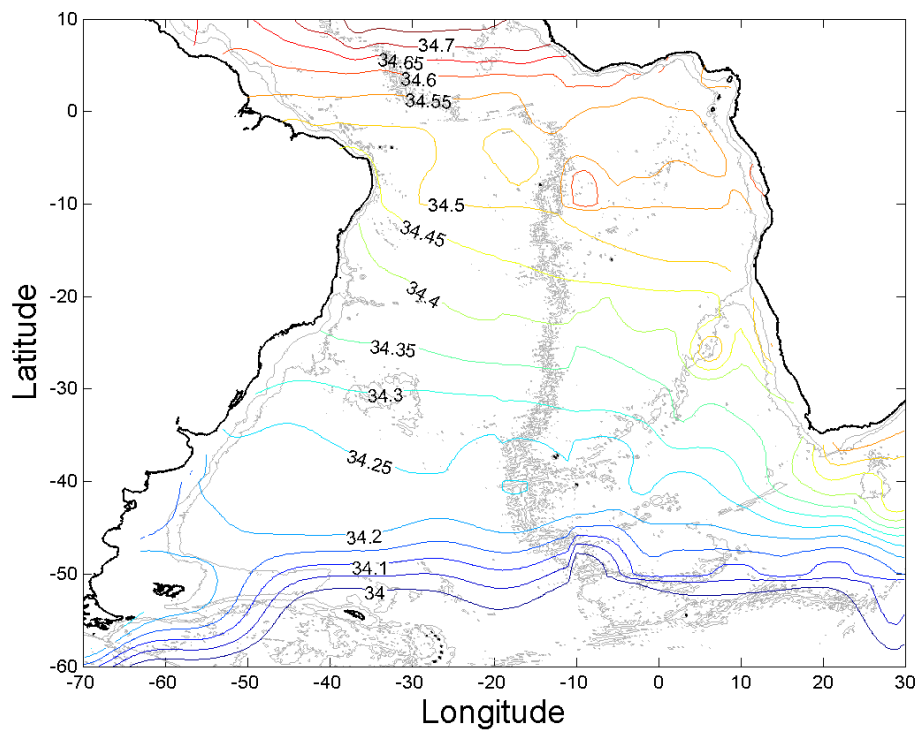


Figure 2.6 Salinity within the AAIW core as defined by the isoneutral surface $\gamma^n = 27.40$.

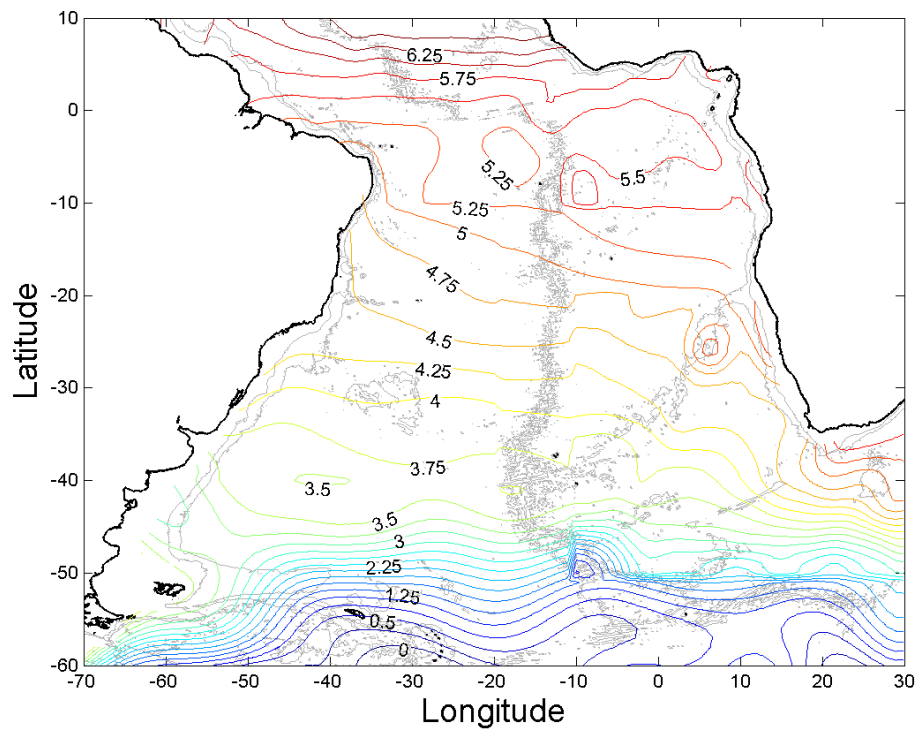


Figure 2.7 Potential temperature ($^{\circ}\text{C}$) at the AAIW core as defined by the isoneutral surface $\gamma^n = 27.40$.

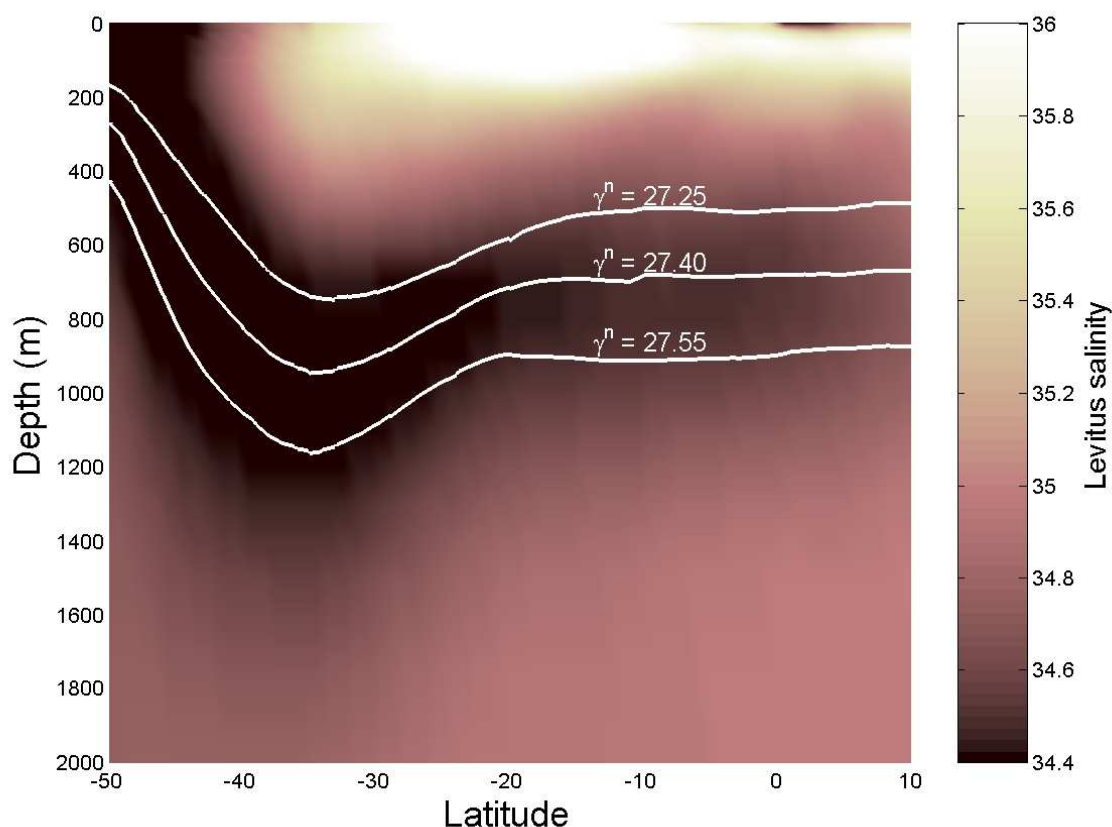


Figure 2.8. Levitus (1994) salinity (zonal and annual mean) in the South Atlantic (color coded). Core and boundaries (zonal mean) of the neutral densities chosen to define the AAIW layer are given by white lines.

Vertical positions of additional neutral density surfaces were calculated between the upper boundary and the core ($\gamma^n = 27.32$), as well as between the core and the lower boundary ($\gamma^n = 27.45$). This (together with the other three surfaces) provided five levels along the water column and within the AAIW layer to calculate geostrophic velocity shear profiles. These data were used to project the float velocities onto the AAIW core.

A visual validation of the selected neutral density surfaces is presented in Figure 2.8, where the meridional structure of the surfaces is compared with the annual mean salinity of Levitus (1994) data. Figure 2.8 shows zonal-annual salinity averages depicting a good agreement between the vertical position of the selected neutral surfaces and the salinity minimum.

2.3 Vertical selection of float data

The first step of float data processing involves the selection of float data in the vertical (step 1 in Figure 3.1). Float displacement vectors were selected according to their vertical position relative to isoneutral surfaces applying three alternative criteria:

- 1) Only floats that drifted at a depth within the AAIW layer, as defined by the uppermost and lowermost neutral surfaces ($\gamma^n = 27.25$ and $\gamma^n = 27.55$) were selected (Figure 2.9 and Table 2.2).

2) These surfaces were displaced 50 m up and down, respectively, yielding an AAIW layer extended in 100 m. The selection of float displacements located within this extended layer obviously embracing more float trajectories (Figure 2.10 Table 2.3).

3) Floats displacements were selected according to their vertical position relative to two isobaric surfaces (650 and 1050 dbar) similar to Boebel et al., (1999a) (Figure 2.11 and Table 2.4).

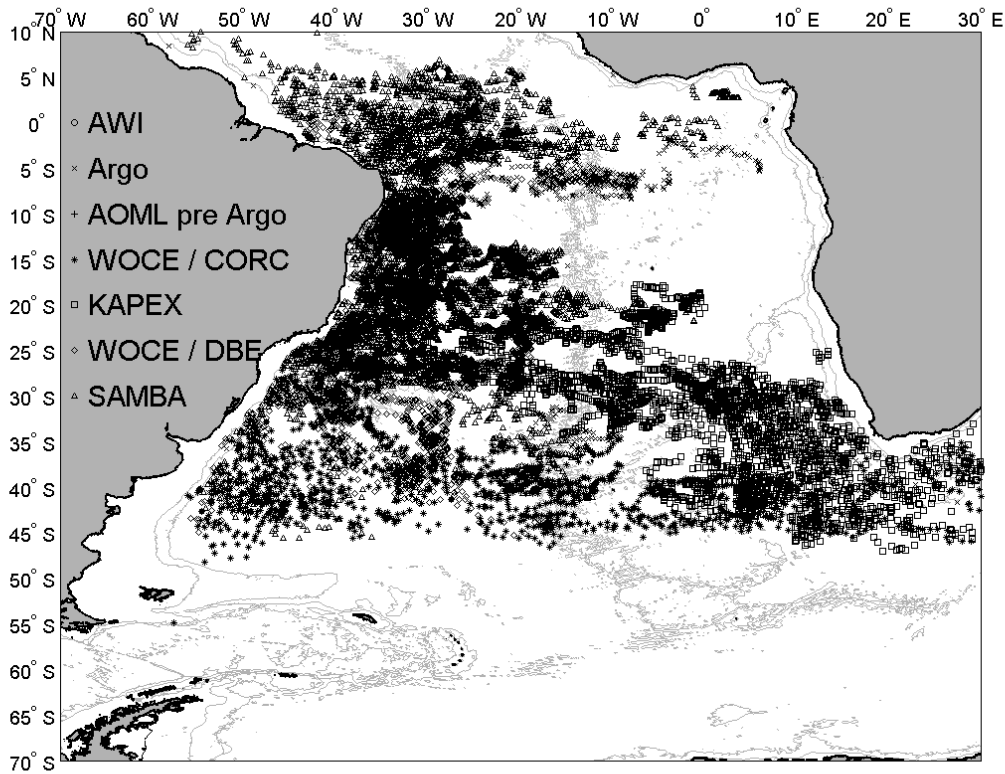


Figure 2.9 Data selected in the vertical by isoneutral surfaces for the upper and lower boundaries of AAIW ($\gamma^n = 27.25$ and $\gamma^n = 27.55$, respectively; 49% of the original data, Figure 2.1). Refer to Figure 2.1 for details. For the number of float years of this data set see Table 2.2

Table 2.2 Data selected in the vertical by isoneutral surfaces for the upper and lower boundaries of AAIW ($\gamma^n = 27.25$ and $\gamma^n = 27.55$, respectively; 49% of the original data, Figure 2.1).

Name of the program	Number of float years
AWI	0
Argo	27
AOML	1
WOCE/CORC	27
KAPEX	77
WOCE/DBE	70
SAMBA	97
Cumulative	299

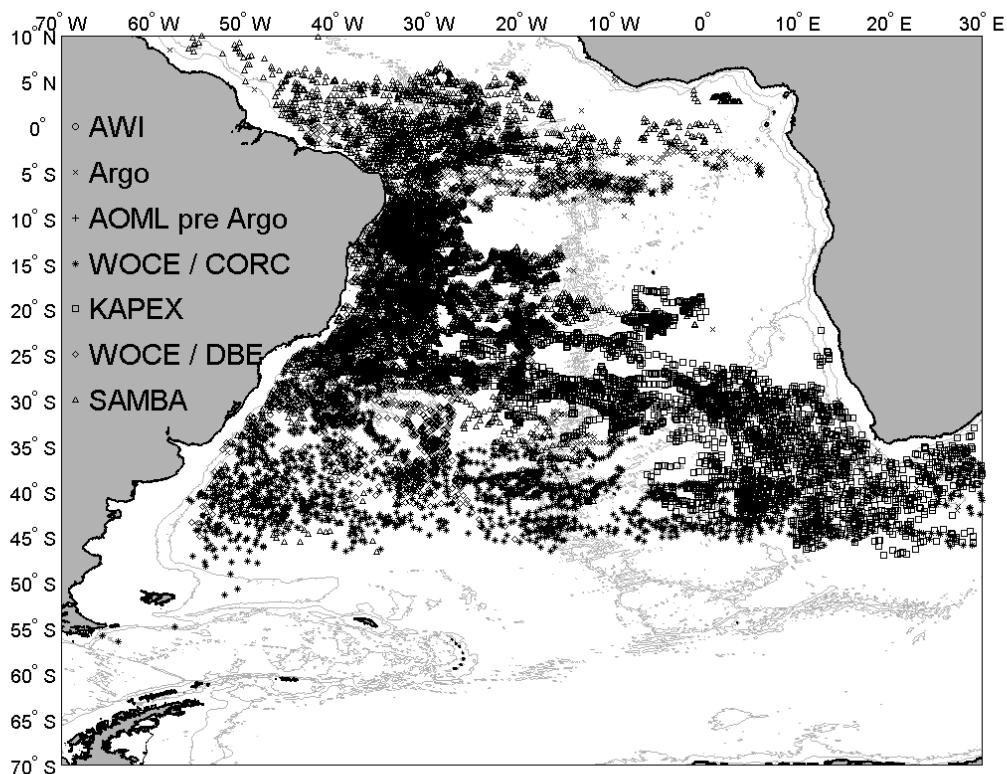


Figure 2.10 Float data selected in the vertical by isoneutral surfaces for the upper and lower boundaries of AAIW ($\gamma^{\theta} = 27.25$ and $\gamma^{\theta} = 27.55$, respectively) displaced 50 m up and down. This is 51% of the original data (Figure 2.1). Refer to Figure 2.1 for details. For the number of float years of this data set see Table 2.3

Table 2.3 Float data selected in the vertical by isoneutral surfaces for the upper and lower boundaries of AAIW ($\gamma^{\theta} = 27.25$ and $\gamma^{\theta} = 27.55$, respectively) displaced 50 m up and down (51% of the original data).

Name of the program	Number of float years
AWI	0
Argo	32
AOML	1
WOCE/CORC	29
KAPEX	81
WOCE/DBE	73
SAMBA	97
Cumulative	313

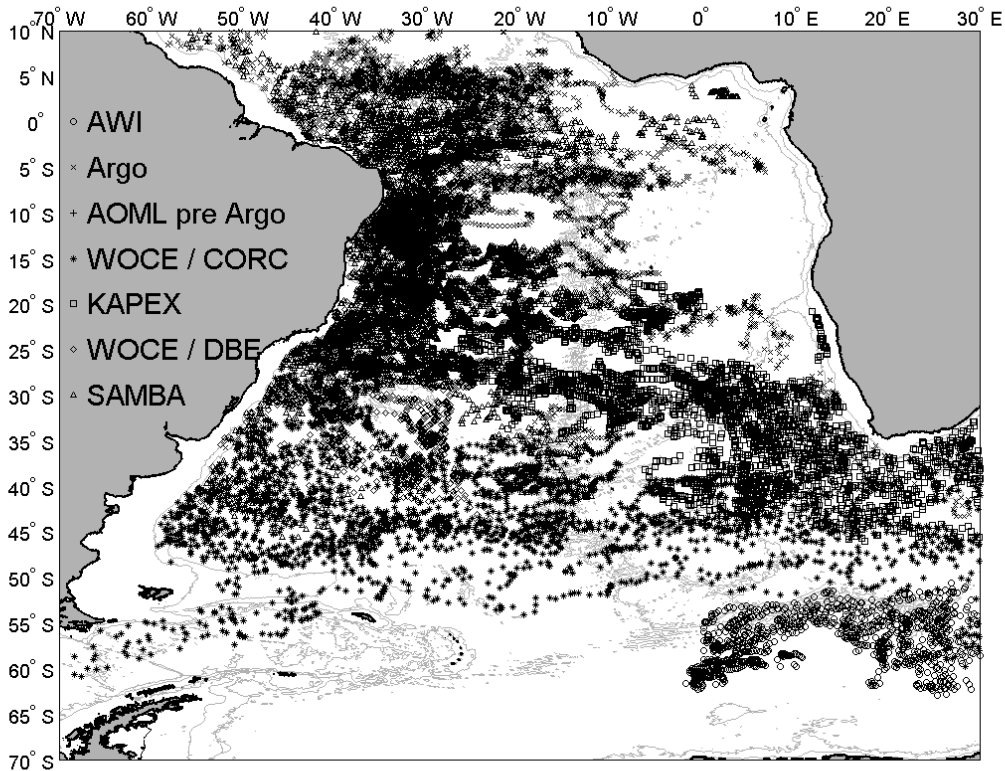


Figure 2.11 Float data selected in the vertical by isobaric surfaces 650, 1050 dbar. This is 63% of the original data (Figure 2.1). Refer to Figure 2.1 for details and to Table 2.4 for the number of float years of this data set.

Table 2.4 Float data selected in the vertical by isobaric surfaces 650, 1050 dbar (63% of the original data).

Name of the program	Number of float years
AWI	19
Argo	77
AOML	1
WOCE/CORC	42
KAPEX	81
WOCE/DBE	69
SAMBA	97
Cumulative	386

In the following, float velocities from these data sets will be called *primal* data or *primal* float velocities to distinguish them from further processed velocities (space-time averages, Section 3.1). The more common expression “raw data” was judged improper considering that the data has been quality-controlled.

2.4 Geostrophic projection: a test

For the data set constrained by neutral surfaces, the float velocities were corrected based on geostrophic profiles (step 2 in Figure 3.1), projecting the float velocities onto the salinity core of AAIW (Richardson and Garzoli, 2003; Gille, 2003). A cubic spline was fitted between the gridded geostrophic velocities that arise from the 5 isoneutral surfaces ($\gamma^n = 27.25, 27.32, 27.40, 27.45$ and 27.55). The reference pressure was 2000 dbars (You, 2002a and b; You et al., 2003), which is an appropriate reference level for geostrophic calculations in the South Atlantic for being located “between AAIW and NADW in the deep Subtropical Gyre” (You et al., 2003, p 217). Shifting the splined velocities as to match the float velocity at the respective (float) depth provided a projected float velocity at the intersection between the splined velocities and the core layer. This velocity was considered to be the float velocity projected onto the AAIW core. These projected float velocities were expected to provide more accurate transports estimates. However, the mean difference between the projected speeds and the original amounted to only 0.43 cm s^{-1} , which yielded only insignificant differences in the objective maps, space-time averages and transports. This relation is visualized in Figure 2.12, which shows geostrophic speeds (cm s^{-1}) for meridional and zonal sections at 20°W (upper panel) and at 45°S (lower panel). The geostrophic field has predominantly a vertical structure, which yields a relatively small shear inside the layer. Therefore, the projected data set was ignored.

It is not discarded that this method could yield rewarding results when projecting velocities of floats that drifted considerably deeper or shallower than the projection depth. However, errors in the geostrophic field (see high values in the upper panel between 40 and 50°W) appear to render such projections disadvantageous.

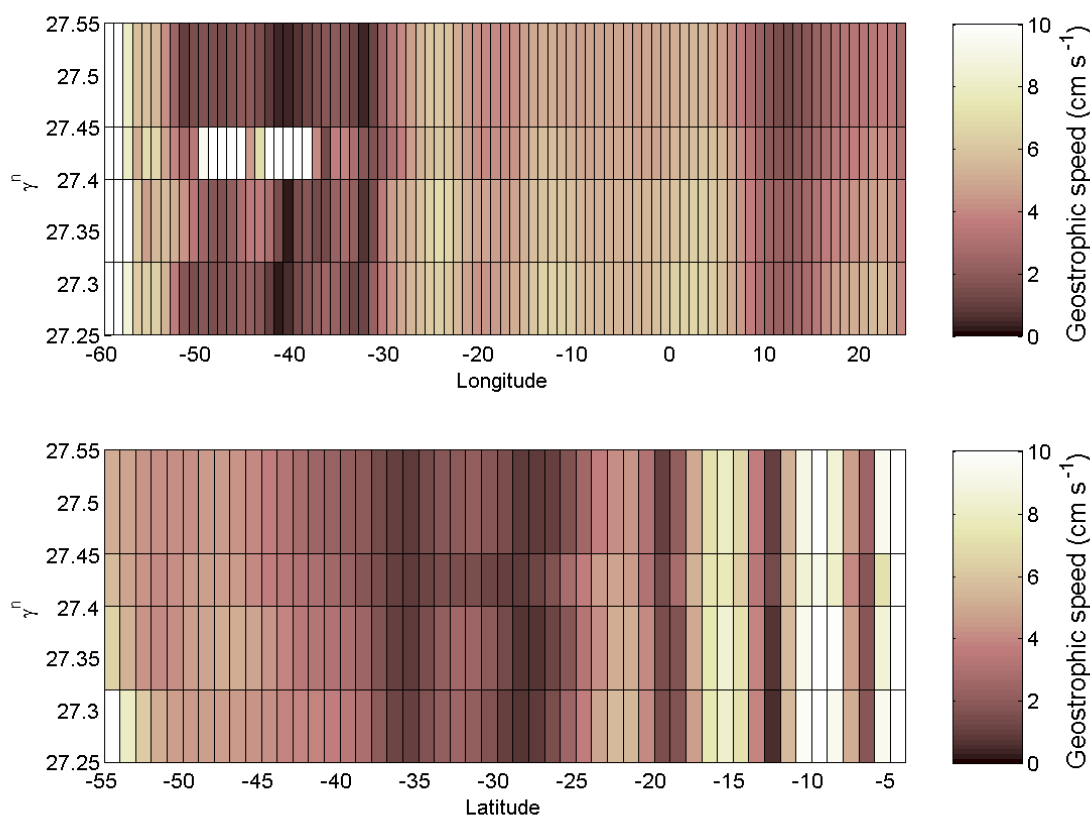


Figure 2.12 Geostrophic speed in the AAIW layer projected onto a zonal section at 45°S (upper panel) and a meridional section at 20°W (lower panel) plotted against neutral density. Values are in cm s^{-1} .

Chapter 3 Data analysis

This chapter describes the processing of data involved in obtaining the circulation scheme of AAIW in the South Atlantic. The isoneutral float data set is mapped by applying Objective Analysis with a Gaussian covariance function to either a) space-time velocity averages (Section 3.1) or b) primal velocities using a direct estimate of the covariance function (Sections 3.2 and 3.3, respectively). Details of these methods (referred to as OMSTA: Objective Mapping of Space Time Averages; and OMPFV: Objective Mapping of Primal Float Velocities) are illustrated in flowcharts (Figure 3.1 and Figure 3.9). Individual steps of these flowcharts are cross-referenced in the text by consecutive numbers. Based on these results, transports and their corresponding errors are estimated in Section 3.4.

3.1 Space-time average

Space-time averages provide a first idea of the general structure of the velocity field. Calculation of space-time averages includes two steps: a) binning of primal floats velocities in cells of an averaging grid (Step 3 in Figure 3.1) and b) the space averaging process proper (Step 4 in Figure 3.1). The selection of the averaging grid introduces a significant degree of subjectivity, as the region in which data (and hence oceanic features) are averaged is defined thereby. Usually, data is organized in a regular grid. However, this can merge primal float velocities originated by different currents. A more objective and possibly adequate averaging grid can be achieved by considering the dynamic constraints of oceanic flows. Currents in the ocean are determined by vorticity and/or bathymetry. Hence, grids with cells mapping these properties are likely to provide a useful framework. Based on a regular grid, Davis (1998, his Equation 9)¹ suggested binning float data according to the norm:

$$r^2 = |\bar{x}_a - \bar{x}_b|^2 + \left[3\mu \frac{X_a - X_b}{X_a + X_b} \right]^2, \quad (3.1)$$

where \bar{x}_a is the position vector of the center of a given cell (located at a position with depth X_a) and \bar{x}_b is the position vector of the center of a given float displacement (located at a position with depth X_b). Velocity vectors are allocated to points for which the effective distance r becomes minimal. The parameter μ regulates the sensitivity of the grid to the bathymetry: the larger μ , the more sensitive the grid is to the bathymetry and the smaller μ , the more regular the grid. Davis (1998) justifies his suggestion by stating: “Because area averages are most accurate if they include observations with similar means and because velocities in boundary currents vary more rapidly across isobaths than along them, the measure r of “distance” between points a and b used to assign observations to grid points depends on both horizontal separation and water-depth difference” (Davis, 1998, p. 24,627).

¹ The equation as displayed in Davis (1998) mistakenly features a variable L (personal communication with the author and Núñez-Riboni et al., 2005).

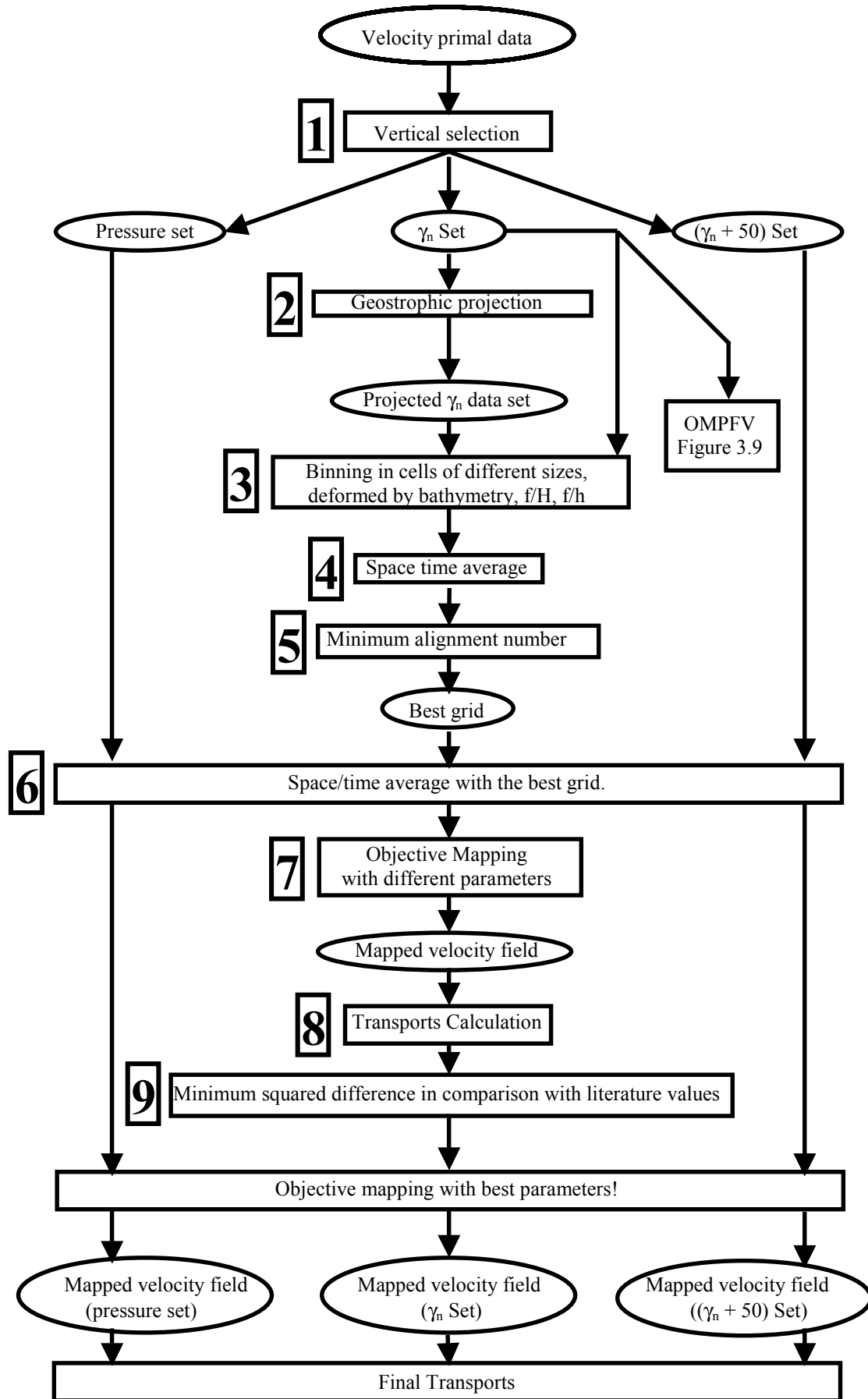


Figure 3.1 Flowchart of data processing involved in OMSTA. Data sets are enclosed by ellipses and processes by boxes. Consecutive numbers identify the processes and are cross-referenced in the text.

Small scale fluctuations of the bathymetry could result in misleading binning of floats displacement vectors. To avoid such undesirable influence, the satellite altimetry bathymetry from Smith and Sandwell (1997) was filtered using twice a 30 point Hanning filter in latitudinal and longitudinal directions (this smoothes in length scales of 1° in both directions; Gille, 2003).

While currents clearly have a tendency to follow isobaths, particularly in regions where they are close to the sea floor, potential vorticity (either from the whole water column or only from the layer) must be considered as constraint as well, due to conservation of potential vorticity. Therefore, the variable X in Equation (3.1) may be understood in a generalized form, representing a physical property such as bathymetry (H from now on), potential vorticity of the whole water column (f/H , with f the local Coriolis parameter) or potential vorticity of the AAIW layer (f/h , where h is the thickness of the AAIW layer).

The property f/h was calculated from the thickness of the AAIW as defined by the neutral density surfaces for the upper and lower boundaries ($\gamma^n = 27.25$ and $\gamma^n = 27.55$). The smoothed bathymetry was used to calculate f/H . Figure 3.2 and Figure 3.3 show examples of the ensuing grids.

After assignment of all primal velocities to cells, they were averaged, yielding one average velocity vector and standard deviation per cell. The resultant velocity was assigned to the center of gravity of all displacement vectors corresponding to the primal velocities binned within the respective cell. Averages based on less than 5 primal velocity vectors were discarded.

Due to the time lag between a float's surfacing and its first position fix by the satellite, as well as a time lag between the last satellite fix and a float's descent, analyses of float trajectories are occasionally preceded by spline-extrapolation (Davis, 1998) or Cokriging¹ (Davis et al., 1992; Schmid et al., 2001) of float ascent and descent positions. However, most of the floats in this study drifted at moderate to high latitudes, where small Rossby numbers imply rather unpredictable surface trajectories. Furthermore, the method used by Schmid et al. (2001) was developed for the tropical band and does not work at higher latitudes (Schmid, personal communication). Hence, an improvement of the floats surfacing and decent positions was considered unlikely and thus rejected.

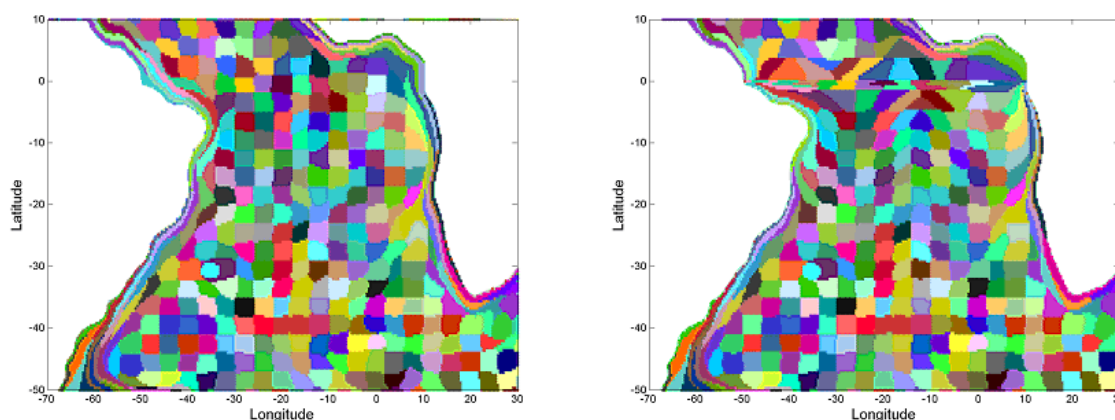


Figure 3.2 Grids constructed with H (left) and f/H (right) using Equation (3.1).

¹ Cokriging is a form of Kriging that involves multiple (correlated) variables.

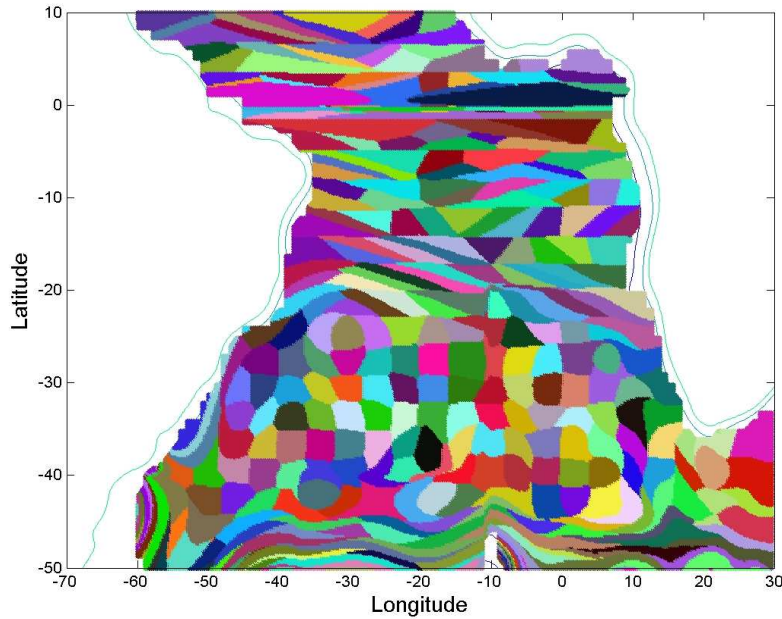


Figure 3.3 Grid constructed with $X = f/h$ in Equation (3.1). The grid parameters are: $\Delta_{\text{lat}} = 3^\circ$, $\Delta_{\text{lon}} = 4^\circ$, $\mu = 6000$. Isopleths of f/h for AAIW as defined by the isoneutral surfaces are shown in Figure 5.6. This grid is used for subsequent space-time averages.

3.1.1 Choice of the best grid

While grids of coarse resolution do not resolve accurately the structure of the velocity field, grids of high resolution may delude the flow field as well. Particularly when data is sparse, high resolution grids likely map mesoscale, transient processes. Interpretation of the ensuing map in terms of long-term mean then results in misleading perceptions of the mean flow field. An extreme example of the first situation would be the averaging of two equally strong currents that flow towards each other within one box, yielding zero flow as a misleading result. An example of the second situation would be the deceptive interpretation of a single transient eddy as a permanent recirculation cell. Hence, the question arises whether it is possible to find a grid that yields the most realistic or “optimum” results, preferably based on some objective measure. Translated into the framework of Equation (3.1), this implies a search for the optimum physical variable X and value for the parameter μ to be used in this equation. To undertake this issue, an approach first presented by LaCasce (2000) is followed hereinafter.

LaCasce (2000) studied the tendency of stochastically modeled floats to follow isopleths of vorticity of the whole water column (f/H). By decomposing float displacements vectors along and across isopleths and integrating the mean and standard deviations of these components, LaCasce obtained measures of the isotropy of the floats’ trajectories with respect to f/H . Following LaCasce’s method, this study projects bin averaged velocities along and across isolines of X (V_{\parallel} and V_{\perp} , respectively; Figure 3.4) from which ensemble averages are formed. From the ratio of the ensemble averages, the *alignment number* A was calculated (Núñez-Riboni et al., 2005, their Equation 2; step 5 in Figure 3.1):

$$A = \frac{\overline{V}_{\perp}}{\overline{V}_{\parallel}} = \frac{\sum_{i=1}^n V_{\perp}^i}{\sum_{i=1}^n V_{\parallel}^i}, \quad (3.2)$$

where the index i refers to the i^{th} averaged velocity or bin, n is the number of cells within the ensemble and V_{\perp}^i and V_{\parallel}^i are the average velocity components perpendicular and parallel to the isolines (Figure 3.4). The alignment number approaches a) $A = 1$ for a totally unaligned field, without preferred direction of flow and b) $A = 0$ for a fully aligned field, with all vectors parallel to the isolines. The optimum grid is, hence, the grid producing a minimal alignment number A . Oceanographically, this implies that the respective variable X has the strongest influence on the AAIW flow field.

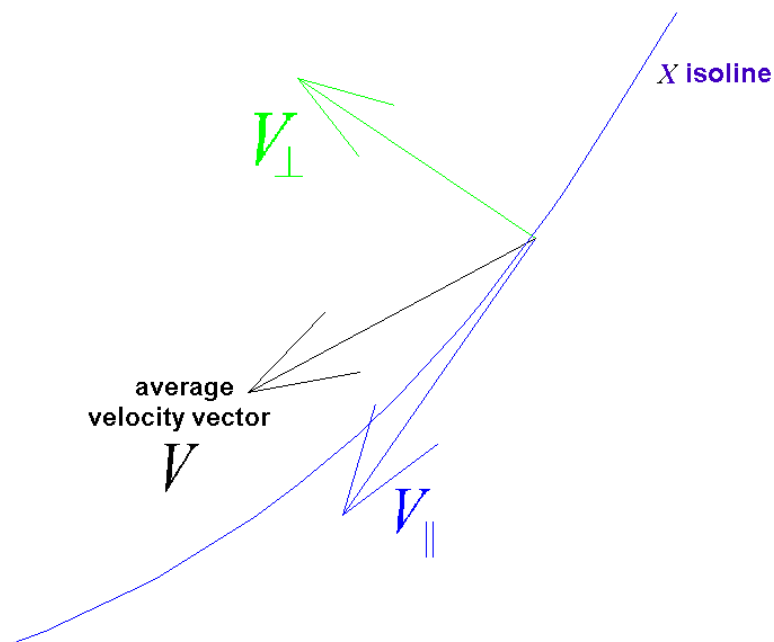


Figure 3.4 Decomposition of an average velocity vector in components parallel and perpendicular to isolines of X .

Núñez-Riboni et al. (2005) constructed approximately 70 grids for each of the 3 implementations of X . The calculations started from 7 combinations of rectangular cell sizes $(\Delta_{\text{lat}}, \Delta_{\text{lon}})$ and assigned subjectively chosen values to the parameter μ . The alignment number was calculated for each of the resulting grids. The results are shown in Table 3.1 (Núñez-Riboni et al., 2005, their Table 2). The first two columns give the dimensions of the original cells before the deformation (referred to as boxes, from now on). The third column indicates the value of μ used to deform the cells. The next three columns specify the alignment number obtained for grids constructed with each of the variables X .

When grouped according to the 7 original grid sizes, the minimum alignment number was obtained 5 times for grids deformed according to f/h , once for grids deformed according to f/H and once for a grid deformed according to bathymetry. Hence the optimal variable to be used in Equation (3.1) is f/h , which agrees with this variable being considered to have a stronger influence on the dynamics of AAIW than f/H or H .

It should be noted that the exact value of the alignment number A depends on the configuration (physical field X and starting resolution $(\Delta_{\text{lat}}, \Delta_{\text{lon}})$) of the grid: the coarser the

resolution, the more zonal the average velocities ¹ and, hence, the smaller A . Therefore, a direct comparison of alignment numbers is only possible between grids that have the same configuration. Unfortunately, this does not allow the comparison of grids with different configurations, which would provide an absolute measure for the best configuration. Therefore, the size of the original cells was not chosen objectively, but rather guided by Davis (1998), where a grid of original cell size of 3° in latitude and 4° in longitude was chosen. This resolution meets the balance between resolving the velocity field and avoiding contamination by mesoscale processes. Therefore, deforming this grid with $\mu = 6000$ (Table 3.1) yielded the bins as used in the space time averaging hereinafter (step 6 in Figure 3.1). This averaging grid is shown in Figure 3.3, while the field $X = f/h$ is shown in Figure 5.6 (Chapter 5).

While the calculations by Núñez-Riboni et al. (2005) were based on a subset of the present float data set (48%), the total amount of data used therein (7564 float displacements) still warrants the assumption that the selection of the optimal grid remains intact for the complete data set. This was tested by repeating some exemplary calculations, as shown in Table 3.2. Once more, the minimum alignment number A was achieved under f/h , with $\mu = 0.660$ (for $\Delta_{lat}=3$ and $\Delta_{lon}=4$) and $\mu = 0.589$ (for $\Delta_{lat}=3$ and $\Delta_{lon}=4$).

3.1.2 Error ellipses

Error ellipses provide the direction and magnitude of variability associated with velocity vector averages. If $V = (\bar{u}, \bar{v})$ is an averaged velocity vector from a cluster of n vectors (u_i, v_i) , the error ellipse associated with V is defined as the ellipse with the following characteristics:

- 1) The ellipses' center is the tip of V . ²
- 2) The ellipses' *semimajor axis* is rotated an angle θ from the North by (derived from Müller, 1987, or from Freeland et al., 1975):

$$\theta = \frac{1}{2} \left[\pi - \arctan \left(\frac{2\overline{u'v'}}{\overline{v'^2} - \overline{u'^2}} \right) \right],$$

where,

$$\overline{u'v'} = \frac{1}{n} \sum_{i=1}^n (u_i - \bar{u})(v_i - \bar{v})$$

and

$$\overline{u'^2} = \frac{1}{n} \sum_{i=1}^n (u_i - \bar{u})^2,$$

¹ A tends to decrease with increasing cell size because a) the larger the cell, the more data it encloses and b) since currents are mainly zonal in most of the regions of the system, meridional variations tend to cancel each other on a shorter scale than zonal variations.

² The center of error ellipses is not compulsive and can be assigned to either the tip or the origin of V as well, with the latter relating it to the significance of the error in comparison to the mean velocity. Here, the center of the error ellipse was assigned to the the tip of the averaged velocity to illustrate the range of possible flow.

Table 3.1 Alignment numbers as calculated for various grid configurations (Núñez-Riboni et al., 2005) based on an subset of float data. The first two columns describe the dimensions of the original rectangular boxes. The third column indicates the corresponding μ value. The next three columns specify the alignment number obtained for each of the grids as deformed following each of the physical variables X . Minimum values for each variable and original grid size are marked in gray and overall minimum value (also for each original grid size) are emphasized by bold letters. Results related to a particular original cell size are enclosed by boxes. The minimum value for each variable and original grid size is marked in gray, whereas the overall minimum value for each original grid size is denoted in bold letters.

Alignment Number						Alignment Number					
Lat	Lon	μ	f/H	f/h	H	Lat	Lon	μ	f/H	f/h	H
2	3	0	0,942	0,929	0,792	4	5	0	0,943	0,799	0,627
2	3	100	0,937	0,777	0,915	4	5	100	0,784	0,612	0,937
2	3	300	0,935	0,772	0,903	4	5	300	0,696	0,61	0,849
2	3	500	0,913	0,776	0,907	4	5	500	0,761	0,623	0,83
2	3	700	0,902	0,779	0,877	4	5	700	0,797	0,622	0,79
2	3	900	0,927	0,77	0,87	4	5	900	0,814	0,632	0,871
2	3	1100	0,931	-	0,858	4	5	1100	0,822	-	0,968
2	3	1500	-	0,755	-	4	5	1500	-	0,643	-
2	3	3000	-	0,785	-	4	5	3000	-	0,586	-
2	3	6000	-	0,751	-	4	5	6000	-	0,635	-
2	4	0	0,939	0,854	0,717	4	8	0	0,756	0,621	0,564
2	4	100	0,849	0,731	0,948	4	8	100	0,649	0,53	0,828
2	4	300	0,863	0,735	0,907	4	8	300	0,637	0,558	0,839
2	4	500	0,848	0,737	0,866	4	8	500	0,69	0,58	0,833
2	4	700	0,832	0,736	0,852	4	8	700	0,627	0,585	0,756
2	4	900	0,856	0,729	0,873	4	8	900	0,648	0,556	0,777
2	4	1100	0,826	0,732	0,87	4	8	1100	0,706	-	0,88
2	4	1500	-	0,742	-	4	8	1500	-	0,612	-
2	4	3000	-	0,742	-	4	8	3000	-	0,622	-
2	4	6000	-	-	-	4	8	6000	-	0,666	-
3	4	0	0,931	0,815	0,707	5	5	0	0,857	0,746	0,740
3	4	100	0,766	0,683	0,922	5	5	100	0,739	0,754	0,871
3	4	300	0,745	0,703	0,922	5	5	300	0,697	0,738	0,868
3	4	500	0,764	0,702	0,944	5	5	500	0,712	0,733	0,828
3	4	700	0,734	0,703	0,912	5	5	700	0,723	0,72	0,816
3	4	900	0,71	0,718	0,929	5	5	900	0,706	0,705	0,809
3	4	1100	0,714	-	0,908	5	5	1100	0,716	-	0,789
3	4	1500	-	0,686	-	5	5	1500	-	0,801	-
3	4	3000	-	0,671	-	5	5	3000	-	0,785	-
3	4	6000	-	0,646	-	5	5	6000	-	0,765	-
3	6	0	1,109	0,919	0,792						
3	6	100	0,853	0,737	1,108						
3	6	300	0,906	0,754	1,116						
3	6	500	0,885	0,757	1,06						
3	6	700	0,866	0,745	1,038						
3	6	900	0,848	0,722	1,02						
3	6	1100	0,833	-	1,013						
3	6	1500	-	0,711	-						
3	6	3000	-	0,58	-						
3	6	6000	-	0,551	-						

Table 3.2 Alignment numbers for exemplary grid configurations using the current data set. For details see the caption of Table 3.1.

Alignment Number					
Lat	Lon	μ	f/H	f/h	H
3	4	100	0.793	0.666	1.011
3	4	6000	0.753	0.660	0.971
4	8	100	0.796	0.601	1.004
4	8	6000	0.770	0.589	1.106

with an analogue expression for $\overline{v'^2}$. In this expression, *arctan* is the four quadrant arctangent, i.e., it yields the angle of the vector $(\overline{v'^2} - \overline{u'^2}, 2\overline{u'v'})$, positive counterclockwise, departing from the positive X axes. Since θ is a geographical angle (positive clockwise, departing from the positive Y axis or North) the required transformation between these two different types of angles is included in the expression presented here (it is related to the value π preceding the arctan).

- 3) The magnitude of the ellipses' axes are defined by (Emery and Thomson, 1997, their Equation 4.3.24):

$$\left. \begin{array}{l} \lambda_1 \\ \lambda_2 \end{array} \right\} = \frac{1}{2} \left\{ \left(\overline{u'^2} + \overline{v'^2} \right) \pm \left[\left(\overline{u'^2} - \overline{v'^2} \right)^2 + 4 \left(\overline{u'v'} \right)^2 \right]^{1/2} \right\},$$

where the + sign is used for λ_1 (variance along major axes or maximum variance direction) and the – sign for λ_2 (variance along minor axes or minimum variance direction).

Ellipses represent a certain confidence interval if scaled by a factor q_a according to:

$$\lambda' = q_a \sqrt{\frac{\lambda}{N_{df}}}.$$

When setting $q_a = 1.414$, the 0.63 confidence interval is chosen (Michel Ollitrault, personal communication; Washington Department of Natural Resources, 1995). The *effective* number of degrees of freedom, N_{df} is given by (Emery and Thomson, 1997, their Equation 3.15.17):

$$N_{df} = \frac{N\Delta t}{T}, \quad (3.3)$$

where N is the number of data values, Δt is the sampling rate (10 days in this study) and T is the *integral timescale*. While pop-up float displacements are assumed uncorrelated (Schmid et al., 2001), 10-day displacements from acoustically tracked floats may be considered statistically independent due to the integral time scale being equal or shorter than 10 days throughout the region and depth horizon considered in this study (Boebel et al, 1999c). Hence, the effective number of degrees of freedom N_{df} is equal to the number of displacement vectors per cell N shown in Figure 3.5.

3.2 Objective Analysis: theory

Objective Analysis (step 7 in Figure 3.1; step 9 in Figure 3.9) or, equivalently, Objective Mapping (OM hereinafter) is an interpolation method used widely in mapping meteorological and oceanographic fields (Gandin, 1963; Bretherton et al., 1976; Bretherton and Williams, 1980; Sarmiento et al., 1982; Hiller and Käse, 1983; Davis, 1985; Olbers et al., 1992; Emery and Thomson, 1997; Wunsch, 1996; Kagan, 1997). The term “objective” – in opposition to “subjective” – emphasizes the fact OM takes into account the number of data in each cell and the errors associated with these. OM is based on the mathematics method called “optimal interpolation” (Liebelt, 1967; Gelb, 1974; Kamen and Su, 1999) or Gauss-Markov estimation.

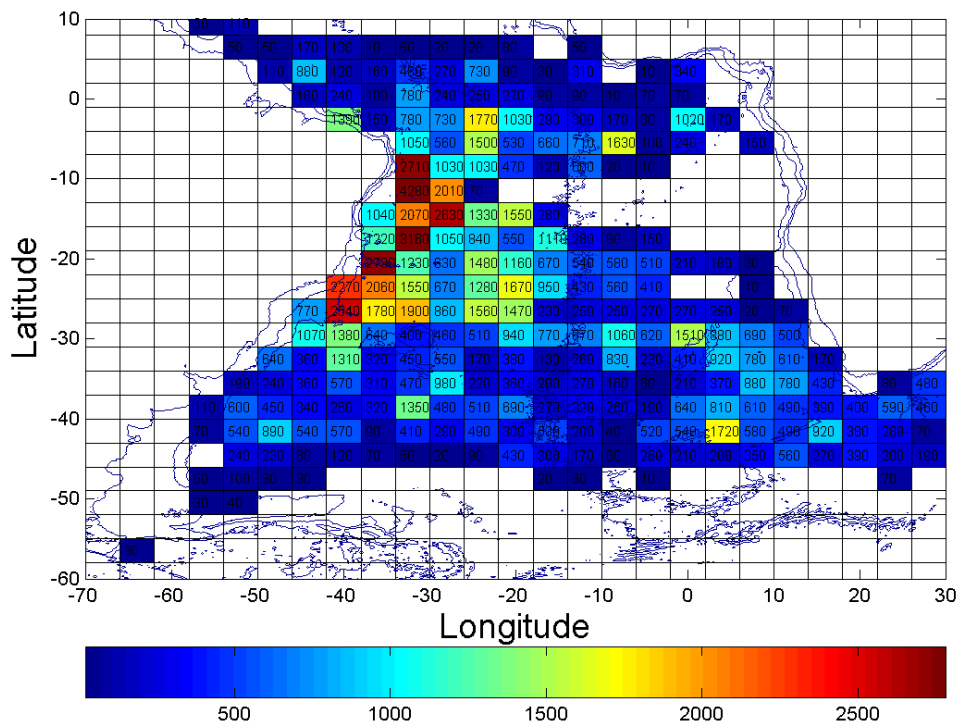


Figure 3.5 Float days of the isoneutral data set for boxes of 3° latitude and 4° longitude. ¹ A float day is the number of days of underwater drift (i.e. 10 days) multiplied by the number float displacements N inside each box.

The text proceeds with a brief description of the theory behind OM, followed by a description of its application to this study. Appendix 1 presents a proof of the Gauss-Markov theorem and Appendix 2 a description of the estimation of the mapping error.

The goal of OM is to determine the value of a physical field $\underline{\eta}$ (referred as the *real* field) at a point $\gamma = (x, y)$ of a graticule,² from values η_i of $\underline{\eta}$ measured at various data points $r_j = (r_{xj}, r_{yj})$, $j = 1 \dots N$ (refer to Figure 3.6). The values η_i are called “observations” and may

¹ While the boxes as displayed here correspond to the undeformed cells, the numbers indicated therein represent the float-days inside the bins of Figure 3.3.

² Within this discussion of OM the word “graticule” rather than “grid” is used to avoid confusions with the grid used previously to make the space-time average.

differ from $\underline{\eta}(r_i)$ by an *uncorrelated* error ε_i . The ensemble of measurements may be combined in a column vector η :

$$\eta = \begin{pmatrix} \eta_1 \\ \eta_2 \\ \eta_3 \\ \vdots \\ \eta_N \end{pmatrix} = \begin{pmatrix} \underline{\eta}(r_1) \\ \underline{\eta}(r_2) \\ \underline{\eta}(r_3) \\ \vdots \\ \underline{\eta}(r_N) \end{pmatrix} + \begin{pmatrix} \varepsilon_1 \\ \varepsilon_2 \\ \varepsilon_3 \\ \vdots \\ \varepsilon_N \end{pmatrix}, \quad (3.4)$$

The error ε is frequently related to noise in the measurements.

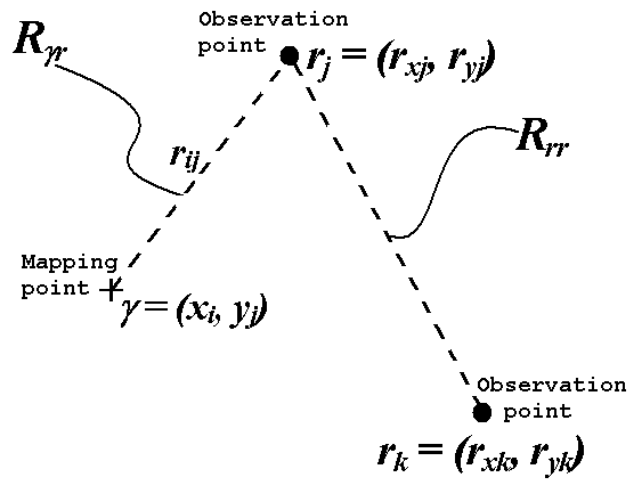


Figure 3.6 Illustration of the OM notation. The positions of observations are denoted with r 's, whereas a graticule point is denoted with γ . The covariance between observations is represented with R_{rr} , whereas the covariance between observations and the mapping point is represented with R_γ .

Let the estimation $\hat{\eta}$ be expressed as a linear combination of these observations:

$$\hat{\eta}(\gamma) = A(\gamma)\eta, \quad (3.5)$$

where A is a row vector with N coefficients to be determined. To find an expression for $A(\gamma)$, the mean square difference between the estimated field $\hat{\eta}$ and the real field $\underline{\eta}$ is minimized, resulting in:

$$A(\gamma) = R_\gamma M^{-1}, \quad (3.6)$$

where M is the autocovariance matrix (of size $N \times N$) of the observations, and R_γ is the covariance row vector (of size N) between the observation data points and the general point γ . Thus, under the necessary prerequisite that the real field has a zero mean (see Appendix 1),

$$\overline{\underline{\eta}(r_k)} = 0,$$

one obtains:

$$R_{\gamma} = (\underline{\eta}(\gamma)\eta_1 \quad \underline{\eta}(\gamma)\eta_2 \quad \dots \quad \underline{\eta}(\gamma)\eta_N). \quad (3.7)$$

The best linear (unbiased) estimation (BLUE) $\hat{\eta}$ of a field $\underline{\eta}$ from a group of observations η at a general point γ is given by substituting (3.6) in (3.5):

$$\hat{\eta}(\gamma) = R_{\gamma} M^{-1} \eta \quad (3.8)$$

This, is called the Gauss-Markov theorem (Appendix 1) forming the basis of OM.

As a consequence of the Gauss-Markov theorem, the error of the mapped field can be estimated by (Equation (A9) from Appendix 2):

$$P = \sqrt{\sigma^2 - R_{\gamma} M^{-1} R_{\gamma}^T}, \quad (3.9)$$

where σ^2 is the variance of the field. For an account of this error estimation, refer to Appendix 2.

Note that (3.5) is not the most general linear estimator for a scalar variable, since it lacks independent coefficients (see Equation 3 from Hiller and Käse, 1983, page 8). Under the Gauss-Markov theorem, the linear coefficients of the most general linear estimator are related to the inverse of the covariance matrix, whereas the independent coefficients are related to mean values of the field. When this “mean” or “background” field is assumed to be zero, the BLUE underestimates the true field, as stated in Emery and Thomson, 1997 (page, 309): “Since the optimal estimator is linear and consists of a weighted sum of all the observations within a specified range of each grid point, the objective mapping (...) produces a smoothed version of the original data field that will tend to underestimate the true field”

The BLUE is essentially a weighted sum of the observations η_i . Hence, considering that a covariance matrix relates directly to the deviations of each measurement from the mean, the weights of the BLUE are related to the measurement errors ε_i . This is shown next.

3.2.1 The error matrix

Considering again a real field with zero mean, the mathematical definition of the covariance matrix M is (Equation (A.4), from Appendix 1):

$$M = \begin{pmatrix} \eta_1\eta_1 & \eta_1\eta_2 & \dots & \eta_1\eta_N \\ \eta_2\eta_1 & \eta_2\eta_2 & \dots & \eta_2\eta_N \\ \vdots & \vdots & \ddots & \vdots \\ \eta_N\eta_1 & \eta_N\eta_2 & \dots & \eta_N\eta_N \end{pmatrix}$$

As a consequence of Equation (3.4) follows:

$$M = \eta\eta^T = \begin{pmatrix} (\underline{\eta}(r_1) + \varepsilon_1)^2 & (\underline{\eta}(r_1) + \varepsilon_1)(\underline{\eta}(r_2) + \varepsilon_2) \cdots (\underline{\eta}(r_1) + \varepsilon_1)(\underline{\eta}(r_N) + \varepsilon_N) \\ (\underline{\eta}(r_2) + \varepsilon_2)(\underline{\eta}(r_1) + \varepsilon_1) & (\underline{\eta}(r_2) + \varepsilon_2)^2 & \cdots (\underline{\eta}(r_2) + \varepsilon_2)(\underline{\eta}(r_N) + \varepsilon_N) \\ \vdots & \vdots & \ddots & \vdots \\ (\underline{\eta}(r_N) + \varepsilon_N)(\underline{\eta}(r_1) + \varepsilon_1) & (\underline{\eta}(r_N) + \varepsilon_N)(\underline{\eta}(r_2) + \varepsilon_2) \cdots & (\underline{\eta}(r_N) + \varepsilon_N)^2 \end{pmatrix}$$

This can be written in a simplified notation:

$$\{M\}_{ij} = (\underline{\eta}(r_i)\underline{\eta}(r_j) + \varepsilon_i\underline{\eta}(r_j) + \underline{\eta}(r_i)\varepsilon_j + \varepsilon_i\varepsilon_j).$$

If the errors are not correlated with each other and the field $\underline{\eta}$, this expression yields:

$$\{M\}_{ij} = (\underline{\eta}(r_i)\underline{\eta}(r_j) + \delta_{ij}\varepsilon_i\varepsilon_j),$$

where δ_{ij} is Kronecker's delta symbol. Finally, if R_{rr} is the covariance matrix of the field $\underline{\eta}$ evaluated at the observational points r_i , i.e.,

$$R_{rr} = \begin{pmatrix} \underline{\eta}(r_1)\underline{\eta}(r_1) & \underline{\eta}(r_1)\underline{\eta}(r_2) & \cdots & \underline{\eta}(r_1)\underline{\eta}(r_N) \\ \underline{\eta}(r_2)\underline{\eta}(r_1) & \underline{\eta}(r_2)\underline{\eta}(r_2) & \cdots & \underline{\eta}(r_2)\underline{\eta}(r_N) \\ \vdots & \vdots & \ddots & \vdots \\ \underline{\eta}(r_N)\underline{\eta}(r_1) & \underline{\eta}(r_N)\underline{\eta}(r_2) & \cdots & \underline{\eta}(r_N)\underline{\eta}(r_N) \end{pmatrix}, \quad (3.10)$$

it follows:

$$M = R_{rr} + R^2,$$

where

$$R^2 = \begin{pmatrix} \varepsilon_1^2 & 0 & \cdots & 0 \\ 0 & \varepsilon_2^2 & \cdots & 0 \\ \vdots & \vdots & \ddots & \vdots \\ 0 & 0 & 0 & \varepsilon_N^2 \end{pmatrix}$$

is a matrix of uncorrelated errors.

The assignment of numerical values to the errors ε_i is not trivial and influences the results of OM significantly. A large uncorrelated error guarantees the positive-definiteness of the covariance matrix (see Appendix 1). Besides, it is reflected in M^I as small diagonal values, which gives a low weight to products of observations with themselves and a larger weight to cross-products of observations, propagating the field signal better than a small error. For this same reason, a large error softens the signal more than a small error and, hence, diminishes its magnitude more. To find a compromise between these opposite effects, knowledge of the field structure and magnitude is required, which normally is not available *a priori*.

3.2.2 Vector fields

To extend the OM algorithm to vector fields such as velocity, a column vector of length $2N$ is defined:

$$\eta = \begin{pmatrix} u_1 \\ u_2 \\ \vdots \\ u_N \\ v_1 \\ v_2 \\ \vdots \\ v_N \end{pmatrix}. \quad (3.11)$$

The corresponding covariance M is constructed from autocovariances R_{uu} and R_{vv} , as well as the cross-covariance R_{uv} in an isotropic second-order two point tensor (Hiller and Käse, 1983):

$$M = R_{rr} + R^2 = \begin{pmatrix} R_{uu} & R_{uv} \\ R_{uv} & R_{vv} \end{pmatrix} + \begin{pmatrix} R_u & O \\ O & R_v \end{pmatrix}^2, \quad (3.12)$$

where R_u and R_v are diagonal submatrices of uncorrelated errors for each velocity component of the observations. The submatrix O is a squared matrix ($N \times N$) of zeros.

Since the elements of the matrix R_{rr} represent the inter-correlation between observations, R_{rr} is a particular realization of R_γ as long as the field to be estimated is the same field of the observations.¹ Therefore, the rows of R_{uu} and R_{vv} in Equation (3.12) are N -dimensional covariance-vectors given by Equation (3.7) where the general point γ is the observational point r_i (see also Equation (3.10) and Equation (A.5) in Appendix 1):

$$R_{rr} = \begin{pmatrix} R_{r_1 r} \\ R_{r_2 r} \\ \vdots \\ R_{r_N r} \end{pmatrix}.$$

Consequently, the covariance between the observations and the mapping point is given by a matrix of 2 rows and $2N$ columns:

$$R_\gamma = \begin{pmatrix} R_{uu} & O \\ O & R_{vv} \end{pmatrix}, \quad (3.13)$$

where, in this case, the covariances R_{uu} and R_{vv} are evaluated in the general point γ and O is an N -dimensional vector of zeros.

¹ This is not necessarily the case, for instance when mapping the stream function.

Note that for vector fields the estimation $\hat{\eta}(\gamma)$ (Equation (3.8)) is a 2-dimensional column vector, where the first element corresponds to u and the second element corresponds to v .

3.2.3 The longitudinal covariance function (LCF)

To evaluate equations (3.12) and (3.13), expressions for R_{uu} , R_{vv} and R_{uv} need to be developed. To find an expression for R_{rr} in Equation (3.12) and the related $R_{\gamma r}$, a general point γ_i out of an ensemble (or grid) of N points will be considered now. This point can be a mapping point, but also an observational point. Thus, for convenience N is also the number of observational points.

Provided the statistics of the data field are stationary, homogeneous and isotropic and the divergence of the field is zero, the velocity covariance matrix $R_{\gamma r}$ can be written in terms of two arbitrary even functions $A(r)$ and $B(r)$ (Hiller and Käse, 1983, their Equation 35; Batchelor, 1990, his Equation 3.4.1):

$$R_{\gamma r} = \begin{cases} \{R_{uu}\}_{ij} = A(r_{ij})(x_i - r_{xj})^2 + B(r_{ij}) \\ \{R_{uv}\}_{ij} = \{R_{vu}\}_{ij} = A(r_{ij})(y_i - r_{yj})(x_i - r_{xj}) \\ \{R_{vv}\}_{ij} = A(r_{ij})(y_i - r_{yj})^2 + B(r_{ij}) \end{cases} \quad (3.14)$$

where (x_i, y_i) is the position of the i^{th} point γ , (r_{xj}, r_{yj}) is the position of the j^{th} observation data point and r_{ij} is the distance between them (Figure 3.6):

$$r_{ij} = \sqrt{(x_i - r_{xj})^2 + (y_i - r_{yj})^2}.$$

Under the same conditions, $A(r)$ and $B(r)$ can be written in terms of a longitudinal covariance function $F(r)$ (Bretherton et al., 1976; Hiller and Käse, 1983; Batchelor, 1990):

$$\begin{aligned} A(r_{ij}) &= -\frac{1}{r_{ij}} \frac{\partial}{\partial r} F(r_{ij}) \\ B(r_{ij}) &= F(r_{ij}) + r_{ij} \frac{\partial}{\partial r} F(r_{ij}), \end{aligned} \quad r_{ij} \neq 0 \quad (3.15)$$

where:

$$F(\vec{r}_{ij}) = \langle (u_{\parallel i} - \bar{u}_{\parallel}) (u_{\parallel j} - \bar{u}_{\parallel}) \rangle, \quad (3.16)$$

where the brackets $\langle \rangle$ denote mean. The longitudinal velocity u_{\parallel} (dashed vectors in Figure 3.7) of a pair of velocity vectors is their projection along the vector \vec{r}_{ij} connecting them.¹

¹ Note that the longitudinal velocity is not defined for $r_{ij} = 0$. Therefore, $F(\vec{r}_{ij})$ must be inferred at the origin by evaluating the limit $r \rightarrow 0$.

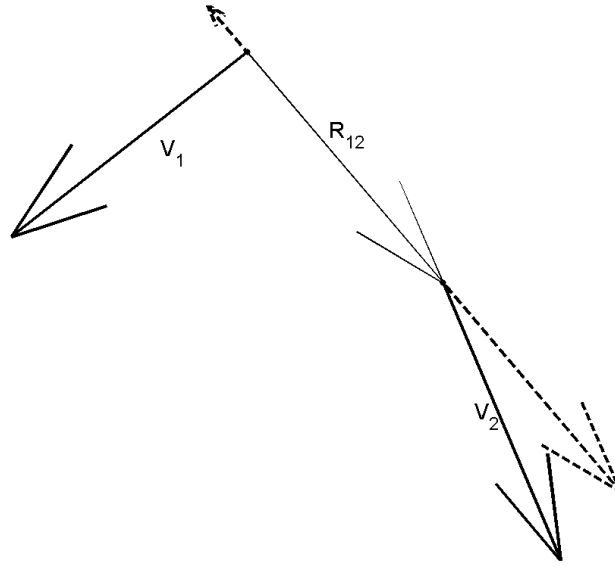


Figure 3.7 The *longitudinal* component of the velocity vectors V_1 and V_2 (dashed arrows) is their projection along the vector R_{12} that connects them.

By inserting (3.15) in (3.14) the covariance matrix $R_{\mathcal{r}}$ can be written as function of $F(r)$ (Hiller and Käse, 1983, their Equation 42):

$$R_{\mathcal{r}} = \begin{cases} \{R_{uu}\}_{ij} = F(r_{ij}) + \frac{(y_i - r_{yj})^2}{r_{ij}} \frac{\partial F(r)}{\partial r} \Big|_{r=r_{ij}} \\ \{R_{uv}\}_{ij} = \{R_{vu}\}_{ij} = -\frac{(x_i - r_{xj})(y_i - r_{yj})}{r_{ij}} \frac{\partial F(r)}{\partial r} \Big|_{r=r_{ij}} \\ \{R_{vv}\}_{ij} = F(r_{ij}) + \frac{(x_i - r_{xj})^2}{r_{ij}} \frac{\partial F(r)}{\partial r} \Big|_{r=r_{ij}} \end{cases}, \quad r_{ij} \neq 0. \quad (3.17)$$

If $r_{ij} = 0$, follows $B(r_{ij}) = F(r_{ij})$, resulting in

$$R_{\mathcal{r}} = \begin{cases} \{R_{uu}\}_{ij} = F(r_{ij}) \\ \{R_{uv}\}_{ij} = \{R_{vu}\}_{ij} = 0, \quad r_{ij} = 0 \\ \{R_{vv}\}_{ij} = F(r_{ij}) \end{cases} \quad (3.18)$$

Substituting the general point $\mathcal{r}_i = (x_i, y_i)$ by an observational point (i.e., $x_i \rightarrow r_{xi}$ and $y_i \rightarrow r_{yi}$ in Equation (3.17)), the covariance matrix R_{rr} between observations is obtained:

$$R_{rr} = \begin{cases} \{R_{uu}\}_{ij} = F(r_{ij}) + \frac{(r_{yi} - r_{yj})^2}{r_{ij}} \frac{\partial F(r)}{\partial r} \Big|_{r=r_{ij}} \\ \{R_{uv}\}_{ij} = \{R_{vu}\}_{ij} = -\frac{(r_{xi} - r_{xj})(r_{yi} - r_{yj})}{r_{ij}} \frac{\partial F(r)}{\partial r} \Big|_{r=r_{ij}} \\ \{R_{vv}\}_{ij} = F(r_{ij}) + \frac{(r_{xi} - r_{xj})^2}{r_{ij}} \frac{\partial F(r)}{\partial r} \Big|_{r=r_{ij}} \end{cases}, \quad r_{ij} \neq 0, \quad (3.19)$$

with (3.18) for the case $r_{ij} = 0$. If γ_i is a mapping point $\gamma = (x,y)$, it follows (refer to Equation (3.13)):

$$R_{\gamma} = \underbrace{\left\{ \begin{array}{l} \{R_{uu}\}_{1k} = F(r_k) + \frac{(y - r_{yk})^2}{r_k} \frac{\partial F(r)}{\partial r} \Big|_{r=r_k} \\ \{R_{vv}\}_{2k} = 0 \end{array} \right\}}_{k=1\dots N} \underbrace{\left\{ \begin{array}{l} \{R_{uu}\}_{1k} = 0 \\ \{R_{vv}\}_{2k} = F(r_k) + \frac{(x - r_{xk})^2}{r_k} \frac{\partial F(r)}{\partial r} \Big|_{r=r_k} \end{array} \right\}}_{k=N+1\dots 2N}, \quad (3.20)$$

with $r_k \neq 0$ the distance between the k^{th} observational point and the general point γ :¹

$$r_k = \sqrt{(x - r_{xk})^2 + (y - r_{yk})^2}. \quad (3.21)$$

For the case $r_k = 0$, an expression similar to Equation (3.18) applies (where $r_{ij} \rightarrow r_k$).

Considering two data points separated a distance r , the *longitudinal* covariance function (LCF hereafter) yields the covariance between the velocity components parallel to the separation vector \vec{r} (Figure 3.7). Following Hiller and Käse (1983), $F(r)$ was defined as a Gaussian bell (Figure 3.8):

$$F(r) = C^2 e^{-\left(\frac{r}{\sigma}\right)^2}, \quad (3.22)$$

where the parameters C and σ , will be defined when implementing three OM algorithms in the next section. Using the derivative of $F(r)$ yields:

$$\frac{\partial F(r)}{\partial r} = -2 \left(\frac{C}{\sigma}\right)^2 r e^{-\left(\frac{r}{\sigma}\right)^2} = -\frac{2r}{\sigma^2} F(r), \quad (3.23)$$

which simplifies the covariance matrix (Equations (3.17) and (3.19)).

Provided the covariance function R_{rr} as defined by Equation (3.19) is positive definite, it yields a positive definite covariance matrix R_{rr} (Bretherton et al., 1976; Emery and Thomson, 1997). However, the positive-definiteness of M depends also on the error matrix R^2 . Therefore, the positive-definiteness of M must be verified regardless of the definition of $F(r)$ (the impact of a positive-definitive M is discussed in detail in Appendix 1).

¹ Without homogeneity and isotropy, r_k must be a vector.

3.2.4 Estimation of the LCF under cylindrical symmetry

The proposition of a model LCF is often necessary due to sparse data prohibiting the calculation of the covariance from observations.¹ However, exploiting the significant size of this study's float data set and its relatively homogeneous spatial distribution, the calculation of a data-based covariance function was attempted using (based on Hiller and Käse, 1983, their Equations 16 and 17; see also Equation (3.16))

$$F(\vec{r}_{ij}) = \frac{1}{n_k} \sum_{C_k} (u_{ij} - \bar{u}_{\parallel})(u_{ij} - \bar{u}_{\parallel}), \quad (3.24)$$

Here the longitudinal velocities u_{\parallel} (dashed vectors in Figure 3.7) of n_k vector pairs (\vec{v}_i, \vec{v}_j) are averaged inside the domain or distance-class C_k defined by \vec{r}_{ij} .

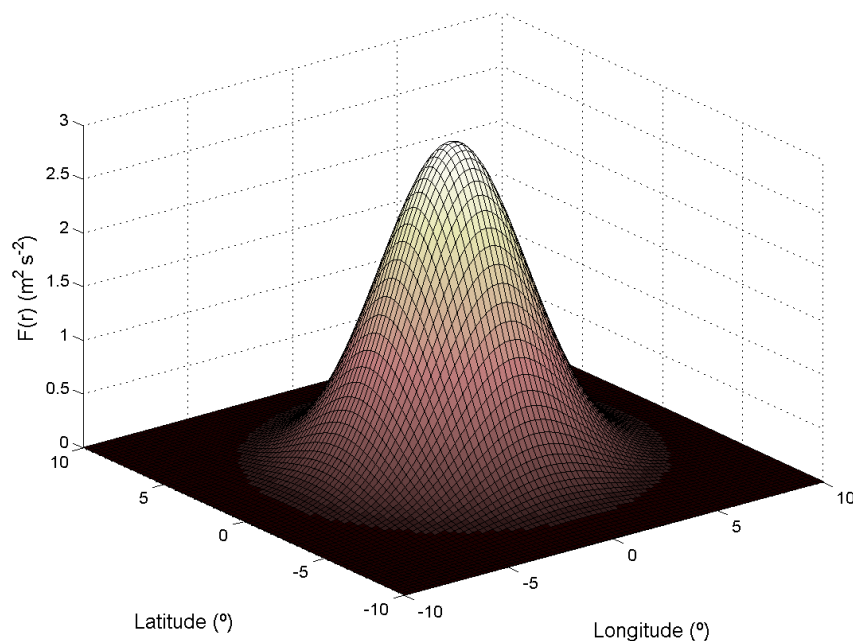


Figure 3.8 Gaussian longitudinal covariance function $F(r)$, Equation (3.22).

Figure 3.9 illustrates the data processing involved in estimating the LCF from the primal float velocities constrained by isoneutral surfaces. First, all combinations of float displacements-pairs were generated, obtaining order of 1×10^8 data pairs (step 1 in Figure 3.9). Next, these pairs were binned in classes C_k . Since Equation (3.24) yields the dependence of the covariance on float-float distances as defined by the classes C_k , the very definition of C_k determines the covariance-functions dependence on the space variables.

¹ Bretherton et al. (1976) suggest the following method to calculate a data-based covariance:

- 1) An initial guess (for instance, a Gaussian function) is chosen.
 - 2) A set of coefficients α_i , subject to the restriction $\sum \alpha_i = 1$, are calculated so that the variance of the estimated function with respect to the first guess is a minimum.
 - 3) A new guess of the covariance function can be calculated as a linear combination of the coefficients α_i .
 - 4) Steps 2 and 3 repeat until the process starts over, continuing until the covariance function converges.
- This complex method aims at constructing a robust covariance function when data is sparse and inhomogeneously distributed in space.

Assuming cylindrical symmetry, the classes C_k were defined here in terms of the absolute distance $\|\vec{r}\|$ between pairs, i.e., neglecting a possible dependence on the relative angular orientation between data points (Figure 3.10; step 2 in Figure 3.9).

Increasing amounts of data within each distance class obviously result in an increasingly robust covariance function. However, maximizing the amount of data within a given class implies a widening of its spatial coverage and, hence, a decrease in the spatial resolution of the covariance function. Therefore, in the definition of classes C_k a balance between resolution, statistical robustness and calculation costs must be achieved while maintaining statistical consistency. The latter criterion suggests each class to contain an about equal number of measurements, which best can be achieved by directly counting the data pairs within subjectively selected classes. Such calculations were performed on a subset of data (1 out of 5 data points) for efficiency reasons. With C_k chosen to embrace approximately 2×10^4 data pairs of the subset, these same distance-classes would embrace order of $5 \times 2 \times 10^4$ pairs in the complete data set (Figure 3.11). Clearly, the number of data pairs is fairly constant but naturally not strictly the same in each class.

The resulting LCF $F(r)$ (step 3 in Figure 3.9) is shown in Figure 3.12 with each dot representing $F(r)$ as calculated inside a distance class C_k . The distances r are defined as the mean value of all the $\|\vec{r}_{ij}\|$ inside a class. The covariance function asymptotically approaches zero with increasing inter-pair distance. Additionally, the pronounced change in the covariance's slope near 4° prohibits the description of the covariance by a simple function, such as a Gaussian bell. Rather, the covariance function may be described by superposing two Gaussian bells. First, assuming that one of these functions had a short range and would tend eventually to zero after a length L , a Gaussian bell was fitted to the covariance points laying at distances larger than L (dashed line in Figure 3.12, eventually superimposed to the thin continuous line). Then, this Gaussian bell was subtracted from the covariance points laying at distances shorter than L and another Gaussian bell was fitted to them (thick line). The optimal L (2.1°) was chosen by minimizing the difference between the fit and the data. (step 4 in Figure 3.9) As it can be seen, the fitted function (continuous thin line) agrees well with the covariance points.

Examination of a LCF obtained without the assumption of symmetry (see next subsection), suggests the following model for $F(r)$ (Figure 3.13):

$$F(r) = F(x, y) = (A_X + A_Y) e^{-\left(\frac{x^2}{\sigma_x^2} + \frac{y^2}{\sigma_y^2} \right)}, \quad (3.25)$$

where A_X and σ_x are the parameters of the narrow Gaussian bell, A_Y and σ_y are the parameters of the wide Gaussian bell and x and y represent longitude and latitude, respectively. The model function implies that the short-range signal (i.e. the narrow bell) is related to the meridional velocity covariance, whereas the long-range signal (i.e. the wide bell) is related to the zonal velocity covariance. However, to maintain the condition of cylindrical symmetry, the zonal part of the LCF (3.25) was neglected. One reason to discard this component is the fact that a long-range covariance does not permit to map mesoscale processes, while the short-scale meridional component of the LCF does allow mapping long-scale features. Another reason justifying the long-range covariance's neglect is related to positive-definitiveness of the covariance matrix M and will be discussed in the next subsection. Hence, the LCF used to map primal velocities was the short-range signal from Figure 3.12, which has parameters $C = 1.97 \text{ cm s}^{-1}$ and $\sigma = 1.61^\circ$ (see Equation (3.22)).

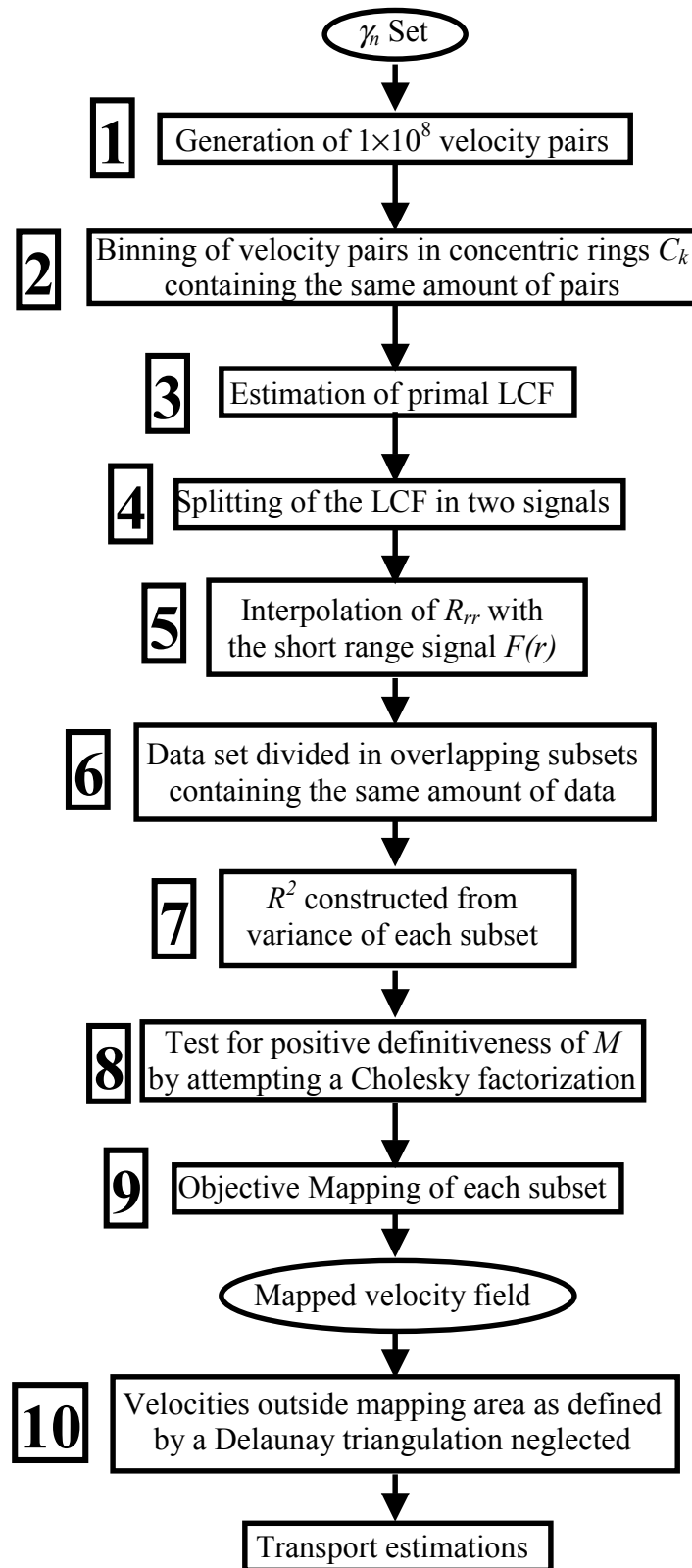


Figure 3.9 Flowchart of data processing involved in the objective mapping of primal float velocities (OMPFV) and longitudinal covariance function (LCF) estimation. Data sets are enclosed by ellipses and processes by boxes. R_{rr} symbolizes the covariance matrix of the real field (evaluated at the observational points r), M is the covariance matrix of the observations and R^2 the error matrix. Consecutive numbers identify the processes and are cross-referenced in the text.

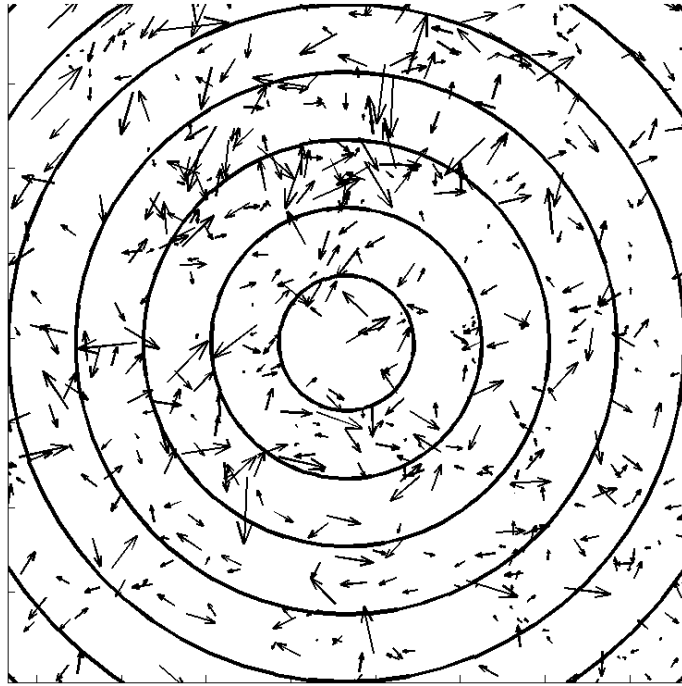


Figure 3.10 Definition of distance-classes C_k in terms of the absolute distance between pairs $\|\vec{r}\|$.

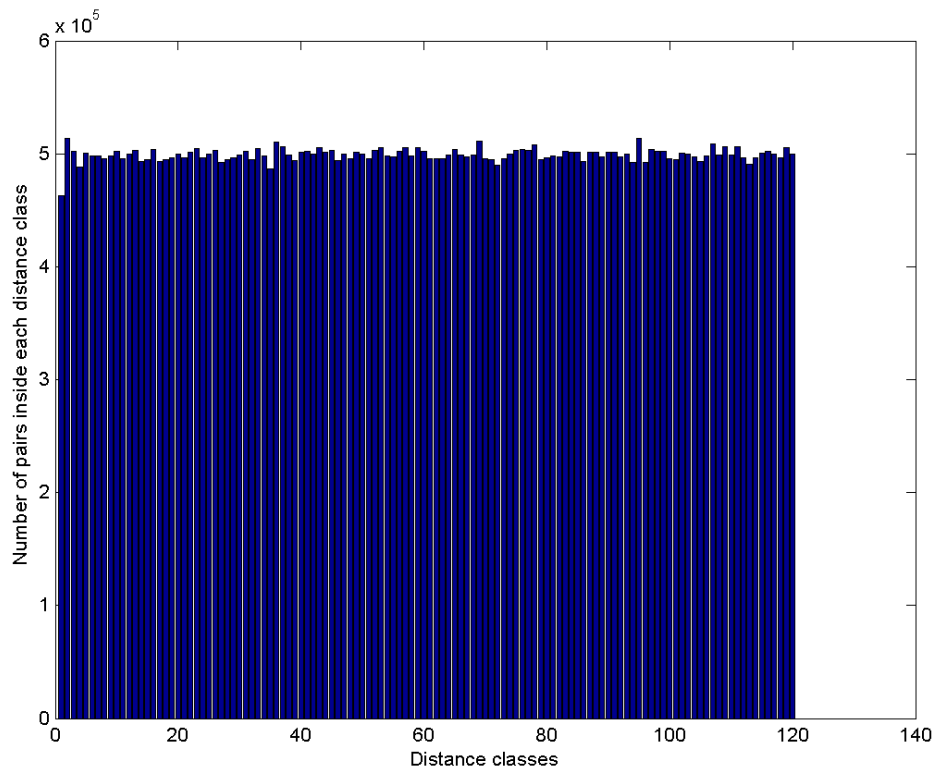


Figure 3.11 Number of velocity pairs inside each distance class C_k (concentric rings, Figure 3.10).

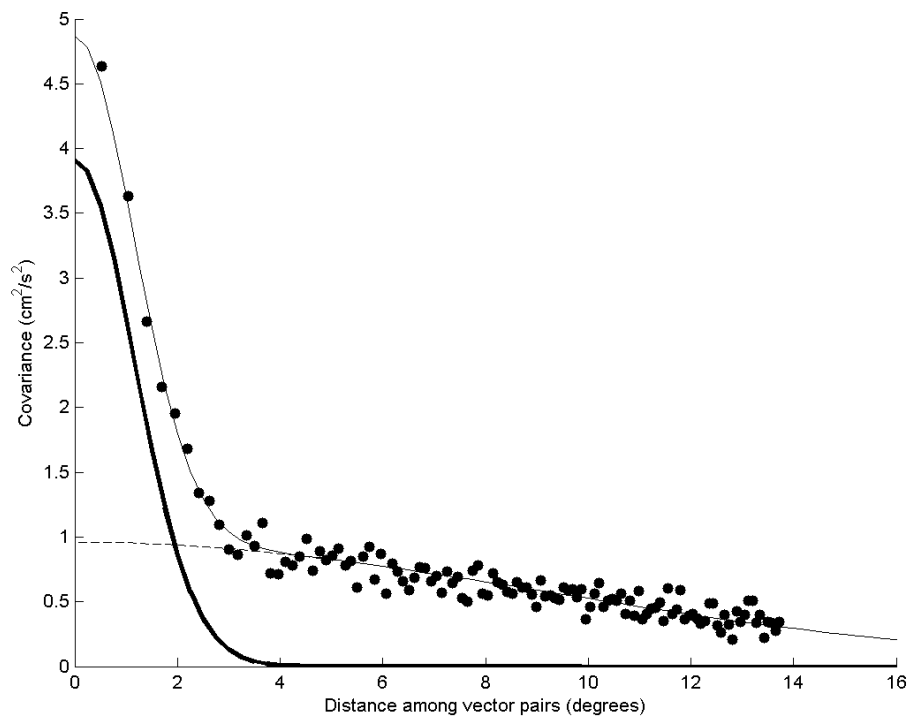


Figure 3.12 LCF estimated ($\text{cm}^{-2} \text{s}^{-2}$) from primal data (dots). The thick continuous line represents the meridional covariance of the field, whereas the dashed line (visible between 0 and 4° only) represents the zonal covariance. The sum of both yields the continuous thin line, which satisfactorily fits the estimated covariance points.

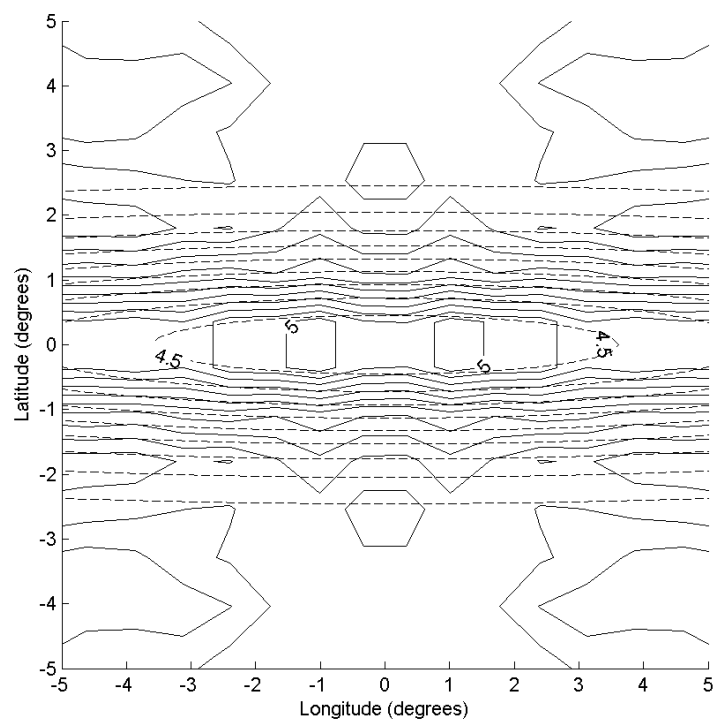


Figure 3.13 Comparison of the LCF calculated while permitting asymmetry (continuous contour lines) and a modeled LCF (dashed contour lines). The modeled LCF is the sum of a longitudinal LCF plus a meridional LCF (Equation (3.25)). The separation between contour lines is $0.25 \text{ cm}^2 \text{ s}^{-2}$.

Note that the decomposition of the covariance function in two components harmonizes with the theoretical frame of OM, since it is based on the assumption of each observation η_i divided as the sum of two quantities (Equation (3.4)). While the separation of the observations into an “error” and a “signal” component may be a matter of convenience in OM, the separation may serve to isolate what would be the main isotropic signal of the velocity field.

Finally, Equations (3.17) and (3.23) indicate that the distance for which $F(r)$ practically becomes zero is the same for R_{uu} , R_{vv} and R_{uv} . Therefore, this distance may be interpreted as the Lagrangian correlation scale for the mapped field. As visible in Figure 3.12, it is approximately 4° .

3.2.5 Estimation of the LCF without assumption of symmetry: an attempt

The assumption of horizontal isotropy is a poor choice, as the interior oceanic motion is governed by vorticity conservation, which sets a strong preference for zonal flow. Figure 3.14 shows the LCF for the tropics, as calculated by defining C_k by longitudinal and latitudinal distance between data pairs. Following Hiller and Käse (1983), different mathematical models were tried to fit the data. Based on the squared difference between the modeled and the primal covariances, the best model was:

$$F(x, y) = A e^{-\left(\frac{x^2}{l_x^2} + \frac{y^2}{l_y^2}\right)} \cdot \cos\left(\frac{2\pi y}{\omega}\right) \ln(|x| + 1) \quad (3.26)$$

The parameters of the model, A , l_x , l_y and ω , were optimized by minimizing the squared differences.¹ As seen in Figure 3.14 and Figure 3.15, the modeled and the primal covariance functions match well. However, the modeled $F(x, y)$ yields a non positive-definitive matrix (see Appendix 1). This might be because the present approach demands an isotropic longitudinal correlation function as a consequence of the symmetry conditions on which it is based.

Averaging the anisotropic correlation function $F(x, y)$ for the entire domain (Figure 3.13) within rings around the origin, reproduces the isotropic $F(r)$ from Figure 3.12 (thin continuous line). However, the ensuing LCF yields also a non positive-definitive covariance matrix M . Since a short range LCF generates a predominantly diagonal matrix, which warrants positive-definitiveness, the non positive-definitiveness of M may be attributed to the zonal LCF. However, beyond the fact that $F(r)$ yields a positive-definitive matrix and good mapped fields, no evidence exists in the present study to prove the inappropriateness of the zonal LCF. For instance, Freeland et al., (1975) calculate also an isotropic LCF out of an anisotropic one by averaging it in circles around the origin and, akin to this study, they obtained a non positive-definitive LCF. However, by computing the Fourier transform of the associated transverse velocity correlation, setting the negative energies equal to zero and transforming back again, Freeland et al., (1975) obtain a positive-definitive LCF out of the non positive-definitive.

In conclusion, in the present study the float velocities were mapped with the short LCF shown in Figure 3.12.

¹ This is the best model only for the tropics. The covariance function as calculated with the whole data set is different and demands another model. This is a consequence of having two different regimes: the tropics and the subtropics.

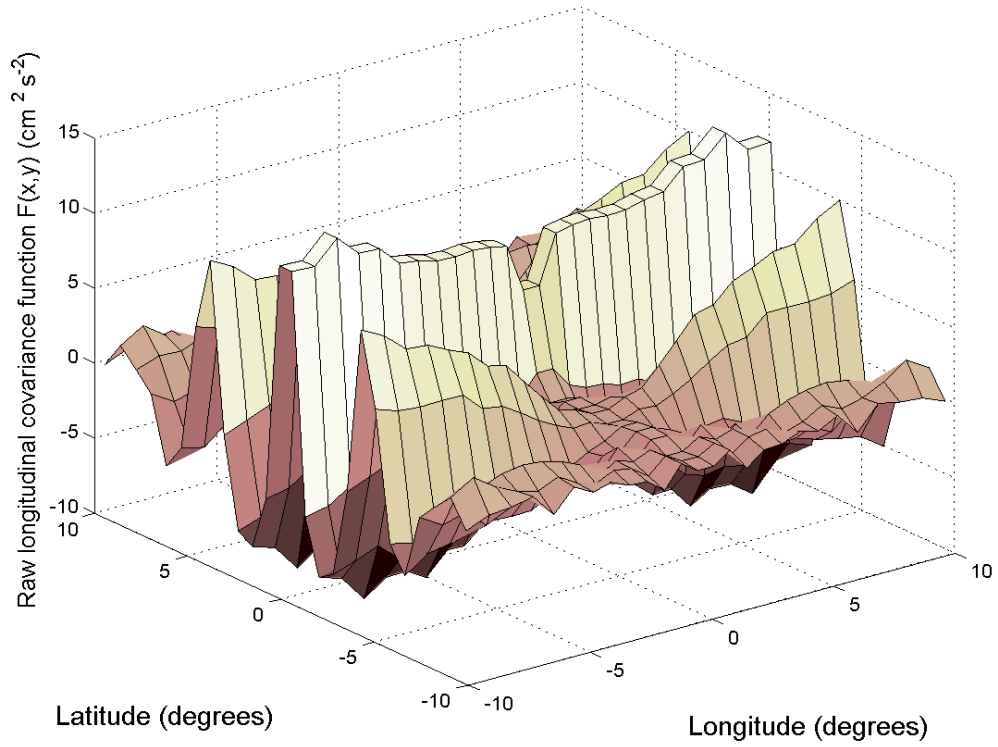


Figure 3.14 LCF $F(x,y)$ from primal float velocities for the tropical region (10°N to 10°S) as calculated by distance classes C_k in longitude and latitude. Units are $\text{cm}^2 \text{s}^{-2}$.

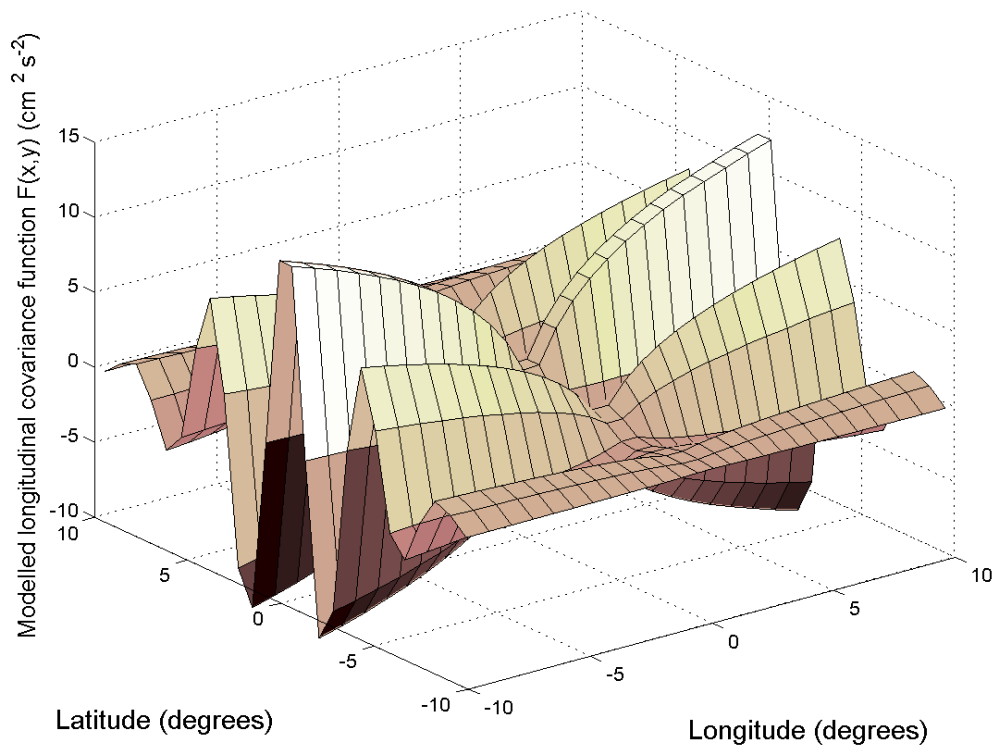


Figure 3.15 Modeled LCF out of the covariance from Figure 3.14 as a function of latitude and longitude. The model used is Equation (3.26). Units are $\text{cm}^2 \text{s}^{-2}$.

3.2.6 The stream function

The Gauss-Markov theorem provides an estimate of the stream function from velocity observations η_i , assuming a non-divergent velocity field and given the covariance L_γ between the velocities and the stream function:

$$\widehat{\phi}(\gamma) = L_\gamma M^{-1} \eta,$$

where M is the auto-covariance matrix between velocity observations η (compare with Equation (3.8)). The choice of M is possible because the optimal coefficients for a field defined by linear operators (i.e. ϕ) are the same as those from the field itself (i.e. velocity v ; Bretherton et al., 1976; Hiller and Käse, 1983).

Next, an expression for L_γ will be sought, starting from the definition of the covariance vector (compare with Equation (3.7)):

$$\{L_\gamma\}_k = \underline{\phi}(\gamma) \eta_k, \quad k = 1 \dots 2N,$$

where $\{L_\gamma\}_k$ represents the k^{th} component of the covariance vector and $\underline{\phi}(\gamma)$ is the “real” stream function evaluated at a general point γ . Assuming homogeneity, isotropy, the definition of η (Equation (3.11)) and the definition of the stream function,

$$\begin{aligned} u &= -\frac{\partial \phi}{\partial r_y}, \\ v &= \frac{\partial \phi}{\partial r_x}, \end{aligned} \tag{3.27}$$

one obtains:

$$\begin{aligned} \{L_\gamma\}_k &= -\underline{\phi}(\gamma) \frac{\partial \phi(r_k)}{\partial \Delta_{yk}}, \quad k = 1 \dots N \\ \{L_\gamma\}_k &= \underline{\phi}(\gamma) \frac{\partial \phi(r_k)}{\partial \Delta_{xk}}, \quad k = N + 1 \dots 2N \end{aligned} \tag{3.28}$$

where the origin of coordinates has been set at $\gamma = (x, y)$. Hence, r_k is the distance between the k^{th} observational point and the general point γ (Equation (3.21)) and $\Delta_{xk} = x - r_{xk}$ and $\Delta_{yk} = y - r_{yk}$. Now, considering $r_k = \sqrt{\Delta_{xk}^2 + \Delta_{yk}^2}$, it follows

$$\frac{\partial \phi}{\partial \Delta_{xk}} = \frac{\Delta_{xk}}{r_k} \frac{\partial \phi}{\partial r_k}, \quad r_k \neq 0$$

with a similar expression for y . Inserting this in Equation (3.28), and noting that γ does not depend on r_k , yields:

$$\begin{aligned} \{L_{\gamma^r}\}_k &= -\frac{\Delta_{yk}}{r_k} \frac{\partial}{\partial r_k} (\underline{\phi}(\gamma)\phi(r_k)), & k = 1 \dots N \\ & & r_k \neq 0 \\ \{L_{\gamma^r}\}_k &= \frac{\Delta_{xk}}{r_k} \frac{\partial}{\partial r_k} (\underline{\phi}(\gamma)\phi(r_k)), & k = N + 1 \dots 2N \end{aligned}$$

Since the mean field is zero, the products $\underline{\phi}(\gamma)\phi(r_k)$ are related to the covariance $\Phi(r_k)$ of the stream function between observations and the mapping point γ . Therefore,

$$\begin{aligned} \{L_{\gamma^r}\}_k &= -\frac{\Delta_{yk}}{r_k} \frac{\partial \Phi(r_k)}{\partial r_k}, & k = 1 \dots N \\ & & r_k \neq 0 \\ \{L_{\gamma^r}\}_k &= \frac{\Delta_{xk}}{r_k} \frac{\partial \Phi(r_k)}{\partial r_k}, & k = N + 1 \dots 2N \end{aligned}$$

Finally, considering (Hiller and Käse, 1983, their Equation 43; Bretherton et al., 1976, their Equation 28d):

$$F(r_k) = -\frac{1}{r_k} \frac{\partial \Phi(r_k)}{\partial r_k},$$

it follows that (Hiller and Käse, 1983; their Equation 50):

$$\begin{aligned} \{L_{\gamma^r}\}_k &= \Delta_{yk} F(r_k), & k = 1 \dots N \\ & & r_k \neq 0. \\ \{L_{\gamma^r}\}_k &= -\Delta_{xk} F(r_k), & k = N + 1 \dots 2N \end{aligned} \quad (3.29)$$

Hence, the provision of a LCF $F(r)$ facilitates the formulation of a covariance vector between the velocity observations and the stream function.

By means of Equation (3.20) it can be shown that:

$$\begin{aligned} \{R_{uu}\}_k &= -\frac{\partial \{L_{\gamma^r}\}_k}{\partial \Delta_{yk}}, & k = 1 \dots N \\ \{R_{vv}\}_k &= \frac{\partial \{L_{\gamma^r}\}_k}{\partial \Delta_{xk}}, & k = N + 1 \dots 2N, \end{aligned}$$

which is in concordance with the definition of the stream function, Equation (3.27). This implies, that (3.29) can be understood as an analytical integration of Equation (3.20). Hence,

the well-known dependence on the path when integrating the velocity field numerically does not concern the present approach of estimating a stream function.

The units of a stream function ϕ arising from this calculation are [$\text{m}^3 \text{s}^{-1} \text{m}^{-1}$], i.e., the stream function represents transport *per depth interval*. To calculate volume transports, the stream function was multiplied by the corresponding depth or layer thickness, giving the barotropic stream function ψ .

3.2.7 Summary

OM is an interpolation method that uses a weighted linear combination based on the spatial distribution and density, as well as the associated errors of the input data. Its main advantages are:

- It is straightforward and relatively simple to implement in a computer program
- It is flexible: while for *each* of the points γ from the mapping grid the covariance(s) between the observations and the field(s) to be estimated must be calculated (i.e., Equations (3.20) and (3.29)), the covariance matrix M between observations must be calculated and inverted only once.
- This permits to map simultaneously various variables defined by linear operators without additional manipulation of the input data.

The weaknesses of OM have been enumerated along with the description of the method (including Appendix 1 and Appendix 2):

- The mean of the field has to be zero or must be subtracted of the input data. When this is not possible, an underestimation of the real field is to be expected.
- The covariance matrix M between observations is subject to an unavoidable mathematical restriction: positive-definitiveness.
- An *a-priori* knowledge of the field's covariance and uncorrelated error is required: the analyst must estimate these from the data set being studied or, alternatively, make corresponding assumptions.
- To obtain mapped errors, a climatological variance of the real field has to be assumed. If the mapped field is the same than the observed field, the observations (or the covariance function) can be used to get an estimate of the climatological variance. However, if this is not the case (e.g. when stream function is mapped from velocity observations), a value has to be guessed.

3.3 Objective Analysis: application

Different choices of the parameters involved in OM introduce considerable differences between the resulting mapped fields. Hence, to explore the sensitivity of the method, various approaches based on the scalar and vectorial algorithms as well as combinations of the input data (average vs. primal velocities) and parameters were performed, using different input errors, variability of the climatological field, correlation length(s) as well as the mapping graticule. As product, three different implementations of OM were developed in the present study. The following subsections provide details thereof, with a brief description of the method's characteristics given at the beginning.

3.3.1 *Scalar OMSTA (objective mapping with space-time averages)*

Input data: space-time average velocities.
 OM algorithm: scalar, applied independently to each velocity component.
 Covariance: Gaussian LCF (Figure 3.8).
 OM parameters chosen by: average grid size and 0.63 probability errors.

With the application of OM to the entire primal data set being impractical due to limited computing capabilities, the first choice was to apply OM to the box-averaged velocity data. The matrix R^2 was chosen as diagonal matrix containing the latitudinal and longitudinal components of the 0.63 probability error ellipses (Subsection 0 and Figure 4.1). The scalar algorithm was applied independently to each velocity component u and v . As a first guess, the correlation lengths for the zonal and meridional directions were chosen equal to the widths of the cells of the averaging grid (4° and 3° , respectively). The mapping graticule was $1^\circ \times 1^\circ$. All graticule points within a cell of the averaging grid either containing data, or being surrounded by at least four cells holding data were mapped (see Subsection 3.3.4 below).

3.3.2 *Vectorial OMSTA (objective mapping with space-time averages)*

Input data: space-time average velocities.
 OM algorithm: vectorial.
 Covariance: Gaussian LCF (Figure 3.8).
 OM parameters chosen by: comparison with literature values (minimizing the quadratic differences).

To estimate a correlation length for the Gaussian covariance function, almost 300 objective velocity maps were calculated, using subjectively chosen climatological value pairs (from 3 to 11 cm s^{-1} for the climatologic error and 1° to 30° for the correlation length; step 7 in Figure 3.1). For each resulting velocity map, zonal and meridional volume transports were calculated (step 8 in Figure 3.1). Finally, the resulting transport estimates were compared against literature values (see Section 5.2.4 below). The analysis based on parameters providing the smallest squared error were chosen as optimal solution (Núñez-Riboni et al., 2005; step 9 in Figure 3.1). The corresponding parameters were $C = 3 \text{ cm s}^{-1}$ and $\sigma = 4^\circ$ (see Equation (3.22)). The input data set, error matrix R^2 , mapping area and graticule were the same than in scalar OMSTA.

A previous approach to estimate a correlation length in this study had to do with the “mixing lengths” of Böning and Cox (1988) (Equation in page 329) and Böning (1988) (Equation between 1 and 2, page 1380). These equations should give estimated correlation lengths, given a known integral timescale and homogeneity of the data set. Correlation lengths for integral time-scales of 10 days were calculated, obtaining values of around 50 Km. This number coincided well with results from Böning (1988). However, mapping with such a correlation length yielded physically unrealistic results for the basin scale general circulation.

3.3.3 *OMPFV (objective mapping with primal float velocities)*

Input data: primal data divided in overlapping subsets.
 OM algorithm: vectorial.
 Covariance: Gaussian LCF (Figure 3.8).
 OM parameters chosen by: fit of a Gaussian model to the experimental isotropic LCF.

The covariance function $F(r)$ was estimated from the primal float velocities as constrained by isoneutral surfaces, assuming cylindrical symmetry (Subsection 3.2.4). R_{rr} was interpolated with Equations (3.18) and (3.7.8) (step 5 in Figure 3.9). To reduce the data volume during the analysis and avoid computational problems or excessive computation time, the data set was divided in smaller overlapping (by 10°) subsets (Figure 3.16), containing similar amounts of data each (approximately 3500 data points; step 6 in Figure 3.9). Results within the outer 4° (one Lagrangian correlation length, Subsection 3.2.4) were discarded from each data set to provide a buffer region. Results within the remaining strip of 2° of overlap between subsets were averaged.

The variance of each subset was used for the error matrix R^2 (see below; step 7 in Figure 3.9). Positive definitiveness was tested for each subset by attempting a Cholesky factorization, which is only possible if the matrix is positive-definitive (step 8 in Figure 3.9). All subsets passed the test. Next, each subset was mapped independently onto a regular graticule of $1^\circ \times 1^\circ$ spacing (step 9 in Figure 3.9). The mapping area was defined as outlined in Subsection 3.3.4 below (step 10 in Figure 3.9).

Maintaining similar amounts of data in each subset is important to control the influence of the input measurement error. Unfortunately, an objective choice for this error is not possible within this analysis, but a natural choice for the input error is the standard deviation of each data set. However, a given value would yield different results of the mapped field, depending on the number of data points used in the OM. Such spurious differences can therefore be minimized by choosing similar amounts of data for each subset.

Due to computational limitations, a direct calculation of the matrix M^{-1} was not possible, despite the division in subsets. Rather, the product $M^{-1}\eta$ was calculated employing the Generalized Minimum Residual Method (GMRES). This, however excludes the calculation of mapped errors (Equation (3.9)), as the product $M^{-1}R_\gamma$ must be determined at each point γ . With each subset consisting of order of 1000 data points, this was impossible (it has been estimated that for the dataset with subsets of 2000 data points the mapping would take 19 days on a 2.8 GHz processor). Therefore, for the purpose of transport estimates, the errors from the scalar OMSTA were used.

3.3.4 The mapping area

Due to the implicit condition of non-divergence, OM tends to close gyres at the boundaries of the data set or in areas with few or no data, thereby generating spurious currents. Hence, care must be taken in the definition of the mapping area, which was chosen here on geometrical considerations:

In the case of scalar and vectorial OMSTA, the grid of the space-time average was used to define a mapping area. All graticule points within a cell of the space-time averaging grid containing data, or being surrounded by at least four cells with data (Figure 3.17) were mapped. The mapped velocities outside this area were neglected. On the other hand, OMPFV is not related to a grid defined prior to the OM and a purely geometric approach is needed. A Delaunay triangulation of the data points was chosen for this case. A Delaunay triangulation of a data set is “a set of triangles such that no data points are contained in any triangle’s circumcircle” (MATLAB manual, 2000, page 12-21). Hence, if a triangle of the Delaunay triangulation had its three sides shorter than 4° , it was considered part of the mapping area. Otherwise it was discarded. The result is shown in (Figure 3.18).

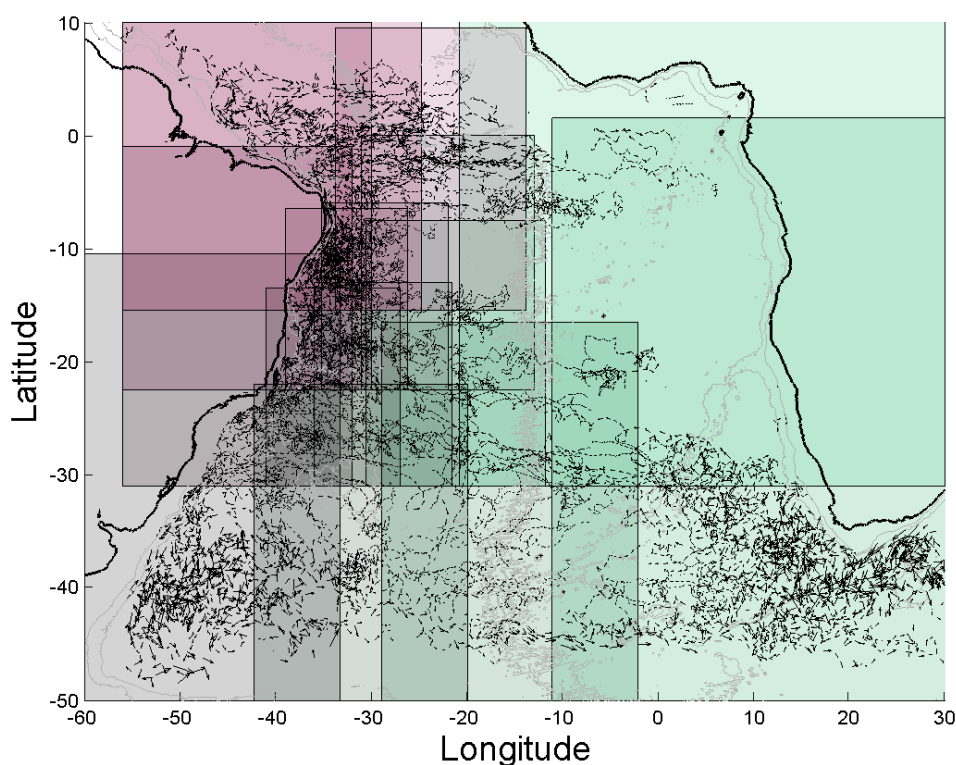


Figure 3.16 Division of the primal data set (as constrained by isoneutral surfaces) in smaller, overlapping subsets to avoid computational problems with OMPFV.

By defining a mapping area independent of the mapping graticule, the graticule is limited only by the computing capabilities and time, and not by its influence on the results. Under these criteria, a mapping graticule of $1^\circ \times 1^\circ$ was chosen for the three methods.

Alternative methods to constrain the mapping region include graticule-selection based on associated error or spatial coincidence with measurement data. Defining the area based on OM output error is a common approach. While the output error depends on the statistical quality of the input data, it also depends inevitably on the variability of the field (see Appendix 2). Omitting mapped data based on limiting “errors” implies (rightly or not) neglecting fields of high variability (examples are the Agulhas System and the Confluence Zone).

3.4 Transports

While transports could be estimated from the stream function, the lack of knowledge of the variability of the climatological field of the stream function does not allow to calculate errors associated to the transport. On the other hand, errors of the mapped velocity arise from the climatological variability defined by the LCF. Hence, the objectively mapped velocities were used to calculate volume and property transports.

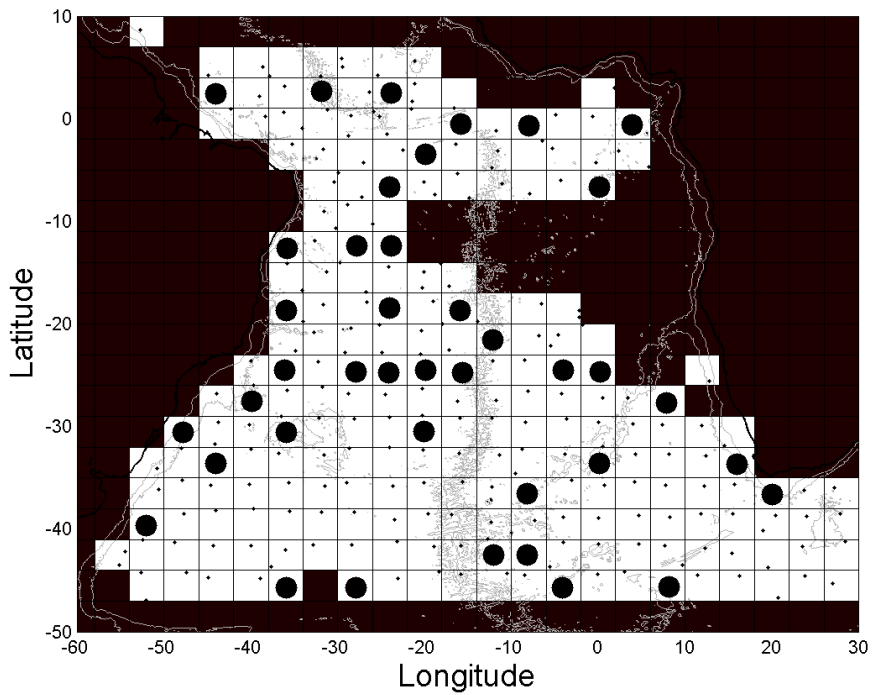


Figure 3.17 Mapping area of scalar and vectorial OMSTA. Small dots represent input data (i.e. the position of bin averaged velocities). The surrounding boxes (of the undeformed averaging grid) define the mapping area. Boxes with zero data but surrounded by at least four cells containing data were also considered as mapping area (boxes with large black dot).

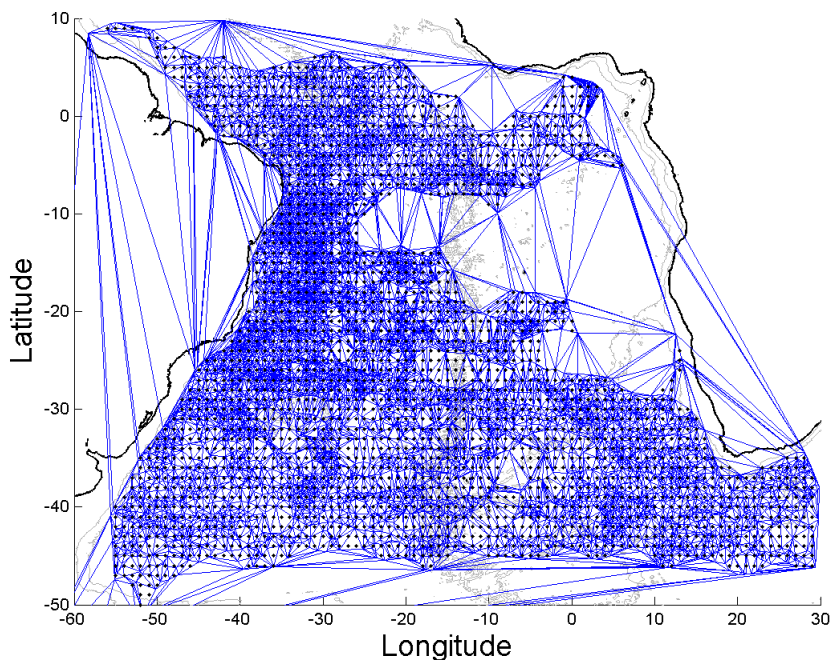


Figure 3.18 Delaunay triangles of the primal float velocity data as constricted by isoneutral surfaces (Figure 2.9). Graticule point (black dots) are assigned to all triangles with all three sides shorter than the Lagrangian correlation length (4°), defining the mapping area for OMPFV.

The overall impact of AAIW for the AMOC in the transport of heat, salinity and freshwater does not only depend on the absolute native transports of the layer, but also on the distribution of heat content and salt throughout the water column and across the ocean. This fact is particularly illustrated by the heat transport: In oceanography, the absolute thermal energy carried by a single layer is rarely used and of little value by itself, since only the heat transport integral spanning the full water depth and basin width provides information on possible warming or cooling of adjacent regions. Such approach ensures that the corresponding mass budget is closed. A heat transport per layer, which implies an open system without conservation of mass, is commonly referred to “temperature transport”. Since this study focuses on the AAIW layer, net contributions of AAIW cannot be formally estimated, given that (to our knowledge) the temperature and salt transports at other horizons (central and surface waters, including Ekman transport, NADW and AABW) are not known. Hence, in the present study, meridional contributions of the AAIW to the heat, salinity and freshwater budgets of the South Atlantic have been estimated by relating transports to the mean vertical temperature and salinity in the basin from Levitus (1994).

3.4.1 Volume transport

To calculate the transport T through the walls of graticule boxes, velocity vectors v [m s^{-1}] were multiplied by the thickness ξ of each objective-map cell, yielding meridional and zonal transports per distance:

$$T_l = v \cdot \xi$$

Multiplying the transport per distance T_l by the zonal (or meridional) widths l of each graticule box in meters yields a transport:

$$T = v \cdot \xi \cdot l \quad (3.30)$$

The width l was calculated by multiplying the width of the cells in radians by the mean equatorial radius of the Earth (6378.1 Km).

Zonally averaged transports and zonally integrated transports (i.e., basinwide meridional transports) were calculated by averaging or summing the values in cells at the same latitude. Transports errors T' in each cell were calculated using Gauss' law of propagation (or combination) of errors (Barlow, 1989, based on his Equation 4.14):

$$T'^2 = \left(\frac{dT}{dv}\right)^2 v'^2 + \left(\frac{dT}{d\xi}\right)^2 \xi'^2 + \left(\frac{dT}{dl}\right)^2 l'^2,$$

where v' is the velocity error from the objective analysis (Equation (3.9)), Δ' is the error of the layer's thickness and l' is the error associated to the boxes' width. With $l'=0$ (the grid's box sizes are free of error by definition), (3.30) yields an error in the transport per cell T' :

$$T' = l \sqrt{(\xi v')^2 + (v \xi')^2} \quad (3.31)$$

Expanding (3.31) with $(v\xi)^2$ and using (3.30) yields: ¹

¹ It is not necessary to clarify that $v \neq 0$, since v is included in T (see Equation (3.30)).

$$T' = T \sqrt{\left(\frac{v'}{v}\right)^2 + \left(\frac{\xi'}{\xi}\right)^2}, \quad (3.32)$$

With transports assuming either positive or negative values, the absolute value of the transport was used in (3.32) to calculate the error T' .

From (3.30) mean longitudinal and basin-wide meridional transports were estimated. The mean zonal error \overline{T}' is the propagation of the *correlated* errors T'_i across each cell i , according to (Núñez-Riboni et al., their Equation 3):

$$\overline{T}'_z = \frac{1}{N_{df}} \sqrt{\sum_{i=1}^N T_i'^2}, \quad (3.33)$$

where N is the number of graticule boxes along a given latitude and N_{df} is the *effective* number of degrees of freedom of each zonal section. For N_{df} a spatial analogous of Equation (3.3) was estimated, considering that the integral length scale equals the distance passed during an integral time scale period (Böning and Cox, 1988; Núñez-Riboni et al., 2005, their Equation 4):

$$N_{df} = \frac{N\Delta l}{L},$$

where Δl is the zonal extent of the graticule boxes (which replaces the sampling period Δt) and L is the integral length scale (which replaces the integral timescale T). In the estimation of the isotropic LCF, a Lagrangian correlation length of 4° has been estimated, which is a reasonable value for L . Δl is defined by the spacing of the mapping graticule, i.e., 1° .

Similarly, to account for the correlation between cells, the error T'_m associated to the basin-wide meridional transports has been weighed with $\frac{\Delta l}{L}$, i.e.:

$$\overline{T}'_m = \frac{\Delta l}{L} \sqrt{\sum_{i=1}^N T_i'^2}, \quad (3.34)$$

3.4.2 Temperature transport

The temperature transport was calculated by multiplying volume transport by heat content (Bryan, 1962; Bennet, 1978; Hall and Bryden, 1982). Based on potential temperature θ and in-situ density ρ , the heat content *q per unit volume* is:

$$q = \rho \cdot C_P \cdot \theta,$$

where C_P is the (mean) specific heat capacity (at constant pressure). Calculation of the temperature transport Q_C in each box of the mapping graticule follows:

$$Q_C = q \cdot T = \rho \cdot C_P \cdot \theta \cdot T.$$

Here T represents the volume transport through the walls of a cell (Equation (3.30)). Zonal or meridional integration yields meridional or zonal temperature transports, respectively. The

total meridional transport can be calculated as a function of latitude by (Jung, 1952; Bryan, 1962; Hall and Bryden, 1982):

$$Q(\lambda) = \sum_{\varphi} Q_C = \rho \cdot C_p \cdot \sum_{\varphi} \theta \cdot T,$$

where the temperature transport Q_C across the walls of cells at the same latitude λ is added along the longitude φ .

To be able to compare the contribution of AAIW to the heat budget of the South Atlantic, the temperature transport estimate above was referred to an estimate of the heat content of the entire water column by:

$$Q_R(\lambda) = \rho \cdot C_p \cdot \sum_{\varphi} (\theta_{AAIW} - \bar{\theta}_{Levitus}) \cdot T,$$

where $\bar{\theta}_{Levitus}$ is the gridded annual vertical mean-temperature from Levitus (1994). This defines the heat content per unit volume of the water column as a zero value (at each latitude), yielding a measurement of the meridional heat contribution of the AAIW to the South Atlantic budget. To stress that this is a temperature transport relative to the mean vertical heat content, Q_R will be called “relative” temperature transport in this study.

The error associated with the temperature transport (per box) can be derived directly from Equation (3.32) by adding a term related to potential temperature θ (note also the footnote to Equation (3.32)):

$$Q' = Q \sqrt{\left(\frac{v'}{v}\right)^2 + \left(\frac{\xi'}{\xi}\right)^2 + \left(\frac{\theta'}{\theta}\right)^2}, \quad (3.35)$$

where θ' is the error associated with the isoneutral surface for temperature.¹

3.4.3 Salinity transport

Salt transports Z_C through the walls of each box of the graticule were calculated by:

$$Z_C = \rho \cdot S \cdot T,$$

where ρ and S are density and salinity of the AAIW and T is its volume transport. Salinity in this study is given in the practical salinity scale (PSS-78; Lewis, 1980). Given that PSS-78 is comparable with the earlier units of parts per thousand (Baum, 2004) a conversion between scales can be performed directly without affecting the resulting transport considerably.²

$$Z_C = \frac{\rho \cdot S \cdot T}{1000} \quad (3.36)$$

The error of the salinity transport can be inferred based on Equation (3.32) by adding a term related to salinity S (see also footnote to Equation (3.32)):

¹ Considering θ is expressed in °K, it can never be zero.

² Hence, the units of the salt transport are kg s^{-1} . Results from this study can be compared with other considering $1 \text{ kg s}^{-1} \cong 1 \times 10^{-9} \text{ (PSU) Sv}$.

$$Z' = Z \sqrt{\left(\frac{v'}{v}\right)^2 + \left(\frac{\xi'}{\xi}\right)^2 + \left(\frac{S'}{S}\right)^2} \quad (3.37)$$

where S' is the error in the salinity data.

The net meridional contribution to the South Atlantic salt budget is obtained using as reference value the vertical salinity mean in the South Atlantic, $\bar{S}_{Levitus}$, as given by Levitus (1994) atlas data:

$$Z_R(\lambda) = \frac{\rho}{1000} \cdot \sum_{\varphi} (S_{AAIW} - \bar{S}_{Levitus}) \cdot T,$$

where the sum takes place along the longitude (φ).

3.4.4 Freshwater transport

An estimate of freshwater transport F of the AAIW layer can be calculated by subtracting the salt transport Z_C from the volume transport T :

$$F = T - \frac{Z_C}{\rho},$$

where ρ is the seawater density. The equivalence between the PSS-78 and the parts-per-mil scales (Equation (3.36)) leads to:

$$F = \frac{T}{1000} (1000 - S),$$

which yields the volume transport F of freshwater for the AAIW layer (i.e. about 97% of the mass transport is comprised of freshwater). To refer this absolute transport to the freshwater budget of the South Atlantic, the corresponding vertical mean freshwater content of the basin is subtracted:

$$F = \frac{T}{1000} (S_{Levitus} - S)$$

Finally, adding longitudinally the values in each cell yields the meridional contribution of AAIW to the budget of freshwater in the South Atlantic:

$$F_R(\lambda) = \frac{T}{1000} \sum_{\varphi} (S_{Levitus} - S)$$

The propagated error of the freshwater transport F is inferred from Equation (3.37) (see also footnote to Equation (3.32)):

$$F' = F \sqrt{\left(\frac{v'}{v}\right)^2 + \left(\frac{\xi'}{\xi}\right)^2 + \left(\frac{S'}{S}\right)^2}.$$

3.4.5 Input data

Vertical mean values of potential temperature (in °K; Talley, 2000) and salinity of the AAIW layer as projected onto the neutral density surfaces for the core, upper and lower boundaries ($\gamma^n = 27.40$, $\gamma^n = 27.25$ and $\gamma^n = 27.55$, respectively) were used for all transport estimates. The objectively mapped velocities were considered to be constant throughout the water column inside the AAIW layer. The thickness ξ of the AAIW layer was calculated in decibars (~meters) by subtracting the depth of the deep boundary from the shallow one as given by the neutral density surfaces. The velocity error v' was the mapped error associated with the velocities.

The density ρ was taken as the density of pure water (1000 kg m^{-3}).¹ C_p was taken from Millero et al., 1973, (their Tables 3 or 7) as $3,984.2 \text{ J kg}^{-1} \text{ °K}^{-1}$, which is the specific heat of seawater with a salinity of 35‰ ² and a temperature of 5°C . The atlas data for salinity and potential temperature was taken from Levitus (1994). The error in the thickness of the AAIW layer ξ' was the error of the density surfaces as reported by Jacket and McDougall (1997), i.e., 10 dbars.

The errors associated with potential temperature θ' and S' (including Levitus data) are considerable smaller than the errors associated with the layer thickness or the velocities (see Equations (3.32), (3.35) and (3.37)), and hence negligible in the error propagation. This is corroborated by the following reasoning: In the AAIW layer as defined by isoneutral surfaces, the total temperature range is less than 2 °K and the total salinity range is less than 0.22 . These variations occur within approximately 500 meters (mean thickness of the layer). This implies variations of $\theta=0.04 \text{ °C}$ and $S=0.004$, assuming a linear response and vertical variation of 10 dbars.

¹ To use the density of seawater (up to 1070 kg m^{-3} after Pickard and Emery, 1990) yields in no visibly difference in the transport estimates.

² By the time Millero et al., 1973, published their study salinity was measured in parts per thousand (parts per mil, ‰). The UNESCO Practical Salinity Scale (PSS-78) was defined in 1978.

Chapter 4 Results.

In this chapter, the circulation pattern and transports of AAIW in the South Atlantic are exposed by the space-time averages and objective maps, focusing on the most significant results from the data set constrained by neutral density surfaces. These results will be discussed in the following chapter.

4.1 Space-time averages and error ellipses

Figure 4.1 shows the results of the space-time averages according to the optimal grid based on $X = f/h$. The map projection used in these and upcoming results is an *Equidistant Cylindrical Projection*, which preserves vectors lengths regardless of their position and their azimuth. Isobaths of 1000 and 3000 meters are displayed. Blue arrows represent westward, red arrows eastward flow. The strongest flow at intermediate depth is the Agulhas current (ca. 20 cm s^{-1}), followed by the easternmost limb of the South Atlantic Current (SAC), the iBC and the tropical region with ca. 10 cm s^{-1} (though no pattern is discernible in this region). The Subtropical Gyre stands out clearly, showing weak currents in the center and increasing speeds towards the perimeter.

Depicted at the tip of the average velocities from Figure 4.1 are 0.63 probability error ellipses. Comparison with Figure 3.5 shows that ellipses of significantly different sizes are associated with regions of approximately the same number of float-days (and hence, with similar sampling errors). These observed differences must therefore be attributed to mesoscale variability. The Confluence Zone, the Agulhas System and the tropical band north of the equator are regions covered by similar number of float-days (light blue in Figure 3.5), as is the SAC region. However, as visible in Figure 4.1, the latter region's error ellipses are significantly smaller in comparison with those of the regions mentioned first. Hence, it is concluded that the Confluence Zone, the Agulhas System and the tropical band north of the equator are regions of high spatial and/or temporal variability in comparison with the SAC. Similarly, small (with respect to the mean velocities) error ellipses in the nBSG indicate reliable mean flow estimates there, since in this region data density is high whereas flow variability low.

The slow flow region between 15°S and 30°S can be divided in a zone west of the MAR, which is the region of highest data density (green, orange and red in Figure 3.5) and a zone east of the MAR, with considerably less data. This difference in data is reflected in the ellipses from the Northern Branch of the Subtropical Gyre (nBSG), which east of the MAR are larger than west of it. Hence, this difference in size is attributed to error measurement or deficient binning in the space-time average rather than differences of variability (though this might contribute as well).

4.2 Objective maps and the flow pattern

While the intensity of the currents is best appreciated in the space-time averages (Figure 4.1), the currents pattern is better appreciable in the objective maps due to their superior spatial resolution. Figure 4.2 shows the result of the vectorial OMPFV (objective mapping with primal float velocities), which will be discussed below. However, due to the tendency of OM to underestimate values, mean velocity components and root-mean-square (rms) speeds for designated currents given hereinafter were calculated with all float primal velocities in the corresponding geographical region (Núñez-Riboni et al, 2005):

$$\bar{s} = \frac{1}{n} \sum_{i=1}^n \sqrt{u_i^2 + v_i^2}, \quad (4.1)$$

$$\bar{u} = \frac{1}{n} \sum_{i=1}^n u_i \quad \text{and} \quad \bar{v} = \frac{1}{n} \sum_{i=1}^n v_i$$

where u_i and v_i are the components of the i^{th} primal velocity vector and n is the number of vectors in each current. The associated errors were calculated according to:

$$\bar{u}' = \sqrt{\frac{1}{n} \sum_{i=1}^n (u_i - \bar{u})^2}, \quad (4.2)$$

with similar equations for v and s . The regions were subjectively chosen, based on the objective map (Figure 4.2).

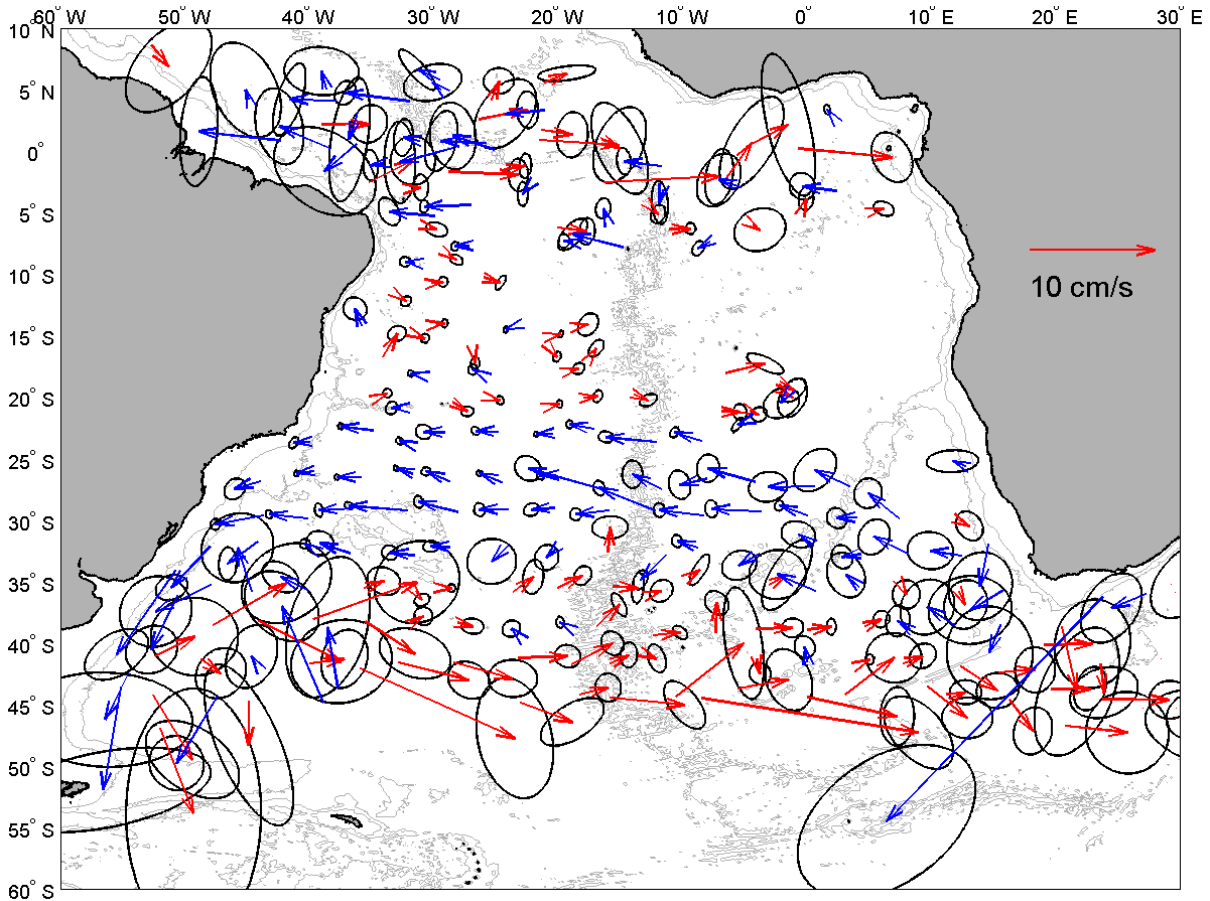


Figure 4.1 Space-time averages and error ellipses of the 0.63 probability interval for the isoneutral data set as calculated for the “optimal grid” based on $X = f/h$ ($\Delta\text{lat} = 3$, $\Delta\text{lon} = 4$, $\mu = 6000$). Red arrows represent eastward, blue arrows westward flow. Arrows are set at centers of gravity of all primal velocities binned within an averaging bin.

As shown in Figure 4.2, the Subtropical Gyre spans a zonal band from 23°S to 45°S. It is centered at about 36°S (see also Subsection 4.3.1). The SAC is centered around 40°S,

meanders between 35°S to 45°S at mean speeds of $12.4 \pm 8.4 \text{ cm s}^{-1}$. The nBSG is located between 22°S and 32°S and flows almost exactly westward with a mean speed of $4.7 \pm 3.3 \text{ cm s}^{-1}$. Between 26° and 44°S the intermediate expression of the Brazil Current (iBC, from now on; Boebel et al., 1999b) emerges at the Santos Bifurcation with a mean speed of $11.6 \pm 7.4 \text{ cm s}^{-1}$, flowing parallel to the South American coast in a southwestward direction. The Agulhas Current at intermediate depth (approximately 900 m, near 38°S and 20°E, Figure 2.5) flows at a speed of $25.3 \pm 14.2 \text{ cm s}^{-1}$, while the intermediate depth flow of the Agulhas Return Current averages to $22.9 \pm 13.2 \text{ cm s}^{-1}$.

The central part of the Subtropical Gyre is unstructured and coincides with the AAIW layer's region of greatest depth (for the isoneutral core layer $\gamma^n = 27.40$, a depth greater than 900 m is reached; see Figure 2.5). The central part of the Subtropical Gyre exhibits local recirculation cells, which might provide direct conduits for a recirculation of the Subtropical Gyre. Part of the isolines describing these recirculation cells are approximately aligned with the mid-Atlantic and Walvis Ridges, which might indicate topographic steering. Immediately north of the Subtropical Gyre an eastward current is located along 20°S, originating at the South American coast and reaching as far as 0°W, with a speed of $4.1 \pm 2.4 \text{ cm s}^{-1}$. In the tropical region, the currents are quasi zonal with speeds of $3.5 \pm 2.2 \text{ cm s}^{-1}$. These currents will be discussed in detail in the Subsections 4.3.1 and 5.2.2.

The Santos Bifurcation is located near 27°S. The northward iWBC is noticeable (see also enlargement, Figure 4.3), featuring a mean speed of $4.7 \pm 2.0 \text{ cm s}^{-1}$ (in the region between 3° and 25°S). A southwards flowing current (probably a southward deflection of the cSEC, see Subsection 4.3.1) between 6° and 12°S is visible as well. The region immediately east of the iWBC, between 12°S and 20°S, is predominantly turbulent.

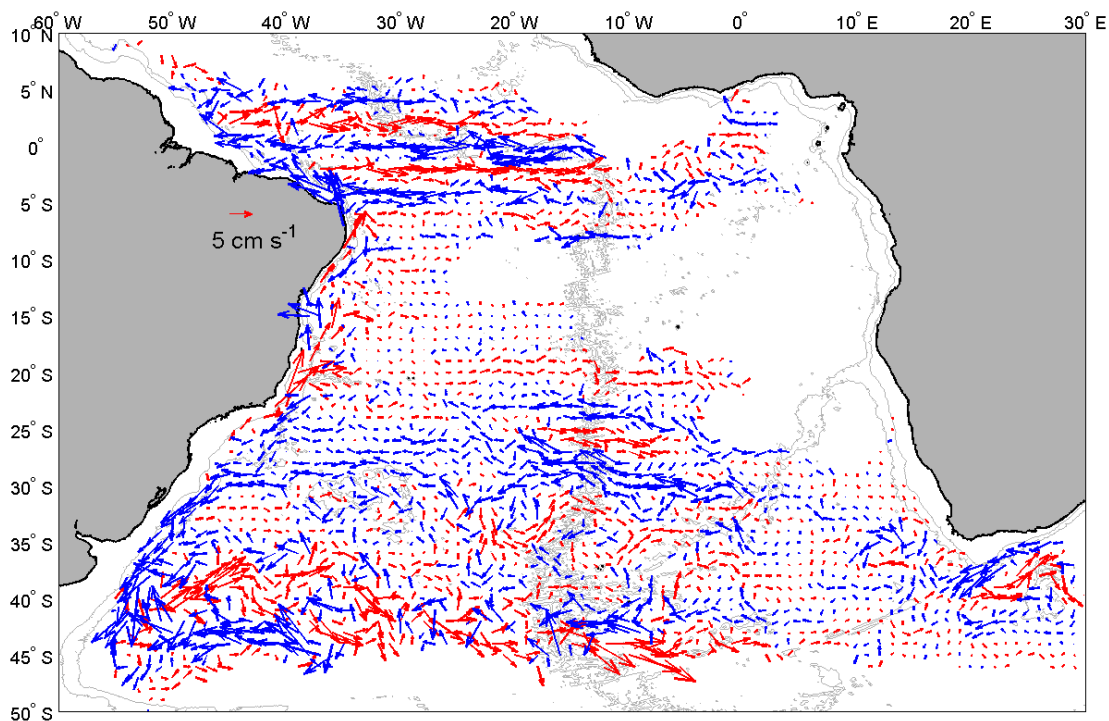


Figure 4.2 Objective map using OMPFV with primal data from the neutral density data set, distributed in overlapping subsets of 3500 data points. Blue arrows represent westward, red arrows eastward flow. A reference arrow of 5 cm s^{-1} is shown.

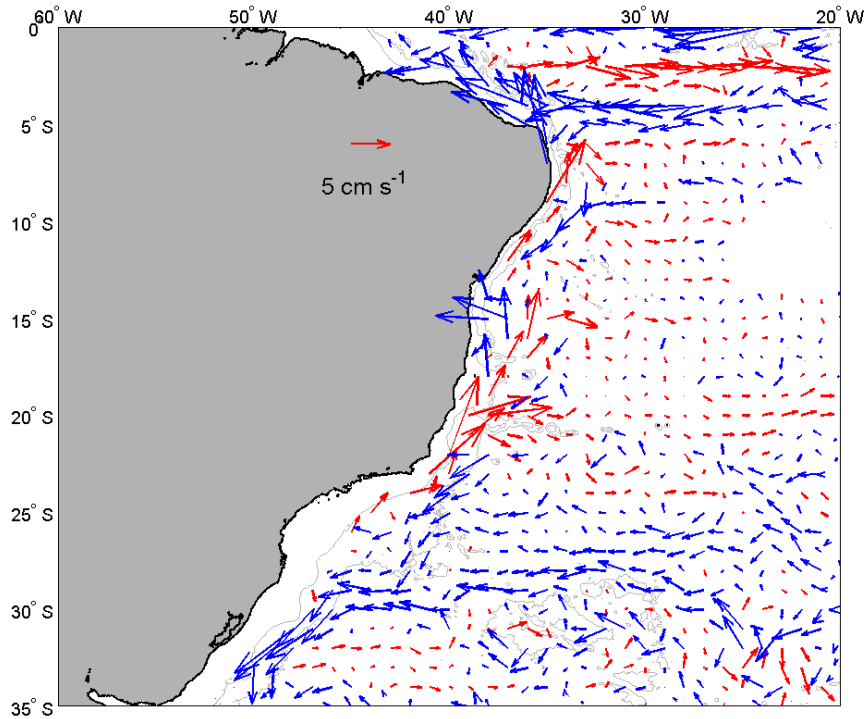


Figure 4.3 Santos Bifurcation (enlargement from Figure 4.2). Blue arrows represent westward, red arrows eastward flow. A reference arrow of 5 cm s^{-1} is shown.

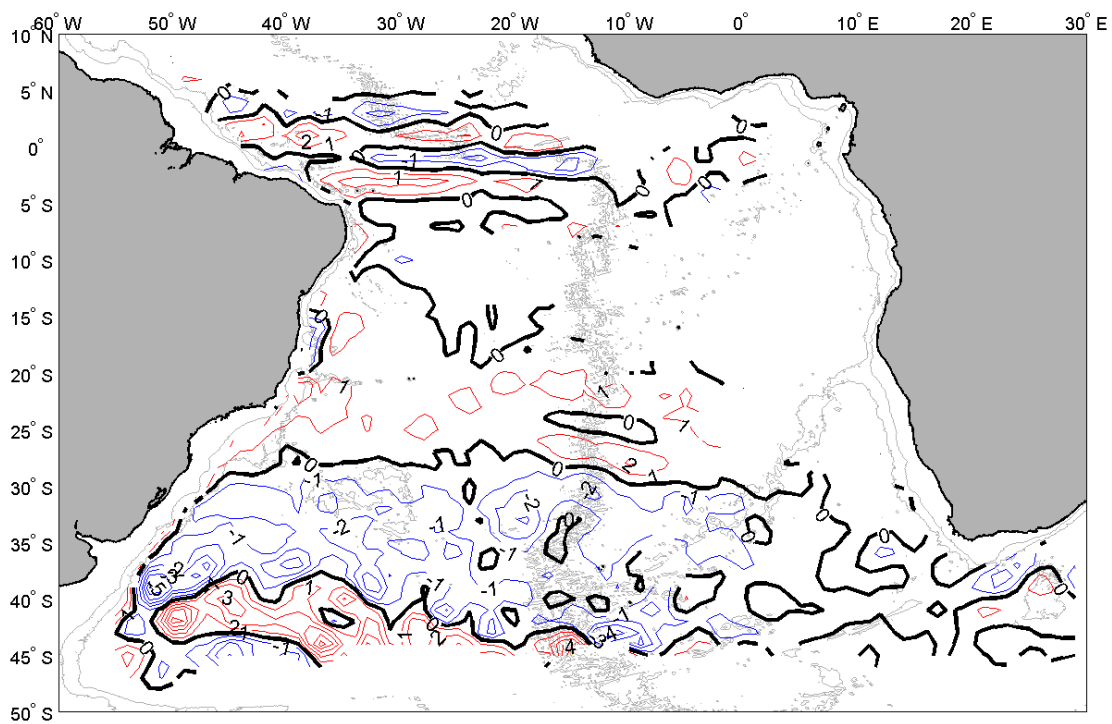


Figure 4.4 Barotropic stream function based on OMPFV. Labels indicate layer transport in [Sv]. The thick black line is the streamline of value zero. The corresponding velocity map is shown in Figure 4.2.

While the intensification of the Subtropical Gyre along the western boundary is quite prominent, the northward flow appears to spread out over several branches inside the gyre. These differences become most pronounced in the stream function (Figure 4.4). Negative contourlines of the stream function (representative of the anticyclonic flow embracing the Subtropical Gyre) are represented in blue and positive contourlines in red. Streamlines are squeezed in the iBC region, along with a local recirculation cell. In the Cape Basin, by contrast, the stream function features a broad col between 0° and 15°E. The stream function's zero isoline connects the Agulhas Current to the nascent Benguela Current (near the 1000 m bathymetric line immediately south of Africa), providing a direct flow path for water from the Indian Ocean into the nBSG. These results suggest that AAIW is injected into the subtropical gyre at both the Agulhas Retroflexion and the Confluence Zone. Similarly, a stream line of 0 Sv suggest that part of the SAC flows farther into the Indian Ocean.

A possible Tropical Gyre is vaguely suggested by quasi-closed streamlines farther north (reaching diagonally across the Atlantic from 15°S to 27°S).

4.3 Volume transports

From all possible transport estimates arising from averaging or integrating zonal or meridional estimates per cell, mean zonal and integrated meridional transports have been chosen because they are related to characteristic oceanic processes and are well reported in the literature.

4.3.1 Mean zonal transport

Figure 4.5 shows the estimate of the mean zonal transport (per degree latitude) for the Subtropical Gyre as calculated with vectorial OMSTA (see Chapter 5 for a justification of this approach). The shaded area is the mean zonal error calculated from transport data from all the graticule boxes at the same latitude (Equation (3.33)). The mean center of the Subtropical Gyre is indicated by the change of sign of the zonal transport at 35.5°S ($\pm 1^\circ$). Nevertheless, it is somewhat misleading to assign the axes of the Subtropical Gyre to a single latitude, since this axes is slightly sloped in latitude (Figure 4.2) being located at more northern latitudes in the West (near 30°S) than in the East. At around 43°S the mean zonal transport is eastwards at a maximum of 1.1 Sv per degree ($1 \text{ Sv} = 1 \times 10^6 \text{ m}^3 \text{ s}^{-1}$). This location may be defined as the core of the SAC. Near 28°S the mean zonal transport is a maximum towards the west ($\sim -1 \text{ Sv per degree}$), which corresponds to the core of the nBSG. In total the SAC carries $7.1 \pm 3.9 \text{ Sv}$ eastwards, whereas the nBSG carries $8.1 \pm 4.7 \text{ Sv}$ westwards (the error associated with the area under the curve is the shaded area divided by two). The cut-off of the SAC is caused by the outcropping of the isoneutral surfaces in conjunction with the definition of the mapping area (see Subsection 3.3.4).

Figure 4.6 shows the transport for the tropics, as calculated with OMPFV. The peak near 20°S corresponds to the eastward current immediately north of the Subtropical Gyre, which spans from 19°S to 21°S and transports $0.9 \pm 0.7 \text{ Sv}$. Between 12°S and 20°S there is a region bound by intense mesoscale activity in the west and most of the transport is meridional due to the iWBC. However, it is important to point out that the data in this region is sparse. North of 14°S, the zonal transport reveals a series of alternating currents, already discernible in the objective map (see zoomed graph, Figure 4.7): westward currents near 8°S, 4°S, the equator and at 4°N; eastward currents near 10°S, 6°S, 2°S and 2°N. The subsequent naming conventions are according to Stramma and Schott (1999), while further details will be given in Subsection 5.2.2, where these currents will be discussed. Rms speeds were calculated with Equation (4.1) (Section 4.1).

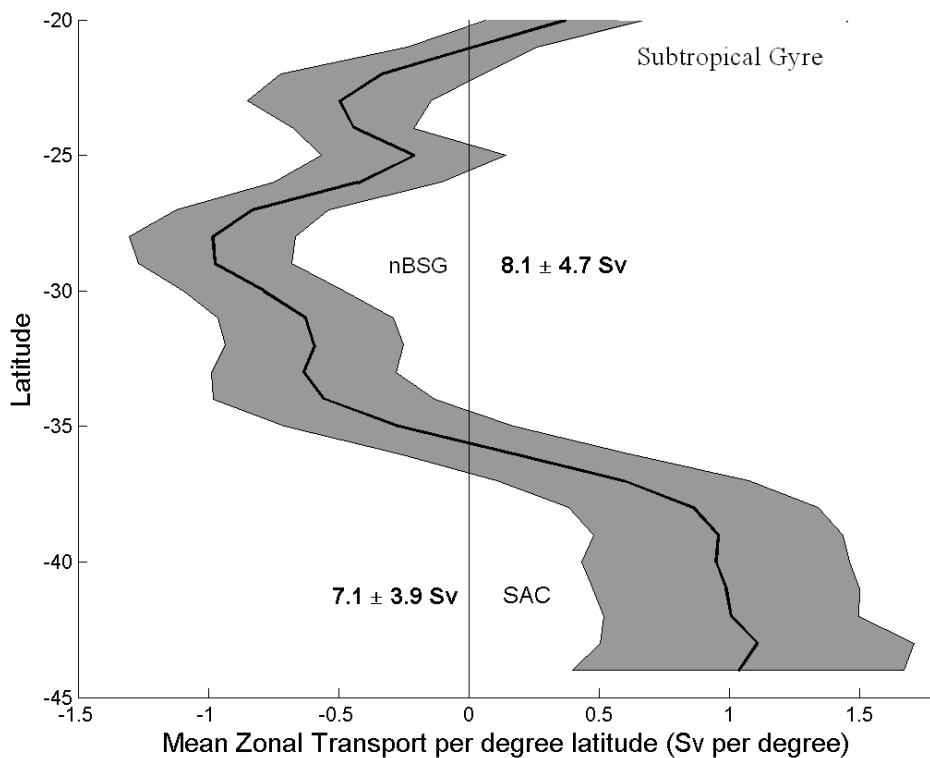


Figure 4.5 Mean zonal transport (Sv) per degree latitude of the Subtropical Gyre estimated with vectorial OMSTA. nBSG: northern branch of the Subtropical Gyre; SAC: South Atlantic Current.

The eastward current between 1°S and 3°S (1.3 ± 0.6 Sv, Figure 4.6, Table 4.1) is the Southern Intermediate Countercurrent (SICC). This current is clearly visible in Figure 4.7 as a band of red arrows of 1.6 ± 0.7 cm s⁻¹ pointing directly eastwards, out of the coast of Brazil (near 37°W) and up to the eastern limit of data at that latitude (10°W). At the equator ($\pm 0.5^\circ$), a band of blue arrows denotes the westward flowing Equatorial Intermediate Current (EIC), revealed as a peak of 1.5 ± 0.9 Sv in Figure 4.6. This current originates (at least) as far east as 15°W, and flows with a mean zonal speed of 1.0 ± 0.4 cm s⁻¹. A quite stable northward meander of this current occurs near 24°W (Figure 4.7), possibly influenced by the nearby Romanche Fracture Zone. Red arrows centered at 2°N are related to the Northern Intermediate Countercurrent (NICC), which transports 1.5 ± 1.2 Sv.

The westward current shown in Figure 4.6 and Figure 4.7 at 4°S (1.3 ± 0.6 Sv) is the equatorial branch of the South Equatorial Current (eSEC; Schott et al., 1998, with the name SEC; Stramma and Schott, 1999; Schmid et al., 2001). The westward current near 4°N (1.0 ± 1.0 Sv) could be a deep expression of the northern branch of the South Equatorial Current (nSEC; Stramma and Schott, 1999). The westward current near 8 or 9°S (0.3 ± 0.3 Sv) is the central South Equatorial Current (cSEC), which seems to deflect to the south as a current counter to the iWBC (between 6° and 12°S). A deep expression of the South Equatorial Undercurrent (SEUC) is related to the eastward current near 6°S, which carries 0.6 ± 0.5 Sv. The eastward current spanning from 10°S to 13°S in Figure 4.6 and Figure 4.7 is the South Equatorial Countercurrent (SECC; Stramma and Schott, 1999). It has a speed of approximately 2 cm s⁻¹ and carries 0.3 ± 0.3 Sv.

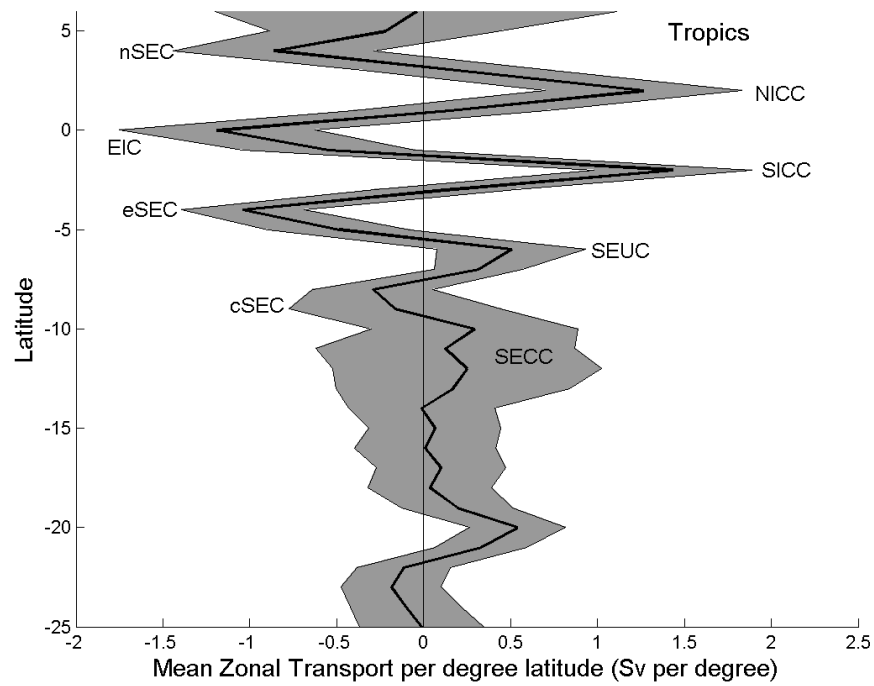


Figure 4.6 Mean zonal transport (Sv) per degree latitude of the tropics estimated with OMPFV. Positive transports point East. Known currents are labeled: Northern Intermediate Countercurrent (NICC), Equatorial Intermediate Current (EIC), Southern Intermediate Countercurrent (SICC), South Equatorial Current (SEC), equatorial SEC (eSEC), central SEC (cSEC), northern SEC (nSEC), South Equatorial Undercurrent (SEUC) and South Equatorial Countercurrent (SECC).

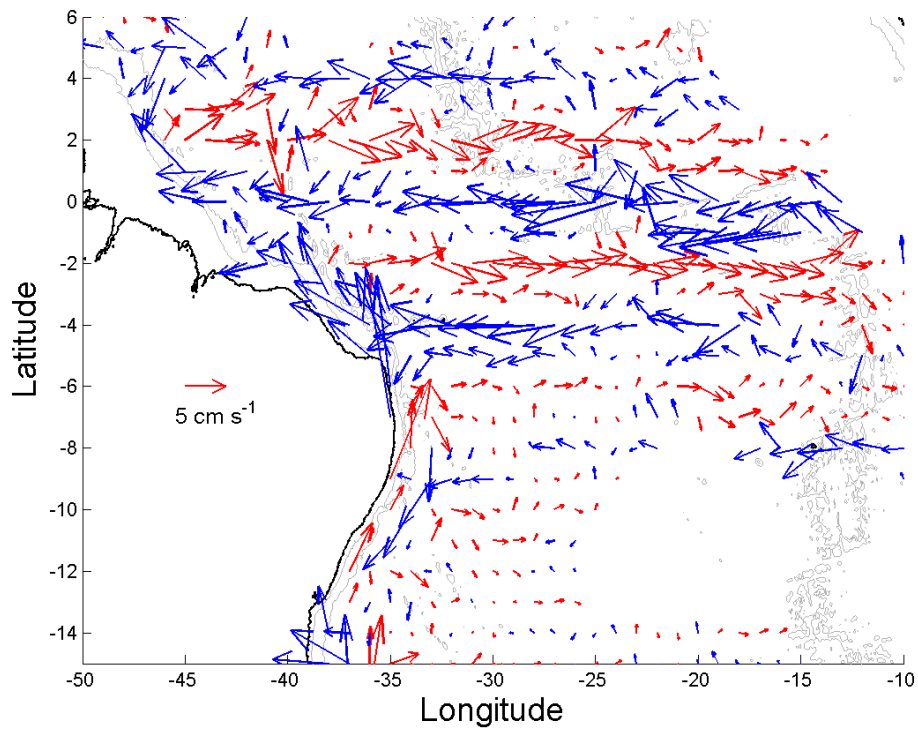


Figure 4.7 Enlargement from Figure 4.2 for the tropical region.

Table 4.1 summarizes the transport, mean velocities and rms speeds of these zonal currents. Roughly, maximum speeds are close to the equator and decrease with latitude. As a rule, zonal velocities exceed the meridional ones in one order of magnitude. Comparing the errors with the velocity values, the strong variability of the region is evident: the meridional error exceeds in one order of magnitude the meridional component of the velocity, denoting strong meandering of the currents; additionally, the zonal error is from 2 to 5 times larger than the zonal component of the velocity, which could be related to flow reversion.

Table 4.1 Mean transports, rms speeds, zonal and meridional velocities of zonal currents in the South Atlantic, at the AAIW horizon. Mean and error velocity components u and v , as well as the rms speed s of the current were computed by individual primal velocities (Equations (4.1) and (4.2)).

Latitude	Current	Transport (Sv)	u (cm s ⁻¹)	v (cm s ⁻¹)	rms speed (cm s ⁻¹)
4°N	nSEC	-1.0 ± 1.0	-4.8 ± 6.9	0.5 ± 4.1	8.3 ± 4.2
2°N	NICC	1.5 ± 1.2	5.2 ± 9.4	0.3 ± 5.6	10.6 ± 6.0
0	EIC	-1.5 ± 0.9	-3.8 ± 10.3	0.3 ± 5.6	10.5 ± 6.4
2°S	SICC	1.3 ± 0.6	4.8 ± 7.9	0.2 ± 4.7	8.8 ± 5.5
4°S	eSEC	-1.3 ± 0.6	-3.1 ± 5.1	0.2 ± 4.9	6.8 ± 3.7
6°S	SEUC	0.6 ± 0.4	1.1 ± 4.7	0.1 ± 4.6	5.7 ± 3.4
8°S	cSEC	-0.3 ± 0.3	-1.0 ± 4.1	-0.5 ± 4.0	4.6 ± 3.5
10°S	SECC	0.3 ± 0.3	1.0 ± 5.6	-0.3 ± 6.2	6.6 ± 5.3
20°S	Unnamed	0.9 ± 0.7	1.1 ± 3.4	0.1 ± 3.1	4.1 ± 2.4
28°S	NBSG	-8.1 ± 4.7	-2.1 ± 3.6	0.2 ± 3.4	4.7 ± 3.3
43°S	SAC	7.1 ± 3.9	5.0 ± 10.0	0.0 ± 10.0	12.4 ± 8.4

4.3.2 Basin wide meridional transport

The zonally integrated, meridional volume transport estimated from the OMPMV results (Figure 4.2) is shown in Figure 4.8 as a function of latitude (thick continuous line), with northwards transports positive and error estimates (shaded area). The shaded area has been calculated with Equation (3.34) (Subsection 3.4.1). The transport undulates showing several peaks and changes of sign (which will be discussed in Subsection 5.2.4). The overall tendency in the meridional transport emerges after applying a running mean over 5 transport estimates. The result (dashed line in Figure 4.8) shows a mainly southward transport south of 26.5°S (the Santos Bifurcation) and northward transport north of this latitude.

Considering the AAIW layer has been properly isolated through isoneutral surfaces (i.e., the data is not biased by entrance of water from other layers), this result implies that the nBSG splits in two branches at the Santos Bifurcation, one of them (the iWBC) flowing northwards along the coast and the other (the iBC) flowing southwards. The southward transport due to the iBC seems not to be balanced by the northward flow within the Atlantic Subtropical Gyre. After the stream function (Figure 4.4), it is expected that the northward flow coming from the Agulhas System and feeding the nBSG cancels (or overcomes) the southward transport of the iBC. However, due to the high variability prevailing in the Cape Cauldron (Boebel et al., 2003), the present study cannot account for this northward transport near the African coast. Diapycnal mixing north of the Santos Bifurcation is another (yet less probable) explanation for the unbalanced southward transport.

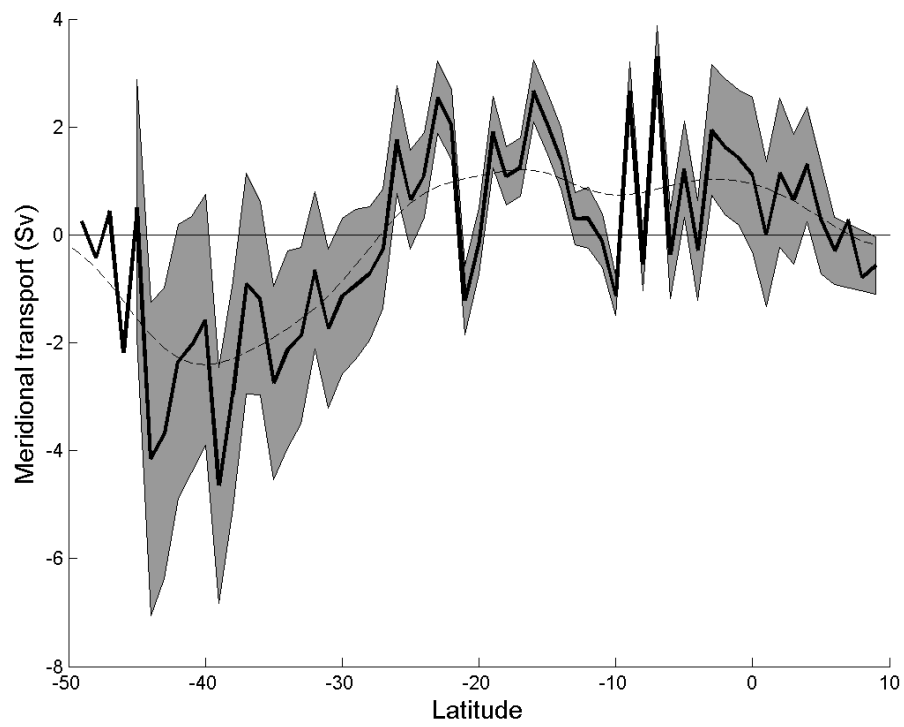


Figure 4.8 Meridional volume transport (Sv; positive north), estimated with OMPFV (thick continuous line). The shaded area is the mean error, the dashed line is given by a 5-point running mean.

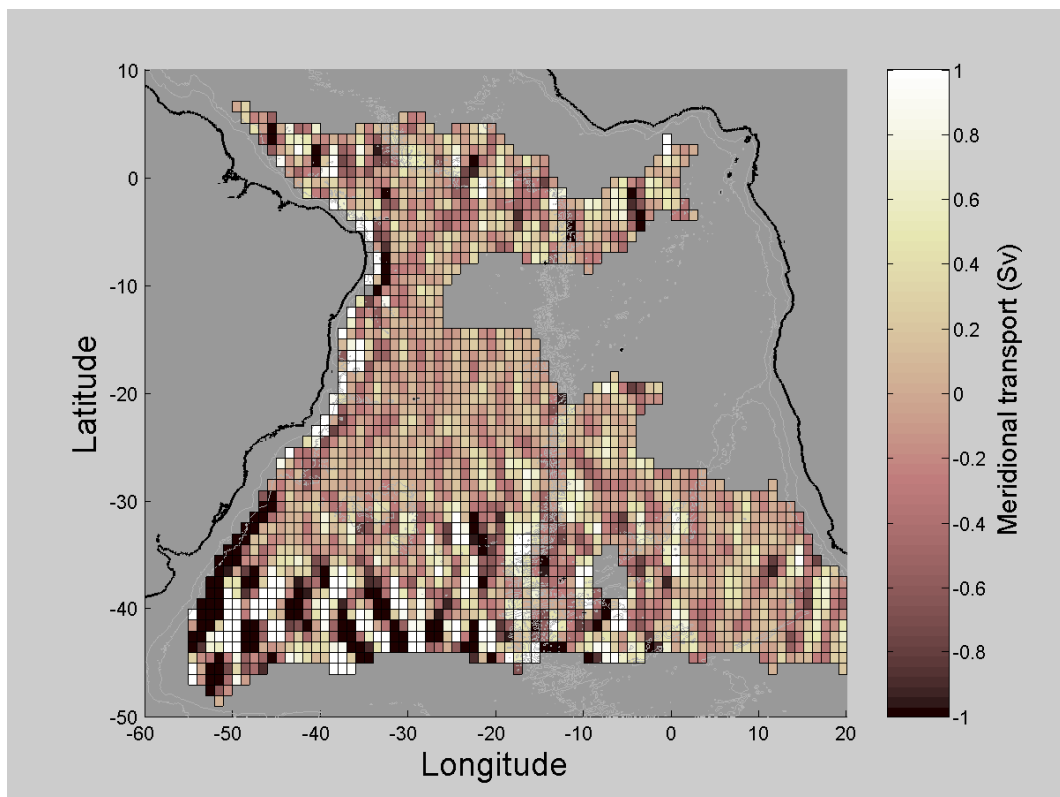


Figure 4.9 Meridional volume transport through the graticule's cells (OMPfV) in Sv. Positive north.

These notions are supported by the structure of the field of meridional transports through graticule boxes (Figure 4.9), where the two western boundary currents (iBC and iWBC) stand out clearly. The dark region along the Brazilian and Uruguayan coast indicates that the southward iBC carries most of the water to the south and the white region along the Brazilian coast indicates that the iWBC carries most of the water to the north, almost continuously up to 5°S. The two negative peaks in the meridional volume transport (Figure 4.8) between 6° and 9°S are related to the current counter to the iWBC (Section 4.2 and Subsection 4.3.1).

4.3.3 *Transport balance*

The schematic diagram of AAIW transports shown in Figure 4.10 was sketched based on Schmid et al., 2000 (their Figure 8). The transports of the nBSG and the SAC are inferred from Figure 4.5 above. Even though this study can only account for 7 Sv for AAIW transport in the SAC, it should be noted that the transport of the SAC can be larger since a part of this current is missing due to lack of float data south of 45°S at the AAIW horizon. The transport of the SAC is estimated to be ca. 2 Sv across a meridional section at 20°E, i.e. south of Africa, which implies a northward flow of ca. 5 Sv inside the Subtropical Gyre, feeding the nBSG (in the chart this transport is divided schematically into two representative flows). The 3 Sv needed to provide the 8 Sv of the nBSG must enter the subtropical South Atlantic through the Cape Cauldron. From the 8 Sv of the nBSG, 3.7 Sv flow northwards with iWBC and at 39°S the flow of the iBC is 9 Sv (the transports of the western boundary currents are discussed in Subsection 4.6 below). The surplus of 4.6 Sv for the iBC is probably related to numerous recirculation cells in the western part of the Subtropical Gyre. These cells are evident in the streamfunction, Figure 4.4.

4.4 Temperature transport

Figure 4.11 shows the relative temperature transport as calculated with the objective map of Figure 4.2, with the shaded area indicating error estimates as outlined in Subsection 3.4.2. The units are PW (Petawatts; $1\text{PW} = 1 \times 10^{15}$ Watts). To expose a tendency in the transport, a 5 point running filter was applied twice. The interpretation of these estimates is aided by Figure 4.12, which gives the meridional relative temperature transport (PW) in each graticule box (more details in Chapter 5). South of 26°S there is a northward temperature transport, which is basically due to southward transport of water cooler than the average by the iBC (white strip in front of the coasts of Brazil and Uruguay). Similarly, the iWBC carries water cooler than average northwards (black strip in front of the Brazilian coast), diminishing the South Atlantic heat budget, which is reflected as a southward temperature transport north of 26°S in Figure 4.11.

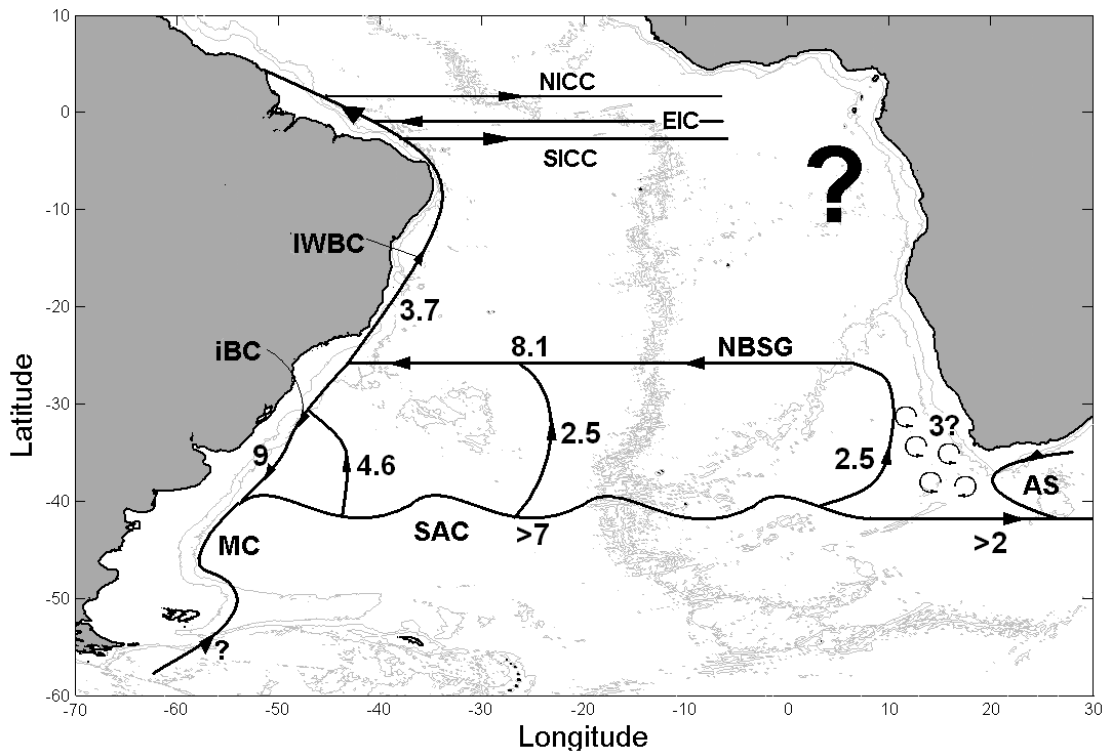


Figure 4.10 Volume transport balance at the AAIW horizon. iWBC stands for Intermediate Western Boundary Current, iBC for Intermediate Brazil Current, MC for Malvinas/Falkland Current, SAC for South Atlantic Current, nBSG for Northern Branch of the Subtropical Gyre and AS for Agulhas System.

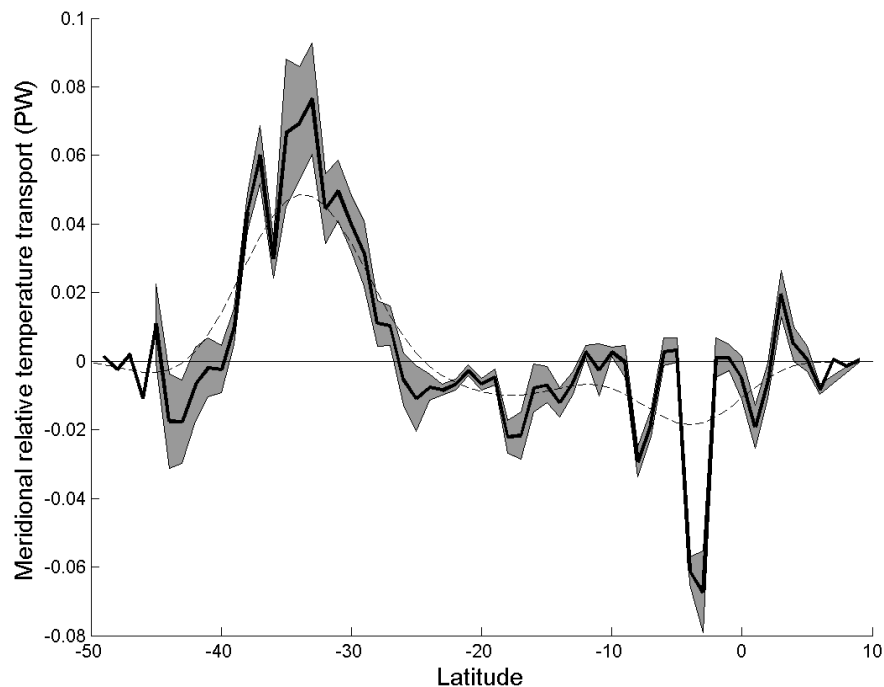


Figure 4.11 Zonally integrated net meridional contribution of AAIW to the heat budget of the South Atlantic (PW; positive values indicate northward relative temperature transport). The reference temperature is the mean annual vertical temperature from Levitus (1994) for each graticule box. The shaded area indicates the estimated error. The dashed line represents a 5-point (i.e. 5°) running mean.

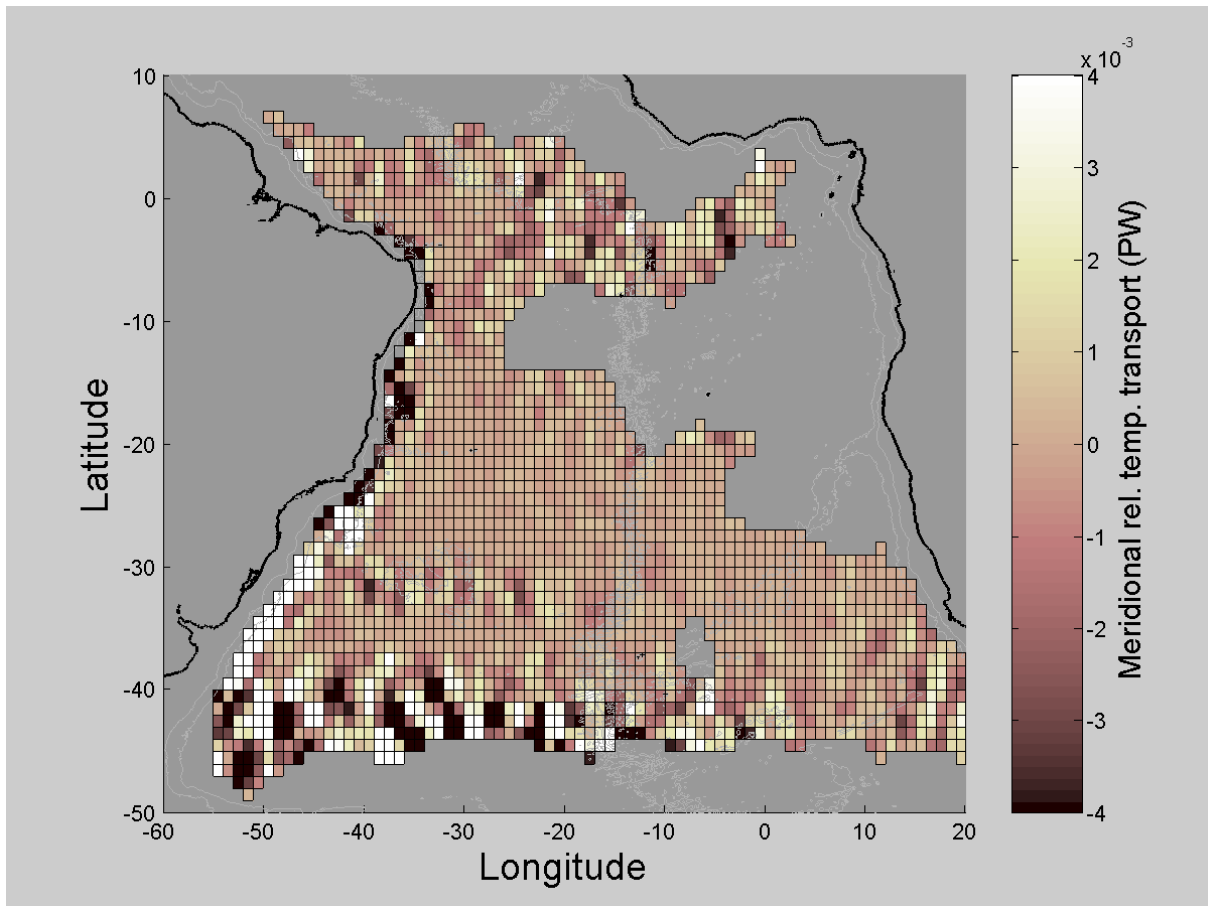


Figure 4.12 Meridional contribution to the heat budget in each OM graticule box (PW; positive values indicate northward relative temperature transports). This energy transport is referred to the mean heat content of the water column, using Levitus (1994) potential temperature cell. Figure 4.11 is a zonal average of this result.

4.5 Salinity and freshwater transports

In Figure 4.13 the net contribution of AAIW to the South Atlantic salt budget is shown as calculated with the objective map of Figure 4.2. The units are 10^9 kg s^{-1} . Once more, the tendency (dashed line) shows that the meridional distributors of water diverge from the Santos Bifurcation, i.e., they are the iWBC and the iBC. The positive (negative) salt transport south (north) of 26°S is a consequence of the iBC (iWBC) carrying water of salinity lower than the mean in comparison with the rest of the water column. As expected, due to its salinity minimum the AAIW mainly contributes to the salt budget of the South Atlantic with freshwater. This can be seen in Figure 4.14, where the net contribution of AAIW to the budget of freshwater in the South Atlantic is shown (to get the tendency this time, the running mean was applied 5 times). Note that this figure is roughly the reflection of Figure 4.13 along the x axis.

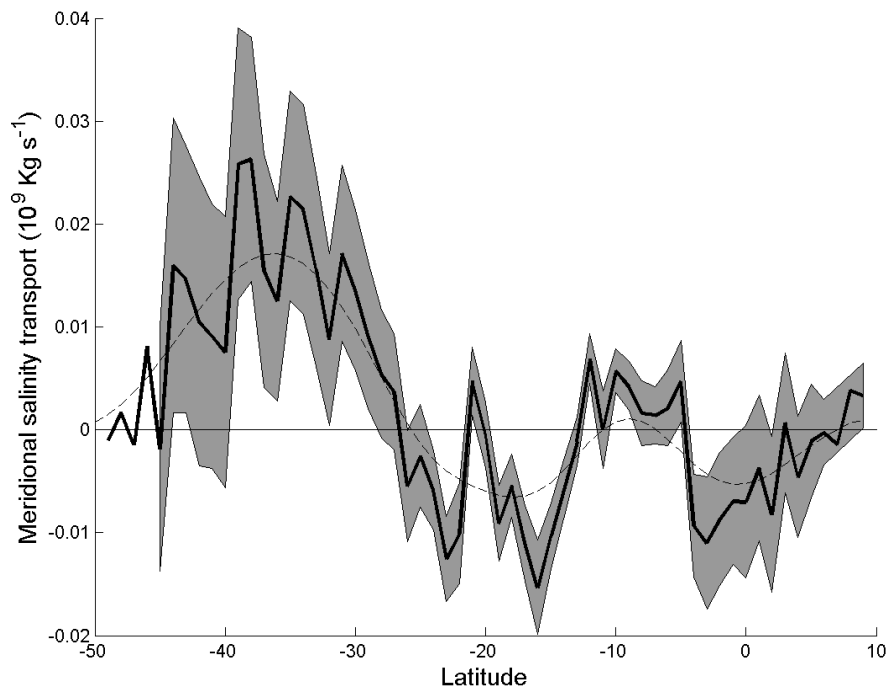


Figure 4.13 Meridional net contribution of AAIW to the salt budget in the South Atlantic (10^9 kg s^{-1} ; positive values indicate northward salinity transports). The reference salinity is the mean annual vertical salinity from Levitus (1994) for each graticule box. The shaded area indicates the error estimate. The dashed line represents a 5-point (i.e. degree) running mean.

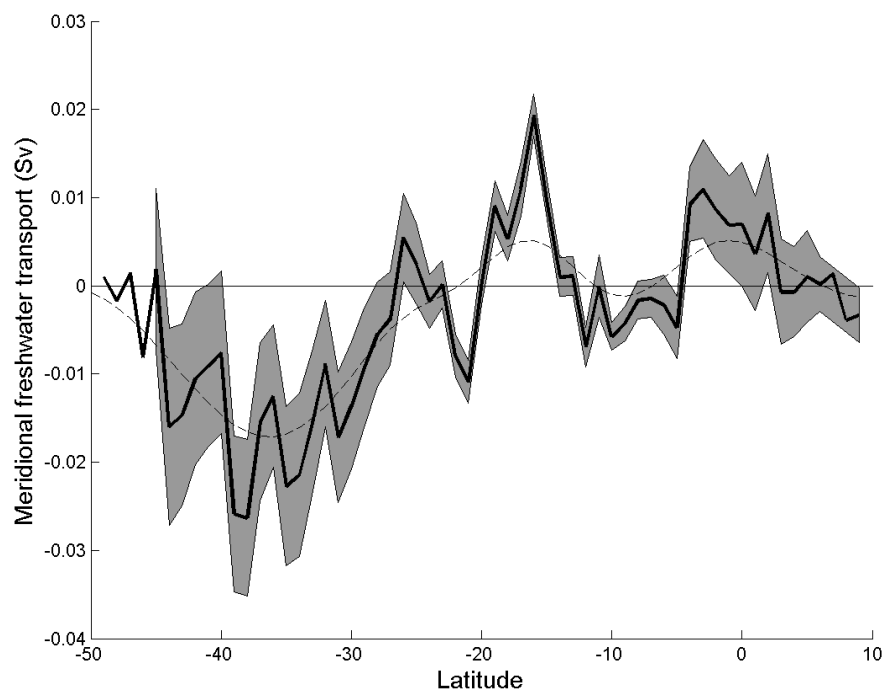


Figure 4.14 Meridional net contribution of AAIW to the budget of freshwater in the South Atlantic (Sv; positive values indicate northward freshwater transports). The reference salinity is the mean annual vertical salinity from Levitus (1994) for each latitude. The shaded area gives the error estimate. The dashed line indicates a 5-point (i.e. degree) running mean.

4.6 Western boundary currents

With the western boundary currents being the main meridional carriers of water in the AAIW horizon (Figure 4.9), they are also likely to carry most of the temperature and salt. To corroborate this notion, meridional velocity and transports of the iWBC and the iBC were estimated with the velocities of the easternmost cells of the objective map (Figure 4.2). By examining the objective map and the transport estimates when choosing different numbers of cells, 1 cell was used for the iWBC and 3 cells for the iBC. The results are shown in Figure 4.15 (upper panel: velocity and volume transport, lower panel: relative temperature and freshwater contributions to the budgets in the South Atlantic). By comparing with the total meridional transports in previous subsections, it is manifest that the major part of the transport of properties at the AAIW horizon is related to these two currents.

Table 4.2 below shows the maximum meridional velocity and transports of the currents. The iWBC carries a volume transport of 3.7 ± 0.4 Sv at 22°S. The maximum temperature and freshwater that the iWBC carries are -0.069 ± 0.069 PW (at 10°S) and 0.017 ± 0.005 Sv (at 9°S), respectively. Similarly, the maximum relative temperature and freshwater that the iBC carries are 0.074 ± 0.044 PW (at 33°S) and -0.040 ± 0.010 Sv (at 39°S). The increase of the iBC transport towards the south is related to the recirculation cells in the western part of the Subtropical Gyre (Subsection 4.3.3).

To quantify the underestimation of velocities due to the OM, histograms of prime float velocity components and speeds are shown in Figure 4.16 for the iWBC and Figure 4.17 for the iBC (with maximum values shown also in Table 4.2). The center of the zonal velocity distribution of the iWBC is negative (ca. -2 cm s⁻¹), implying that the north-west section of this western boundary current (i.e., north of 5°S) is faster than the north-east section (south of 5°S). The large number of negative zonal float velocities is mainly related to the narrowness of the iWBC and the ensuing difficulty to isolate it from adjacent counter-currents. Despite this, as expected, the center of the meridional velocity distribution is positive (i.e., northward), as is the tendency of the distribution as a whole. There are roughly four float displacements showing a meridional velocity of 28 cm s⁻¹ (speed of 30 cm s⁻¹), which is almost three times the maximum mapped meridional-velocity.

The tendency of the iBC (Figure 4.17) is clearly south-west. At least one float showed a southward meridional displacement of 30 cm s⁻¹, which is almost twice the maximum mapped meridional-velocity.

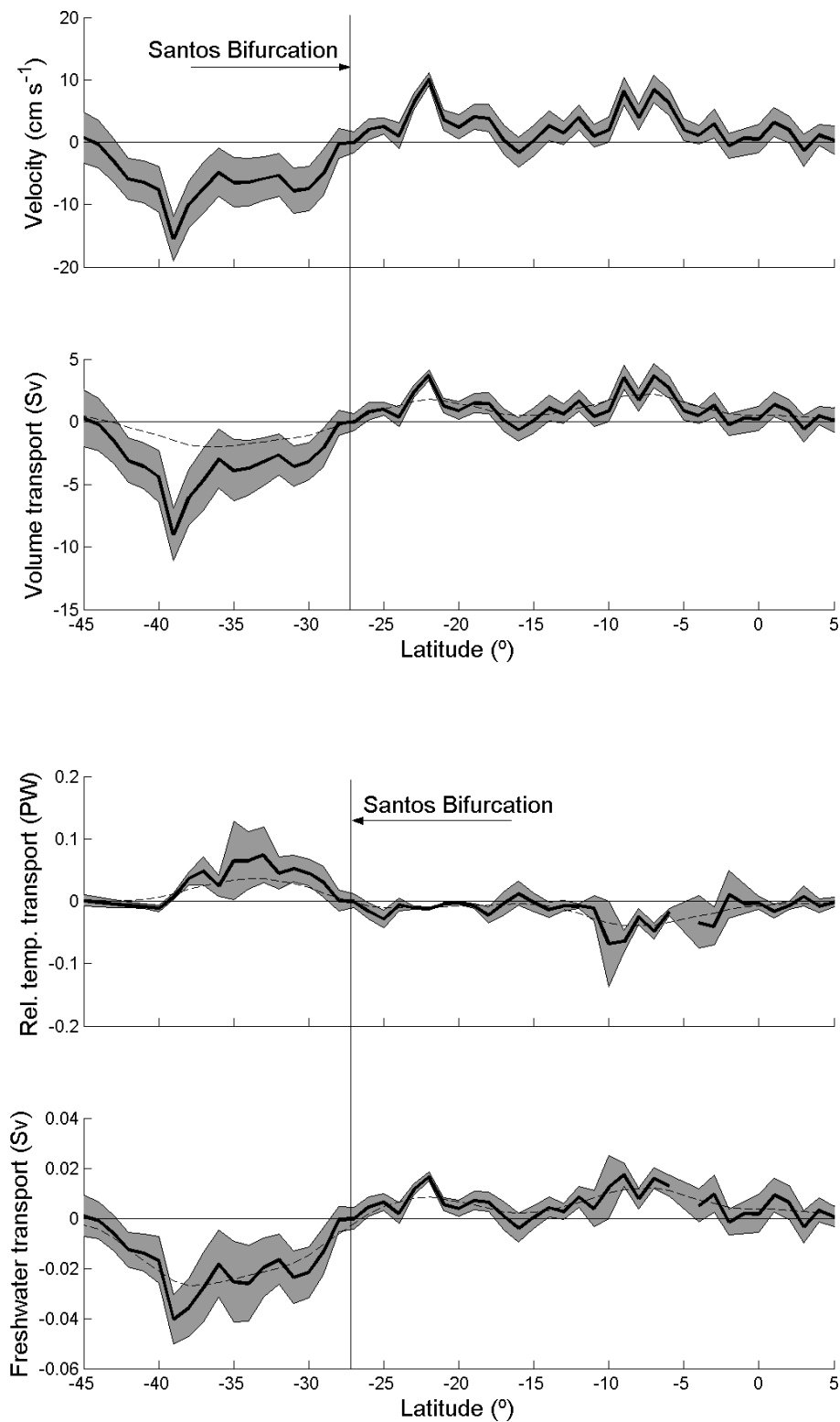
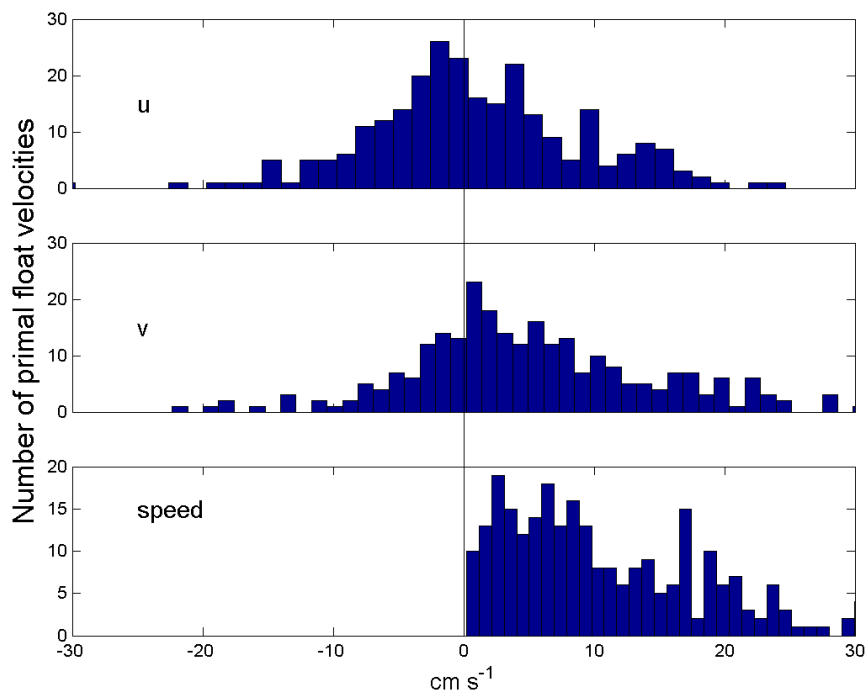


Figure 4.15 Meridional velocity and transports of the western boundary currents in the South Atlantic at the AAIW horizon as calculated by taking the first cell of the objective map from Figure 4.2. Upper panel: meridional velocity (cm s⁻¹) and volume transport (Sv). Lower panel: relative temperature (PW) and freshwater transport (Sv). The shaded areas indicate error estimates. The main tendency of the transport (dashed line) is emphasized by a 5-point running mean (dashed curve). Positive values indicate northward transports.

Table 4.2 Locations and maximum values of meridional velocities, speed and transports of the western boundary currents.

	Maximum value	Latitude
iWBC		
Meridional velocity	$10.1 \pm 1.2 \text{ cm s}^{-1}$	22°S
Primal float meridional velocity	28 cm s^{-1}	-
Primal float speed	30 cm s^{-1}	-
Volume transport	$3.7 \pm 0.4 \text{ Sv}$	22°S
Relative temperature transport	$-0.069 \pm 0.069 \text{ PW}$	10°S
Freshwater transport	$0.017 \pm 0.005 \text{ Sv}$	9°S
iBC		
Meridional velocity	$-15.4 \pm 3.6 \text{ cm s}^{-1}$	39°S
Primal float meridional velocity	30 cm s^{-1}	-
Primal float speed	30 cm s^{-1}	-
Volume transport	$-9.0 \pm 2.1 \text{ Sv}$	39°S
Relative temperature transport	$0.074 \pm 0.044 \text{ PW}$	33°S
Freshwater transport	$-0.040 \pm 0.010 \text{ Sv}$	39°S

**Figure 4.16 Histogram of zonal (upper panel) and meridional (middle panel) velocity components and speeds (lower panel) of primal float velocities in the iWBC region (as subjectively chosen by the objective map from Figure 4.2). Units are cm s^{-1} .**

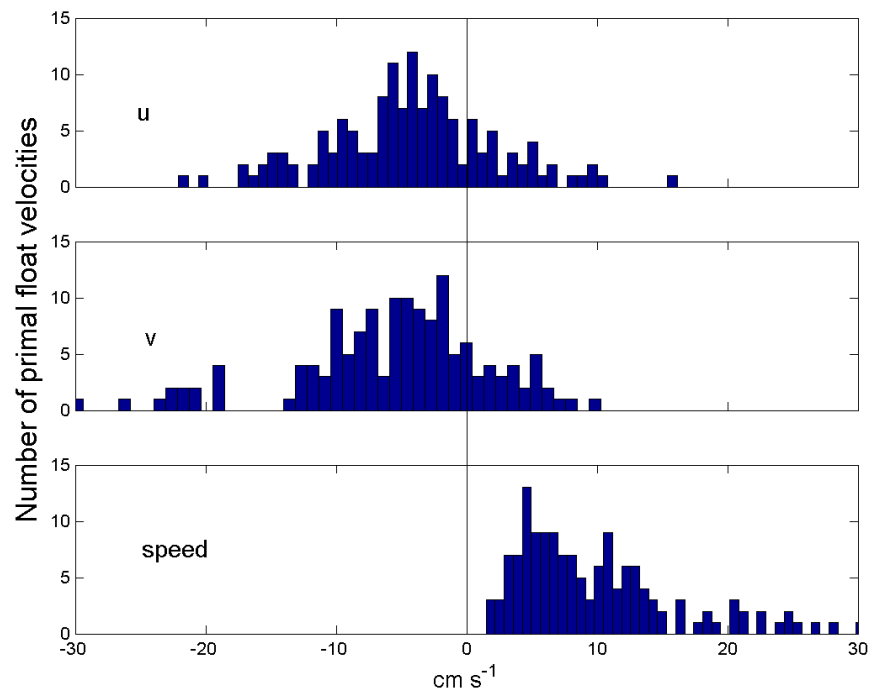


Figure 4.17 Histogram of zonal (upper panel) and meridional (middle panel) velocity components and speeds (lower panel) of primal float velocities in the iBC region (as subjectively chosen by the objective map from Figure 4.2). Units are cm s^{-1} .

Chapter 5 Discussion

5.1 Comparison of methods and data sets

The space-time averages, objective maps and transports estimates described above depend on the cut-off threshold chosen for the minimum number of data points per cell, the OM method and parameters as well as the vertical constraint of the primal float velocity data. To select the optimal solution from the ensuing large variety of maps, a comparison between various results as well as values from the literature is presented in this chapter. Particularly, to explain discrepancies with transport estimates found in the literature, which are based on different methods, data and definitions of the AAIW layer, the sensitivity of the results of this study to similar choices had to be tested. Hence, the discussion given herein provides the justification for the specific selections made in the previous chapter.

5.1.1 Isobaric versus isoneutral data set

Scrutiny of the isoneutral and isobaric space time averages (Figure 4.1 and Figure 5.1) reveals the following differences for the isobaric results:

- A wider SAC (probably including part of the ACC); parts of the Falkland/Malvinas current emerge between 40° and 45°S with a velocity of around 12 cm s⁻¹;
- The anticyclonic Zapiola Eddy is revealed (near 50°S and 45°W);
- Strong currents in a region where data is not available in the isoneutral data set (between 5° and 15°S, east of 30°W);
- Currents in the tropics seem to be stronger but have less structure and are less zonal.

These differences are reflected in a comparison of the mean zonal transports of the isoneutral with the isobaric data set (Figure 5.2). Similar results are found only between 20°S and 40°S and north of 5°S, while noteworthy differences exist in the equatorial and subequatorial region.

These differences are explicable by the contamination of the AAIW layer in the isobaric data set with flow elements of additional, adjacent water masses. A prime example is the outcropping region and southernmost extent of AAIW (see Figure 0.2 and Figure 0.4). Here, the isobaric constraint of primal float velocities permits the inclusion of currents from layers beneath the AAIW. While, south of 45°S, the AAIW resides at depth shallower than 400 m, all floats displacement vectors in this region belong to depths greater than 500 m.

A comparison of transport estimates based on the data set constrained by neutral density surfaces displaced 50 meters up and down (not shown) differ significantly from the estimates based on the isoneutral and isobaric data sets across the entire domain. It is assumed that the enhanced data set comprises significant amounts of adjacent water masses (particularly NADW, which is moving in the opposite direction), and hence is discarded altogether.

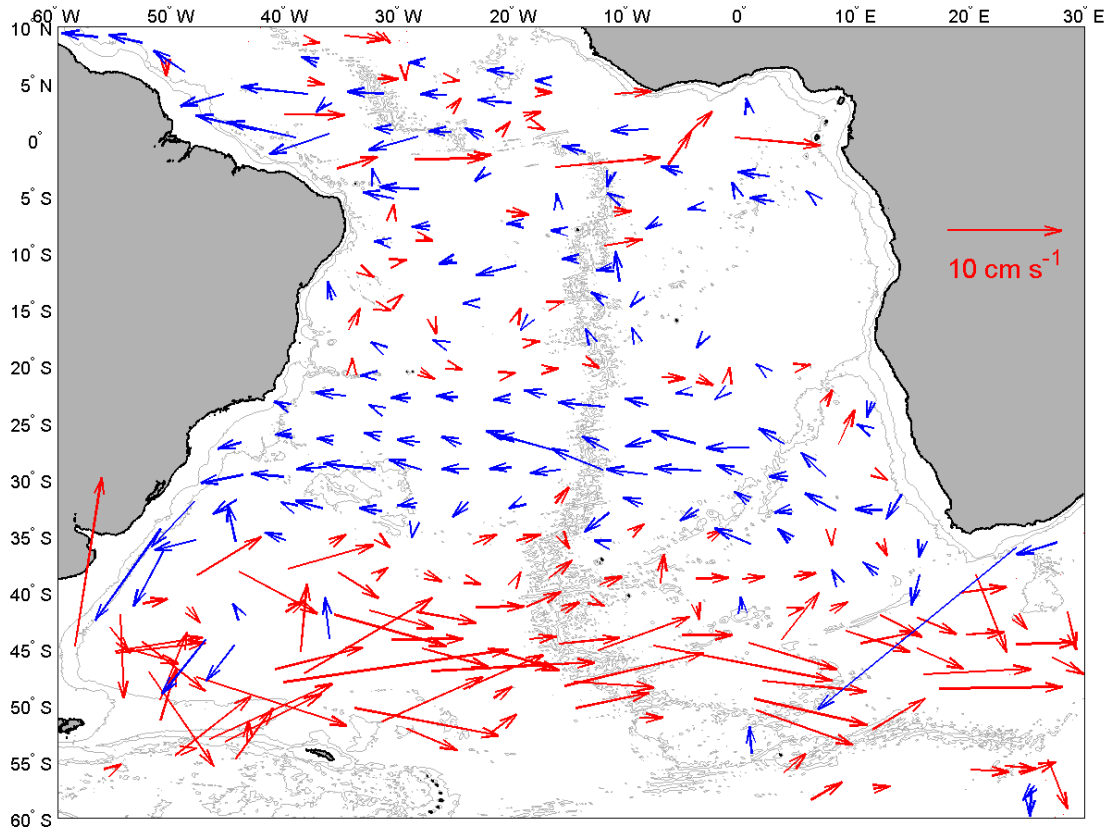


Figure 5.1 Space-time average of 850-1350m depth flow (isobaric data set). Averages were formed within the “optimum grid” ($\Delta\text{lat} = 3$, $\Delta\text{lon} = 4$, $\mu = 6000$). Red arrows point eastward and blue arrows westward.

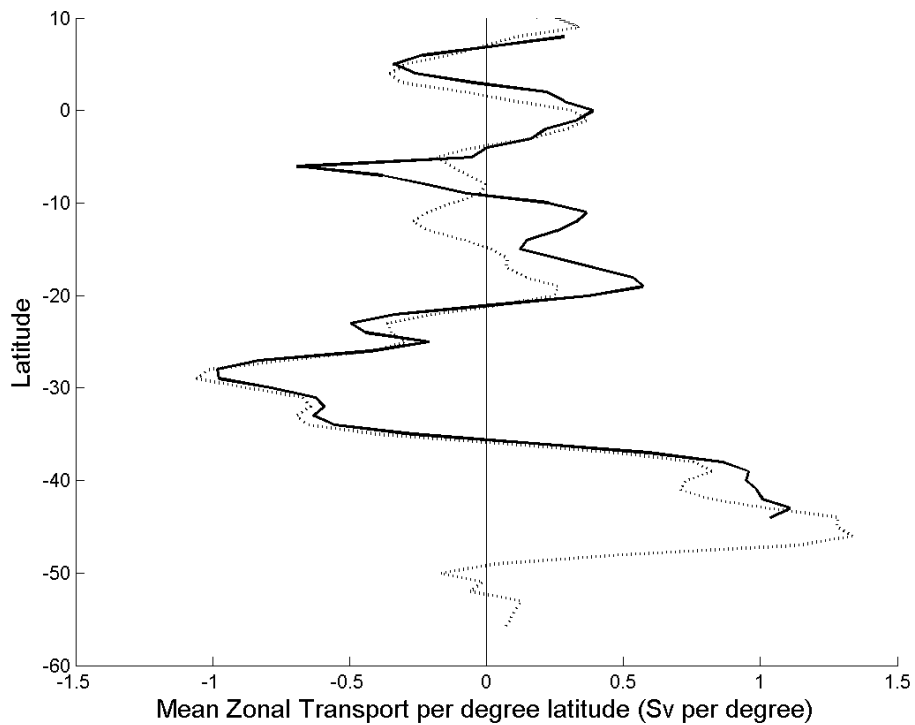


Figure 5.2 Comparison of zonal transport estimates with data sets constrained by neutral density surfaces (continuous line) and isobaric surfaces (dotted line). The corresponding objective maps were obtained by vectorial OMSTA. Units are Sv per degree latitude. Positive east.

5.1.2 Scalar versus vectorial OM approaches

The velocity fields obtained by scalar and vectorial OMSTA of the isoneutral data sets are shown in Figure 5.3 and Figure 5.4. In the equatorial and sub-equatorial regimes, scalar mapping emphasizes the zonal component of currents in comparison with vectorial mapping, which generates several meanders. The predisposition of the scalar mapping is related to its neglect of the correlation between velocity components u and v , which introduces spurious results.

Details of the Santos Bifurcation elucidate further differences between the OM approaches. Figure 5.3 and Figure 5.4 place the splitting of the nBSG at about 20°S near the South American coast. While Reid (1989) positioned the split between the northward and the southward western boundary flows at the Vitoria-Trinidad Ridge (i.e., at about 20°S) (as cited in You, 2003), more detailed studies have placed it farther south (Boebel et al., 1999a).

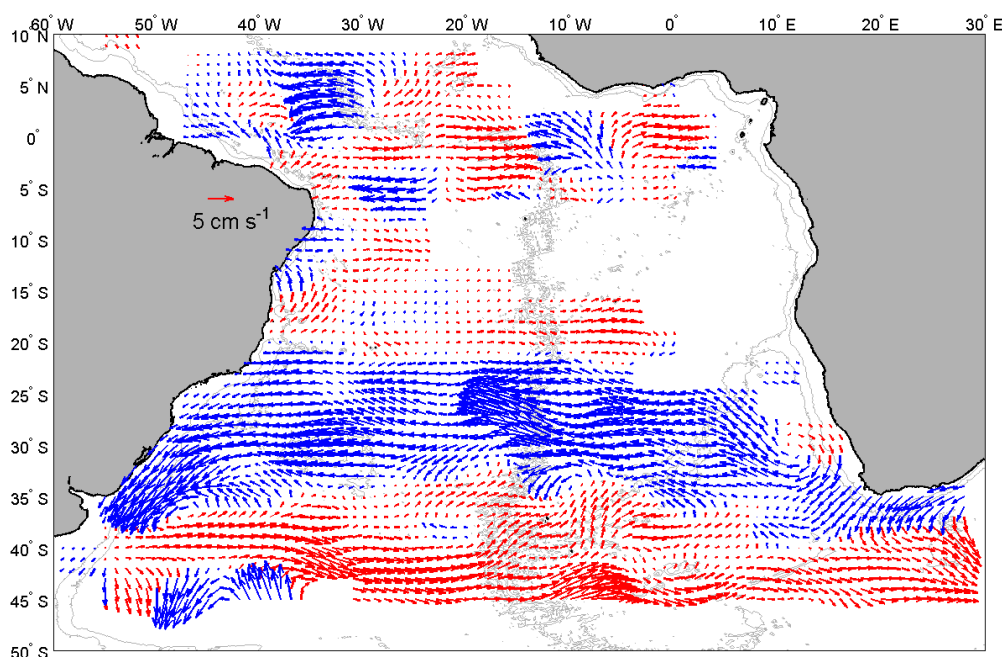


Figure 5.3 Scalar OMSTA of isoneutral data set (Figure 2.9). Arrows are shown only at graticule points positioned within a cell of the averaging grid containing data or surrounded by four cells holding data (see Figure 3.17). Red arrows point eastward, blue arrows westward.

5.1.3 OMFPV versus vectorial OMSTA

Scalar and vectorial OMSTA, which both use space-time averages as input data, yielded unsatisfactory results when compared with published meridional transport estimates (Núñez-Riboni et al., 2005, for vectorial OMSTA). This was attributed to the inability of the averaging process to properly represent the Intermediate Western Boundary Current (iWBC). In spite of considerable efforts to develop an optimal, yet systematic, grid for the space-time average, the grid's resolution remained always too coarse for such narrow structures like the iWBC. Additionally, the grid-shaping field $X = f/h$ itself does not include the iWBC (see next subsection). These deficiencies were reflected in the objective maps and transport estimates.

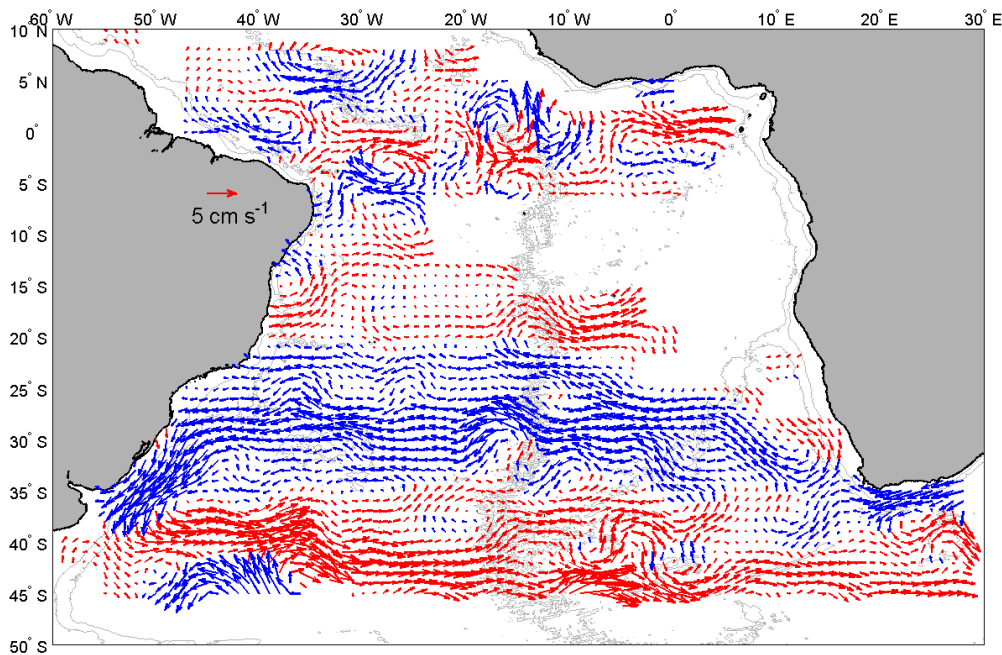


Figure 5.4 Vectorial OMSTA of isoneutral data set (Figure 2.10). Arrows are shown only at graticule points positioned within a cell of the averaging grid containing data or surrounded by four cells holding data (see Figure 3.17). Red arrows point eastward, blue arrows westward.

The need to optimize the spatial resolution prompted the use of OMPFV, where primal float data is mapped directly by OM. This method reveals the current's structure at mesoscale resolution, as exemplified by the Santos Bifurcation, the iWBC (Figure 4.3) and, particularly, the tropical jets (Figure 4.7): Whereas scalar and vectorial OMSTA suggest a disordered flow without trends in the tropical region, OMPFV reveals an ordered set of alternating, zonal jets. The resulting zonal transport estimates of these jets agree well in positions and magnitudes of previous studies (see Sections 5.2.2 below). OMPFV's ability to resolve these structures is related to this method's neglect of the long-range zonal covariance. On the downside, however, this approach yields a poorly defined Subtropical Gyre (Figure 4.2 and Figure 4.4). By contrast, the space-time averages of vectorial OMSTA smooth the fine structure by merging flow patterns within the same grid bin, deemphasizing the mesoscale and emphasizing large scale structures, i.e. the Subtropical Gyre.

This failure of OM (and the associated covariance function that best matches the input data) to simultaneously represent optimally the tropics and the subtropics confirms the two regimes underlying different dynamics (and two different Lagrangian correlation scales and times).¹ Because of this, results obtained with OMPFV and vectorial OMSTA are both relevant: the tropical region and iWBC are better described with OMPFV, whereas vectorial OMSTA yields results better suited for the description of the Subtropical Gyre. Comparison of published transport estimates with results from vectorial OMSTA support this notions for the Subtropical Gyre: the zonal transports of vectorial OMSTA is closer to previous results than transports obtained by OMPFV as indicated by calculation of root-mean-squared differences.

The comparison between the stream functions obtained with vectorial OMSTA and OMPFV is particularly interesting: As expected, the stream function produced by OMPFV

¹ As mentioned before, OM is only able to map correctly homogeneous regimes featuring isotropic statistics.

(Figure 4.4) shows the iWBC, the tropical jets and a disordered Subtropical Gyre, in contrast with the smooth stream function produced by vectorial OMSTA (Figure 5.5). On the other hand, the innermost streamlines of the Subtropical Gyre represented by vectorial OMSTA close in the western part of the Cape Basin, near the Walvis Ridge, suggesting a direct advective route for AAIW.

Similarities between vectorial OMSTA and OMPFV stream functions are evident as well: the connection between the Agulhas System and the Subtropical Gyre is also present in both (Figure 4.4 and stream line of -1 Sv immediately south of the tip of Africa in Figure 5.5), being more marked in vectorial OMSTA than in OMPFV. At 15°S to 27°S the same structure that suggested a Tropical Gyre in OMPFV is present in vectorial OMSTA (Figure 5.5), i.e. the broken isolines starting near the coast of Africa at 30°S and 10°E up to the MAR and ca. 15°S. In this case (OMSTA), the gyre seems to be divided into a western and eastern subcell. The central part of the Subtropical Gyre in Figure 5.5 exhibits local recirculation cells centered at 35°S 41°W, 35°S 29°W and 33°S 10°W.

The superiority of OMPFV in comparison with OMSTA in the resolution of the mesoscale is corroborated by the structure of the isolines of potential vorticity of the AAIW (f/h), as calculated from the isoneutral surfaces $\gamma^{\theta} = 27.25$ and $\gamma^{\theta} = 27.55$ (Figure 5.6). The main elements of the AAIW circulation are reflected in this figure: North of 22°S the isolines of f/h are almost entirely zonal (implying the jets in the tropics), farther south the Subtropical Gyre, the Confluence Zone and the iBC stand out clearly. Topographic steering due to the MAR is visible in both the SAC and the nBSG and the Subtropical Gyre remains unclosed in the South Atlantic region (no contour line connects the SAC with the nBSG). The OMPFV result (Figure 4.4) resembles the structure of the f/h field (Figure 5.6), even though the calculation of OMPFV did not *a priori* involve the vorticity field f/h . Interestingly, results obtained with scalar and vectorial OMSTA from the averaging grid shaped by f/h , lack of this resemblance with the f/h field.

The iWBC is not present in the f/h field, probably because it is too narrow to significantly influence the hydrographic field at the $1^{\circ} \times 1^{\circ}$ resolution provided. This is a major reason why the use $X = f/h$ as grid-shaping variable yields an averaging grid that does not reveal the iWBC. This shortcoming could be overcome if appropriate mesoscale resolving averaging grid were to be found. For instance, better results are obtained by binning primal float data according to a grid shaped by the abovementioned stream function (i.e. $X = \psi$, with ψ obtained through vectorial OMSTA), as shown in Figure 5.7. The existence of the iWBC in ψ is reflected in the resulting averages (vectors along the Brazilian coast; for instance: at 5°S and 36°W). This suggests the iterative use of the stream function for X , until no change is observed in two consecutive maps, a concept to be pursued in future studies.

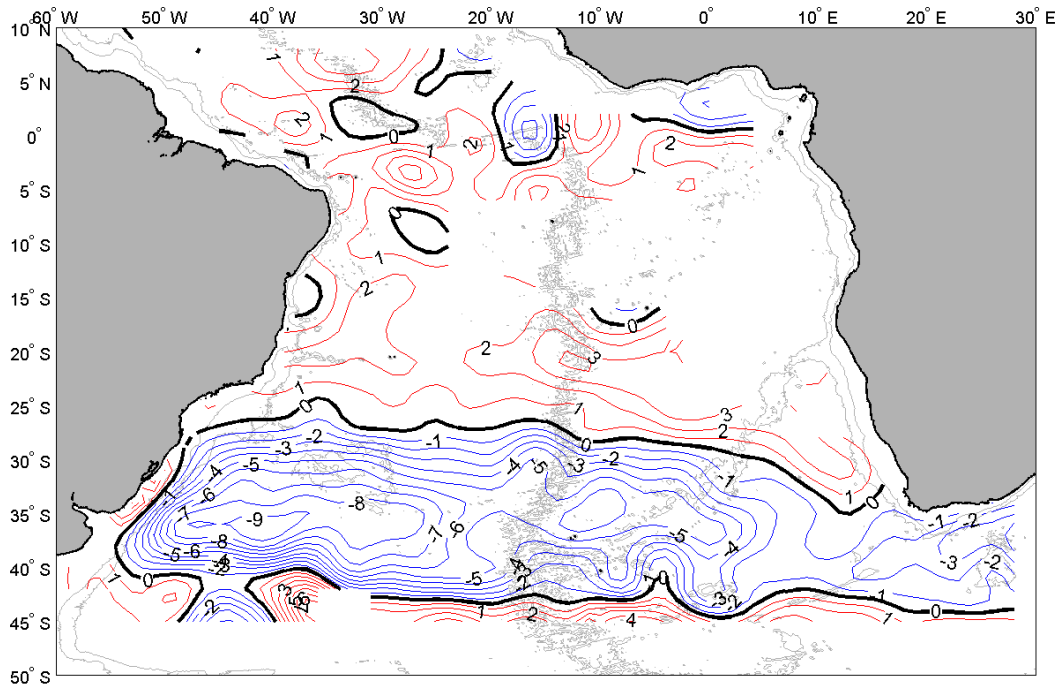


Figure 5.5 Barotropic stream function ψ [Sv] obtained by vectorial OMSTA from Figure 2.9. The thick black line indicates $\psi = 0$ Sv . The corresponding velocity map is shown in Figure 5.3.

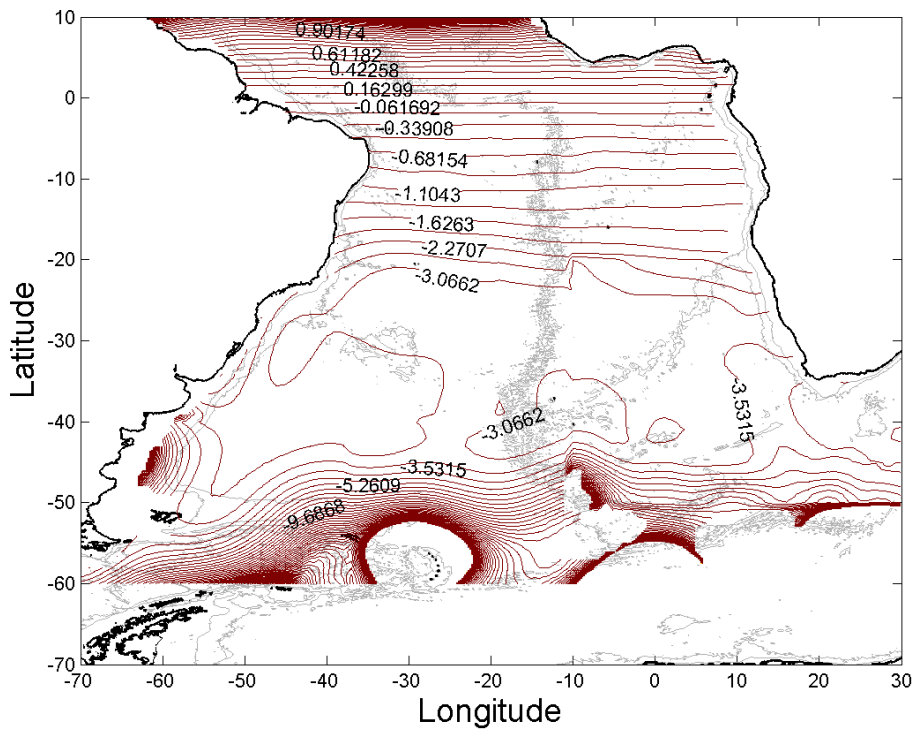


Figure 5.6 Potential vorticity (f/h) isopleths calculated for the AAIW layer from its thickness as defined by isoneutral surfaces ($\gamma^{\sigma} = 27.25$ and $\gamma^{\sigma} = 27.55$). Units are $1 \times 10^8 \text{ s}^{-1} \text{ m}^{-1}$.

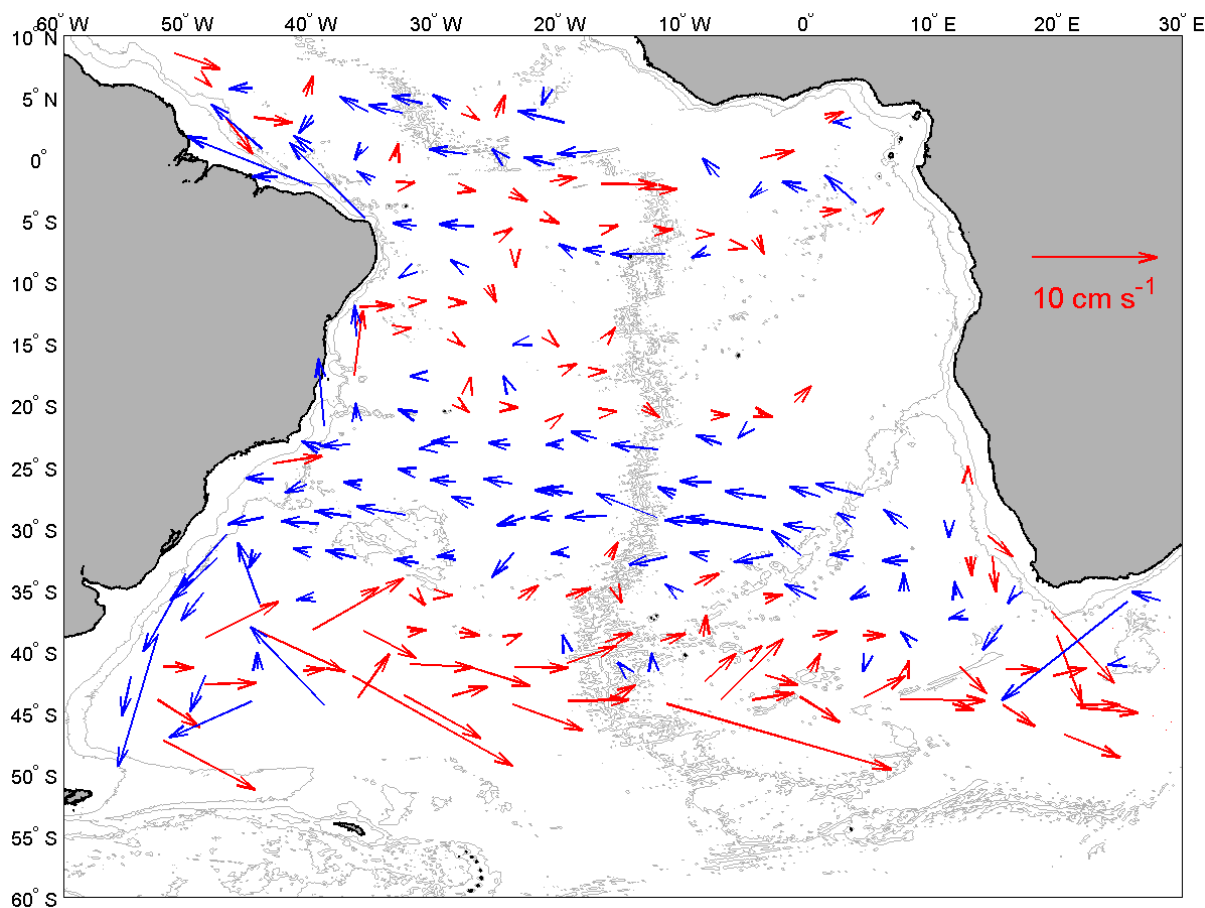


Figure 5.7 Space time average of the isoneutral data set calculated on grid as shaped by $X = \psi$ (stream function) with $\Delta\text{lat} = 3$, $\Delta\text{lon} = 4$, $\mu = 200$. Red arrows represent eastward, blue arrows westward flow.

5.2 Currents and transports

Next, the various results obtained in the last chapter will be compared with each other and with results of previous and additional studies to discuss oceanographic aspects of the AAIW circulation (currents as well as volume and property transports).

5.2.1 The subtropical region

Results of this study in the subtropical region match previous findings: The nBSG is located between 22°S and 32°S (Figure 4.2) and flows almost exactly westward, which agrees well with findings presented by Richardson and Garzoli (2003). The mean center of the Subtropical Gyre as indicated by the change of sign of the zonal transport (35.5°S; Figure 4.6) lies in good agreement with the 34°S from Reid (1989), the 35°S from Schmid (1998) and Boebel et al. (1999c). The geostrophic analysis of Defant (1941) (Figure 0.7) revealed recirculating patterns in the central part of the Subtropical Gyre similar to those exposed in the present study (Figure 4.2).

The stream function's isolines ($\psi = 0$ Sv in OMPFV and $\psi = -1$ Sv in vectorial OMSTA) connecting the Agulhas Current to the Benguela Current (Figure 4.4) suggests a direct flow from the Indian Ocean into the nBSG, which agrees with the proposition of a Subtropical Atlantic-Indian Supergyre (de Ruijter, 1982; Gordon et al., 1992) and its extent to intermediate depths (see also Subsection 5.2.3). However, the advective connection

between the Indian and the Atlantic oceans appears to be inhibited by turbulent inter-ocean exchange in the Cape Basin (i.e. the Cape Cauldron, Boebel et al., 2003), where eddy fluxes dominate both the closure of the Subtropical Gyre and cause increasing salinities of fresh Atlantic AAIW by less fresh Indian Ocean AAIW (Lutjeharms, 1996).

To account for the 8 Sv flowing in the nBSG, a transport of 3 Sv is required to flow from the Indian Ocean through the Cape Cauldron into the Atlantic (Subsection 4.3.3). This value is not unrealistic as it constitutes a reasonable fraction of the previous estimates which include the surface layer: As cited by Lutjeharms (1996, page 151), some of the “estimates of the effective inter-basin volume flux by Agulhas rings” are 5 Sv (Byrne et al., 1995), 8 Sv (Stramma and Peterson, 1990), 4-8 Sv (Boddem and Schlitzer, 1994) and 15 Sv (Gordon, 1985). Furthermore, the scheme of AAIW flowing in the South Atlantic through the Agulhas System (in addition to the Confluence Zone) agrees well with the study of dianeutral mixing of You (1999), who identifies the Agulhas Retroflexion and the Confluence Zone as the two most likely regions of entrainment of AAIW into the South Atlantic.

While the condition of zero-divergence inherent to OMPFV tends to close streamlines outside the data set, thereby forming spurious mesoscale gyres, the constraint of the mapping area through a Delaunay triangulation (Section 3.3) omits such artifacts. Hence the suggestion of the existence of a Tropical Gyre as revealed by the stream function appears reasonable. On the other hand, while the stream function from OMSTA suggested a Tropical Gyre divided into a western and eastern subcell, sparse data at these latitudes on the eastern side of the basin do not permit reliable conclusions, and the observations neither confirm nor contradict the concept of three meridionally stacked subcells as proposed by Suga and Talley (1995).

The eastward current directly north of the Subtropical Gyre along 20°S (visible as a peak in the zonal transport, Figure 4.6) corresponds to an unnamed current reported by Richardson and Garzoli (2003).

5.2.2 *Tropical region*

The currents in the tropical region revealed by the present study have been already reported in previous studies (Schott et al., 1995 and 1998; Boebel et al., 1999c; Stramma and Schott, 1999; Schmid et al., 2001 and 2003). However, some inconsistencies exist as some of these currents have been reported 1° to 2° farther north than observed here. A summary of the current state of knowledge on the flow structure is given in Figure 5.8.

The positions reported for the SICC, EIC and NICC by Stramma and Schott (1999), Schott et al. (1998) and Schmid et al. (2001 and 2003) agree well with those of this study. The fate of these three currents near the African coast remains obscure due to sparse data in that region. Schott et al. (1998) hypothesize that the SICC may feed the EIC. Recirculation of the NICC into the EIC is also considered feasible. Other studies (Schott et al., 1998; Boebel et al., 1999c; Molinari et al., 1999; Schmid et al., 2001 and 2003) suggested an annual flow reversion of the equatorial flow. For instance, a recent float study by Schmid et al., 2003, suggests that “the equatorial flow is predominantly eastward (westward) during the first (second) half of the year” (Schmid et al., 2003, page 249). This notion explains the large error associated with the zonal velocity of the EIC (Table 4.1), however, with the westward flow component being predominant (see Figure 4.6 and Figure 4.7). A prevalent westward flowing EIC agrees also with results from Boebel et al. (1999c) and Stramma and England (1999).

Similarly, the fact that the meridional error exceeds in one order of magnitude the meridional component of the velocity (Table 4.1) denotes strong meandering of the tropical jets in agreement with Schmid et al., 2003. An explanation of this strong variability in the

South Atlantic tropics could be related to planetary waves (Molinari et al., 1999; Schmid et al., 2003).

The transports of the SICC, EIC and NICC of the present study are one order of magnitude smaller than the transport estimates by Schott et al. (1998): for the SICC, Schott et al. (1998) estimated 8.5 ± 2.7 Sv, for the NICC, 11.9 ± 8.4 Sv and for the EIC, 22.1 ± 9.8 Sv. These discrepancies might be related to the definition of the AAIW layer. Schott et al. (1998) constrained the layer from $\sigma_\theta = 26.8$ (around 300 m depth) to 1000 m. Hence, their layer is approximately 300 m thicker than this study's (which is ca. 400 m thick in the tropics). In addition, Schott et al. (1998) include currents above the isoneutral AAIW layer used herein. Such currents are likely to be stronger than the AAIW flow proper (see also Subsection 5.2.4 for a discussion about the underestimation of volume transports in this study).

The westward current near 8 or 9°S related to the cSEC and its deflection to the south as a current counter to the iWBC (between 6° and 12°S) are also represented in the schematics of Stramma and Schott (1999) (Figure 5.8). The South Equatorial Countercurrent (SECC) has been reported by Reid (1964) at the surface as an eastward-flowing countercurrent in the latitudinal belt 7°-9°S. A deep expression of this current has been reported by Stramma and Schott (1999). Even though located farther south, the eastward current spanning the zonal band between 10°S and 13°S in Figure 4.6 and Figure 4.7 has been related in this study to the SECC.

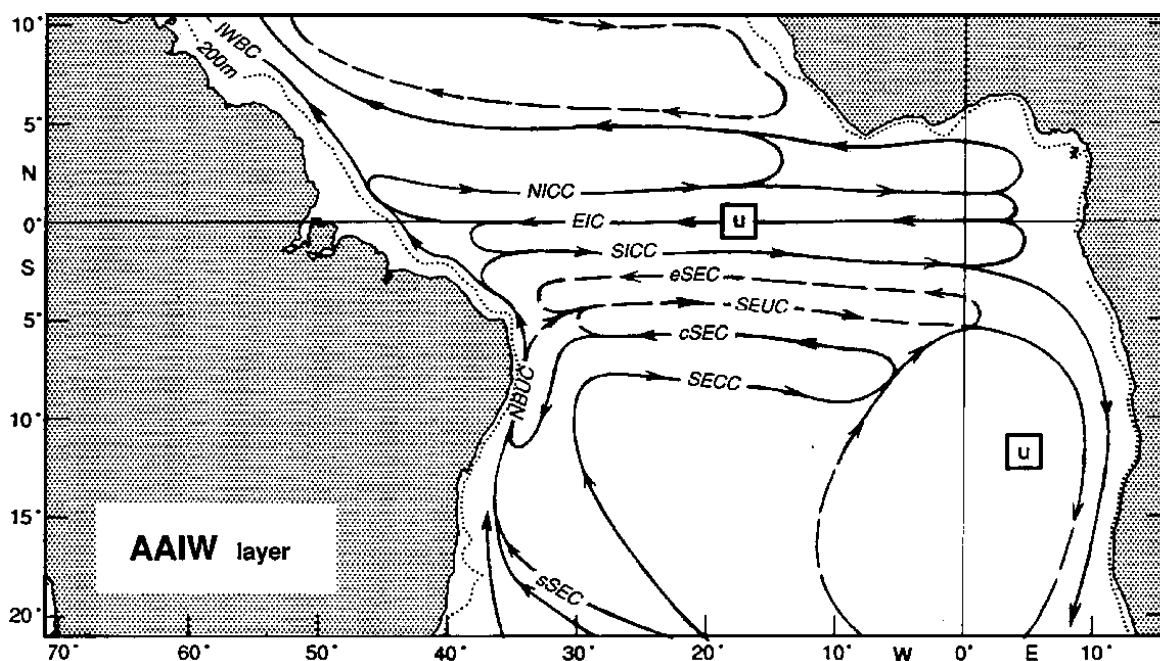


Figure 5.8 Schematic flow diagram for 500 to 1200 m depth layer. Modified from Stramma and Schott, 1999 (their Figure 6). The abbreviations are: Northern Intermediate Countercurrent (NICC), Equatorial Intermediate Current (EIC), Southern Intermediate Countercurrent (SICC), South Equatorial Current (SEC), equatorial SEC (eSEC), central SEC (cSEC), southern SEC (sSEC), South Equatorial Undercurrent (SEUC), South Equatorial Countercurrent (SECC), North Brazil Undercurrent (NBUC), and Intermediate Western Boundary Current (iWBC).

Similarly, the SEUC at intermediate depth is a deep expression of the surface SEUC and (after the schematics from Stramma and Schott, 1999) it is the first eastward current found south of the SICC. After the latitudinal position reported by Stramma and Schott (1999), the current identified in this study with the SEUC could be the SECC (Figure 4.6 and Figure 5.8). Harmonizing with that, Schmid et al. (2001) call SECC the eastward current at

6°S. This implies that the SEUC would be missing in the present study due to a coarse spatial resolution and the eastward current near 10°S could be a current not yet reported. However, it is more probable that Schmid et al. (2001) identified the eastward current immediately south of the SICC as the SECC because they did not find the eastward current at 10°S (due to sparse data in comparison to the present study).

Schott et al. (1998) suggest that the equatorial branch of the South Equatorial Current (eSEC; Stramma and Schott, 1999; Schmid et al., 2001) might reach the AAIW horizon (Schott et al., 1998 call it SEC). While located farther south, the westward current shown in Figure 4.6 and Figure 4.7 at 4°S has been identified with the eSEC in this study, for being the first westward current found south of the SICC. However, Schmidt et al. (2003) assert that their data do not support the presence of the eSEC at intermediate depths and call the westward current at 4°S cSEC. If this would be true, the westward current reported here at 8°S would be an unreported one. However, like with the SECC, it is more probable that Schmid et al. (2001) attributed the name cSEC to what is actually the eSEC because they did not find a “second” westward current south of the SICC.

Since these differences in position are larger than the uncertainty of the objective maps (0.5°) and considering that the spatial resolution used in this study (1°×1°) should be appropriate to resolve the entire structure, an explanation for these discrepancies could be related to the variability of the tropical region: the present trajectory float analysis includes data from different years and seasons, spanning approximately a full decade. Therefore, differences in the current positions with respect to results from hydrographic surveys should not be surprising. Schmid et al., 2003 discuss the differences between Schmid et al. (2001) and Schott et al. (1999) and draw a similar conclusion: “...south of the SICC, Schmidt et al. (2001) could not identify as many zonal currents as depicted by Stramma and Schott (1999). Schmid et al. (2001) also noted that the latitudes of the mean eastward and westward currents do not always match the Stramma and Schott (1999) schematic (Figure 5.8). This difference may be due to the temporal variability of the flow, which can be more readily analyzed from time series derived with floats than from several consecutive hydrographic surveys”¹ (Schmid et al., 2003, page 235). Despite the names of the currents, the position, direction and speeds of all currents reported in this study agree well with Schmid et al. (2001 and 2003).

A westward current at 4°N at the AAIW horizon has been already reported by Molinari et al. (1999) and by Schmid et al., (2001 and 2003), both using a subset of the float data set considered herein (PALACE floats from WOCE). In this study, this current has been related to a deep expression of the northern branch of the South Equatorial Current (nSEC; Stramma and Schott, 1999).

Arrows pointing rather meridionally in Figure 4.7 (for instance at 25°W and 1 and 3°N), could be evidence of permanent meridional flow in the ocean interior, in contrast with findings of Schmid et al., 2003.

5.2.3 *Western boundary currents*

The location of the Santos Bifurcation at 27°S is in good agreement with the finding of Boebel et al. (1999a). The fact that most of AAIW is continuously carried by the iWBC as far North as 5°S (Figure 4.9) agrees well with previous results, where the iWBC is thought to transport the bulk of AAIW across the equator (Defant, 1941; Gordon and Bosley, 1991; Boebel, et al., 1999c; Jochum and Malanotte-Rizzoli, 2003). The maximum volume transport of 3.7 ± 0.4 Sv for the iWBC lies in excellent agreement with the 4 Sv from Boebel et al. (1999a) and the 5 Sv from Schmid et al. (2000). However, this study’s transport

¹ With “several consecutive hydrographic surveys” they refer to the method from Schott et al., 1999.

estimate is somewhat smaller compared with the 6.4 Sv of Schott et al. (1998) (the North Brazil Current at the AAIW horizon and the equator). The turbulent region immediately east of the iWBC between 12°S and 20°S, where most of the transport is meridional due to this western boundary current, agrees well with the observation of intense mesoscale activity reported by Boebel et al. (1999c) and Schmid et al. (2003).

The meridional transports of vectorial and scalar OMSTA are presented in Figure 5.9 and Figure 5.10. Together with Figure 4.8, the negative transport south of 28°S is remarkable for being present in all three estimates. The fact that this region is well covered across the corresponding zonal band (see Figure 3.5) suggests that this estimate is robust. The results (objective map, Figure 4.2, for instance) indicate that the southward transport is caused by the iBC (see Section 4.3). This is explained by AAIW entering the South Atlantic from the Indian Ocean (in addition to the primary entrainment point at the Confluence Zone), feeding the nBSG and eventually the iBC. Considering mass conservation, the iBCs southward transport would be balanced only north of the tip of Africa (35°). However, this northward transport (which takes place in the Cape Cauldron) is primarily turbulent and related to mesoscale processes, which apparently cannot be accounted for in the present analysis. South of the tip of Africa, the iBCs southward transport is unbalanced by the northward flows inside the Subtropical Gyre, implying that AAIW flows farther with the SAC into the Indian Ocean, where the circuit closes.

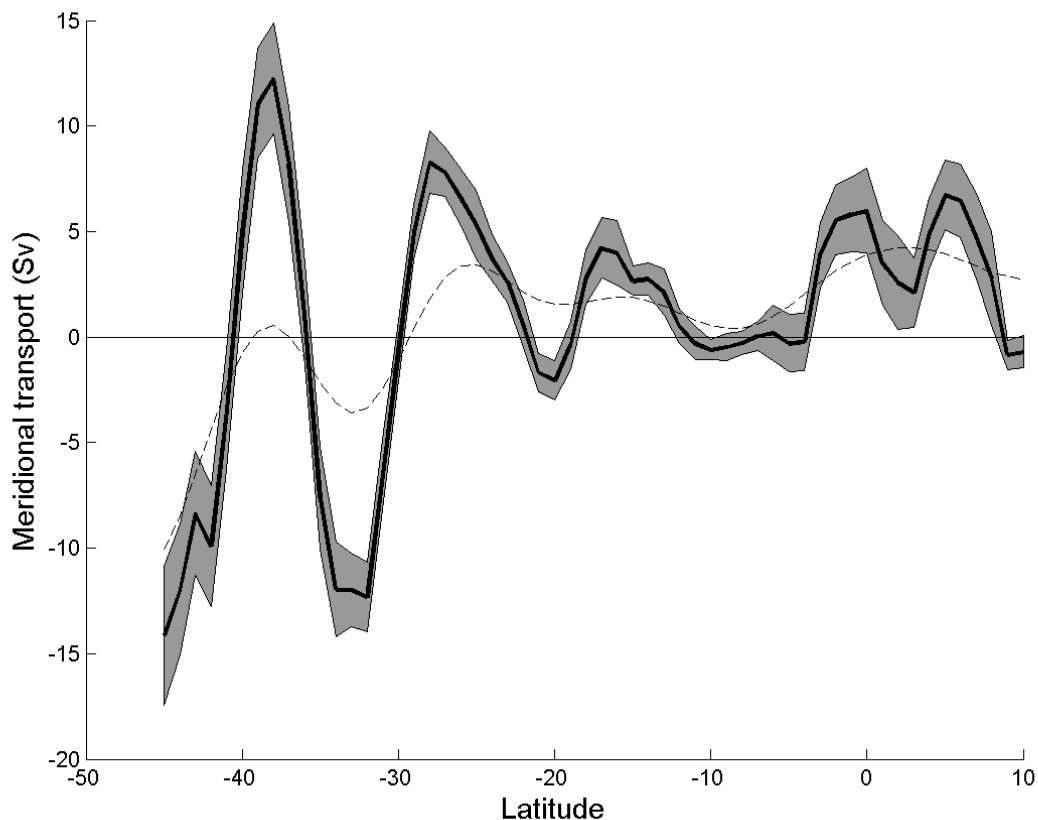


Figure 5.9 Meridional, zonally integrated transport obtained with scalar OMSTA (Sv; positive north). The dashed line represents 5-point (i.e. degree) running mean. The shaded area provides error estimates.

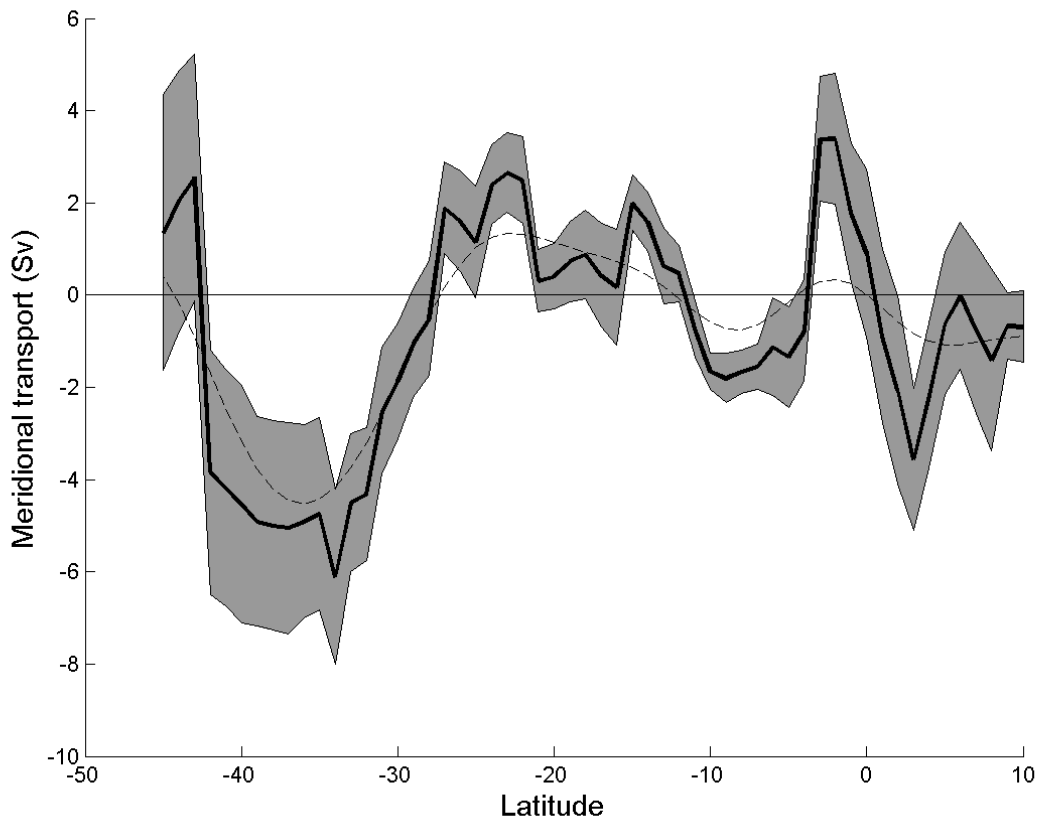


Figure 5.10 Meridional, zonally integrated transport obtained with vectorial OMSTA (Sv; positive north). The dashed line provides a 5-point (degree) running mean. The shaded area is the mean error as calculated by Gauss law of propagation of errors using the errors out of the OM and the error of the layer thickness as defined by neutral density.

5.2.4 Volume transport

In the following, the results of this study will be compared with a comprehensive collection of transport estimates in the literature (model and inverse model calculations). Direct comparisons of these findings are however difficult, due to the diversity of measurement and analysis methods used: Lagrangian and Eulerian measurements, inverse models and geostrophy. Additionally, the definition of the AAIW layer (i.e. vertical boundaries) varies as well. The thickness of the layer in previous studies has been chosen as $450 \text{ m} \pm 50 \text{ m}$ (i.e., it differs in as much as 100 m from study to study). For these reasons, a general agreement of the transports calculated here with those found in the literature is not to be expected.

Figure 5.11 compares meridional volume transport across the entire basin (as a function of latitude) from this study (solid line and shaded area indicating error estimates) with literature values (symbols). For the latter, error bars are displayed when available and a dashed line connects the unweighted mean for multiple values at the same latitude. Transport estimates from this study oscillate, showing several peaks and changes of sign, being significantly smaller than estimates from the literature and barely covered by the uppermost extreme of the error estimates. Besides the different AAIW layer definitions used in each model, these deficiencies are most likely due to four reasons:

- 1) Shortcomings in the mapping procedure related to data distribution: Western boundary currents belong to regions with sparse data for being close to the coast.

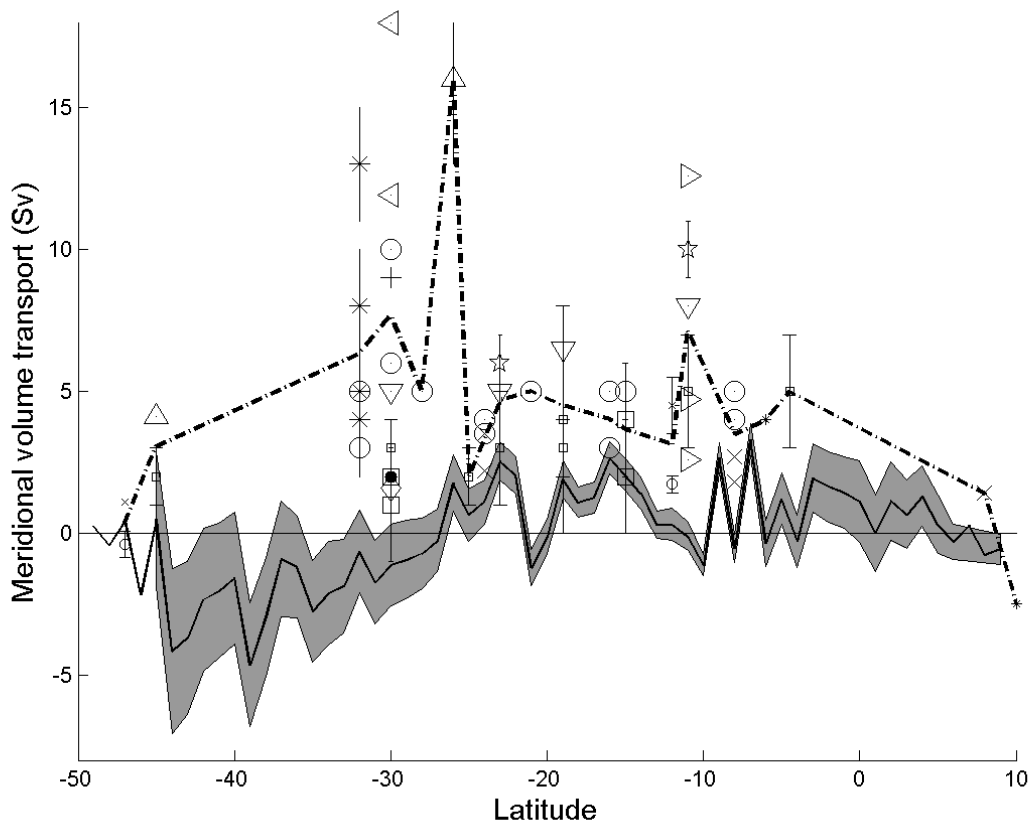
This makes OM resolve these currents badly in comparison with currents in the ocean interior. For instance, the current counter to the iWBC is reflected in the meridional transport as two negative peaks between 6 and 12°S. However, this does not mean necessarily that this current is stronger than the iWBC in this region, but rather that the data related to the iWBC is sparser.

- 2) Scarcity of data in general: Particularly between 8° and 18°S the float data of the isoneutral data set is sparse. The contribution to the meridional transport from currents not resolved in the present analysis could yield differences with inverse models, which use hydrographic data spanning the entire basin.
- 3) The western boundary currents represent a separate regime with particular dynamics: Most of the data used to estimate the LCF comes from the ocean interior (Subsection 3.2.4) and, hence, the LCF resolves currents better in the ocean interior than at the boundaries.
- 4) The underestimation of values by OM, due to the softening of the field and the lack of knowledge of the mean field.

Despite this, the present study agrees acceptably with previous studies. Estimates from inverse models that are quite close or in the shaded area of Figure 5.11 are: Fu (1981), at 24° and 16°S; Roemmich (1983) at 24° and 8°S and 8°N; MacDonald (1993) at 30° and 15°S (this latter, remarkably in good agreement with this study); Matano and Philander (1993) at 30°S; Holfort (1994) at 23°S; Solyan and Rintoul (2001a) at 12°S and Vanicek and Siedler (2002) at 19°, 23° and 25°S. On the other hand, estimates from inverse models suggest positive transports south of 27°S, particularly at 30°S, which is backed up well by 8 previous studies yielding mainly a positive transport. The only exception is the lowest estimate from Macdonald (1993) (1 ± 2 Sv), which may yield 1 Sv southwards in agreement with this study's notion of a negative transport south of the Santos Bifurcation. This discrepancy, together with the estimates at 32°S, is the largest difference between estimates of the meridional transport of this study and previous ones. Indeed, a northward transport north of the tip of Africa (35°S) is in better agreement with mass conservation than a negative one (neglecting isopycnal mixing). However, this study suggests that if this northward transport is correct, it would be related to currents in the Cape Cauldron, which are not appropriately resolved by the present analysis.

Some estimates from the literature must be considered with caution: Geostrophic estimates from Defant, 1941 (as cited by Fu, 1981) and Ganachaud and Wunsch (2000) include the mixed layer; results from Saunders and King (1995) as well as from Sloyan and Rintoul (2001a, 2001b) belong to sections not entirely zonal.

Comparisons with various regional sections (Stramma and Peterson, 1989; Peterson 1992; Schmid, 1998; Boebel et al., 1999a; Richardson and Garzoli, 2003; You et al., 2003) are listed in Table 5.1 and Table 5.2. The corresponding sections are shown in Figure 5.12 and Figure 5.13, with the transport given in Sv per degree. Zonal transports were calculated with vectorial OMSTA, whereas meridional transports were calculated with OMPFV (to involve the iWBC). To account all the South Atlantic transport estimates of the AAIW horizon (to our knowledge), all literature values are comprised, including those geographically outside the isoneutral data set.



- Defant, 1941. Geostrophy.
- Fu, 1981. Potential density.
- × Roemmich, 1983. Potential density.
- * Rintoul, 1991. Neutral density.
- Macdonald, 1993. Potential density.
- ◇ Matano and Philander, 1993. Pot. temp.
- ▽ Holfort, 1994. Neutral density.
- △ Saunders and King, 1995. Isobars
- + Barnier et al., 1996. Sigma levels.
- ◁ Schlitzer, 1996. Potential density.
- ▷ Speer et al., 1996. Potential temperature.
- ☆ Macdonald, 1998. Potential density.
- △ Ganachaud and Wunsch, 2000. Inverse Model.
- Holfort and Siedler, 2001. Potential density.
- Sloyan and Rintoul, 2001a. Neutral density.
- × Sloyan and Rintoul, 2001b. Neutral density.
- * Zhang et al., 2002. Potential density.
- Vanicek and Siedler, 2002. Neutral density.

Figure 5.11 Meridional transport obtained by OMPFV (continuous line) compared with literature values. The shaded area indicates the estimated error. Error bars for the literature values are shown when available. Units are Sv. Positive north. The dashed line joins the mean of literature values reported for the same latitude.

Only six zonal sections of meridional transports are currently published, (Stramma and Peterson, 1989, and You et al, 2003), all of them in the eastern part of the basin. Only two of these overlap partially with the isoneutral data set (Figure 5.12). The results given in Table 5.1 (gray row with bold fonts) indicate good agreement with geostrophic calculations from Stramma and Peterson (1989) across a section at 32°S (reference, $\sigma_0 = 27.4 \text{ kg m}^{-3}$). Only a small part of the sections at 25 and 28°S is inside the region with data (isoneutral data set) and, hence, estimates across these sections cannot be taken into account. On the other hand, the zonal transport obtained by Peterson (1992) across 45°W disagrees in sign with the results from this study. Peterson obtains an eastward transport in a region mainly inside the SAC (see Figure 5.13), which is rather unlikely.

The least differences between zonal transports are in comparison with Schmid (1998) (red rows with bold fonts in Table 5.2). Her geostrophic calculations using either reference surfaces $p = 1500 \text{ dbar}$ (across sections at 1°E 22, 25, 27 and 30°W) or $\sigma_3 = 41.55 \text{ kg m}^{-3}$ (section at 1°E), as well as her Lagrangian transport across 28°W, differ from this study's values between 2 and 6 Sv. Similar results emerge with regard to the transport provided by

Peterson (1992) across a section at 45°W (geostrophy with the ocean floor as reference level): the difference amounts to 7.5 Sv. Even less agreement is found in comparison with most of the RAFOS float based estimates from Schmid (1998) as well as her geostrophic calculations across sections at 33 and 25°W. Other estimates from Schmid (1998) and Peterson (1992) as well as all the estimates from Boebel et al (1999a) and Richardson and Garzoli (2003) differ from the values reported here by more than 10 Sv (and up to 25 Sv).

Unfortunately, the deviation between the estimates from this study and those from the literature is larger than the error in all the cases. While the agreements with the geostrophic transports could merely be a coincidence, the poor concordance with previous Lagrangian transport-estimates (Schmid, 1998; Boebel et al., 1999a; Richardson and Garzoli, 2003) stands out.

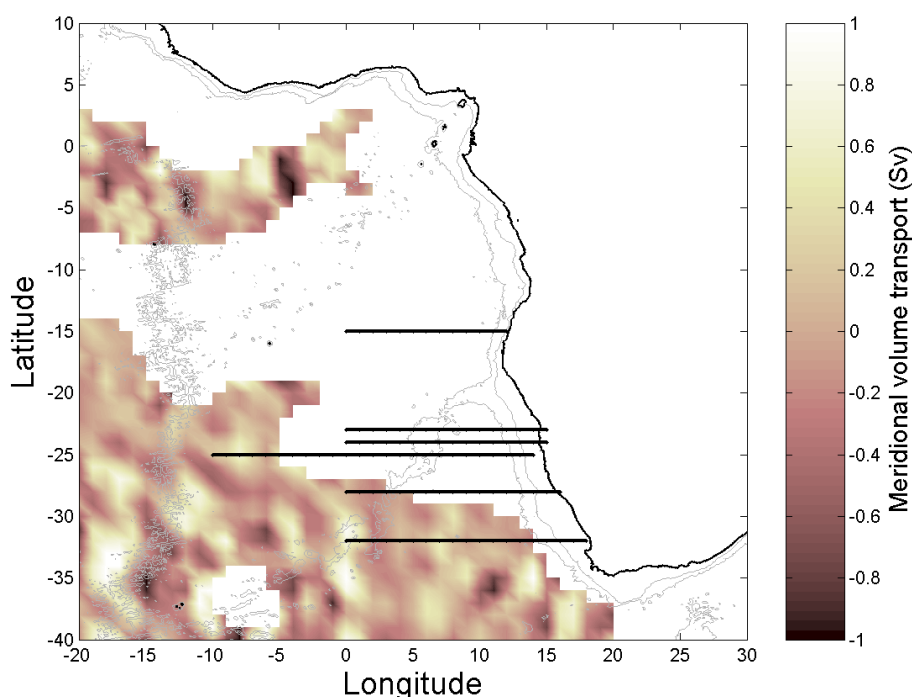


Figure 5.12 Meridional volume transport in each cell (Sv per degree) of the objective mapping graticule (OMPFV) with positive values indicating northward transport. Thick horizontal lines indicate sections across which the transports of Table 5.1 have been calculated.

5.2.5 Temperature transports

Since the volume transport in the AAIW horizon is northward north of the Santos Bifurcation, it could be expected that the AAIW contributes to the northward meridional heat transport. Hence, the southward relative temperature transport at the AAIW horizon reported north of 27°S in this study (Figure 4.11) could be interpreted as being contradictory to the well established idea of a total northward heat transport in the South Atlantic (Model, 1950; Jung, 1955; Bryan, 1962; Bennett, 1978; Hastenrath, 1980; Fu, 1981; Hastenrath, 1982; Rintoul, 1991; Holfort and Siedler, 2001). However, it should be clearly stated that this study does not dispute the total meridional heat transport in the South Atlantic as being northward, but only focuses on the role that AAIW plays in this transport.

Table 5.1 Comparison of values from the literature (3rd column) with estimates of meridional volume transport from this study (Sv; 4th column) across regional sections. The corresponding sections are indicated in Figure 5.12. The longitude of the section is indicated in the 2nd column and the its latitude-range in the 1st column. Errors of the estimates from this study are in the 5th column. The column marked by δ (6th column) is the difference between this study's estimate and the literature one. NA stands for "no applicable", which corresponds to sections in areas where data is not available.

Lat.	Lon. range	Lit. value	This study	Error	δ	Source	Remarks
-25	(-10 14)	3,1	1,4	1,1	1,7	You et al, (2003), p = 2000 dbar	
-25	(-10 14)	6	1,4	1,1	4,6	You et al, (2003), RAFOS,	
-15	(0 12)	0,3	NA	NA	NA	Stramma and Peterson (1989), $\sigma_0 = 27,4 \text{ kg m}^{-3}$	
-15	(0 12)	-2,1	NA	NA	NA	Stramma and Peterson (1989), $\sigma_0 = 27,75 \text{ kg m}^{-3}$	
-15	(0 12)	1,5	NA	NA	NA	Stramma and Peterson (1989), Ocean bottom	
-23	(0 15)	0,7	NA	NA	NA	Stramma and Peterson (1989), $\sigma_0 = 27,4 \text{ kg m}^{-3}$	
-23	(0 15)	1,2	NA	NA	NA	Stramma and Peterson (1989), $\sigma_0 = 27,75 \text{ kg m}^{-3}$	
-23	(0 15)	0	NA	NA	NA	Stramma and Peterson (1989), Ocean bottom	
-24	(0 15)	0	NA	NA	NA	Stramma and Peterson (1989), $\sigma_0 = 27,4 \text{ kg m}^{-3}$	
-24	(0 15)	-1	NA	NA	NA	Stramma and Peterson (1989), $\sigma_0 = 27,75 \text{ kg m}^{-3}$	
-24	(0 15)	-0,2	NA	NA	NA	Stramma and Peterson (1989), Ocean bottom	
-28	(0 16)	2,6	-0,4	1,1	3	Stramma and Peterson (1989), $\sigma_0 = 27,4 \text{ kg m}^{-3}$	
-28	(0 16)	5,7	-0,4	1,1	6,1	Stramma and Peterson (1989), $\sigma_0 = 27,75 \text{ kg m}^{-3}$	
-28	(0 16)	9,5	-0,4	1,1	9,9	Stramma and Peterson (1989), Ocean bottom	
-32	(0 18)	2,9	1,8	0,7	1,1	Stramma and Peterson (1989), $\sigma_0 = 27,4 \text{ kg m}^{-3}$	
-32	(0 18)	5,3	1,8	0,7	3,5	Stramma and Peterson (1989), $\sigma_0 = 27,75 \text{ kg m}^{-3}$	
-32	(0 18)	10	1,8	0,7	8,2	Stramma and Peterson (1989), Ocean bottom	

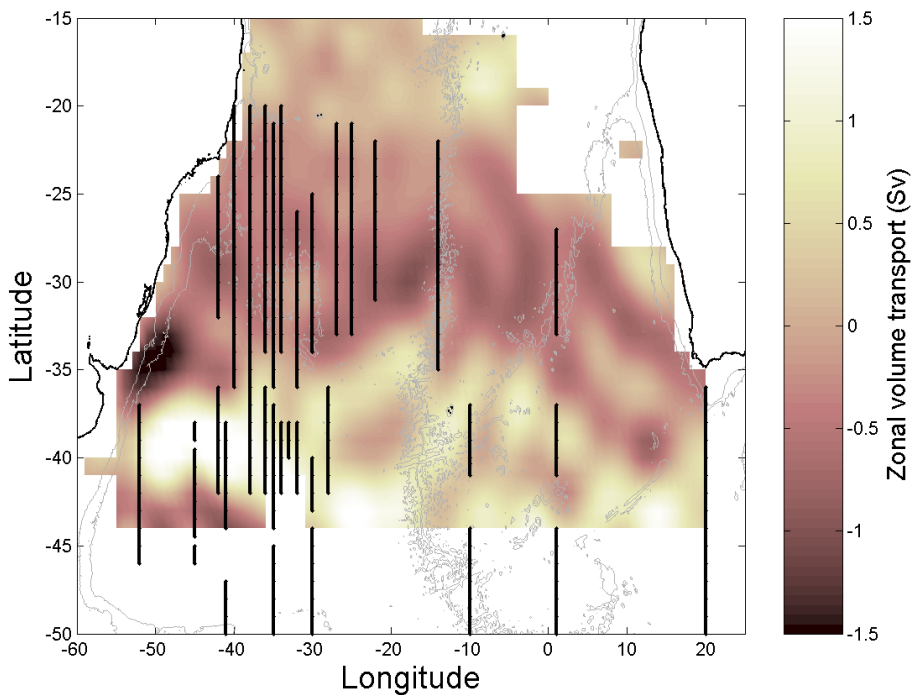


Figure 5.13 Zonal volume transport in each cell (Sv per degree) of the objective mapping graticule (vectorial OMSTA) with positive values indicating eastward transport. Thick vertical lines indicate sections across which the transports of Table 5.2 have been calculated.

Table 5.2 Comparison of values from the literature (3rd column) with estimates of zonal volume transport from this study (Sv; 4th column) across regional sections. The corresponding sections are indicated in Figure 5.13. The longitude of the section is indicated in the 2nd column and the latitude-range in the 1st column. Errors of the estimates from this study are in the 5th column. The column marked by δ (6th column) is the difference between this study's estimate and the literature one. NA stands for "not applicable", which corresponds to sections in areas where data is not available. R&G stands for Richardson and Garzoli.

Lat. range	Lon	Lit. value	This study	Error	δ	Source
(-50 -36)	20	13	NA	NA	NA	You et al, (2003), p = 2000 dbar
(-40 -36)	20	-4	NA	NA	NA	You et al, (2003), p = 2000 dbar
(-46 -36)	20	7	NA	NA	NA	You et al, (2003), RAFOS
(-46 -36)	20	7	NA	NA	NA	You et al, (2003), p = 2000 dbar
(-46 -37)	-52	26	1	2,4	25	Schmid (1998), p = 1500 dbar
(-52 -47)	-41	27	NA	NA	NA	Schmid (1998), $\sigma_3 = 41,55 \text{ kg m}^{-3}$
(-44 -38)	-41	18	6,8	2,2	11,2	Schmid (1998), $\sigma_3 = 41,55 \text{ kg m}^{-3}$
(-40 -38)	-33	11	2,1	2,4	8,9	Schmid (1998), p = 1500 dbar
(-52 -44)	-30	13	NA	NA	NA	Schmid (1998), $\sigma_3 = 41,55 \text{ kg m}^{-3}$
(-43 -40)	-30	16	3,2	3,1	12,8	Schmid (1998), $\sigma_3 = 41,55 \text{ kg m}^{-3}$
(-52 -44)	-30	8	NA	NA	NA	Schmid (1998), p = 1500 dbar
(-43 -40)	-30	9	3,2	3,1	5,8	Schmid (1998), p = 1500 dbar
(-51 -44)	-10	17	NA	NA	NA	Schmid (1998), $\sigma_3 = 41,55 \text{ kg m}^{-3}$
(-41 -37)	-10	15	1,7	1,8	13,3	Schmid (1998), $\sigma_3 = 41,55 \text{ kg m}^{-3}$
(-53 -44)	1	25	NA	NA	NA	Schmid (1998), $\sigma_3 = 41,55 \text{ kg m}^{-3}$
(-41 -37)	1	6	1,2	1,5	4,8	Schmid (1998), $\sigma_3 = 41,55 \text{ kg m}^{-3}$
(-39 -38)	-45	-4	3,4	3,9	7,5	Peterson (1992), Ref = ocean floor
(-45 -40)	-45	15	1,1	1,9	14,2	Peterson (1992), Ref = ocean floor
(-46 -45)	-45	-4	NA	NA	NA	Peterson (1992), Ref = ocean floor
(-42 -36)	-42	15	7	2,2	8	Schmid (1998), RAFOS
(-42 -36)	-38	19	7,3	2,2	11,7	Schmid (1998), RAFOS
(-42 -36)	-36	12	5	1,9	7	Schmid (1998), RAFOS
(-42 -38)	-34	10	2,4	2,8	7,6	Schmid (1998), RAFOS
(-42 -38)	-32	9	2	1,9	7	Schmid (1998), RAFOS
(-42 -36)	-28	9	4,7	1,3	4,3	Schmid (1998), RAFOS
(-33 -27)	1	-13	-2,8	0,9	10,2	Schmid (1998), $\sigma_3 = 41,55 \text{ kg m}^{-3}$
(-31 -22)	-22	-6	-4,1	0,8	1,9	Schmid (1998), p = 1500 dbar
(-33 -21)	-25	-12	-4,5	0,5	7,5	Schmid (1998), $\sigma_3 = 41,55 \text{ kg m}^{-3}$
(-33 -21)	-25	-7	-4,5	0,5	2,5	Schmid (1998), p = 1500 dbar
(-33 -21)	-27	-6	-4,1	0,7	1,9	Schmid (1998), p = 1500 dbar
(-34 -25)	-30	-18	-4	0,7	14	Schmid (1998), RAFOS
(-36 -26)	-32	-18	-2,9	0,6	15,1	Schmid (1998), RAFOS
(-34 -20)	-34	-19	-4	0,7	15	Schmid (1998), RAFOS
(-34 -20)	-36	-29	-4,4	0,6	24,6	Schmid (1998), RAFOS
(-36 -20)	-38	-22	-4,1	0,8	17,9	Schmid (1998), RAFOS
(-36 -20)	-40	-19	-5,8	0,6	13,2	Schmid (1998), RAFOS
(-32 -24)	-42	-13	-4,3	1,2	8,7	Schmid (1998), RAFOS
(-35 -22)	-14	-14	-3,8	0,8	10,3	R&G (2003), RAFOS
(-35 -22)	-14	-13	-3,8	0,8	9	R&G (2003), RAFOS
(-36 -21)	-35	-12	-3,4	0,6	8,6	Boebel et al (1999a), RAFOS
(-44 -37)	-35	15	3,5	2,3	11,5	Boebel et al (1999a), RAFOS
(-53 -45)	-35	19	NA	NA	NA	Boebel et al (1999a), RAFOS

The main argument to back up this study's findings is that AAIW seems to be warmer than the water column average only in the ocean interior. At the coasts (and particularly near the west coast) the AAIW layer is colder than the water column, in a mean sense. This can be seen in Figure 5.14, where the difference between the AAIW mean temperature and the mean vertical temperature of the water column (Levitus, 1994) is shown. Positive values (ranging from 1 to 3°C) prevail only in the ocean interior (excluding the nBSG)¹, which means that, there, AAIW is colder than the water column average. Conversely, values near the coasts are negative, which implies AAIW being colder than the water column average in these regions.

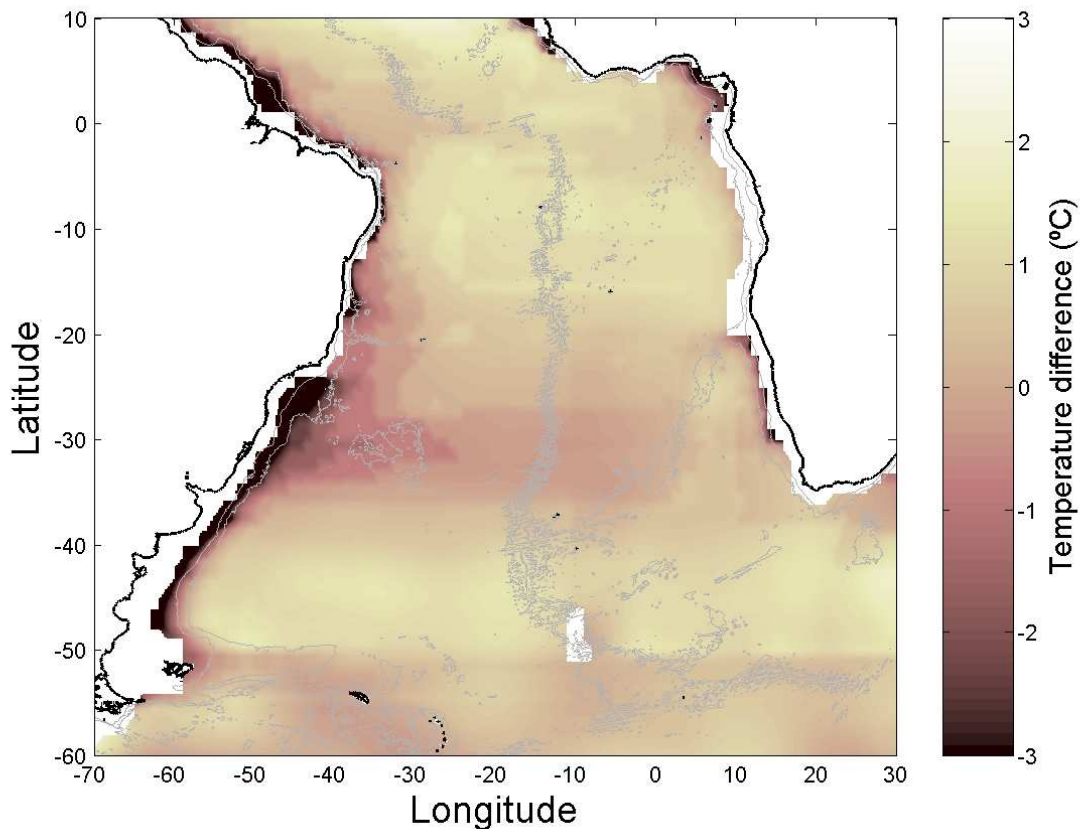


Figure 5.14 Difference between the mean temperature along the water column, as calculated from Levitus (1994) atlas data, and the mean temperature of the AAIW layer, as calculated on the three isoneutral surfaces ($\sigma^{\theta} = 27.25$, $\sigma^{\theta} = 27.40$ and $\sigma^{\theta} = 27.55$). Units are °C.

By inspecting the mean temperature of Levitus (1994) (not shown), it is clear that the high vertical mean temperature near the coasts is not related to a particular horizontal temperature structure, but merely to the bathymetry which excludes the deep cold waters from the averaging process. This is particularly true at the western boundary because in this region the continental shelf is wider than at the eastern boundary. Additionally, water is carried northwards in the South Atlantic mainly at the west coast by the iWBC (Section 4.3). Hence, the main carrier of heat at the AAIW horizon acts in a region that is particularly warm due to its shallowness and this yields a *negative* contribution of heat to the budget of the South Atlantic at the AAIW horizon (in the subtropics). Similarly, the South Brazil

¹ This would be related to the surface warm water coming from the Indian Ocean.

Current carries relative temperature northwards because it actually carries “negative heat” southwards.

But if not AAIW, what is carrying heat to the tropics and beyond into the North Atlantic? The most feasible answer would be the surface and central water drifts, mainly due to the North Brazil Current (NBC), which carries 22.4 Sv northwards above 300 m (Schott et al., 1998). Water above the AAIW layer is warmer and currents near the surface are stronger. These two factors together make the surface drift the best candidate for the northward heat transport in the South Atlantic.

Table 5.3 Heat transport calculations in the South Atlantic (chronological order). None of these studies consider the meridional heat transport of AAIW.

Paper	Method
Bryan, 1962.	Direct method.
Bunker, 1976.	Unknown
Bennett, 1978.	Direct method. Inverse model.
Fu, 1981.	Direct method. Inverse model.
Georgi and Toole, 1982.	unknown
Hastenrath, 1982.	Bulk formulas. Atmospheric data. / Satellite measurements.
Roemmich, 1983.	Direct method. Inverse model.
Hsiung, 1985.	Bulk formulas. Atmospheric data.
Russell et al., 1985.	Bulk formulas. Atmospheric circulation model.
Philander and Pacanowski, 1986.	Direct method. Circulation model.
Rintoul, 1991.	Direct method. Inverse model.
MacDonald, 1993.	Direct method. Inverse model.
Matano and Philander, 1993.	Direct method. Circulation model.
Holfort, 1994.	Direct method. Inverse model.
Saunders and King, 1995.	Direct method. Inverse model.
Barnier et al., 1996.	Direct method. Circulation model.
Macdonald and Wunsch, 1996.	Direct method. Inverse model.
Schlitzer, 1996.	Direct method. Circulation model.
Speer et al., 1996.	Direct method. Inverse model.
Holfort and Siedler, 1997.	Direct method. Inverse model.
Ganachaud and Wunsch, 2000.	Direct method. Inverse model.
Sloyan and Rintoul, 2001a	Direct method. Inverse model.
Holfort and Siedler, 2001.	Direct method. Circulation model.
Bryden and Imawaki, 2001.	Review of previous studies.
Ganachaud and Wunsch, 2002.	Direct method. Inverse model.

The question remains, what is the magnitude of the meridional temperature transport of AAIW in comparison with other horizons? Is the iWBC transport of -0.064 ± 0.016 PW (Table 4.2) significant? Unfortunately, to our knowledge, all studies on temperature transport in the South Atlantic (Table 5.3) report heat transport only, i.e., temperature transport across sections spanning the entire water column from coast to coast, which prohibits a direct comparison. Hence, to get an insight of the role that AAIW play in heat budget of the South Atlantic, a comparison with heat estimates across the whole water column is the only possible approach (Figure 5.15). In general, present estimates of the contribution of AAIW to the heat budget are smaller than most of the estimates across the whole water column of previous studies in one order of magnitude. The only exceptions are the values of Hsiung (1985) at 30°S and Fu (1981) at 8°S. This suggests that the heat

transport at the AAIW layer horizon plays a secondary role in the AMOC, compared with the transport at other horizons.

Instead of a separation by water masses, in previous studies a separation related to physical processes (wind driven circulation, overturning circulation, meddies) is performed with the goal of understanding the heat transport dynamics (Bennett, 1978; Bryden and Imawaki, 2001). These decompositions are related to the calculation of a mean value and related anomalies (shear) that do not suit the present float trajectory analysis. Hence, the present study does not permit to look into the physical processes of heat transport in more detail. However, this separation approach has been criticized by Ganachaud and Wunsch (2002), who assert that “any decomposition is arbitrary and difficult to relate to physically meaningful processes. (...) Decompositions like these are useful kinematic/descriptive tools, but not easily related to driving forces” (Ganachaud and Wunsch, 2002, page 703). While estimates of meridional heat transport are only achievable with inverse or direct models, direct transport estimates in the ocean (for instance, with floats or tracers) are increasing every day. These estimates lead to a better understanding of the particular role that each water mass plays in the heat budget of the ocean. Hence, to compare observations with models in this aspect, this study suggest that instead of a separation in physical processes, model efforts should concentrate in calculating meridional temperature transports of the different water masses.

5.2.6 *Freshwater transport*

What is the contribution of AAIW to freshwater transport within the AMOC? The South Atlantic receives water from the Amazon river, which transports 20% of all the freshwater that enters the world ocean, i.e., 0.2 Sv (Baumgartner and Reichel, 1975; Dagg et al., 2004).¹ This is two orders of magnitude larger than the contribution of the iWBC to the meridional freshwater budget (0.018 ± 0.005 Sv; Table 4.2). Considering additional river runoffs and the rainfall, the AAIW influx appears negligible. However, these waters (due to their low density) are unlikely to mix down below the seasonal thermocline. Hence, due to its low salinity, the AAIW is the principal deep source of freshwater in the South Atlantic, playing a special role in resupplying the deep and intermediate layers with freshwater.

To our knowledge, transport estimates of freshwater only at the AAIW horizon are, up to date, unavailable in the literature (Table 5.4). Hence, a comparison with the total meridional freshwater transport from the literature (Figure 5.16) is the only possible procedure to estimate the impact of AAIW in the freshwater budget. In comparison with typical total meridional transports of freshwater, this study’s transport is undistinguishable from zero (because of that, a graphical comparison is omitted). While most authors agree that the total meridional transport of fresh water declines to the north due to the increase of evaporation over precipitation in the tropics (see the Introduction), the flow direction is a matter of debate. One proposition (Oort and Peixóto, 1983; Rahmstorf, 1996; Barnier et al., 1996; Wijffels, 2001) states that the freshwater transport in the South Atlantic (south of 10°S, at least) is mainly northward. Due to the decrement towards the north, the freshwater transport eventually changes its sign, becoming southward. For this region (somewhere in the tropics, immediately south of the equator), AAIW could be the main contributor to the meridional transport of freshwater. Further north, the AAIW compensates the southward freshwater transport with a transport that ranges between 1 to 10% of the total transport.

¹ In Figure 2.8 the effect of the Amazon river is exposed by a low salinity spot in the surface centred at the equator.

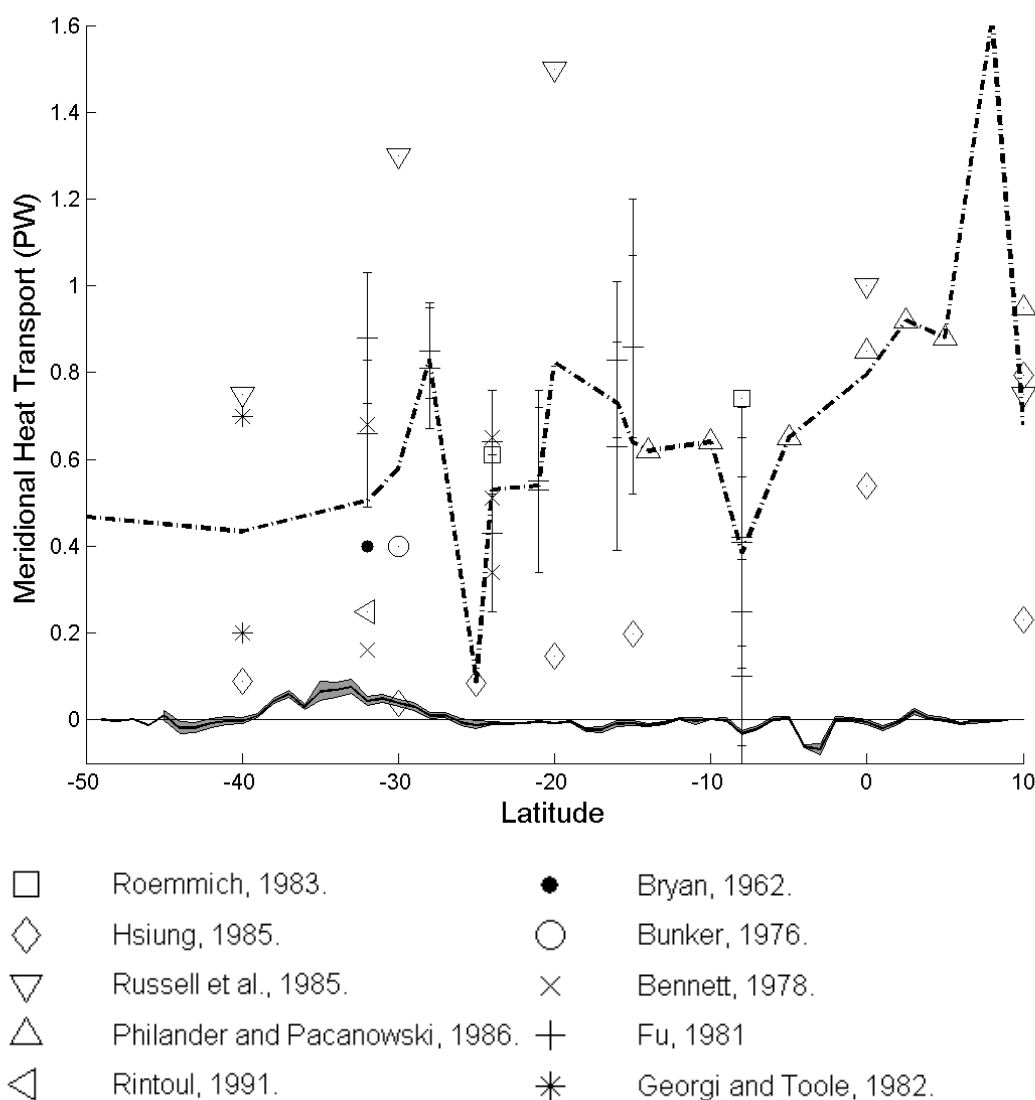
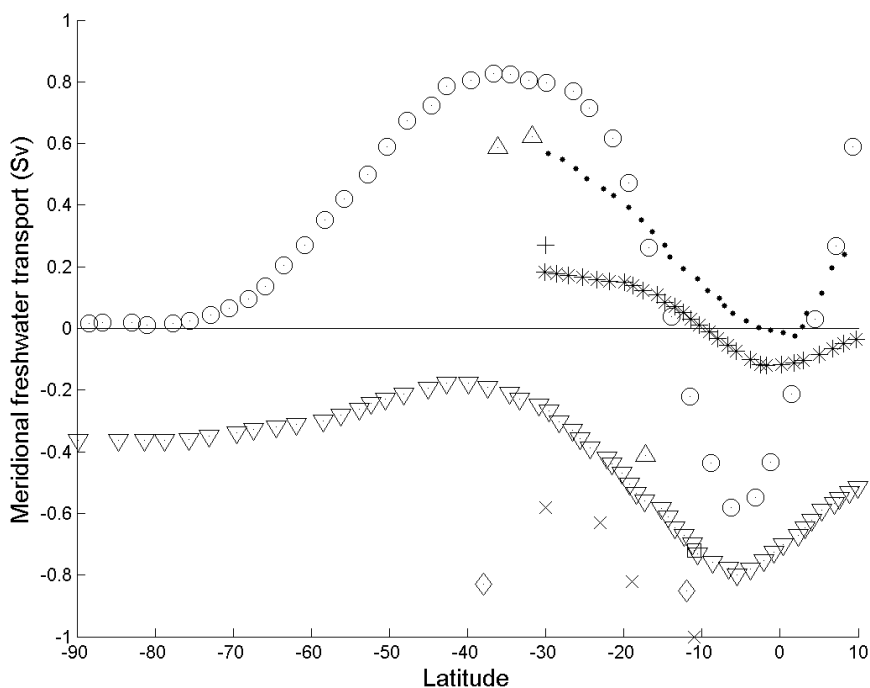


Figure 5.15 Literature values of total meridional heat transport in the South Atlantic (error bars shown when available) and comparison with this study's estimate of the meridional contribution to the relative temperature transport of the South Atlantic. The dashed line connects the mean value of literature estimates at the same latitude. Positive values indicate northward relative temperature transport. Units are PW.

Other studies (Holfort, 1994; Holfort and Siedler, 2001; Sloyan and Rintoul, 2001b) show freshwater transport in the South Atlantic being southward at all latitudes with values as high as 1 Sv. In this sense, the AAIW layer compensates the southward transport with a northward and rather minor one (order of 1% of the total). Hence, the role that AAIW plays in the AMOC concerning meridional freshwater seems to be, like in the case of heat transport, rather negligible. However, a question still remains unanswered: which element of the AMOC carries freshwater southwards? The surface drift is mainly northward, due to the NBC and, in spite of river runoff, saltier than AAIW on the average (see Figure 2.8). On the other hand, NADW is drifting southwards and, even though it is also saltier than AAIW, it is fresher than the surface waters. Due to its vast volume transport, the southward flow of NADW would bias the vertical average salinity, resulting in an effective freshwater transport to the South.

Table 5.4 Salinity or freshwater transport estimates in the South Atlantic (chronological order). Note that some of these papers are the same as those in Table 5.3 above.

Paper	Method
Baumgartner, et al., 1975	Direct method. Observations.
Bennett, 1978.	Direct method. Inverse model.
MacDonald, 1993.	Direct method. Inverse model.
Holfort, 1994.	Direct method. Inverse model.
Saunders and King, 1995.	Direct method. Inverse model.
Barnier et al., 1996.	Direct method. Circulation model.
Rahmstorf, 1996.	Direct method. Circulation model.
Speer et al., 1996.	Direct method. Inverse model.
Holfort and Siedler, 1997.	Direct method. Inverse model.
Sloyan and Rintoul, 2001b	Direct method. Inverse model.
Holfort and Siedler, 2001.	Direct method. Circulation model.
Wijffels, 2001	Review of previous studies.
Ganachaud and Wunsch, 2002.	Direct method. Inverse model.



- Baumgartner and Reichel, 1975 *
- Oort and Piexoto, 1983
- × Holfort, 1994
- + Barnier et al., 1996
- * Rahmstorf, 1996
- Holfort and Siedler, 1997
- ◇ Sloyan and Rintoul, 2001b **
- ▽ Holfort and Siedler, 2001
- △ Wijffels, 2001

Figure 5.16 Some literature values of total meridional freshwater transport in the South Atlantic (Sv, positive values indicate northward freshwater transports).

* As reported by Rahmstorf, 1996.

** Mean latitude of section SAVE4.

Chapter 6 Summary and conclusions

A total of 436 pop-up and acoustically tracked floats drifting throughout more than one decade in the tropical and south Atlantic (from 60°W to 30°E and 70°S to 10°N) provided the basis for this study's unprecedented collection of 611 float years of velocity data (Table 2.1). Floats displacements were homogenized by simulating a pop-up behavior for the acoustically tracked floats and neglecting displacements longer than 10 days. From this data set, three subsets were obtained (Section 2.3) by constraining displacements of floats that drifted between two neutral density surfaces ($\gamma^{\theta} = 27.40$ to $\gamma^{\theta} = 27.55$), these same surfaces displaced symmetrically 50 m up and down and two isobaric surfaces (650 to 1050 dbars). Considering that from a theoretical frame results from the first data set would be superior, the large differences between transports out of this set and the sets obtained under isobaric and displaced isoneutral surfaces lead to neglect these latter two. The constriction by isobars proved to be a good choice only between 17°S and 40°S only. Float velocities were projected onto the salinity core of AAIW using geostrophic velocities in 5 isoneutral surfaces ($\gamma^{\theta} = 27.25, 27.32, 27.40, 27.45$ and 27.55). However, the mean difference between the projected speeds and primal speeds was 0.43 cm s^{-1} , yielding minor differences in the results and warranting the projected data set to be ignored.

The isoneutral data set was averaged within grid cells of various sizes and shapes (Section 3.1). according to isolines of bathymetry (H), potential density of the entire water column (f/H) and potential density of the AAIW layer (f/h) as defined by the isoneutral surfaces ($\gamma^{\theta} = 27.25$ and 27.55). The quality of the grids was assessed through the alignment of the mean velocities relative to the field that shaped the cells (Subsection 3.1.1). The grids yielding optimum results were those following f/h , which implies that it is this property (rather than H of f/H) that most strongly influences the flow pattern of AAIW.

Within the group of f/h -shaped grids, a grid developed from the 3° latitude and 4° longitude achieved the optimum balance between space resolution and elusion of mesoscale processes. Based on averaged velocities from this grid, 300 objective maps were calculated using multiple combinations of OM parameters (Subsection 3.3.1). All graticule points within a cell of the space-time averaging grid containing data, or being surrounded by at least four cells with data, were mapped. For each of these maps, zonal and meridional transports were estimated using the thickness of the AAIW as defined by the neutral density surfaces ($\gamma^{\theta} = 27.25$ and 27.55). Mean root squared differences between meridional transport and literature values were a minimum when a correlation length of 4° and a climatological variability of 3 cm s^{-1} were assumed.

Given that the space-time averages and, in consequence, the corresponding objective maps were unable to reveal the narrow intermediate western boundary current along the South American coast, an alternative approach of mapping primal data was followed. Since attempts of calculating a longitudinal covariance function (LCF) from primal float velocities without symmetry conditions lead to a non positive-definitive covariance function (Subsection 3.2.4), cylindrical symmetry was assumed *a priori*. The ensuing isotropic LCF (with parameters $C = 1.97 \text{ cm s}^{-1}$ and $\sigma = 1.61^{\circ}$; see Equation (3.22)) was estimated from the primal float velocities as constrained by the isoneutral surfaces, neglecting the zonal covariance (Subsection 3.2.4). OM with this LCF was performed in overlapping subsets of approximately 3500 data points each, using as uncorrelated input error the variance of each subset and checking for positive-definitiveness by a Cholesky factorization (Subsection 3.3.3). Mapped velocities located outside an area defined by a Delaunay triangulation were neglected (Subsection 3.3.4). The optimum lattice resolution for mapping was identified to be $1^{\circ} \times 1^{\circ}$ in all the cases.

These analyses reveal a Subtropical Gyre, spanning from $23^{\circ}\pm 1^{\circ}\text{S}$ to $45^{\circ}\pm 1^{\circ}\text{S}$, centered near 36°S on the average. Its central part exhibits local recirculation cells and coincides with the AAIW layer's region of greatest depth. The gyres southern branch, the South Atlantic Current (SAC) meanders from 35°S to 45°S and has a rms speed of $12.4 \pm 8.4 \text{ cm s}^{-1}$ ($7.1 \pm 3.9 \text{ Sv}$). The Northern Branch of the Gyre flows westwards with a rms speed of $4.7 \pm 3.3 \text{ cm s}^{-1}$ ($8.1 \pm 4.7 \text{ Sv}$) and spanning from 22°S to 32°S . The Santos Bifurcation occurs at 27°S . An eastward current lies immediately north of the Subtropical Gyre (20°S), flowing with a rms speed of $4.1 \pm 2.4 \text{ cm s}^{-1}$. The Agulhas Current shows a rms speed of $25.3 \pm 14.2 \text{ cm s}^{-1}$ and the Agulhas Return Current of $22.9 \pm 13.2 \text{ cm s}^{-1}$.

Error ellipses reveal high variance in the Confluence Zone, the Agulhas Current System and the tropics, whereas low values occur in the northern branch of the Subtropical Gyre.

The stream function derived by vectorial OMSTA suggests an advective connection between the SAC and the nBSG, while the stream function derived by OMPFV reveals a rather weak connection. In both cases, the function clearly shows the western intensification, suggests the existence of a Tropical Gyre divided in two subcells by the Midatlantic Ridge and shows that part of the transport of the SAC flows farther into the Indian Ocean. A streamline connecting the Agulhas System with the South Atlantic Subtropical Gyre supports the notion of a Subtropical Supergyre. However, the connection appears weak, which can be a consequence of the Cape Cauldron masking the advective link between the Indian and the South Atlantic oceans with high mesoscale activity.

Volume transport estimations expose the Subtropical Gyre as a non-balanced system with a divergence point: the Santos Bifurcation. From there, two western boundary currents flow along the South American coast carrying most of the meridional transport at the AAIW horizon: the iWBC northwards (mapped meridional velocity: $10.1 \pm 1.2 \text{ cm s}^{-1}$; maximum primal float speed: 30 cm s^{-1} ; volume transport: $3.7 \pm 0.4 \text{ Sv}$; relative temperature transport: $-0.069 \pm 0.069 \text{ PW}$; freshwater transport: $0.017 \pm 0.005 \text{ Sv}$) and the iBC southwards (mapped meridional velocity: $-15.4 \pm 3.6 \text{ cm s}^{-1}$; maximum primal float speed: 30 cm s^{-1} ; volume transport: $-9.0 \pm 2.1 \text{ Sv}$; relative temperature transport: $0.074 \pm 0.044 \text{ PW}$; freshwater transport: $-0.040 \pm 0.010 \text{ Sv}$). The southward flow of the iBC seems to be unbalanced, which is explicable if water flows into the nBSG through Indian-Atlantic interocean exchange. This northward transport in the Cape Cauldron could be equal (or larger) than the southward transport due to the iBC. However, for being related to mesoscale processes in the Cape Cauldron, this transport is not properly revealed in the present results, as is the connection between the South Atlantic and Indian oceans.

The tropical region is divided into 8 zonal jets (Table 4.1). The EIC flows westward at the equator, with a rms speed of $10.5 \pm 6.4 \text{ cm s}^{-1}$ and transporting $-1.5 \pm 0.9 \text{ Sv}$. North and south thereof, currents with alternating direction follow a symmetrical pattern: westward currents at 2°S and 2°N : the SICC ($1.3 \pm 0.6 \text{ Sv}$; $8.8 \pm 5.5 \text{ cm s}^{-1}$) and the NICC ($1.5 \pm 1.2 \text{ Sv}$; $10.6 \pm 6.0 \text{ cm s}^{-1}$), respectively; eastward currents at 4°S and 4°N : the eSEC ($-1.3 \pm 0.6 \text{ Sv}$; $6.8 \pm 3.7 \text{ cm s}^{-1}$) and the nSEC ($-1.0 \pm 1.0 \text{ Sv}$; $8.3 \pm 4.2 \text{ cm s}^{-1}$), respectively. Farther south, at 6°S the eastward flowing SEUC carries $0.6 \pm 0.4 \text{ Sv}$ ($5.7 \pm 3.4 \text{ cm s}^{-1}$), at 8°S the westward flowing cSEC carries $-0.3 \pm 0.3 \text{ Sv}$ ($4.6 \pm 3.5 \text{ cm s}^{-1}$) and at 10°S the westward flowing SECC carries $0.3 \pm 0.3 \text{ Sv}$ ($6.6 \pm 5.3 \text{ cm s}^{-1}$). The positions of the EIC, NICC and SICC agrees thoroughly with other studies, while the eSEC, SEUC and SECC are in agreement with some, and disagreement with other studies.

In comparison with literature transport estimates, values from this study tend to be low, which could be related to the underestimation inherent to the objective mapping, the way in which the different authors have defined the AAIW layer in their studies, and due to shortcomings in the mapping procedure related to data distribution and due to mapping

various regimes (subject to different dynamics) with only one covariance function. However, there is some agreement in the meridional volume transport with results from previous studies.

The role of AAIW in the AMOC regarding freshwater transport would lie in one of two scenarios: On the one hand, immediately south of the equator, the iWBC would be the most important freshwater carrier in the AMOC. On the other hand, the input of AAIW to the freshwater budget of the South Atlantic would be minor all along the basin (1% of the total). In both cases, AAIW would be flowing (together with the central and surface waters) northward and opposite to the main carrier of freshwater in the South Atlantic, i.e. the NADW.

Due to the temperature differences between AAIW and the central and surface waters, the iWBC carries cold water into the tropics (between 26°S and 13°S), diminishing thus the heat budget in the South Atlantic. However, the role that AAIW plays in the meridional heat transport of the South Atlantic seems to be minor, since the iWBC carries approximately 1% of the total northward transport as calculated by inverse models. Hence, the well-established northward heat transport in the South Atlantic can only be maintained through the central and upper layers, most likely due to the NBC.

To know which is the contribution of heat, salt and freshwater of each of the water masses involved in the AMOC to the corresponding budgets of the South Atlantic, as well as the mechanisms involved in their transports, it is vital to accurately estimate the transports of each water mass participating in the AMOC.

Comparison between maximum mapped and primal float velocities for the western boundary currents (Section 4.6) shows that velocities (and in consequence, transports) could be underestimated 50% (or more). Future implementations of the OM method shall undertake this problem by estimating a background of the field or quantifying the underestimation with primal float velocities by regions. An alternative approach to deal with the underestimation of values is to transform mapped velocity components u and v with the inverse cumulative density function that best fits the primal float velocities.

Other schemes that could be followed in future studies are: separation of the system in regimes with quasi-homogeneous statistics to calculate independent LCFs, iterative use of the stream function in the averaging process and the use of finite element grids.

Appendix 1 The Gauss-Markov theorem.

To map a physical field $\underline{\eta}$ in a point γ_k as a linear combination of N observations (in a column vector η),

$$\hat{\eta}(\gamma_k) = A(\gamma_k)\eta, \quad (A.1)$$

the Gauss-Markov theorem states that the best linear (unbiased) estimator $\hat{\eta}(\gamma_k)$ is given when the row vector $A(\gamma_k)$ equals:

$$A(\gamma_k) = R_{\gamma_k} M^{-1},$$

where R_{γ_k} is a N -dimensional row covariance-vector between the observations η and the point γ_k and M is the $N \times N$ covariance matrix of the observations. This estimator minimizes the variance of the dispersion of the estimated field with respect to the real field,

This theorem was achieved by the German mathematician Carl Friedrich Gauss, as a byproduct while proving the correctness of the least squares method. Proofs of the Gauss-Markov theorem can be found in a number of references (for instance: Jenkins and Watts, 1968; Bretherton et al., 1976, and Box and Jenkins, 1976). The proof presented here is mainly based on Wunsch (1996), with different notation and amendments intended to clarify blurred aspects of his demonstration.

Since a variable's variance cannot be calculated without evaluating the variable in a large number of points, first of all an hypothetical ensemble of m test-points γ_k will be considered, where $m \gg 1$. Hence, the variance of the dispersion of the estimated field with respect to the real field is given by:

$$P^2 = \frac{1}{m} \sum_{k=1}^m (\Delta\eta(\gamma_k) - \overline{\Delta\eta})^2,$$

where the over-bar denotes mean value and

$$\Delta\eta(\gamma_k) = \hat{\eta}(\gamma_k) - \underline{\eta}(\gamma_k)$$

is the dispersion of the estimated field $\hat{\eta}$ with respect to the real field $\underline{\eta}$. Assuming that $\overline{\hat{\eta}(\gamma_k)} = 0$ and $\overline{\underline{\eta}(\gamma_k)} = 0$ implies $\overline{\Delta\eta} = 0$. Hence, the quantity to minimize is:

$$P^2 = \frac{1}{m} \sum_{k=1}^m (\hat{\eta}(\gamma_k) - \underline{\eta}(\gamma_k))^2.$$

For convenience, P will be rewritten as:

$$P^2 = \frac{1}{m} \text{trace} \{ (\hat{z} - z)(\hat{z} - z)^T \}, \quad (A.2)$$

where \hat{z} and z are column vectors with m elements defined as:

$$\hat{z} = \begin{pmatrix} \hat{\eta}(\gamma_1) \\ \hat{\eta}(\gamma_2) \\ \hat{\eta}(\gamma_3) \\ \vdots \\ \hat{\eta}(\gamma_m) \end{pmatrix} \quad z = \begin{pmatrix} \underline{\eta}(\gamma_1) \\ \underline{\eta}(\gamma_2) \\ \underline{\eta}(\gamma_3) \\ \vdots \\ \underline{\eta}(\gamma_m) \end{pmatrix},$$

and *trace* denotes the trace of the matrix, i.e., the sum of the elements of the diagonal:

$$\text{trace}\{a_{ij}\} = \sum_i a_{ii}$$

Considering that the estimated field is expressed as a linear combination of the observations (Equation A.1), one has:

$$\hat{z} = \underline{\underline{A}}\eta,$$

where $\underline{\underline{A}}$ is an $m \times N$ matrix whose rows are the vectors $A(\gamma_i)$:

$$\underline{\underline{A}} = \begin{pmatrix} A(\gamma_1) \\ A(\gamma_2) \\ A(\gamma_3) \\ \vdots \\ A(\gamma_m) \end{pmatrix}. \quad (A.3)$$

Inserting this expression for \hat{z} into (A.2), simple matrix algebra yields:

$$P^2 = \frac{1}{m} \text{trace}\{(\underline{\underline{A}}\eta)(\underline{\underline{A}}\eta)^T - z(\underline{\underline{A}}\eta)^T - (\underline{\underline{A}}\eta)z^T + zz^T\}.$$

Using the identity $(\underline{\underline{A}}\eta)^T = \eta^T \underline{\underline{A}}^T$ results in:

$$P^2 = \frac{1}{m} \text{trace}\{\underline{\underline{A}}(\eta\eta^T)\underline{\underline{A}}^T - z\eta^T \underline{\underline{A}}^T - \underline{\underline{A}}\eta z^T + zz^T\}.$$

Now, since $\overline{\underline{\eta}(\gamma_k)} = 0$ and $\overline{\hat{\eta}(\gamma_k)} = 0$ one also has $\bar{\eta} = 0$. Hence,

$$\eta\eta^T = \begin{pmatrix} \eta_1\eta_1 & \eta_1\eta_2 & \cdots & \eta_1\eta_N \\ \eta_2\eta_1 & \eta_2\eta_2 & \cdots & \eta_2\eta_N \\ \vdots & \vdots & \ddots & \vdots \\ \eta_N\eta_1 & \eta_N\eta_2 & \cdots & \eta_N\eta_N \end{pmatrix} \equiv M \quad (A.4)$$

is the covariance matrix M among observations. On the other hand,

$$z\eta^T = \begin{pmatrix} \underline{\eta}(\gamma_1)\eta_1 & \underline{\eta}(\gamma_1)\eta_2 & \cdots & \underline{\eta}(\gamma_1)\eta_N \\ \underline{\eta}(\gamma_2)\eta_1 & \underline{\eta}(\gamma_2)\eta_2 & \cdots & \underline{\eta}(\gamma_2)\eta_N \\ \vdots & \vdots & \ddots & \vdots \\ \underline{\eta}(\gamma_m)\eta_1 & \underline{\eta}(\gamma_m)\eta_2 & \cdots & \underline{\eta}(\gamma_m)\eta_N \end{pmatrix} \equiv R \equiv \begin{pmatrix} R_{\gamma_1 r} \\ R_{\gamma_2 r} \\ R_{\gamma_3 r} \\ \vdots \\ R_{\gamma_m r} \end{pmatrix} \quad (A.5)$$

is the field covariance matrix between the observational points r_i and each of the points γ_k (recall that $\underline{\eta}(\gamma_k) = 0$). And zz^T is the field covariance matrix $R_{\gamma\gamma}$ among the test-points γ_k :

$$zz^T = R_{\gamma\gamma} = \begin{pmatrix} \underline{\eta}(\gamma_1)\underline{\eta}(\gamma_1) & \underline{\eta}(\gamma_1)\underline{\eta}(\gamma_2) & \cdots & \underline{\eta}(\gamma_1)\underline{\eta}(\gamma_m) \\ \underline{\eta}(\gamma_2)\underline{\eta}(\gamma_1) & \underline{\eta}(\gamma_2)\underline{\eta}(\gamma_2) & \cdots & \underline{\eta}(\gamma_2)\underline{\eta}(\gamma_m) \\ \vdots & \vdots & \ddots & \vdots \\ \underline{\eta}(\gamma_m)\underline{\eta}(\gamma_1) & \underline{\eta}(\gamma_m)\underline{\eta}(\gamma_2) & \cdots & \underline{\eta}(\gamma_m)\underline{\eta}(\gamma_m) \end{pmatrix} \quad (A.6)$$

Hence, equation (A.2) can be written as:

$$P^2 = \frac{1}{m} \text{trace} \{ \underline{\underline{A}}M\underline{\underline{A}}^T - R\underline{\underline{A}}^T - \underline{\underline{A}}R^T + R_{\gamma\gamma} \}.$$

By the matrix identity

$$\underline{\underline{A}}M\underline{\underline{A}}^T - R\underline{\underline{A}}^T - \underline{\underline{A}}R^T = (\underline{\underline{A}} - RM^{-1})M(\underline{\underline{A}} - RM^{-1})^T - RM^{-1}R^T$$

one gets to

$$P^2 = \frac{1}{m} \text{trace} \{ (\underline{\underline{A}} - RM^{-1})M(\underline{\underline{A}} - RM^{-1})^T - RM^{-1}R^T + R_{\gamma\gamma} \}. \quad (A.7)$$

If it is *assumed* that M and $R_{\gamma\gamma}$ are positive definite (i.e., with no negative eigenvalues), the *diagonal* elements of all the summands inside the brackets are positive (Wunsch, 1996). Hence, P would be a minimum only when the first summand vanishes. This is the case if:

$$\underline{\underline{A}} = RM^{-1} \quad (A.8)$$

Note that this equation is valid “row-wise” and, considering the definition of R in terms of the row vectors $R_{\gamma_k r}$ (Equation A.5) and of $\underline{\underline{A}}$ in terms of the row vectors $A(\gamma_k)$ (Equation A.3), it follows:

$$A(\gamma_k) = R_{\gamma_k r} M^{-1},$$

for every γ_k , which concludes the proof.

Note that two important conditions for the validity of the Gauss-Markov theorem are that the the mean value of the physical field must be “considered” zero and the covariance

matrix M *must* be positive definite. Bretherton et al. (1976) have shown that when M is not positive definite the results of OM are “disastrous”. Therefore, to check that the covariance matrix is positive definite is essential in any OM algorithm.

Appendix 2 Estimated error.

An expression for the error involved in the estimated field can be obtained by inserting (A.8) in (A.7):

$$P^2 = \frac{1}{m} \text{trace} \{ R_{\gamma\gamma} - RM^{-1}R^T \}.$$

Expanding this expression and using the definitions of the covariance matrices (Equations (A.5) and (A.6)) yields:

$$P^2 = \frac{1}{m} \sum_{k=1}^m \left[\underline{\eta}^2(\gamma_k) - \sum_{i=1}^N \sum_{j=1}^N \left(\underline{\eta}(\gamma_k) \eta_k \{M^{-1}\}_{ij} \underline{\eta}(\gamma_k) \eta_j \right) \right],$$

where $\{M^{-1}\}_{ij}$ denotes the elements of the inverse of M . Note that this is the mean of the dispersion of the estimated field with respect to the real field as evaluated in each of the m test-points γ_k . The individual dispersion P_k^2 for any point γ_k is given by the expression inside the brackets, which can be rewritten in matricial notation as (Bretherton et al., 1976, his Equation 29; Hiller and Käse, 1983, their Equation 33; Wunsch, 1996, his Equation 3.6.11):

$$P_k^2 = \underline{\eta}^2(\gamma_k) - R_{\gamma_k r} M^{-1} R_{\gamma_k r}^T, \quad (A9)$$

where the row vector $R_{\gamma_k r}$ is given by (A.5).¹

Now, the Gauss Markov theorem states that

$$\hat{\underline{\eta}}(\gamma_k) = R_{\gamma_k r} M^{-1} \underline{\eta}$$

is an estimation of the field $\underline{\eta}$ evaluated in the point γ_k , out of the observations $\underline{\eta}$. Hence,

$$\hat{\rho}(\gamma_k) = R_{\gamma_k r} M^{-1} R_{\gamma_k r}^T$$

is an estimation of the covariance $R_{\gamma_k r}$ between the real field evaluated in γ_k and the observations, i.e., an estimation in which what is being mapped is:

$$R_{\gamma_k} = \begin{pmatrix} \underline{\eta}(\gamma_k) \eta_1 \\ \underline{\eta}(\gamma_k) \eta_2 \\ \vdots \\ \underline{\eta}(\gamma_k) \eta_3 \end{pmatrix}.$$

¹ $\underline{\eta}^2(\gamma_k) - R_{\gamma_k r} M^{-1} R_{\gamma_k r}^T$ are simply the diagonal elements of $R_{\gamma\gamma} - RM^{-1}R^T$. Despite the apparent connection, this is not necessarily obvious and cannot be proved without the intermediate step shown here.

If the estimation point γ_k would be one observational point and if the observation is “perfect”, we have $\eta_k = \underline{\eta}(\gamma_k)$ which, in turn implies

$$\widehat{\rho}(\gamma_k) = R_{\gamma_k^r} M^{-1} R_{\gamma_k^r}^T = \underline{\eta}^2(\gamma_k),$$

Hence, by (A9), a perfect observation implies $P_k^2 = 0$. On the other hand, a measurement completely uncorrelated to the real field would yield $\widehat{\rho}(\gamma_k) = 0$, which in turn implies $P_k^2 = \underline{\eta}^2(\gamma_k)$. With other words: while a measurement that represents the real field *exactly* yields $P_k^2 = 0$, the “worst” possible measurement yields $\underline{\eta}^2(\gamma_k)$, i.e., the variance of the field $\underline{\eta}$. Therefore, the dispersion P_k^2 is a measure of the quality of the observations or, equivalently, a measure of the error involved in the mapping as well as of the variability of the field.

Note that, since the real field is not known, an estimation for $\underline{\eta}^2(\gamma_k)$ must be given *a priori*. This value can be chosen as a “long-term” variance of the field (sometimes called the *variance of the climatological field*).

Index of results' figures

The first row shows the method name. The numbers indicate the figure where the results obtained with each method (as described in the first column) are shown.

	Scalar OMSTA	Vectorial OMSTA	OMPFV
Space-time average		4.1 / 5.1 / 5.7	
Error ellipses		4.1	
Objective map	5.3	5.4	4.2 / 4.3 / 4.7
Stream function		5.5	4.4
Zonal transport		4.5 / 5.2	4.6 / 5.13
Meridional volume transport	5.9	5.10	4.8 / 4.9 / 5.11 / 5.12
Meridional temperature transport			4.11 / 4.12 / 5.15
Meridional salinity transport			4.13
Meridional freshwater transport			4.14
Estern boundary currents			4.15

Bibliography

Barlow, R. J., 1989. *Statistics. A guide to the Use of Statistical Methods in the Physical Sciences.* John Wiley and Sons. 222 pp.

Barnier, B., Marchesiello, P., Miranda, A. P. d., 1996. The impact of seasonal forcing on the variability of the meridional heat flux at 30°S using a sigma-coordinate primitive equation model. *International WOCE Newsletter*(24), 16-23.

Batchelor, G. K., 1990. *The theory of homogeneous turbulence.* Cambridge Science Classics. Cambridge University Press. 197 pp.

Baum, S. K., 2004. Glossary of physical oceanography and related disciplines. Internet webpage. <http://stommel.tamu.edu/~baum/paleo/ocean/ocean.html>. Access: 24th of June, 2004

Baumgartner, A., Reichel, E., 1975. *The world water balance.* R. Oldenbourg. 179 pp.

Bearman, G., 1989. *Ocean circulation.* Open University course team. Pergamon Press. 238 pp.

Belkin, I. M., Gordon, A. L., 1996. Southern Ocean fronts from the Greenwich meridian to Tasmania. *Journal of Geophysical Research. C. Oceans [J. GEOPHYS. RES. (C OCEANS)]* 101 (C2), 3675-3696.

Bennett, A. F., 1978. Poleward heat fluxes in southern hemisphere oceans. *Journal of Physical Oceanography* 8 785-798.

Berger, W. H., Wefer, G., 1996. Central themes of South Atlantic circulation. *The South Atlantic: present and past circulation.* G. Wefer, W. H. Berger, G. Siedler and D. Webb, Springer. pp. 644.

Bishop, J. K. B., Davis, R. E., Sherman, J. T., 2002. Robotic observations of dust-storm enhancement of carbon biomass in the north Pacific. *Science* 298 817–821.

Boddem, J., Schlitzer, R., 1994. Interocean exchange and meridional mass and heat fluxes in the South Atlantic. *Journal of Physical Oceanography* 100 (C8), 15821-15834.

Boebel, O., Schmid, C., Zenk, W., 1997. Flow and recirculation of Antarctic Intermediate Water across the Rio Grande Rise. *Journal of Geophysical Research* 102 (C9), 20967 - 20986.

Boebel, O., Davis, R. E., Ollitrault, M., Peterson, R. G., Richardson, P. L., Schmid, C., Zenk, W., 1999a. The intermediate depth circulation of the western South Atlantic. *Geographical Research Letters* 26 (21), 3329 - 3332.

Boebel, O., Schmid, C., Podestá, G., Zenk, W., 1999b. Intermediate water at the Brazil-Malvinas confluence zone: a Lagrangian view. *Journal of Geophysical Research* 104 (C9), 21063-21082.

Boebel, O., Schmid, C., Zenk, W., 1999c. Kinematic elements of Antarctic Intermediate Water in the western South Atlantic. *Deep-Sea Research II* 46 (1/2), 355-392.

Boebel, O., Anderson-Fontana, S., Schmid, C., Ansorge, I., Lazarevich, P., Lutjeharms, J., Prater, M., Rossby, T., Zenk, W., 2000. KAPEX RAFOS float data report 1997-1999; Part A: The Agulhas- and South Atlantic current components. Kiel. Institut für Meereskunde an der Christian-Albrechts-Universität-Kiel. 318 194 pp.

Boebel, O., Lutjeharms, J., Schmid, C., Zenk, W., Rossby, T., Barron, C., 2003. The Cape Cauldron: A regime of turbulent interocean exchange. *Deep-Sea Research II* 50 (1), 57-86.

Böning, C. W., 1988. Characteristics of particle dispersion in the North Atlantic: An alternative interpretation of SOFAR float results. *Deep-Sea Research* 35 1379 - 1385.

Böning, C. W., Cox, M. D., 1988. Particle dispersion and mixing of conservative properties in an eddy-resolving model. *Journal of Physical Oceanography* 18 320-338.

Box, G. E. P., Jenkins, G. M., 1976. *Time series analysis : forecasting and control*. San Francisco. Holden Day. 575 pp.

Brennecke, W., 1921. Die ozeanographischen Arbeiten der deutschen Antarktischen Expedition, 1911-1912. *Arch. deutsch. Seewarte* XXXIX. Hamburg.

Bretherton, F. P., Davis, R. E., Fandry, C. B., 1976. A technique for objective analysis and design of oceanographic experiments applied to MODE-73. *Deep-Sea Res.* 23 559-582.

Bretherton, F. P., Williams, J. C., 1980. Estimations from irregular arrays. *Reviews of Geophysics and Space Physics* 18 (4), 789-812.

Broecker, W. S., Peteet, D., Rind, D., 1985. Does the ocean-atmosphere have more than one stable mode of operation? *Nature* 315 21-25.

Broecker, W. S., 1987. The biggest chill. *Natural History Magazine* 97 74-82.

Broecker, W. S., 1991. The great ocean conveyor. *Oceanography* 4 (2), 79-88.

Broecker, W. S., 1997a. Will Our Ride into the Greenhouse Future be a Smooth One? *GSA Today* 7 (5), 1-7.

Broecker, W. S., 1997b. Thermohaline circulation, the Achilles heel of our climate system: Will man-made CO₂ upset the current balance? *Science* 278 (5343), 1582-1588.

Broecker, W. S., 1999. What If the conveyor were to shut down? Reflections on a possible outcome of the great global experiment. *GSA Today* 9 (1), 2-4.

Bryan, K., 1962. Measurements of meridional heat transport by ocean currents. *Journal of Geophysical Research* 67 3403–3414.

Bryden, H. L., Imawaki, S., 2001. Ocean heat transport. *Ocean Circulation and Climate*. G. Siedler and J. Church, Academic Press.

Buchanan, J. Y., 1877. On the distribution of salt in the ocean, as indicated by the specific gravity of its waters. *Journal of the Royal Geographical Society* 47 72-86.

Budyko, M. I., 1963. Atlas of heat balance of the earth (in Russian). Moscow. Akad. Nauk SSSR (URSS Academy of Sciences), Prezidium. Mezhdovedomstvennyi Globnaia Geofiz. Observ. Komitet. 69 pp.

Bunker, A. F., 1976. Computations of the surface energy flux and annual air-sea interaction cycles of the North Atlantic Ocean. *Monthly Weather Review* 108 720-732.

Buscaglia, J. L., 1971. On the circulation of the Intermediate Water in the southwestern Atlantic Ocean. *Journal of Marine Research* 29 245-255.

Byrne, D. A., Gordon, A. L., Haxby, W. F., 1995. Agulhas eddies: A synoptic view using Geosat ERM data. *Journal of Physical Oceanography* 25 (5), 902-917.

Carter, R. M., McCave, I. N., Carter, L., 2004. Leg 181 synthesis: fronts, flows, drifts, volcanoes, and the evolution of the southwestern gateway to the Pacific Ocean, eastern New Zealand. In Richter, C. (Ed.), Proc. ODP, Sci. Results, 181.

Dagg, M., Benner, R., Lohrenz, S., Lawrence, D., 2004. Transformation of dissolved and particulate materials on continental shelves influenced by large rivers: plume processes. *Continental Shelf Research* 24 833 -858.

D'Asaro, E. A., D.M. Farmer, J.T. Osse, G. T. Dairiki, 1996. A Lagrangian float. *Journal of Atmospheric and Oceanic Technology* 13 (6), 1230-1246.

Davis, R. E., 1985. Objective Mapping by Least Squares Fitting. *Journal of Geophysical Research* 90 (C3), 4773-4777.

Davis, R. E., 1991. Lagrangian ocean studies. *Annual Review of Fluid Mechanics* 23 43-64.

Davis, R. E., Webb, D. C., Regier, L. A., Dufour, J., 1992. The Autonomous Lagrangian Circulation Explorer. *Journal of Atmospheric and Oceanic Technology* 9 264 - 285.

Davis, R. E., Killworth, P. D., Blundell, J. R., 1996. Comparison of Autonomous Lagrangian Circulation Explorer and Fine Resolution Antarctic Model results in the South Atlantic. *Journal of Geophysical Research* 101 (C1), 855 - 884.

Davis, R. E., 1998. Preliminary results from directly measuring mid-depth circulation in the tropical and south Pacific. *Journal of Geophysical Research* 103 (C11), 24619-24639.

de Ruijter, W., 1982. Asymptotic analysis of the Agulhas and Brazil Current systems. *Journal of Physical Oceanography* 12 361-373.

de Ruijter, W. P. M., Biastoch, A., Drijfhout, S. S., Lutjeharms, J. R. E., Matano, R. P., Pichevin, T., van Leewen, P. J., Weijer, W., 1999. Indian-Atlantic interocean exchange: Dynamics, estimation and impact. *Journal of Geophysical Research* 104 (C9), 20885-20910.

Deacon, G. R. E., 1933. A general account of the hydrology of the South Atlantic Ocean. *Discovery Reports* 7 171 - 238.

Defant, A., 1941. Quantitative Untersuchungen zur Statik und Dynamik des Atlantischen Ozeans. *Wissenschaftliche Ergebnisse der Deutschen Atlantischen Expedition auf dem*

Forschungs und Vermessungsschiff METEOR 1925-27. Berlin und Leipzig, Walter de Gruyter und Co. 6, pp. 191-260.

Emerson, S., Stump, C., Johnson, B., Karl, D. M., 2002. In-situ determination of oxygen and nitrogen dynamics in the upper ocean. *Deep-Sea Research I* 49 941–952.

Emery, W. J., 1977. Antarctic Polar Frontal Zone from Australia to the Drake Passage. *Journal of Physical Oceanography* 7 (6), 811–822.

Emery, W. J., Thomson, R. E., 1997. *Data analysis methods in physical oceanography*. Oxford. Elsevier. 634 pp.

Freeland, H. J., Rhines, P. B., Rossby, T., 1975. Statistical observations of the trajectories of neutrally buoyant floats in the North Atlantic. *Journal of Marine Research* 33 (3), 383-404.

Fu, L.-L., 1981. The general circulation and meridional heat transport of the subtropical South Atlantic determined by inverse methods. *Journal of Physical Oceanography* 11 1171-1193.

Ganachaud, A., Wunsch, C., 2000. Improved estimates of global ocean circulation, heat transport and mixing from hydrographic data. *Nature* 408 453-457.

Ganachaud, A., Wunsch, C., 2002. Large-scale ocean heat and freshwater transports during the World Ocean Circulation Experiment. *Journal of Climate* 16 696-705.

Gandin, L. S., 1963. *Objective Analysis of Meteorological Fields*. Leningrad. Gidrometizdat. 287 pp.

Garzoli, S. L., Gordon, A. L., 1996. Origins and variability of the Benguela current. *Journal of Geophysical Research. C. Oceans* 101 (1), 897-906.

Gelb, A., 1974. *Applied optimal estimation*. The MIT Press. 382 pp.

Georgi, D. T., Toole, J. M., 1982. The Antarctic Circumpolar Current and the oceanic heat and fresh water budgets. *Journal of Marine Research Supplement to* 40 183-197.

Gille, S. T., 2003. Float observations of the Southern Ocean, Part1: estimating mean fields, bottom velocities and topographic steering. *Journal of Physical Oceanography* 33 1167-1181.

Gordon, A. L., 1985. Indian-Atlantic transfer of thermocline water at the Agulhas Retroflection. *Science (Washington)* 227 (4690), 1030-1033.

Gordon, A. L., 1986. Interocean exchange of thermocline water. *Journal of Geophysical Research* 91 5037-5046.

Gordon, A. L., Bosley, K. T., 1991. Cyclonic gyre in the tropical South Atlantic. *Deep Sea Research*. 38, pp. 323-343.

Gordon, A. L., Weiss, R. F., Smethie, W. M., Jr., Warner, M. J., 1992. Thermocline and intermediate water communication between the South Atlantic and Indian Oceans. *Journal of Geophysical Research* 97 (C5), 7223-7240.

Gould, J., 2002. A brief history of float developments. Southampton Oceanography Centre. Internet webpage. <http://www.soc.soton.ac.uk/JRD/HYDRO/argo/history.php>. Access: June, 2005

Gould, W. J., 2005. From Swallow floats to Argo—the development of neutrally buoyant floats. *Deep-Sea Research II* 52 529–543.

Hall, M. M., Bryden, H. L., 1982. Direct estimates and mechanisms of ocean heat transport. *Deep-Sea Research* 29 (3A), 399-359.

Hastenrath, S., 1980. Heat budget of tropical ocean and atmosphere. *Journal of Physical Oceanography* 10 (159-170).

Hastenrath, S., 1982. On meridional heat transports in the world ocean. *Journal of Physical Oceanography* 12 922-927.

Hiller, W., Käse, R. H., 1983. Objective Analysis of Hydrographic Data Sets from Mesoscale Surveys. *Berichte aus dem Institut für Meereskunde an der Christian-Albrechts-Universität Kiel* 116 78 pp.

Hogg, N. G., Owens, B., W., 1999. Direct measurement of the deep circulation within the Brazil Basin. *Deep-Sea Research Part II* 46 (1-2), 335 - 353.

Holfort, J., 1994. Großräumige Zirkulation und meridionale Transporte im Südatlantik,. Ph.D. Thesis. Abt. Meeresphysik. Institut für Meereskunde. Kiel. 96 pp.

Holfort, J., Siedler, G., 1997. The heat and mass transport in the South Atlantic. *International WOCE Newsletter* 28 3-5.

Holfort, J., Siedler, G., 2001. The meridional oceanic transports of heat and nutrients in the South Atlantic. *Journal of Physical Oceanography* 31 (1), 5-29.

Hsiung, J., 1985. Estimates of global oceanic meridional heat transport. *Journal of Physical Oceanography* 15 (11), 1405-1413.

Institut français de recherche pour l'exploitation de la mer, 2004. Le flotteur de subsurface MARVOR. Internet webpage. <http://www.ifremer.fr/francais/produits/base.htm>. Access: June, 2005

International Argo project, 2005. Argo.Net. Internet webpage. <http://www.argo.net/>. Access: June, 2005

Izawa K., Mizuno, K., Miyazaki, M., Inoue, A., Ando, K., Takatsuki, Y., Kobayashi, T., Takeuchi, K., 2002. On the weight adjustment of profiling floats. Argo technical report FY2001, JAMSTEC 18-35.

Jackett, D. R., McDougall, T. J., 1997. A neutral density variable for the world's oceans. *Journal of Physical Oceanography* 27 (2), 237-263.

Jenkins, G. M., Watts, D. G., 1968. *Spectral analysis and its applications*. Holden-Day. 525 pp.

Jochum, M., Malanotte-Rizzoli, P., 2003. The flow of AAIW along the equator. *Interhemispheric Water Exchanges in the Atlantic Ocean* In Press.

Jung, G. H., 1955. Heat transport in the Atlantic Ocean. Ref. 53-34T, Dep. of Oceanography. Texas A&M, College Station.

Kagan, R. L., 1997. *Averaging of Meteorological Fields*. Kluwer Academic Publishers. 279 pp.

Kamen, E. W., Su, J., 1999. *Introduction to Optimal Estimation*. Springer-Verlag Telos. pp.

Kirwan, A. D., 1963. Circulation of Antarctic Intermediate Water deduced from isentropic analysis. Texas A&M University Reference 63-34F.

LaCasce, 2000. Floats and f/H. *Journal of Marine Research* 58 61-95.

Levitus, S., 1994. Climatological atlas of the world ocean. International Research Institute for Climate Prediction (IRI). Internet webpage. <http://iridl.ldeo.columbia.edu/SOURCES/.LEVITUS/>. Access: 20th of July, 2004

Lewis, E. L., 1980. The practical salinity scale 1978 and its antecedents. *IEEE Journal of Oceanic Engineering* OE-5 (1), 3-8.

Liebelt, P. B., 1967. *An Introduction to Optimal Estimation*. Addison-Wesley. 273 pp.

Lutjeharms, J. R. E., van Ballegooyen, R. C., 1988. The retroflection of the Agulhas Current. *Journal of Physical Oceanography* 18 (11), 1570-1583.

Lutjeharms, J. R. E., 1996. The exchange of water between the South Indian and South Atlantic Oceans. *The South Atlantic: present and past circulation*. G. Wefer, W. H. Berger, G. Siedler and D. Webb. Berlin-Heidelberg, Springer-Verlag. pp. 122 - 162. submitted

Lutjeharms, J. R. E., Cooper, J., 1996. Interbasin leakage through Agulhas current filaments. *Deep-Sea Research I* 43 (2), 213-238.

Macdonald, A., Wunsch, C., 1996. An estimate of global ocean circulation and heat fluxes. *Nature* 382 436-439.

Macdonald, A. M., 1993. Property fluxes at 30°S and their implications for the Pacific-Indian troughflow and the global heat budget. *Journal of Geophysical Research* 98 6851-6868.

Martineau, D. P., 1953. The influence of the current systems and lateral mixing upon the AAIW in the South Atlantic. WHOI 53-72. 11 pp.

Matano, R., Philander, G., 1993. Heat and mass balances of the South Atlantic ocean calculated from a numerical model. *Journal of Geophysical Research* 98 (C1), 977-984.

MATLAB, 2000. User's guide. Fifth printing. Revised for MATLAB 6 (Release 12). The MathWorks, Inc. November 2000.

McCartney, M. S., 1977. Subantarctic Mode Water. A voyage of DISCOVERY, George Deacon Anniversary Volume. M. Angel, Pergamon Press. pp. 103 - 119.

McDougall, T. J., 1987. Neutral surfaces. *Journal of Physical Oceanography* 17 (11), 1950-1964.

Millero, F. J., Perron, G., Desnoyers, J. F., 1973. Heat capacity of seawater solutions from 5 to 35 °C and 0.05 to 22 ‰ chlorinity. *Journal of Geophysical Research* 78 (21), 4499 -4506.

Model, F., 1950. Warmwasserheizung Europas. *Berichte Deutsche Wetterdienstes* 12 51-60.

Molinari, R. L., Voituriez, B., Duncan, P., 1981. Observations in the subthermocline undercurrent of the equatorial South Atlantic Ocean: 1978-1980. *Oceanologica Acta* 4 451-456.

Molinari, R. L., Garzoli, S. L., Schmitt, R. W., 1999. Equatorial currents at 1000m in the Atlantic Ocean. *Geophysical Research Letters* 26 (3), 361-364.

Molinelli, E., 1981. The Antarctic influence on Antarctic intermediate Water. *Journal of Marine Research* 39 267-293.

Müller, T. J., 1987. Analyse niederfrequenter Strömungsschwankungen im Nordostatlantik. *Berichte aus dem Institut für Meereskunde Kiel* 170 134.

Munk, W. H., 1950. On the wind-driven ocean circulation. *Journal of Meteorology* 7 (2), 79-93.

Núñez-Riboni, I., Boebel, O., Ollitrault, M., You, Y., Richardson, P., Davis, R., 2005. Lagrangian circulation of Antarctic Intermediate Water in the subtropical South Atlantic. *Deep-Sea Research II* 52 545-564.

Olbers, D., Gouretski, V., Seiß, G., Schröter, J., 1992. *Hydrographic Atlas of the Southern Ocean*. Bremerhaven. Alfred Wegener Institut. 82 pp.

Ollitrault, M., 1994. The TOPOGOLF experiment: Lagrangian data. Brest, France. IFREMER - Centre de Brest. 622 pp.

Ollitrault, M., Loaec, G., Dumortier, C., 1994. MARVOR: A multi-cycle RAFOS float. *Sea Technology* 35 (2), 39-44.

Ollitrault, M., Auffret, Y., Cortès, N., Hémon, C., Jégou, P., Le Reste, S., Loaëc, G., Rannou, J.-P., 1995. The SAMBA experiment: SAMBA I Lagrangian and CTD data, February 1994 - August 1995. *Repères Océan* nr. 14. Plouzané, France, IFREMER. pp. 1 - 488.

Oort, A. H., J. P. Peixoto, 1983. Global angular momentum and energy balance requirements from observations. *Advances in Geophysics* 25 355-490.

OPTIMARE Sensorsysteme AG, 2005. Operational Oceanography. Internet webpage. http://www.optimare.de/sensor/operationaloceanography_EN.html. Access: June, 2005

Peterson, R. G., Stramma, L., 1991. Upper-level circulation in the south atlantic. *Progress in Oceanography* 26 1-73.

Peterson, R. G., 1992. On the boundary currents in the western Argentine Basin. *Deep-Sea Research* 39 623-644.

Philander, S. G. H., R.C. Pacanowski, 1986. The mass and heat budget in a model of the tropical Atlantic ocean. *Journal of Geophysical Research* 91 (C12), 14212-14220.

Pickard, G., Emery, W. J., 1990. *Descriptive physical oceanography: An introduction*. Pergamon Press. 320 pp.

Piola, A. R., Georgi, D. T., 1982. Circumpolar Properties of Antarctic Intermediate Water and Subantarctic Mode Water. *Deep-Sea Research* 29 687-711.

Piola, A. R., Gordon, A. L., 1989. Intermediate waters in the southwest South Atlantic. *Deep-Sea Research* 36 (1A), 1-16.

Pond, S., Pickard, L., 1978. *Introductory dynamic oceanography*. Pergamon Press. 349 pp.

Rahmstorf, S., 1996. On the freshwater forcing and transport of the Atlantic thermohaline circulation. *Climate Dynamics* 12 799-811.

Rahmstorf, S., 1999. Currents of change: Investigating the ocean's role in climate. Essay for the McDonnell Foundation Centennial Fellowship 1999.

Reid, J. L., 1964. Evidence of a south equatorial counter current in the Atlantic Ocean in July 1963. *Nature* 203 (182).

Reid, J. L., Nowlin, W. D., Patzert, W. C., 1977. On the characteristics and circulation of the southwestern Atlantic Ocean. *Journal of Physical Oceanography* 7 (1), 62-91.

Reid, J. L., 1989. On the total geostrophic circulation of the South Atlantic Ocean: Flow patterns, tracers and transports. *Progress in Oceanography* 23 (3), 149-244.

Reid, J. L., 1994. On the total geostrophic circulation of the North Atlantic Ocean: flow patterns, tracers and transports. *Progress in Oceanography* 33 1 - 92.

Reid, J. R., 1996. On the circulation of the South Atlantic Ocean. *The South Atlantic: Present and past circulation*. G. Wefer, W. H. Berger, G. Siedler and D. J. Webb. Berlin Heidelberg, Springer-Verlag. pp. 13 - 44.

Richardson, P. L., 1992. Velocity and eddy energy of the Gulf Stream System from 700-m SOFAR floats subsampled to simulate Pop-Up floats. *Journal of Atmospheric and Oceanic Technology* 9 495-503.

Richardson, P. L., Schmitz, W. J., 1993. Deep cross-equatorial flow in the Atlantic measured with SOFAR floats. *Journal of Geophysical Research* 98 8371 - 8388.

Richardson, P. L., Garzoli, S. L., 2003. Characteristics of Intermediate Water flow in the Benguela Current as measured with RAFOS floats. *Deep Sea Research II* 50 (1), 87-118.

Rintoul, S. R., 1991. South Atlantic interbasin exchange. *Journal of Geophysical Research* 96 2675-2692.

Rintoul, S. R., Hughes, C. W., Olbers, D., 2001. The Antarctic Circumpolar Current System. *Ocean Circulation and Climate*. G. Siedler, J. Church and J. Gould, Academic Press. 77,

Roemmich, D., 1983. The balance of geostrophic and Ekman transports in the tropical Atlantic Ocean. *Journal of Physical Oceanography* 13 1534-1539.

Rossby, H. T., Webb, D. C., 1970. Observing abyssal motions by tracking swallow floats in the SOFAR channel. *Deep-Sea Research* 17 359-365.

Rossby, H. T., Levine, E. R., Connors, D. N., 1985. The isopycnal Swallow Float - a simple device for tracking water parcels in the ocean. *Progress in Oceanography* 14 511-525.

Rossby, H. T., Dorson, D., Fontaine, J., 1986. The RAFOS System. *Journal of Atmospheric and Oceanic Technology* 3 (4), 672-679.

Russell, G. L., Miller, J. R., Tsang, L.-C., 1985. Seasonal oceanic heat transports computed from an atmospheric model. *Dynamics of Atmosphere and Oceans* 9 253-271.

Sarmiento, J. L., Willebrand, J., Hellerman, S., 1982. Objective Analysis of Tritium Observations in the Atlantic Ocean During 1971-74. *Ocean Tracers Laboratory Technical Report #1*.

Saunders, P. M., King, B. A., 1995. Bottom currents derived from shipborne ADCP on WOCE cruise A11 in the South Atlantic. *Journal of Physical Oceanography* 25 329-347.

Schlitzer, R., 1996. Mass and heat transports in the South Atlantic derived from historical hydrographic data. *The South Atlantic. Present and Past Circulation*. G. Wefer, W. H. Berger, G. Siedler and D. J. Webb, Springer.

Schmid, C., 1998. Die Zirkulation des Antarktischen Zwischenwassers im Südatlantik. Ph. D. Thesis. Dept. of Ocean Physics. University of Kiel. Kiel. 104 pp.

Schmid, C., Siedler, G., Zenk, W., 2000. Dynamics of intermediate water circulation in the subtropical South Atlantic. *Journal of Physical Oceanography* 30 (12), 3191-3211.

Schmid, C., Molinari, R. L., Garzoli, S. L., 2001. New observations of the intermediated depth circulation in the tropical Atlantic. *Journal of Marine Research* 59 281-312.

Schmid, C., Garraffo, Z., Johns, E., Garzoli, S. L., 2003. Pathways and variability at intermediate depths in the tropical Atlantic. *Interhemispheric Water Exchange in the Atlantic Ocean*. G. J. Goni and P. Malanotte-Rizzoli, Elsevier. pp. 233-268.

Schmitz, W. J., 1995. On the interbasin-scale thermohaline circulation. *Reviews of Geophysics* 33 (2), 151-173.

Schott, F. A., Stramma, L., Fischer, J., 1995. The warm water inflow into the western tropical Atlantic boundary regime, spring 1994. *Journal of Geophysical Research* 100 (C12), 24745 - 24760.

Schott, F. A., Fischer, J., Stramma, L., 1998. Transports and pathways of the upper-layer circulation in the western tropical Atlantic. *Journal of Physical Oceanography* 28 1904-1928.

Sloyan, B. M., Rintoul, S. R., 2001a. The Southern Ocean limb of the global deep overturning circulation. *Journal of Physical Oceanography* 31 143-173.

Sloyan, B. M., Rintoul, S. R., 2001b. Circulation, renewal, and modification of Antarctic Mode and Intermediate Water. *Journal of Physical Oceanography* 31 (4), 1005-1030.

Smith, W. H. F., Sandwell, D. T., 1997. Global seafloor topography from satellite altimetry and ship depth soundings. *Science*.

Speer, K. G., Holfort, J., Reynaud, T., Siedler, G., 1996. South Atlantic heat transport at 11°S. *The South Atlantic: Present and Past Circulation*. G. Wefer, W. Berger, H., G. Siedler and D. J. Webb. Berlin Heidelberg, Springer-Verlag. pp. 105 - 120.

Speich, S., Blanke, B., Vries, P. d., Drijfhout, S., Döös, K., Ganachaud, A., Marsh, R., 2002. Tasman leakage: A new route in the global ocean conveyor belt. *Geographical Research Letters* 29 (10), 55-1 -- 55-4.

Stewart, R. H., 2002. *Introduction To Physical Oceanography*. Texas A & M University. 342 pp.

Stommel, H., 1948. The westward intensification of wind-driven ocean currents. *Transactions American Geophysical Union* 29 (2), 202–206.

Stramma, L., Peterson, R. G., 1989. Geostrophic transport in the Benguela current region. *Journal of Physical Oceanography* 19 1440-1448.

Stramma, L., Ikeda, Y., Peterson, R. G., 1990. Geostrophic transport in the Brazil current region north of 20°S. *Deep Sea Research* 37 (12), 1875-1886.

Stramma, L., Peterson, R., 1990. The South Atlantic Current. *Journal of Physical Oceanography* 20 (6), 846 - 859.

Stramma, L., England, M., 1999. On the water masses and mean circulation of the South Atlantic Ocean. *Journal of Geophysical Research* 104 (C9), 20863-20883.

Stramma, L., Schott, F. A., 1999. The mean flow field of the tropical Atlantic Ocean. *Deep-Sea Research II* 46 279-303.

Suga, T., Talley, L. D., 1995. Antarctic Intermediate Water circulation in the tropical and subtropical South Atlantic. *Journal of Geophysical Research* 100 (C7), 13441-13453.

Sverdrup, H. U., 1947. Wind-driven currents in a baroclinic ocean: with application to the equatorial currents of the eastern Pacific. *Proceedings of the National Academy of Sciences* 33 (11), 318–326.

Swallow, J. C., 1955. A neutral-buoyancy float for measuring deep currents. *Deep-Sea Research* 3 (1), 74-81.

Swallow, J. C., Worthington, L. V., 1961. An observation of a deep countercurrent in the western North Atlantic. *Deep-Sea Research* 8 1 - 19.

Swift, D. D., Riser, S. C., 1994. RAFOS floats: defining and targeting surfaces of neutral buoyancy. *Journal of Atmospheric and Oceanic Technology* 11 (4), 1079–1092.

Taft, B. A., 1963. Distribution of salinity and dissolved oxygen on surfaces of uniform potential specific volume in the South Atlantic, South Pacific, and Indian oceans. *Journal of Marine Research* 21 (2), 129-146.

Talley, L. D., 1996. Antarctic Intermediate Water in the South Atlantic. *The South Atlantic: present and past circulation*. G. Wefer, W. H. Berger, G. Siedler and D. Webb. Berlin-Heidelberg, Springer-Verlag. pp. 219-238.

Talley, L. D., 2000. *Introduction to Physical Oceanography*, Fall, 2000. Scripps Institution of Oceanography. University of California San Diego. Internet webpage. <http://sam.ucsd.edu/sio210/>. Access: July, 2005

Tomczak, M., Godfrey, J. S., 1994. *Regional oceanography: An introduction*. Pergamon. 422 pp. Now downloadable from Internet at: <http://gaea.es.flinders.edu.au/~mattom/regoc/pdfversion.html> (18th of may, 2004).

Treguier, A. M., Hogg, N. G., Maltrud, M., Speer, K., Thierry, V., 2003. The Origin of Deep Zonal Flows in the Brazil Basin. *Journal of Physical Oceanography* 33 (3), 580–599.

Trenberth, K. E., Caron, J. M., 2001. Estimates of meridional atmosphere and ocean heat transports. *Journal of Climate* 14 3433-3443.

University of California San Diego, 2004. Argo home page of the UCSD. Internet webpage. <http://www-argo.ucsd.edu/solo2.html>. Access: May, 2004

Vanicek, M., Siedler, G., 2002. Zonal fluxes in the deep water layers of the western south atlantic ocean. *Journal of Physical Oceanography* 32 (8), 2205-2235.

Von Drygalski, E. V., 1927. Deutsche Südpolar Expedition, 1901-1903, VII, Ozeanographie.

Washington Department of Natural Resources, 1995. Surveyor's guidebook on relative accuracy. Report from the Public Land Survey Office and Survey Advisory Board. 74 pp.

Webb Research Corporation, 2004. Apex float. Internet webpage. <http://www.webbresearch.com/apex.htm>. Access: June, 2005

Wijffels, S. E., 2001. Ocean transport of fresh water. *Ocean Circulation and Climate*. G. Siedler, J. Church and J. Gould, Academic Press.

Woods Hole Oceanographic Institution, 2003. Autonomous Temperature and Salinity profiling. Internet webpage. <http://hrp.whoi.edu/floats/>. Access: June 2005

Wunsch, C., 1996. The ocean circulation inverse problem. Cambridge University Press. 442 pp.

Wüst, G., 1935. Schichtung und Zirkulation des Atlantischen Ozeans, Die Stratosphäre. *Wissenschaftliche Ergebnisse der Deutschen Atlantischen Expedition auf dem Forschungs- und Vermessungsschiff "Meteor" 1925-1927*. 6. 180 pp. English translation edited by William J. Emery: "The stratosphere of the Atlantic Ocean. Scientific Results of the German Atlantic Expedition of the Research Vessel 'Meteor' 1925-27". Published by Amerind Publishing Co., 1978.

Wüst, G., 1957. Stromgeschwindigkeiten und Strommengen in den Tiefen des Atlantischen Ozeans. *Wissenschaftliche Ergebnisse der Deutschen Atlantischen Expedition "Meteor" 1925/27*. Berlin 6, Part 2, pp. 261 - 420.

You, Y., 1999. Diapycnocline mixing, transformation and transport of Antarctic Intermediate Water in the South Atlantic Ocean. *Deep-Sea Research II* 46 393-435.

You, Y., 2002a. Quantitative estimate of Antarctic Intermediate Water contributions from the Drake Passage and the southwest Indian Ocean to the South Atlantic. *Journal of Geophysical Research* 107 (C4).

You, Y., 2002b. Diapycnocline exchange between intermediate and deep water in the tropical Atlantic. *Journal of Geophysical Research* 107 (C3).

You, Y., Lutjeharms, J., Boebel, O., de Ruijter, W. P. M., 2003. Quantification of the interocean exchange of intermediate water masses around southern Africa. *Deep-Sea Research II* 50 (1), 197-228.

Acknowledgements

With the hope that I did not forget a name and that the order will not upset someone:

- My deepest gratitude belongs to Dr. Olaf Boebel, who never lost a chance to take me to the edge of my capabilities. His patience, teaching aptitudes and passion for physical oceanography were the main motor of this study.
- Dr. John Y. You (University of Sydney Institute of Marine Science, Australia) provided the neutral density surfaces and geostrophic velocities of the AAIW layer, as well as Figure 0.8 and Figures 2.2 to 2.4. The extensive correspondence with him about neutral density and other topics is highly appreciated.
- Besides Olaf Boebel and John Y. You, the other co-authors of Núñez-Riboni et al., 2005, Michel Ollitrault (Institut Français de Recherche pour l'Exploitation de la Mer, France), Russ Davis (Scripps Institution of Oceanography, USA) and Philip L. Richardson (Woods Hole Oceanographic Institution, USA), have influenced the development of this study as well. Michel Ollitrault and Russ David also provided a large amount of the historical float data (SAMBA and WOCE/CORP, respectively).
- Prof. Peter Lemke and the head of my group (Ocean Field Studies, OFIS) in the Alfred Wegener Institute (AWI), Dr. Eberhard Fahrbach, always had the best attitude to enrich this work by supporting my participation in meetings and summer schools. Eberhard Fahrbach (together with Olaf Boebel) is also responsible for the float data from AWI.
- My colleagues from the OFIS group in AWI have assisted me constantly during my PhD: Marietta Weigelt has helped me with enduring diligence in so many administrative processes that I do not have words to express my gratitude to her. Gerd Rohardt supported always my computing problems and discussions with Olaf Klatt and Ursula Schauer about heat transport were very helpful.
- Discussions with my PhD colleagues and friends, Dmitry Sidorenko and Sven Harig, were always enriching. This study owns to them more than I can account for.
- Claudia Schmid (Atlantic Oceanographic and Meteorological Laboratory, National Oceanic and Atmospheric Administration, USA) helped with access to the NOAA-AOML/Argo dataset with which this work started in February 2002.
- Prof. Reiner Schlitzer (AWI) gave good advices about Objective Analysis.
- Discussions with Prof. Wolfgang Hiller (AWI) about Objective Analysis, in general, and about Hiller and Käse (1983), in particular, were very useful.
- Prof. Lynne Talley (Scripps Institution of Oceanography, USA) promptly provided an original of Figure 0.4 under the pressing circumstances of meeting the publication deadline of Núñez-Riboni et al. (2005) together with boarding RS Polarstern for a survey of two months and a half. Due to a lack of time, an acknowledgement to her in the paper was not possible.

- Correspondence with Prof. Thomas Rossby (Graduate School of Oceanography, University of Rhode Island, USA) about the estimated longitudinal covariance function led to a better interpretation of it.
- Igor M. Belkin (Graduate School of Oceanography, University of Rhode Island, USA) kindly provided Figure 0.5.
- Prof. Dirk Olbers from AWI suggested to refer the temperature and salt transports of AAIW to the mean vertical values in the South Atlantic to get the contributions of the water mass to the corresponding budgets in the basin.
- Thierry Penduff and Jean-Marc Molines (both from the Laboratoire des Ecoulements Géophysiques et Industriels, France) kindly provided the output of the circulation model CLIPPER to contrast our meridional transport. Due to a time issue, this comparison was not possible but their solicitous involvement is appreciated.
- Hendrick Sander from Bremen University dragged my attention to variograms and covariance functions.
- Arthur J. Mariano and William E. Johns (both from the University of Miami, USA) commented by e-mail about the transport of the North Brazil Current and the iWBC.
- Dr. Martin Losch (AWI) helped with advices about differential equations in an attempt to infer Equation (3.28) by integrating Equation (3.20).
- The International Argo Program and Coriolis, as well as all their individual providers of float data are highly acknowledged.
- Jon Eric Gilson (Scripps Institution of Oceanography, USA) and Young-Gyu Park (Korea Ocean Research and Development Institute, Korea) provided directly float data from Argo before I got familiarized with the data acquirement.
- This work was partially supported through (USA) MSN-Grant no. OCE-0095647 and a Dokstorstelle BAT/2 from the Alfred Wegener Institut für Polar- und Meeresforschung.
- Gratitude words for my nearest and dearest, like my parents, my brother and my friends, do not fit in these pages. I will rather try to thank them in some other way.

Printed the 10th of August, 2005,
in Bremerhaven, Germany